

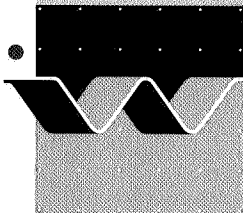
number 476

publications

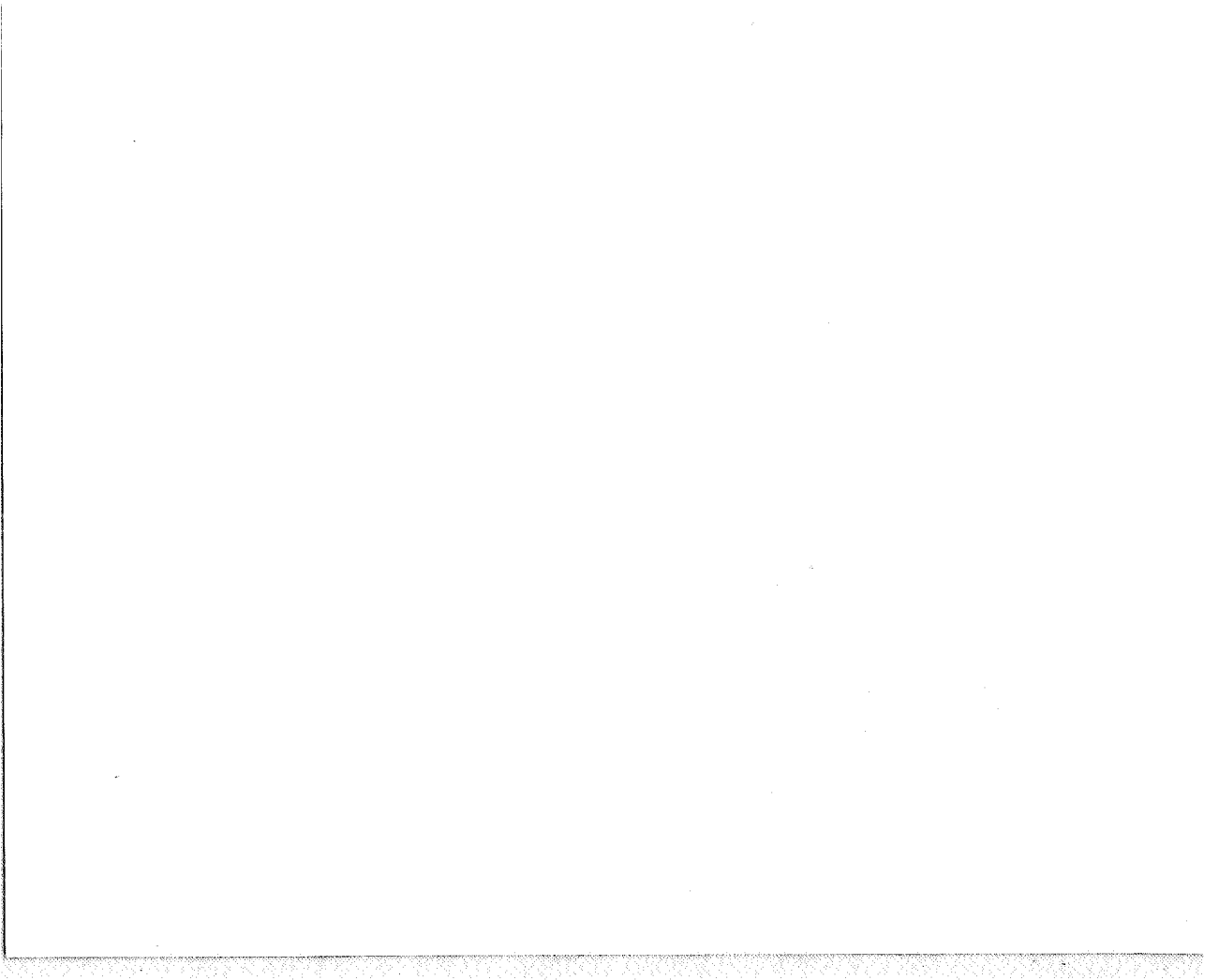
Cross-shore Transport
during Storm Surges

H.J. Steetzel

September 1993



delft hydraulics



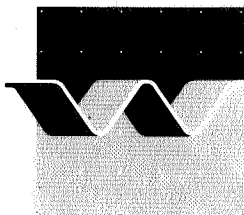
publication no. 476

**Cross-shore Transport
during Storm Surges**

Doctoral thesis approved by
Delft University of Technology

H.J. Steetzel

September 1993



delft hydraulics

Printed and bound by DELFT HYDRAULICS.

This publication is also published as
Ph.D. Thesis (ISBN 90-9006345-5) and
Report No. C1-9305 of the Technical Advisory
Committee on Water Defences (TAW)

Cross-shore Transport during Storm Surges

Proefschrift

Ter verkrijging van de graad van doctor aan de Technische Universiteit Delft, op gezag van de Rector Magnificus, prof.ir. K.F. Wakker, in het openbaar te verdedigen ten overstaan van een commissie aangewezen door het College van Dekanen op maandag 13 september 1993 te 14.00 uur precies.

door

Hendrik Jan Steetzel

geboren te Groesbeek

civiel ingenieur

1993

Dit proefschrift is goedgekeurd door de promotor Prof.dr.ir. E.W. Bijker.

Dr.ir. J. van de Graaff heeft als toegevoegd promotor in hoge mate bijgedragen aan het totstandkomen van dit proefschrift.

*Aan Dorine,
Anneloes, Coen en Marjolein
en mijn ouders.*

The research project described in this thesis was for the most part carried out under contract at DELFT HYDRAULICS, De Voorst location, for working group 'Sandy Coasts' of the Technical Advisory Committee on Water Defences (TAW) of the Minister of Transport and Public Works in the Netherlands.

Samenvatting

DWARSTRANSPORT TIJDENS STORMVLOED

Tijdens stormvloedomstandigheden (hoge waterstand in combinatie met zware golfaanval) vindt er aan een duinenkust afslag van zand uit het duinfront plaats als gevolg van zeewaarts gericht transport van zand. Met het oog op de veiligheid van het achterland dient de grootte van met name de afslag als gevolg van een zogenaamde 'superstormvloed' bekend te zijn.

Het hiertoe benodigde inzicht in het duinafslagproces werd verkregen door nabootsing van stormvloedomstandigheden en dwarsprofielveranderingen in schaalmodellen. Tijdens enkele van deze proeven werden gedetailleerde metingen uitgevoerd ter bepaling van golfhoogten, stroomsnelheden, zandconcentraties en dwarsprofielveranderingen.

Uit een analyse van deze gegevens komt naar voren dat de grootte van het dwarstransport tijdens stormvloedomstandigheden in goede benadering kan worden beschreven door het produkt van tijdsgemiddelde snelheden en tijdsgemiddelde zandconcentraties. Op basis van deze beschrijving is een mathematisch rekenmodel ontwikkeld waarbij snelheids- en concentratieverticalen zijn gerelateerd aan de lokale hydraulische omstandigheden.

Uitgaande van een initieel dwarsprofiel en een beschrijving van het stormvloedverloop (o.a. waterstanden, golfhoogten), wordt met het model de ontwikkeling van het dwarsprofiel tijdens de stormvloed berekend. Het rekenmodel is getoetst aan de hand van een serie proeven waarbij op systematische wijze de voor duinafslag bepalende factoren werden gevarieerd, alsmede voor een aantal andere afslagdata waaronder enkele buitenlandse gegevens.

Het model zal (op termijn) de basis vormen van een nieuwe methode waarmee door de verantwoordelijke kustbeheerders de beoordeling van de veiligheid van de duinen als primaire waterkering zal moeten worden uitgevoerd.

Abstract

CROSS-SHORE TRANSPORT DURING STORM SURGES

During storm surge conditions, viz. both high water levels and intensive wave attack, a dune coast is subjected to erosion. The dune face will be eroded due to a nett seaward transport of sand. With respect to the safety of a low-lying polder behind the dune row, the amount of erosion during the 'design storm surge' has to be known.

The insight in the process of dune erosion was enlarged by simulating storm surge conditions and profile developments in scale models. During some of these tests detailed measurements of wave heights, velocities, sediment concentrations and profile changes were conducted.

From a thorough analysis of these data it was concluded that cross-shore transport during storm surge conditions could be computed from the product of time-averaged flow profiles and time-averaged sediment concentrations. Based on this description a mathematical model has been developed in which the velocities and concentrations are related to the local hydraulic conditions.

Starting with an initial pre-storm profile and a description of the storm surge (water level and wave heights), the model computes the development of the cross-shore profile during the storm. The outcomes of the model have been verified for a series of tests in which dune-erosion governing parameters were systematically varied, as well as for a number of other data.

The model will (on a long-term) be used by the authorities responsible for a coastal stretch to assess and check the safety of the dunes as a primary sea defence structure.

Acknowledgements

Since most of the research described in this thesis was carried out under contract for the Technical Advisory Committee on Water Defences (TAW), I would like to express my heart-felt thanks for the opportunity to carry out the research involved. Moreover, the financial support during the last phase of the completion of this dissertation was highly appreciated.

Especially acknowledged are Eco Bijker and Jan van de Graaff for their comments and stimulating support during the writing of this thesis. I would also like to thank Hans Dette and Klemens Uliczka for providing me with data suitable for an additional verification of the mathematical model.

I also wish to express my appreciation for the stimulating and helpful environment provided at DELFT HYDRAULICS. Finally, Jan van de Graaff and Ben van Rosmalen are thanked for their critical review of the final draft.

The final accomplishment of this thesis required some family sacrifices, which were gracefully endured by my wife Dorine and the children, Anneloes, Coen and Marjolein.

CONTENTS

	<i>page</i>
Samenvatting (abstract in Dutch)	vii
Abstract	viii
Acknowledgements	ix
Contents	x
1 INTRODUCTION	
1.1 Introduction to dune erosion	1
1.2 Background of present research	1
1.3 Outline of contents	2
2 BACKGROUND AND OBJECTIVES	
2.1 Introduction	5
2.2 Coastal erosion	5
2.2.1 Types of processes (5)	
2.2.2 Long-term developments (5)	
2.2.3 Short-term developments (7)	
2.2.4 Example of coastline development (7)	
2.3 Problems related with short-term erosion	8
2.4 Objective of the present study	9
2.5 Description of existing model	9
2.6 Remaining problems	11
2.7 Strategy and approach	12
3 LITERATURE REVIEW	
3.1 Introduction	17
3.2 Model categorization	17
3.2.1 Cross-shore process scales (17)	
3.2.2 Categories (18)	
3.2.3 Review approach (19)	
3.3 Equilibrium profile models	20
3.3.1 General (20)	
3.3.2 Examples of formulations (20)	
3.3.3 Conclusions (22)	
3.4 Quasi-equilibrium models	23
3.4.1 General (23)	
3.4.2 Examples of formulations (23)	
3.4.3 Conclusions (23)	
3.5 Formulae for local transport rates	24
3.5.1 General (24)	
3.5.2 Classification formulae (25)	
3.5.3 Empirical transport formulae (25)	
3.5.4 Shear stress related transport rates (25)	
3.5.5 Energy dissipation related transport (26)	
3.5.6 Energy dissipation related suspension (26)	
3.5.7 Velocity related transport (26)	
3.5.8 Using estimates for intra-wave results (27)	
3.6 Other related research	27

CONTENTS *(continued)*

	<i>page</i>
3.7 Summary and conclusions	28
4 FORMULATION	
4.1 Introduction	29
4.2 Approach to cross-shore transport computation	29
4.2.1 Introduction (29)	
4.2.2 Basic procedure (30)	
4.2.3 General considerations (31)	
4.2.4 Strategies to component assessment (32)	
4.2.5 Analytical and mathematical approximations (33)	
4.2.6 Results of relevant measurements (44)	
4.2.7 Conclusions on relative contributions (45)	
4.2.8 Implications for transport computation (46)	
4.2.9 Approach to transport model development (47)	
4.3 Sediment concentration	48
4.3.1 Introduction (48)	
4.3.2 General distribution function (51)	
4.3.3 Mixing coefficient distribution (53)	
4.3.4 Suspended sediment distribution (58)	
4.3.5 Concentration profile (61)	
4.3.6 Sediment load (62)	
4.3.7 Summary and conclusions (64)	
4.4 Secondary flow	65
4.4.1 Introduction (65)	
4.4.2 Shear stress distribution (65)	
4.4.3 Basic flow profile formulation (67)	
4.4.4 Present formulation (67)	
4.4.5 Continuity condition (70)	
4.4.6 Boundary conditions and solution procedure (71)	
4.4.7 Fit procedure (73)	
4.4.8 Summary and conclusions (74)	
4.5 Nett cross-shore transport computation	75
4.5.1 Introduction (75)	
4.5.2 Transport below the mean trough level (75)	
4.5.3 Transport above the mean trough level (77)	
4.5.4 Total nett transport formulation (78)	
4.5.5 Example of nett transport computation (78)	
4.6 Justification of the proposed computation method	80
4.6.1 Introduction (80)	
4.6.2 Measured transport rates (80)	
4.6.3 Comparison of estimated transport rates (82)	
4.6.4 Conclusion (84)	
4.7 Set-up of computational model	85
4.7.1 Introduction (85)	
4.7.2 Input data (85)	
4.7.3 Flow-chart (87)	
4.7.4 Computation of wave height decay (87)	
4.7.5 Averaging procedures (88)	
4.7.6 Local modification of transport rates (88)	
4.7.7 Bottom changes and time step assessment (89)	
4.8 Additional extension of the model	90
4.8.1 Introduction (90)	
4.8.2 Effect of structures (90)	

CONTENTS *(continued)*

page

- 4.8.3 Longshore transport (90)
- 4.8.4 Longshore transport gradients (95)
- 4.8.5 Summary and conclusions (98)

5 CALIBRATION

5.1	Introduction	99
5.1.1	Internal and external process parameters (99)	
5.1.2	Calibration phases (99)	
5.1.3	Calibration procedure (100)	
5.2	Wave heights	101
5.2.1	Introduction (101)	
5.2.2	Objective and approach (102)	
5.2.3	Fit of wave-height decay (102)	
5.2.4	Assessment of optimal calibration (104)	
5.2.5	Accompanying deep water conditions (106)	
5.2.6	Local hydraulic conditions (107)	
5.3	Mixing distribution	107
5.3.1	Introduction (107)	
5.3.2	Reference mixing coefficient (107)	
5.3.3	Mixing gradient parameter (110)	
5.3.4	Conclusions (112)	
5.4	Sediment concentrations	112
5.4.1	Introduction (112)	
5.4.2	General considerations (112)	
5.4.3	Effect of wave breaking intensity (113)	
5.4.4	Effect of way of wave breaking (115)	
5.4.5	Final formulation (117)	
5.4.6	Verification/justification (119)	
5.4.7	Summary and conclusions (120)	
5.5	Overall large-scale calibration	120
5.5.1	Introduction (120)	
5.5.2	Large-scale profile development (121)	
5.5.3	Slope correction factor (122)	
5.5.4	Swash factor (122)	
5.5.5	Transport correction factor (122)	
5.5.6	Summary and conclusions (123)	
5.6	Additional small-scale calibration	124
5.6.1	Introduction (124)	
5.6.2	Small-scale profile development (124)	
5.6.3	Results (125)	
5.6.4	Summary and conclusions (125)	
5.7	Preliminary validation	126
5.7.1	Introduction (126)	
5.7.2	Sediment concentrations (126)	
5.7.3	Secondary flow (127)	
5.7.4	Conclusions (128)	

6 VERIFICATION

6.1	Introduction	129
6.1.1	General (129)	
6.1.2	Approach (129)	
6.1.3	Sediment balance (130)	
6.2	Laboratory data for unprotected dunes	131

CONTENTS (continued)

	<i>page</i>
6.2.1	Introduction (131)
6.2.2	Large-scale data (131)
6.2.3	Small-scale data (144)
6.2.4	Other laboratory data (162)
6.2.5	Summary and conclusions (168)
6.3	Additional field data 169
6.3.1	Introduction (169)
6.3.2	The 1953 storm surge (169)
6.3.3	Hurricane Eloise (170)
6.3.4	Extreme event in South Africa (171)
6.3.5	Other Dutch storm events (172)
6.3.6	Summary and conclusions (173)
6.4	Systematic comparisons 174
6.4.1	Introduction (174)
6.4.2	Effect of the water level (174)
6.4.3	Effect of the wave height (175)
6.4.4	Effect of the wave period (175)
6.4.5	Summary of the tested hydraulic effects (177)
6.4.6	Effect of the dune height (177)
6.4.7	Effect of initial cross-shore profile (177)
6.4.8	Overall summary of tested parameters (178)
6.5	Accuracy of the prediction model 179
6.5.1	Introduction (179)
6.5.2	Comparison of dune erosion quantities (179)
6.5.3	Summary and conclusions (183)
6.6	Structures 184
6.6.1	Introduction (184)
6.6.2	High revetments (184)
6.6.3	Low and hidden revetments (188)
6.6.4	Scour hole development (192)
6.6.5	Effect of dune erosion (192)
6.6.6	Summary and conclusions (193)
6.7	Longshore effects 194
6.7.1	Introduction (194)
6.7.2	Longshore transport rates (194)
6.7.3	Effect of longshore transport gradients (196)
6.7.4	Summary and conclusions (197)
6.8	Summary and conclusions 198
6.8.1	Introduction (198)
6.8.2	Unprotected dunes (198)
6.8.3	Impact of structures (198)
6.8.4	Longshore effects (198)
6.8.5	Overall performance (198)
7	SENSITIVITY ANALYSIS
7.1	Introduction 199
7.1.1	Objectives (199)
7.1.2	Governing parameters (199)
7.1.3	Approach (199)
7.2	Reference input and results 200
7.2.1	Introduction (200)
7.2.2	Reference profile (200)
7.2.3	Standard sediment characteristics (200)

CONTENTS *(continued)*

	<i>page</i>	
7.2.4	Standard hydraulic conditions (201)	
7.2.5	Result of computation (203)	
7.3	Effect of pre-storm profile	203
7.3.1	Introduction (203)	
7.3.2	Various forms (204)	
7.3.3	Slope of the nearshore zone (204)	
7.3.4	Conclusions (205)	
7.4	Effect of sediment characteristics	205
7.4.1	Introduction (205)	
7.4.2	Direct effects (205)	
7.4.3	Summary and conclusions (206)	
7.5	Effect of hydraulic conditions during a storm surge	206
7.5.1	Introduction (206)	
7.5.2	Storm surge level (207)	
7.5.3	Storm duration (208)	
7.5.4	Wave height (209)	
7.5.5	Wave period (210)	
7.5.6	Wave height and period combined (210)	
7.5.7	Time shift of high water peaks (211)	
7.5.8	Gust surges and gust oscillations (213)	
7.5.9	Conclusions (213)	
7.6	Effect of successive storm surges	214
7.6.1	Introduction (214)	
7.6.2	Additional storm event (214)	
7.6.3	Dune erosion quantity (215)	
7.6.4	Long-term 'near-equilibrium' profile (216)	
7.7	Summary and conclusions	217
7.7.1	Introduction (217)	
7.7.2	Pre-storm profile (217)	
7.7.3	Sediment characteristics (217)	
7.7.4	Hydraulic conditions during a storm surge (218)	
7.7.5	Effect of successive storms (218)	

8 APPLICATIONS

8.1	Introduction	219
8.2	Assessment of hydraulic conditions	219
8.2.1	Approach (219)	
8.2.2	Water level (220)	
8.2.3	Wave height (221)	
8.2.4	Wave period (223)	
8.2.5	Application (224)	
8.3	Standard case for comparison	225
8.3.1	Cross-shore profile (225)	
8.3.2	Hydraulic conditions (225)	
8.3.3	Computed profile development (225)	
8.4	Effect of a beach/dune nourishment	227
8.5	Effect of structures	228
8.5.1	Introduction (228)	
8.5.2	High revetments (seawall) (228)	
8.5.3	Low revetments (229)	
8.5.4	Nearshore low dam (230)	
8.6	Effect of oblique wave attack	231
8.6.1	Introduction (231)	

CONTENTS *(continued)*

	<i>page</i>
8.6.2 Computational results (231)	
8.6.3 Erosion quantities (231)	
8.6.4 Longshore transport rates (232)	
8.6.5 Coastal curvature (234)	
8.7 Conclusions	234
9 CONCLUDING REMARKS	
9.1 Introduction	235
9.2 Evaluation and main findings	235
9.2.1 Contributions to the cross-shore transport rate (235)	
9.2.2 Sediment concentrations (236)	
9.2.3 Secondary flow (236)	
9.2.4 Cross-shore transport computation (237)	
9.2.5 Mathematical model (237)	
9.2.6 Performance, sensitivity and accuracy (237)	
9.2.7 Effect of structures (238)	
9.2.8 Longshore effects (238)	
9.2.9 Overall conclusion (238)	
9.3 Recommendations for further research	239
9.3.1 Introduction (239)	
9.3.2 Further update of the present model (239)	
9.3.3 Supplementary extension of model (240)	
References	243
List of Symbols	253
List of Tables	261
List of Figures	263
Appendix	269
Curriculum Vitae	275

1 INTRODUCTION

1.1 Introduction to dune erosion

During storm surges the sea level off the coast rises considerably above the normal high water level. As a result storm-driven waves reach the front of the dunes and erosion occurs. The eroded sand is moved from the dune in offshore direction and settles on the beach. In this way a new beach profile is developed at a more elevated level (see Figure 1.1). In fact this process of dune erosion can be considered as an extreme case of the continuous adjustment of the coastal profile to the permanently changing hydraulic and meteorological conditions.

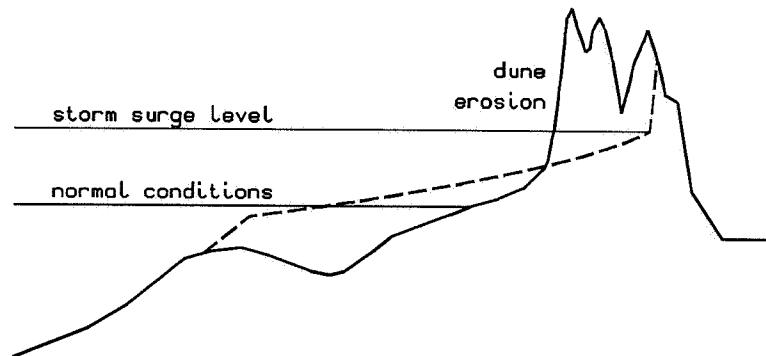


Figure 1.1 *Dunes as a primary sea defence system.*

This thesis deals with mathematical modelling of beach and dune profile changes due to such extreme hydraulic conditions, especially the modelling of cross-shore sediment transport processes during these conditions. The research project described in this work can be considered as a follow up on the studies on erosion profiles due to storm surges carried out by Vellinga (1986).

1.2 Background of present research

Most of the inhabitants of the Netherlands live well below mean sea level. At some locations the population and the goods are only protected from the sea by a narrow stretch

of sandy beaches and dunes.

Due to long-term erosion this row of dunes is thinning and many parts tend to become critical with respect to the vital role of the dunes as a primary sea defence system, see e.g. (Verhagen, 1989). Reinforcement works will therefore be necessary to prevent a break-through during storm surges. This situation calls for a detailed knowledge of the dune erosion process. It is for that reason that the latter has for several years been one of the main items in the research programme of the Dutch Technical Advisory Committee on Water Defences (TAW), being the principal for the research described in this thesis. It is noted that the next important item in the long-term research programme of this committee concerns the effects of initial breaching of dunes and dikes, see e.g. (Steetzel, 1992a; Steetzel and Visser, 1992).

1.3 Outline of contents

The research described in this thesis reflects the major part of the studies carried out by the author on the dune erosion phenomena during the period 1985 until 1991.

As a general introduction, Chapter 2 deals with the phenomena which are responsible for beach and dune erosion in general, ultimately focusing on the energetic process of (beach and) dune erosion during storm surge conditions. The problems related to the effects of this process are summarized and both the strategy and approach of the present study are specified. It is concluded that in order to predict the amount of dune erosion due to a storm surge, a mathematical model for cross-shore transport during extreme hydraulic conditions has to be developed.

Prior to the description of model development, Chapter 3 summarizes and evaluates the results of investigations carried out by other researches in the field of cross-shore transport modelling. Various sorts of cross-shore process scales and cross-shore transport models are categorized and discussed briefly in a systematical manner. Some comments on the main results are presented. Detailed knowledge on the processes involved is not (yet) present.

The different basic phases of the model development, such as formulation, calibration, verification and application are elaborated in the next chapters, viz. Chapter 4 through 8.

In Chapter 4 the formulation of the model is explained in detail.

Firstly, the basic assumptions with respect to the theoretical formulation of cross-shore transport are supported by elaboration of relevant terms and analysis of measurements. During a storm with intensive wave breaking, suspended sediment transport is predominant and the nett cross-shore transport rate can be related to the time-averaged sediment concentrations and the time-averaged cross-shore flow profiles.

Next, in Section 4.3 and 4.4, the time-averaged sediment concentration profile and secondary flow profile are investigated and described using the results of some large-scale model tests. Both vertical profiles are to be related to local hydraulic conditions as described in the calibration phase (see Chapter 5).

The final transport computation, based on the depth-integrated product of time-averaged sediment concentration and the time-averaged (secondary) flow profiles, is described and justified in Section 4.5 and 4.6 respectively.

Finally, the set-up of the mathematical model which computes the profile development due to the derived transport processes is described and the additional extension of this model to incorporate the effects of structures and alongshore transport gradients on the profile development is outlined (Sections 4.7 and 4.8).

For calibration and verification purposes, two groups of process parameters have been identified, namely 'internal' and 'external' process parameters. The first group denotes the basic input data of the transport model as described earlier, whereas the second set is essentially related to process results such as the actual development of the cross-shore profile or the related dune erosion rate.

Chapter 5 summarizes the basic outcomes of the calibration of the computational model which is predominately based on formulation and tuning of sediment suspension and mixing processes.

Governing unknown parameters are related to the estimated local hydraulic conditions. Although a large amount of scatter is present, useful first-order relations have been defined.

The results of the verification of the model are described in Chapter 6. This verification is principally based on the 'external' parameters such as the profile development and the amount of dune erosion above the maximum surge level. The final verification is accomplished by comparing measured dune erosion quantities with the outcomes of computed profile development for several model tests and a number of prototype data. The measured and computed profile development agree well.

The results of a systematic sensitivity analysis for the three main governing parameters are presented in Chapter 7. The effect of the pre-storm profile, the sediment characteristics and the hydraulic conditions on the resulting storm surge profile are elaborated in detail.

With regard to the uncertainty of the latter, the effects of the (maximum) surge level, the duration of the storm, the (detailed) wave conditions as well as the timing of the storm surge itself (relative to the regular astronomical variations) on the erosion rate are computed. The storm surge level is shown to be one of the major governing parameters.

In Chapter 8 some additional applications are presented to demonstrate the capability of the model. Results on the computed effects of beach nourishments and structures in the coastal profile as well as the effects of oblique wave attack are illustrated. Moreover, general assessment of the hydraulic conditions is discussed briefly.

In summary, it is concluded that the mathematical cross-shore transport model results in reliable outcomes, even for applications well beyond the standard ones as described in the former chapters.

Although at the end of every chapter a brief outline of the main conclusions is presented, an overall summary is given in Chapter 9. Concluding remarks on the derived procedure for cross-shore transport computation and the performance of the derived model as well as some recommendations for further improvement of the model are presented.

The cross-shore model DUROSTA, which also predicts the beach profile changes in front of dune revetments, is to be used as a tool to check the safety of the narrow stretch of sandy beaches and dunes which protects the Dutch population against the sea. It should be used in addition to (or will replace at the long-term) the present DUROS model as described by Vellinga (1986) (see Section 2.5).

It is noted that, due to the fact this thesis is also meant to be a summarizing report for the Technical Advisory Committee on Water Defences (TAW), the number and range of the topics dealt with is somewhat beyond the scope which is covered by the title of this thesis.

2 BACKGROUND AND OBJECTIVES

2.1 Introduction

This chapter summarizes in more detail the background and objectives of the research described in this thesis.

Initially, a general introduction on coastal erosion is presented particularly focusing on beach and dune erosion during storm events. Next, some problems involved with this energetic process are illustrated, whereas the detailed objective of the present study is summarized in Section 2.4.

In order to compare the proposed new developments described in this thesis with the existing Dutch dune erosion prediction method, the latter is described briefly in Section 2.5. Section 2.6 deals with problems and limitations involved with the general use of the existing model. The strategy and approach for the development of the new model are elaborated in Section 2.7.

2.2 Coastal erosion

2.2.1 Types of processes

There are two distinct types of erosion processes which affect a sandy coast, namely erosion due to mean hydraulic conditions and erosion due to extreme hydraulic conditions. Both result in beach and dune erosion although the related effects occur on different time scales. Generally, mean hydraulic conditions have an impact on large time scales (seasons, years), whereas the influences of extreme events are primarily restricted to small time scales, say hours to days.

An overview of relations involved is presented in Figure 2.1.

2.2.2 Long-term developments

In the case of beach and dune erosion at large time scales (seasons, years), there is usually a nett positive, longshore transport gradient. This gradient may be due to various origins, for example the presence of a longshore gradient in wave attack or currents occurring at non-straight coastlines.

Due to an increase in longshore transport along a coastal stretch (say in between two cross-shore rays), the total amount of sand in between both boundaries will reduce in time.

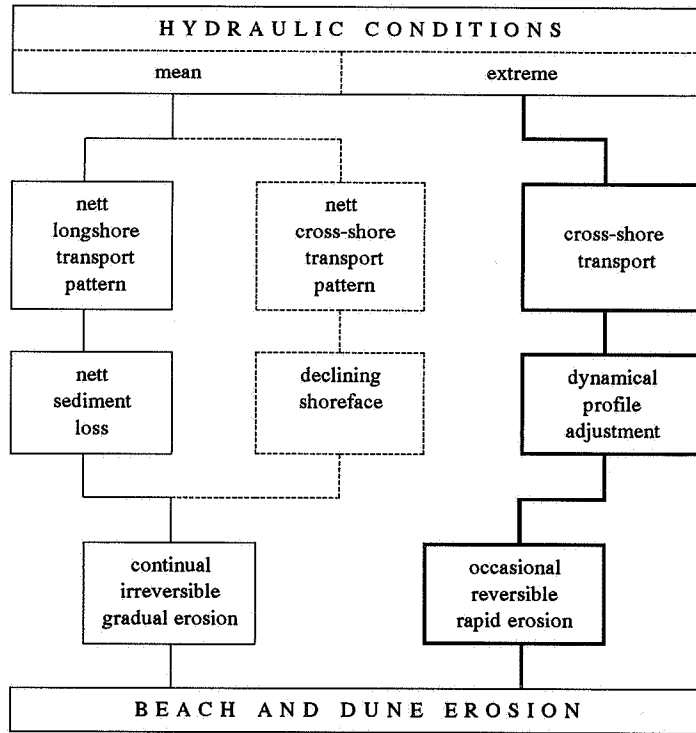


Figure 2.1 *Overview of causal relations for beach and dune erosion.*

Consequently, the cross-shore profile will shift in landward direction, resulting in erosion of both the beach and the duneface. Of course a negative gradient (decreasing longshore transport rate) will have the opposite effect. However, the latter will generally not lead to problems.

Although in most cases the presence of positive longshore transport gradients is accountable for coastal erosion, sediment loss in the upper part of the cross-shore profile may also be due to a nett cross-shore transport pattern, for example due to a significant sea level rise. In this case, erosion will occur in a smaller part of the cross-shore profile, viz. the coastal profile will get less steeper due to erosion of the upper part of the profile. This declining of the shoreface takes place without any nett sediment exchange with adjacent rays.

Both effects are illustrated on the left side in Figure 2.1.

It is clear that combinations, so erosion due to both longshore and cross-shore transport patterns, may occur also.

In general, negative long-term developments result in a gradual, though continual (on a yearly basis), irreversible type of beach and dune erosion.

2.2.3 Short-term developments

In contrast to long-term erosion, short-term erosion takes place occasionally during less frequent extreme events, such as storm surges and hurricanes. Moreover, the significant profile changes are in that case restricted to the upper part of the coastal profile only, say beach and dune and take place in a very short period of time (hours, days).

In absence of longshore transport gradients the total amount of sand in the coastal profile (viz. in between two adjacent rays) is not affected, although the formation of a post-storm profile (as shown in Figure 1.1) will result in local erosion at the duneface.

In most cases this erosion is only temporarily, since the mean hydraulic conditions will tend to reconstruct the pre-storm profile, which principally is of a more or less equilibrium shape.

The effects of extreme conditions are presented on the right side in Figure 2.1. In fact these short-term developments can be considered to be only a momentary disturbance of the long-term development of the coastal profile. However, the amount of dune erosion involved may lead to serious problems.

2.2.4 Example of coastline development

A typical example of the development of a coastline is shown in Figure 2.2.

The evolution of the position of the dunefoot (one of the several indicators of the behaviour of the coastline) is shown for the period 1910 until 1980. The long-term average retreat of the dunefoot position (visualized by the dashed line) is about 1.1 m/year. The actual position shows a short-term scatter of 5 to 10 m with respect to this average trend.

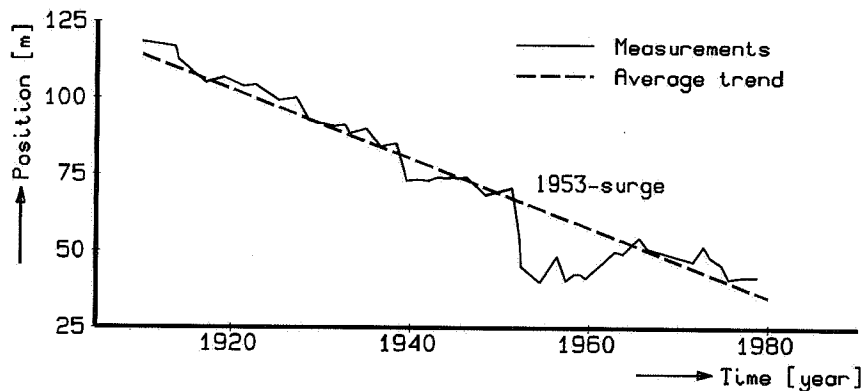


Figure 2.2 Position of the dunefoot in the period 1910 until 1980 at the coast of Den Helder.

The extreme 1953-storm surge caused an instantaneous additional erosion of about 30 m. However, from the succeeding evolution it can be observed that this effect was only present during a time interval of about 10 years after the event in which the position of the dunefoot is even moving seaward after 1953. Records from the coastline at Delfland showed even a more rapid recovery.

It is therefore concluded that even excessive erosion due to a very extreme storm surge is only temporarily.

2.3 Problems related with short-term erosion

Even on a stable coast without any long-term erosion, the dynamical adjustment of the cross-shore profile due to, especially very infrequent, short-term developments may lead to safety problems or may even result in a break-through of the dune and successive inundation of the polder behind it.

It also may affect other functions in the dune area, for example recreation sites, buildings, parking places, sources of drinking water and so on, as indicated in Figure 2.3, see also (Verhagen, 1989).

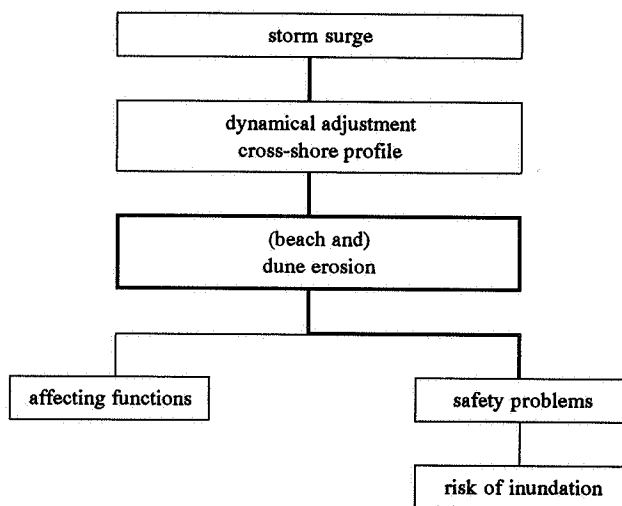


Figure 2.3 *Effects of a storm surge.*

Although these problems will not be solved just by a detailed knowledge of the accountable erosion process, insight into the process of dune erosion needs to be enlarged to yield a reliable prediction of the effects of a storm surge.

2.4 Objective of the present study

In order to predict the amount of dune erosion due to a storm surge, a universal method for the determination of the effects of a storm surge on beach and dune has to be developed. In more detail, the quantification of the amount of dune erosion for arbitrary cross-shore profiles and hydraulic conditions is the main goal of the present study.

Although by the use of the existing Dutch erosion profile ('equilibrium') model a fair estimate of the amount of erosion can already be obtained, a number of coastal erosion problems needs still to be solved.

In the next section this Dutch model will be outlined in more detail, this in order to provide the required information for the development of a new model.

2.5 Description of existing model

At this moment the safety of the Dutch dunes is determined by the use of a probabilistic design method, which is based on a so-called erosion profile model (TAW, 1984, 1990) (see Chapter 3 for more details on transport-model categorization). An extensive research programme has been carried out to achieve the required insight, see e.g. (Edelman, 1970; Van de Graaff, 1977). The model describes the dune erosion profile which is present after a storm surge, based on experiments and analyses by Vellinga (1983, 1986) (DELFT HYDRAULICS, 1982a).

Essentially, the procedure of this method is outlined in Figure 2.4.

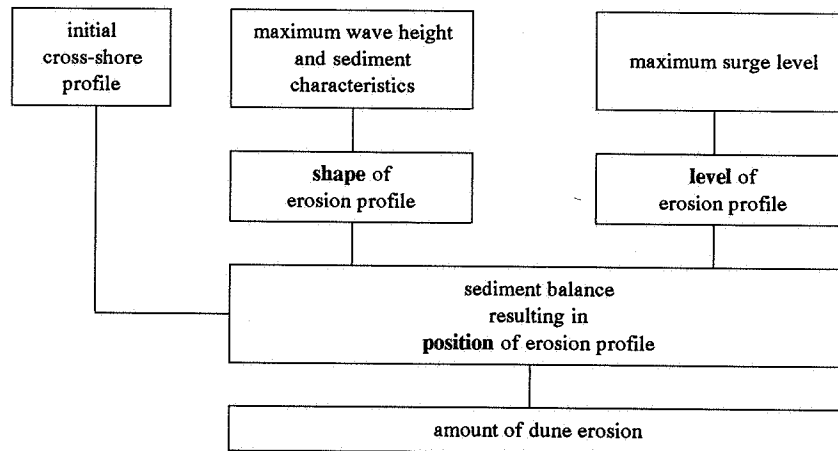


Figure 2.4 Outline of the erosion-profile method according to Vellinga.

The maximum significant wave height H_{0s} (at deep water) as well as the sediment characteristics of dune sand (characterized by the free-fall velocity w_s) determine the shape of the erosion profile. The vertical level of this profile is related to the maximum storm surge level.

This erosion profile is described by:

$$\left(\frac{7.6}{H_{0s}}\right) d = 0.47 \left[\left(\frac{7.6}{H_{0s}}\right)^{1.28} \left(\frac{w_s}{0.0268}\right)^{0.56} x + 18 \right]^{0.5} - 2.00 \quad (2.1)$$

in which x and d are the seaward distance from the dunefoot and the vertical distance below the maximum storm surge level, viz. the water depth, respectively.

The former equation is valid up to a seaward limit $x = x_{max}$ according to:

$$x_{max} = 250 \left(\frac{H_{0s}}{7.6}\right)^{1.28} \left(\frac{0.0268}{w_s}\right)^{0.56} \quad (2.2)$$

The maximum water depth at this position equals:

$$d_{max} = 5.72 \left(\frac{H_{0s}}{7.6}\right) = 0.75 H_{0s} \quad (2.3)$$

Seaward of this position a uniform bottom slope of $1:12.5$ is present down to the point of intersection with the actual bottom profile, whereas the landward slope of the dune front (for $x < 0$) equals $1:1$.

By combination of this erosion profile description with the initial pre-storm profile, the horizontal position of this profile and thus the dune erosion quantity can be computed using the idea of a closed sediment balance.

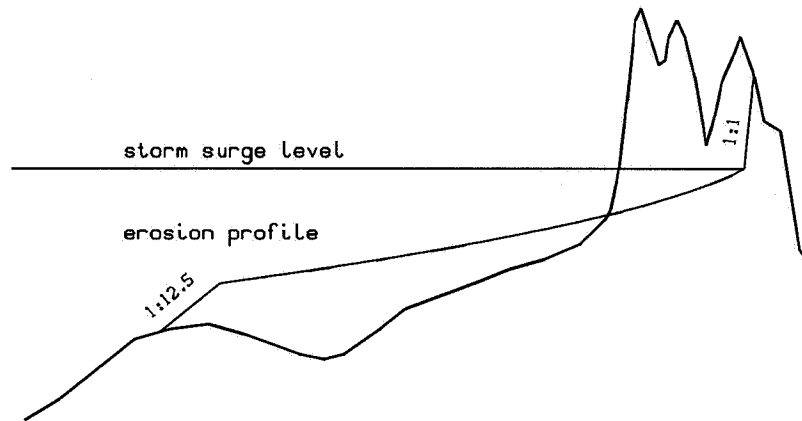


Figure 2.5 Example of erosion profile and subsequent dune erosion according to Vellinga.

Figure 2.5 shows an example of the erosion profile and subsequent dune erosion computed by this method. The amount of erosion above the storm surge level due to a characteristic design storm surge (with a 10,000 year recurrence interval) varies roughly between 100 and 500 m³/m. The related retreat of the duneface amounts to 25 to 75 m.

This model has also been used by other researchers, see e.g. (Sargent and Birkemeier, 1985).

2.6 Remaining problems

The application of the former described dune erosion model has some restrictions, since the model (viz. the storm profile) is determined for a more or less standard cross-shore profile and standard storm surge conditions.

The cross-shore profile has been derived from the average cross-shore profile along the Dutch coast. For a profile with a very steep bottom slope (tidal gully) or a nearshore bank, the outcomes of the model have been proved to be not always reliable, see e.g. (Steetzel, 1987c). Moreover, the impact of a shallow nearshore region on the wave height which determines the shape of the erosion profile and ultimate dune erosion is still subject to much discussion, see for example (DELFT HYDRAULICS, 1987b).

The standard surge used for the model development was composed out of an astronomical tide (tidal effect) and a surge effect, both with a specific shape and mutual timing, as shown in Figure 2.6.

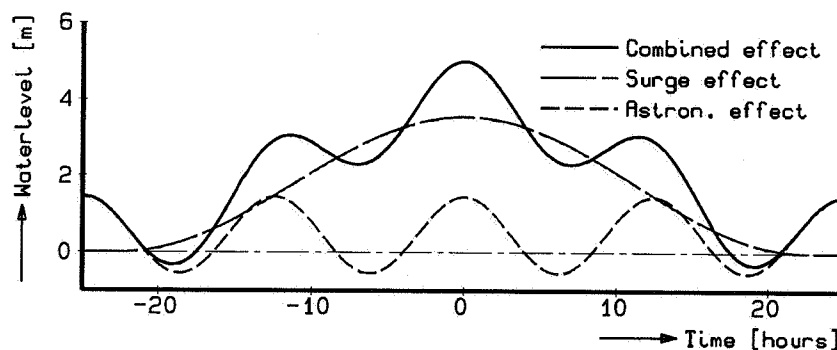


Figure 2.6 Example of the standard North Sea storm surge hydrograph.

Furthermore, some coastal problems cannot adequately be solved by the use of this kind of dune erosion model.

In brief, three types of problems can be identified, namely:

- the behaviour of 'non-standard' coastal profiles as well as the effect of 'non-standard' hydraulic conditions;
- the interference with structures in the coastal profile;
- the effect of longshore transport gradients.

Some examples of these problems are presented in the left side of Table 2.1.

type of problem	related examples	solution	development phase
non-standard coastal profiles or hydraulic conditions	- nearshore banks - tidal gully - other surges	local description of cross-shore transport	basic formulations
interference with structures	- dune revetments - alongshore dams	cross-shore transport (gradient) modification	extension of basic model
effect of longshore transport gradients	- shoreline curvature - tidal gradients	longshore transport computation	

Table 2.1 Existing problems, related examples, proposed solutions and model development phases.

It will be obvious that the model to be developed should be able to deal with these problems.

2.7 Strategy and approach

The approach is to develop a cross-shore transport model which is based on the physics of the erosion process involved, namely transport of sediment during extreme hydraulic conditions. Instead of a description of the final (post-storm) erosion profile, the actual profile development will be computed from the instantaneous cross-shore transport distribution. In this way, a basic solution for the problems can be achieved according to the right-hand side of Table 2.1.

In an additional phase of the model development the basic formulations will be extended in order to deal also with the effects of structures and longshore transport gradients.

In order to develop this cross-shore transport model, some additional series of investigations in two wave flumes have been carried out and existing data on storm-induced profile change has been re-analyzed.

The model tests used for the model development have been conducted on different depth scales as indicated in Table 2.2, ranging from small scale ($n_d = 30$) to full scale ($n_d = 1$). The so-called depth scale n_d equals the ratio between the depth in the prototype d_{prot} and the depth in the model d_{model} . The flume tests dealt with cross-shore transport only.

scale		degree of protection of duneface		
		unprotected	partly	protected
small	$n_d = 30$	x	-	x
large	$n_d = 5$	x	x	x
full	$n_d = 1$	x	-	x
prototype		x	-	x

Table 2.2 General overview of investigations and additional data.

Most investigations concern unprotected dunes. Furthermore, there are a few tests with dune revetments (seawalls) and three large-scale tests with partly protected dunes. Most of those tests have been carried out in the large Deltaflume of DELFT HYDRAULICS. Figure 2.7 shows an example of the profile development in the case of an unprotected dune which was observed in a large-scale model test.

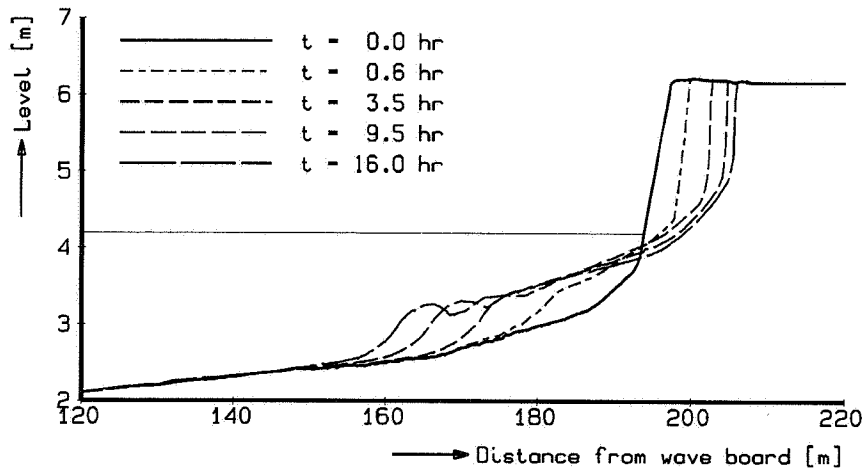


Figure 2.7 Example of large-scale model test result for an unprotected dune; test T5 of H298-I-test series.

The photo shown in Figure 2.8 gives an impression of wave attack in the flume, with waves propagating towards the modelled dune coast which is situated inside the building. This photo also shows the measurement carriage (see also Figure 4.9).

Other tests have been conducted in the 40 m long Scheldeflume. An overview of all the test series carried out in DELFT HYDRAULICS' facilities which have been used for the development of the present model are summarized in Table 2.3 on page 15.

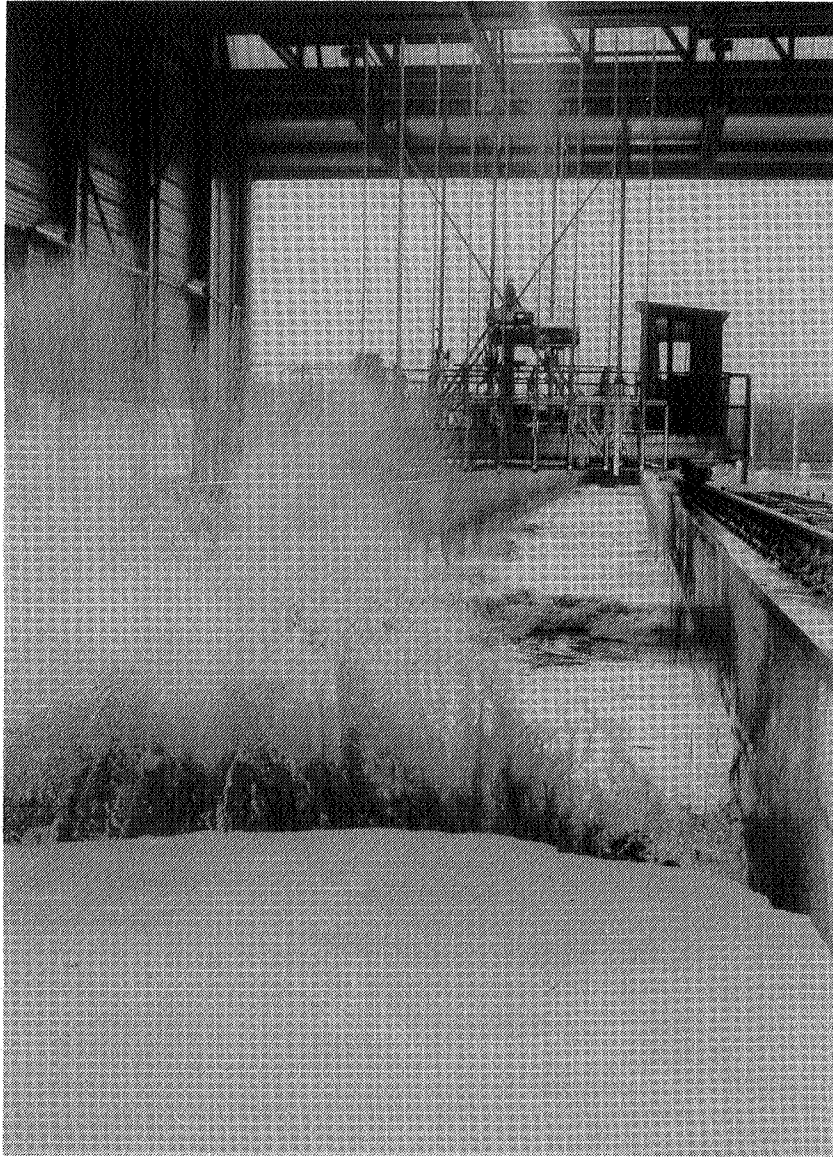


Figure 2.8 *Photo of wave attack on a dune in the Deltaflume.*

The amount of information gathered during a particular test varies from only initial and final profile to a detailed profile development, supplemented with data on wave heights, currents and sediment concentrations.

Consequently, the use of a specific test result is related to a particular phase of the model development as indicated in this table.

Model tests provided with much reliable data, for example profile development, final profile, wave height decay, secondary currents and sediment concentrations are used for

series	facility	tests used	reference	remarks
Model formulation		(aimed at formulation of the transport model)		
H298-I	Deltaflume	test T1-T3, T5	DELFT HYDRAULICS, 1987a	transport process formulation
Model calibration		(aimed at specification/tuning of the governing parameters)		
M1819-I	Scheldeflume	test T04	DELFT HYDRAULICS, 1982d	small-scale 'high-level' tuning
M1263-III	Deltaflume	test T2	DELFT HYDRAULICS, 1984a	large-scale 'high-level' tuning
H298-I	Deltaflume	test T1-T3, T5	DELFT HYDRAULICS, 1987a	additional 'low-level' tuning
Model verification		(aimed at extensive verification of the model's output)		
M1653	Basin	test T1-T4	DELFT HYDRAULICS, 1981b	three-dimensional tests
M1797	Deltaflume	test T1 and T2	DELFT HYDRAULICS, 1982b	with and without revetment
M1811	Deltaflume	test T1	DELFT HYDRAULICS, 1982c	
M1819-I	Scheldeflume	29 tests in total	DELFT HYDRAULICS, 1982d	systematic research
M1819-III	Scheldeflume	test T1-T4	DELFT HYDRAULICS, 1983d	several revetment levels
M1263-III	Deltaflume	test T1, T3-T5	DELFT HYDRAULICS, 1984a	also used by Vellinga
M2051-II	Scheldeflume	test T1-T4	DELFT HYDRAULICS, 1986a	revetments
H298-I	Deltaflume	test T1-T5	DELFT HYDRAULICS, 1987a	several revetment levels

Table 2.3 *Overview of test series carried out at DELFT HYDRAULICS which were used for the development of the present model.*

the development and formulation of the cross-shore transport model. As can be seen from the table, the data obtained in the H298-I-series have been applied for this purpose.

Tests with only pre- and post-storm profiles are used for verification purposes and presented in chronological order in the table. It is noted that also some non-Delft data have been applied for the verification of the model (see Chapter 6).

In the case of an application of the model, the available information is restricted to the initial cross-shore profile only.

The plan of approach, together with the actual phase of model development is outlined in Figure 2.9. The related chapter is also given to facilitate reading.

As indicated, several successive phases in the model development have been distinguished. The basic three phases are the formulation, the calibration and the verification of the model as presented extensively in Chapter 4 through 6. In order to achieve insight in the sensitivity of the model results to the main governing input data, the results of a systematic sensitivity analysis are presented next. Moreover, to show some other applications of the model these outcomes are also presented.

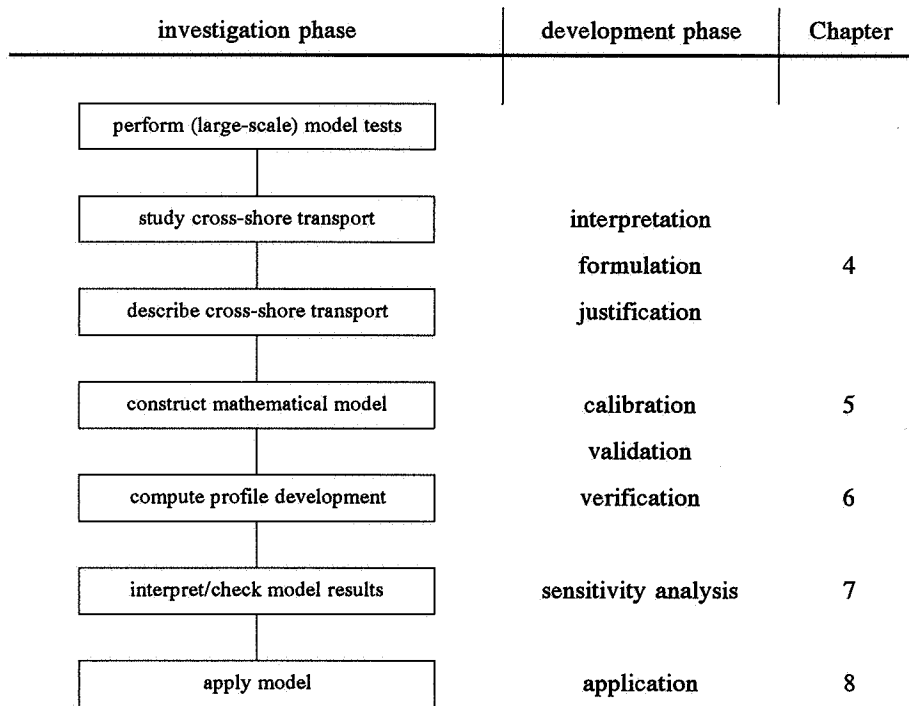


Figure 2.9 *Plan of approach for model development.*

However, before dealing with these topics, in the next chapter a short systematic literature review on cross-shore transport modelling of beach and dune erosion will be presented.

3 LITERATURE REVIEW

3.1 Introduction

Preceding and parallel with the research described in this thesis, other investigators have also been working on experimental and numerical modelling of cross-shore sediment transport.

Some of the principal results of various investigations are discussed briefly hereafter.

Firstly, some comments on the different scales of modelling will be given in order to classify the numerous approaches in cross-shore transport modelling. Next, this classification is used to separate the distinct categories of dune erosion transport models and some comments are given on each of them. Finally, a brief synthesis is presented.

3.2 Model categorization

3.2.1 Cross-shore process scales

Cross-shore processes and their subsequent modelling, can be categorized on the basis of the scales they consider. As indicated in Figure 3.1, one can classify these processes by their own specific time and space scale. It should be noted that in the original form this diagram was presented for coastal processes in both cross- and longshore direction, whereas in the present case the space scale is restricted to the cross-shore direction only (Stive, 1991).

Subsequently, by reducing scales involved, one may come up with three distinct types of coastal processes, namely:

- Shoreface evolution;
- Surfzone evolution;
- Dune erosion.

The evolution of the shoreface profile takes place on relatively large scales. Typical scales are decades for the time scale and of the order of several kilometres for the (cross-shore) space scale.

Profile evolution in the surfzone (say in between the outer bar and duneface) takes place on middle scales. Typical evolutions, including bar and berm features, take place over wave climate seasons like a summer and winter season, while return periods in profile evolution

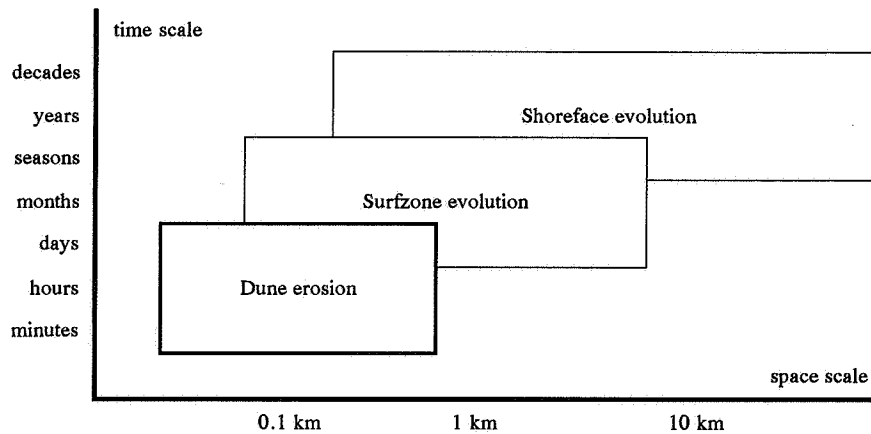


Figure 3.1 *Cross-shore evolution scales; after (Stive, 1991).*

may occur between one and several years. Significant profile variations extend to depths of twice the wave height extreme which is exceeded for example 12 hours per year, relative to the mean sea level, see e.g. (Hallermeier, 1978).

The process of dune erosion is characterized by relatively small scales. Significant profile variations are established on a time scale of hours, the extent of these variations being limited to a depth of less than about twice the incident significant wave height relative to the storm surge level.

Since only small time scales are studied in this work, the next section focuses in more detail on dune erosion processes (upper shoreface or surfzone, including beach and duneface), in order to categorize the various approaches present for modelling these phenomena.

3.2.2 Categories of dune erosion models

Starting with a relatively small time and space scale, the main approaches to dune erosion model development are distinguished into a number of principal categories, depending on the scale of integration. Consequently, with respect to this integration, two scales can be separated, namely:

- Space integration;
- Time integration.

In the case of space integration, the shape of the complete cross-shore profile is described, whereas in the second case, the nett effect of the complete storm surge is accounted for.

Using these two integration scales, three main categories of dune erosion modelling are distinguished, namely:

- Time and space integrated concept;
- Space integrated, instantaneous concept;
- Local and instantaneous concept.

It should be noted that this categorization in an adjusted form is also applicable for the classification of transport models dealing with surfzone evolution.

The first category, viz. the time and space integrated concept of the dune erosion process, results in a prediction of the erosion profile which is supposed to be present after a specific storm event. This can be characterized by a so-called equilibrium or erosion profile model method. The DUROS-model, as described in Section 2.5, is a good example of this category of cross-shore transport models (Vellinga, 1986).

In the second case, the development of the shape of the cross-shore profile (space integration) is described during the storm event (time-dependent shape function). Consequently, the term 'quasi-equilibrium model' can be used for this category of dune erosion models.

The latter category of models, in which the local transport rate has to be known at every position across the cross-shore profile, can be used for a dynamical mathematical program to compute the profile development during a storm surge.

It is noted that the virtual fourth concept, viz. the local and time integrated concept, is meaningless.

The presented technique in this thesis is according to the third concept, viz. the direct assessment of local transport rates. In Chapter 4 more details on the related formulations will be presented.

3.2.3 Review approach

Based on the previously presented model categorization, the findings from a concise literature survey are divided into three different sections.

Section 3.3 summarizes the background and relevant details with respect to the equilibrium profile and storm profile models, while some relevant facts on quasi-equilibrium models are presented in Section 3.4.

In Section 3.5 several formulations on the cross-shore transport rate are divided into a number of subcategories and reviewed next.

Relevant data, which is not covered by one of the former classes, is discussed in Section 3.6. Finally, Section 3.7 presents a brief synthesis of the previous work discussed here. It forms the starting-point for model development as elaborated in Chapter 4.

3.3 Equilibrium profile models

3.3.1 General

Basically, an equilibrium profile can be defined as a cross-shore profile of constant shape which is approached if exposed to fixed wave and water level conditions for a sufficiently long time.

If referred to as storm profile method, the final cross-shore profile is approached if exposed to (fixed) pre-defined wave and water level conditions during a pre-defined time (thus not infinitely long).

This method is based on two principal assumptions, namely:

- i)* During a storm surge a smooth (uniform) erosion profile develops. The shape of this profile is determined by both the incoming wave height and the fall velocity of the bed material, whereas its elevation is related to the storm surge level;
- ii)* Assuming a closure depth (depth up to where this profile is supposed to be present) and a specific shape (e.g. a uniform slope) of both the seaward and landward transition zones, the horizontal position of this erosion profile is resolved using a closed mass balance of sand in the coastal profile.

Some examples of formulations are summarized in the next section.

3.3.2 Examples of formulations

The existence of an equilibrium profile was already proved to be a valid concept under (probably constant) laboratory conditions by Waters (1939) and Rector (1954). However, since in nature the profile-forcing hydraulic conditions will definitely not be constant in time, an absolute equilibrium shape (with zero transport rates all across the profile) will not exist. In fact one has to deal with some sort of average shoreface profile cross-section and, consequently, the term 'near-equilibrium profile' could be a safe alternative. A critical review on the concept of shoreface equilibrium is given by Pilkey et al. (1993), who question both the validity of the concept of equilibrium profiles as used in standard coastal engineering practice as well as using one equilibrium profile equation to describe all shoreface profiles.

Nevertheless, some formulations of equilibrium profiles can be found in the literature.

Bruun

Bruun developed a predictive equation for an equilibrium beach profile by studying beaches along the Danish North Sea coast and the California coast and proposed a simple power law to relate the water depth d to the offshore distance x , according to (Bruun, 1954):

$$d = A x^m \quad (3.3.1)$$

in which the exponent equals:

$$m = \frac{2}{3} \quad (3.3.2)$$

The non-dimensionless constant A (which dimension depends on the magnitude of the x -exponent) denotes a so-called shape factor, depending on the stability characteristics of the bed material. Bruun found that $A = 0.135 \text{ m}^{1/3}$ provided the best correlation for North Sea beaches in the Thyborøn area in Denmark.

Bruun applied his empirical equation in 1962, to estimate the amount of erosion to occur along the Florida coast as a result of long-term sea level rise (Bruun, 1962). This approach is nowadays known as the famous 'Bruun-rule'.

Dean

The Bruun hypothesis (simple power law) was supported by Dean (1977) on theoretical grounds by reasoning that nature aims at a uniform energy dissipation D_{eq} (loss in wave power) per unit volume of water across the surf zone (in W/m^3). So:

$$\frac{1}{d} \frac{d(Ec_g)}{dx} = -D_{eq} \quad (3.3.3)$$

where d denotes the water depth. Based on monochromatic waves and a constant breaker index with $\gamma = H/d$, the magnitude of the exponent m in Equation (3.3.1) can be derived and the same (2/3)-power curve is found. Furthermore, for this case the non-dimensionless shape factor A (in $\text{m}^{1/3}$) can be described by:

$$A = \left(\frac{24}{5} \frac{D_{eq}}{\rho g \sqrt{g} \gamma^2} \right)^{\frac{2}{3}} \quad (3.3.4)$$

in which the equilibrium energy dissipation rate D_{eq} (in W/m^3) depends on both the particle diameter and shape.

The magnitude of the related shape factor A varies from 0.079 to 0.398 (Dean, 1977). Hughes and Chiu (1978) show that $A = 0.10 \text{ m}^{1/3}$ provided the best correlation for beaches along the coast of Florida (Dean, 1982).

This empirical shape parameter A was later related to the median grain size by Moore (1982), showing that a coarser grain size implies a larger value of A and thus a steeper beach. More recently Dean (1987) showed that this relation could be transformed to a relation using the fall velocity w as an argument, viz.:

$$A = 0.067 w^{0.44} \quad (3.3.5)$$

For general applications however, the constant A remains an unknown factor which is likely to be also dependent on several other variables, like wave climate, water-level variations and coastal currents. Ergo, a universal application of 'Dean'-profiles seems troublesome, although some applications of equilibrium profiles were presented recently, see e.g. (Kriebel, 1990; Dean, 1991).

Vellinga

A well-known Dutch example of the erosion profile approach was presented by Vellinga (1986), who extended the earlier work of Van de Graaff (1977). This erosion profile method is presently used to check the safety of the Dutch dunes. The formulations are presented in more detail in Section 2.5.

Based on the scale relation showing the effect of the grain size on the erosion profile according to:

$$n_l/n_d = (n_d/n_w^2)^{0.28} \quad (3.3.6)$$

in which w denotes the fall velocity of a sand particle in stagnant water, a power curve can be derived according to:

$$d = A x^{0.78} \quad (3.3.7)$$

in which the non-dimensionless shape factor equals $A = 0.14$. Using the scale relation of Equation (3.3.6), a general expression for the shape factor can be found according to:

$$A = 0.39 w^{0.44} \quad (3.3.8a)$$

or:

$$A = 0.70 (H_o/L_o)^{0.17} w^{0.44} \quad (3.3.8b)$$

The quotient of the significant wave height H_o and wave length L_o (both at deep water) denotes a characteristic offshore wave steepness. Both a coarser grain size and a larger wave steepness imply a larger value of A and thus a steeper beach (Vellinga, 1986). It should be noted that this particular erosion profile is definitely not in equilibrium (or even 'near-equilibrium') shape, since the period of wave attack is limited by the duration of the specific storm surge considered.

3.3.3 Conclusions

From the definition of equilibrium profile methods it is almost obvious that this particular method is not suited to compute the detailed effect of the impact of an arbitrary storm event (which only lasts several hours or one day at most) on an arbitrary initial cross-shore profile. Moreover, if there is any equilibrium profile at all, it will definitely not be reached within such a short time interval. It is interesting to quote Bruun (1992) who states that "Dean's as well as Bruun's assumptions may be more academic than real in a highly three-dimensional and irregular environment. That they give the same result may be incidental, but neither Dean's nor Bruun's results should be extended beyond their capacity. A beach/bottom profile is a very dynamic feature subject to considerable variances. Its behaviour may be better described in statistical, rather than in physical terms."

Moreover, it is clear that the use of an equilibrium model will not allow for assessment of the effect of a storm surge on a beach with a revetment or seawall, although some

preliminary examples are presented in (Dean, 1991).

3.4 Quasi-equilibrium models

3.4.1 General

A space-integrated, though instantaneous concept is also based on the assumption of the existence of an (at least local) equilibrium profile as discussed in the former section. This contour will be approached when the cross-shore profile is exposed to fixed hydraulic conditions for a sufficiently long time.

The rate of change in a quasi-equilibrium model is related to the deviation of the actual situation from a pre-defined equilibrium condition. Typically, this approach results in a negative exponential development of the profile (for constant hydraulic conditions).

3.4.2 Examples of formulations

Swart

Swart (1974) proposed a definition of an equilibrium D -profile determined by the deep water wave height, the deep water steepness and the particle diameter. Moreover, the offshore transport at any location in this D -profile at any time is proportional to the difference between the equilibrium profile form and the actual form.

SBEACH-model

Larson (1988) developed the SBEACH-model that simulates the macro-scale profile change, such as growth and movement of bars and berms. Based on an extensive analysis of two large wave-tank experiments (with regular waves), a number of semi-empirical transport rate relations have been developed for different regions of the cross-shore profile (Larson and Kraus, 1989a).

DUIN-model

Roelvink developed a quasi-equilibrium version of the original DUROS-model of Vellinga, known as the DUIN-model. The preliminary research version of this model is used by a few authorities to simulate the behaviour and effectiveness of measures on beach and dune (DELFT HYDRAULICS, 1990d).

3.4.3 Conclusions

Although the approach of Larson seems useful, the application of regular wave data for the model development diminishes the general use of the SBEACH-model. In order to provide a reliable assessment of the development of a cross-shore profile due to arbitrarily varying

hydraulic conditions, one has to rely on formulae describing the local transport rate as will be discussed in more detail in the next section.

3.5 Formulae for local transport rates

3.5.1 General

In the third category of dune erosion models, an expression for the local transport rate has to be assessed. Although an instantaneous estimate of the transport rate is needed and thus only very small time scales are of interest by definition, once again several approaches are available depending on the actual time scale and sequence of the time integration, for example:

- Using instantaneous (intra-wave) transport rates from which the nett transport rate is computed by averaging over the wave period;
- Straight forwardly using time-averaged (several wave periods) transport rates.

The first strategy, known as the intra-wave approach, is in fact the best method, although all other formulae describing a local transport rate could be considered to be the ultimate result of intra-wave transport processes.

Basically, the computation of a local nett sediment transport rate S should be based on a both time- and depth-integrated product of flow velocity and sediment concentration, which can be schematized as:

$$S = UC \tag{3.5.1}$$

in which U and C are characteristic values of flow velocity and sediment concentration respectively. The presented schematic transport relation is only used to indicate the principle of a category of transport models, whereas the proper transport formulations are elaborated in detail in Section 4.2. A more detailed form of the previously mentioned equation is presented in Equation (4.2.1).

The various transport formulae can be categorized by the way they assess the magnitude of the right-hand term of Equation (3.5.1).

In order of increasing simplification one can identify a number of possible approaches, namely:

- Indeed using the basic equation;
- Using best estimates of both U and C to compute S ;
- Using an estimate of U and assuming C to be related to (some power of) U ;
- Assuming C to be related to wave energy dissipation;
- Assuming S to be related to wave energy dissipation;
- Assuming S to be related to (bottom) shear stress;
- Estimating S by an empirical relation;
- Estimating only the sign of S by an empirical relation.

It is obvious that the first method is preferable, although elaboration of the detailed transport equation is troublesome. Some first attempts will be presented in Section 4.2 of this thesis.

In the next sections some relevant results of the other seven classes are discussed but here in the opposite order.

3.5.2 Classification formulae

Empirically based relations have been derived to predict only the direction of the sediment transport. They can be used in order to classify a particular beach state. In fact they present the transition between erosion and accretion.

The various formulae typically use dimensionless parameters, such as wave steepness H/L and the relative grain size D/H . A well-known example is presented by Dean (1977), viz. the (H/Tw) -ratio.

Also a number of Japanese criteria are present, see e.g. (Shibayama and Horikawa, 1982; Kajima et al., 1982; Shimizu et al., 1985).

3.5.3 Empirical transport formulae

These formulae show empirical relationships for the computation of the transport rate. An example is Larson's SBEACH-model as already described in Section 3.4 (Larson and Kraus, 1989a).

3.5.4 Shear stress related transport rates

This kind of formulae are based on shear-stress equations. Examples are the relations presented by Madsen and Grant (1976), Shibayama and Horikawa (1980) and Watanabe (1982). Since suspended sediment transport is predominant, it is arguable that shear stresses are useful for the transport computation in the case of storm surge conditions.

3.5.5 Energy dissipation related transport

These formulae use the wave energy dissipation rate to estimate sediment transport rates. According to Dean (1977), off-shore transport continues until the wave energy dissipation per unit volume of water is constant and equal to a pre-described value over the entire surfzone. Based on this consideration, the rate of local cross-shore sediment transport in the surf zone can be expressed in terms of the difference between the actual and the equilibrium condition of wave energy dissipation in the surf zone (Kriebel and Dean, 1985). Consequently, the local cross-shore transport is expressed as:

$$S = K (D - D_{eq}) \quad (3.5.2)$$

in which:

S	the rate of (cross-shore) sediment transport	($m^3/m^1/s$)
K	a non-dimensionless parameter	($m^5/W/s$)
D	the actual energy dissipation per unit volume of water	(W/m^3)
D_{eq}	the energy dissipation per unit volume of water for equilibrium profile conditions	(W/m^3)

This computational model comprises two unknown coefficients, namely A in the power curve (or D_{eq} in the shape parameter) and K in the transport formula. Although for a specific location and condition the magnitudes may be known, both constants may vary from site to site and from one condition to another. It is clear that there should be a relation with sediment characteristics and hydraulic conditions. Additional results and small extensions of this model are presented by Kriebel (1986, 1987, 1990).

3.5.6 Energy dissipation related suspension

These formulae use the wave energy dissipation rate to compute sediment loads. Next, the actual transport is computed from the product of this load with the mean velocity as occurs under breaking waves (the so-called undertow). An example of this kind of approach is presented by Dally (1980). It is noted that the present model also uses the energy dissipation due to wave breaking to assess the sediment load (see Chapter 4 and 5 for more details).

3.5.7 Velocity related transport (energetics approach)

These formulae use an energetic approach to compute the sediment concentration from the velocity field, basically starting with a relation for the concentrations according to:

$$C = M |U|^N \quad (3.5.3)$$

Bagnold (1962, 1966) developed formulae for calculating sediment transport rate based on

this energy approach and made a distinction between bed load and suspended load. This elementary work has been refined afterward, by including cross-shore transport due to wave energy. After this it was widely applied by several others, for instance Bailard and Stive, see for example (Bailard and Inman, 1981; Bailard, 1982; Stive, 1987; Roelvink and Stive, 1989; Nairn, 1990).

Assuming the relation between velocity and concentration to be valid within the wave period, the effects of asymmetry of the velocity on the transport rate can be accounted for. The superimposed steady current (e.g. the undertow) moves the grains along the bed. The transport vector due to the combined actions of steady current, wave orbital motion and bottom slope effect can now be elaborated. The four basic transport contributions are controlled by so-called velocity moments, $\overline{|u|^m u^n}$, which can be approximated by Taylor series, containing separate terms for the wave orbital motion \tilde{u} and the steady current \bar{u} . These formulations are used in the Bailard transport model of DELFT HYDRAULICS (viz. the CROSTRAN or UNIBEST-TC-model) of DELFT HYDRAULICS, see e.g. (Stive, 1988a; Roelvink and Stive, 1989).

3.5.8 Using estimates for intra-wave results

In this approximation the sediment transport is computed from the instantaneous product of velocities and sediment concentrations, see e.g. (Steetzel, 1990a, 1990d). This procedure to compute cross-shore transport during storm surges is described in this thesis.

In fact, this seems a rather complicated procedure. However, based on the arguments presented in the next chapter, the computation procedure can be simplified. A detailed outline of this procedure will be presented in Chapter 4.

3.5.9 Conclusions

Relative to the other methods, especially the Kriebel/Dean approach using a relation between local transport rates and energy dissipation due to wave breaking seems valuable. The powerful wave breaking processes will indeed control the beach profile development processes in a dominant way.

3.6 Other related research

This section summarizes the outcomes of some investigations into erosion processes which are related to cross-shore transport modelling.

The impact of a single wave on a duneface and the successive erosion have been thoroughly by Overtorn and Fisher, in order to achieve a mechanics based swash-induced dune erosion model. As a result of the numerous experiments, carried out to determine the relationship

between the swash characteristics and dune erosion under a variety of conditions, a linear relationship between the specific swash force and the specific erosion volume has been found (Overtorn et al., 1987; Overtorn and Fisher, 1988). The most recent developments with respect to this research programme are presented by Pratikto (1992).

This very fundamental approach to dune erosion due to a storm surge seems too profound at this moment.

Finally, reference is made to the attempt to describe the dune erosion process by an analytical solution as elaborated by Kobayashi (1987). Notwithstanding the profound elaboration, this approach will never yield a general model able to describe the impact of arbitrarily varying hydraulic conditions on an arbitrary coastal profile.

3.7 Summary and conclusions

Both the equilibrium and the quasi-equilibrium approach are not suitable for the assessment of the effects of arbitrary hydraulic conditions on a cross-shore profile. Since under breaking-wave conditions the transport of suspended sediment seems to be the dominant transport mechanism, the transport formula to be used in the mathematical model should be related to the wave energy dissipation rate.

A further elaboration of this finding is presented in the next chapter.

4 FORMULATION

4.1 Introduction

In order to obtain a reliable procedure for the computation of cross-shore transport rates, first some general considerations on cross-shore transport contributions are presented. This is done to be able to establish a suitable schematization which is as close as possible to the actual physical process.

Based on a number of considerations, a deliberate approach for the computation of transport rates in the case of intensive breaking waves is established in Section 4.2.

The formulation of the transport model, as elaborated in more detail in Section 4.3 to 4.6, has been split up in several different parts, viz. the description of the vertical distribution of both suspended sediment concentrations and secondary flow and, ultimately, the suggested nett transport computation, see also (Steetzel, 1990d). Finally, some justification of the cross-shore transport computation is presented.

Section 4.7 summarizes the set-up of the computational model which computes the development of a cross-shore profile by means of the previously derived transport process. Furthermore, the additional extension of this model to incorporate the effects of structures and alongshore transport gradients is outlined in Section 4.8.

It is noted that complete derivations of four basic expressions (integrals) are presented in the Appendix.

4.2 Approach to cross-shore transport computation

4.2.1 Introduction

It is noted that, for this particular case, a procedure for cross-shore transport computation during storm surge conditions has to be derived. An important feature occurring during these conditions is the transport of suspended sediment caused by intensive breaking of waves. This dominates over other contributions, since relative to non-breaking waves, breaking waves result in a dramatic increase in turbulence level and therefore lift sediment into suspension over almost the whole water depth. This characteristic will be shown to have a great impact on the transport process as a whole and on the nett effect of instantaneous transport rates in particular.

This section continues with a brief recapitulation of the basic procedure for nett cross-shore transport computation. In order to examine (and afterwards justify) the (later) presented derivation for cross-shore transport computation for conditions with intensive breaking waves, first two distinct basic contributions to the total nett transport rate are distinguished. Next a number of trial estimations is presented and some reference to applicable measurements conducted by other researchers is made, this in order to assess the relative importance of both contributions to the nett transport rate. From these, a new approach to cross-shore transport modelling is derived which will be explained and elaborated in more detail in the succeeding sections.

4.2.2 Basic procedure

In general, the nett local (thus time-averaged) cross-shore sediment transport rate through a vertical plane with unit width, should be computed from the (well-known) basic equation, according to:

$$S(x) = \frac{1}{nT} \int_{t=0}^{nT} \int_{z=0}^{\eta(x,t)} u(x,z,t) C(x,z,t) dz dt \quad (4.2.1)$$

in which:

S	the (x-component of the) nett transport	(m ³ /m/s)
u	the (x-component of the) cross-shore velocity	(m/s)
C	the sediment concentration	(-)
x	the (horizontal) position	(m)
t	time	(s)
T	the wave period	(s)
z	a vertical ordinate with respect to $z = 0$ at the (sand) bottom	(m)
η	the instantaneous water level	(m)
n	a sufficiently high number	(-)

Note that in this formulation already is assumed that the velocity of suspended sediment particles corresponds with the velocity of the fluid particles.

For the solution and elaboration of this equation, one should be able to compute or describe the time and space variation of both the velocity and sediment concentration.

Since no detailed knowledge on these fluctuations (especially not for randomly breaking waves during storm surge conditions) is present yet, some simplifications have to be made. Therefore, in the next section this basic expression, viz. Equation (4.2.1), is studied in more detail, in order to identify different contributions to the nett transport rate and, ultimately, to make some reliable simplifications.

4.2.3 General considerations

The expression for the nett sediment transport $S(x)$ at a particular position x , can be simplified to:

$$S = \int_d s(z) dz \quad (4.2.2)$$

in which the (time-averaged) mean transport s is restricted to a certain elevation above the bottom.

This (time-averaged) mean transport rate s can basically be described by the mean (time-averaged) magnitude of the product of an instantaneous horizontal velocity $u(t)$ and an instantaneous sediment concentration $C(t)$ as occurs at the specific level of interest, according to:

$$s = \overline{u(t) C(t)} \quad (4.2.3)$$

in which the overbar denotes time-averaging with an averaging time based on the lowest frequency of the signals involved (actual wave period). If both time functions are split up into a mean (denoted by an overbar) and a fluctuating part (accent added), according to:

$$u(t) = \bar{u} + u' \quad (4.2.4)$$

and:

$$C(t) = \bar{C} + C' \quad (4.2.5)$$

respectively, the nett transport rate s , according to Equation (4.2.3), can be elaborated further as:

$$\begin{aligned} s &= \overline{(\bar{u} + u')(\bar{C} + C')} \\ &= \overline{\bar{u}\bar{C}} + \overline{\bar{u}C'} + \overline{u'\bar{C}} + \overline{u'C'} \\ &= \bar{u} \bar{C} + \bar{u} \overline{C'} + \overline{u' \bar{C}} + \overline{u' C'} \end{aligned} \quad (4.2.6a)$$

Since the mean value of both the fluctuating parts equals zero by definition, ergo both $\overline{u'} = 0$ and $\overline{C'} = 0$, this finally yields:

$$s = \bar{u} \bar{C} + \overline{u' C'} = s_{mean} + s_{corr} \quad (4.2.6b)$$

Consequently, the nett transport at a certain level above the bottom consists out of two contributions, namely a mean component of time-averaged velocity times time-averaged concentration and a more complex correlation component, thus:

- mean component $s_{mean} = \bar{u} \bar{C}$;
- correlation component $s_{corr} = \overline{u' C'}$.

With respect to the first component it is noted that, especially during storm surge conditions with intensive breaking waves, a considerable (offshore-directed, thus negative) mean current occurs. This so-called undertow amounts to 0.3 to 0.6 m/s under prototype conditions. Among other sources, the latter (wave-induced) component originates from the asymmetry of the waves and is clearly far more difficult to elaborate than the first term.

A similar result can be obtained for the depth-integrated total transport rate S , this according to:

$$S = \int_d s \, dz = \int_d (s_{mean} + s_{corr}) \, dz = \int_d s_{mean} \, dz + \int_d s_{corr} \, dz = S_{mean} + S_{corr} \quad (4.2.7)$$

It is obvious that a reliable estimate of the magnitude of both contributions, viz. S_{mean} and S_{corr} , to the nett transport rate is essential in order to develop a schematized, though reliable procedure for the computation of the nett depth-integrated total cross-shore transport rate S . Especially the relative contribution of the complicated correlation component S_{corr} (say S_{corr}/S_{mean} -ratio) is important, since this term has a great impact on the ultimate complexity of the formulations involved with cross-shore transport modelling.

4.2.4 Strategies to component assessment

There are several methods by which one can get insight in the relative importance of the transport components in Equation (4.2.7), viz.:

- Using analytical and mathematical approximations;
- Conducting detailed intra-wave measurements;
- Comparing measured transport rates with a computed nett mean contribution to the transport.

Some preliminary approaches to assess the contributions to the nett transport rate by using analytical and mathematical approximations will be elaborated in the next section.

With respect to the above second method, some results are available for neat laboratory conditions (Chen, 1992a, 1992b; Ribberink and Al-Salem, 1991; Al-Salem, 1993). Some applicable results are summarized in Section 4.2.6, although for intensive random breaking waves occurring during storm surge conditions, currently no data are known to the author.

In the latter, third approach, the mean component to the transport rate S_{mean} is computed from measured time-averaged $u(z,t)$ - and $C(z,t)$ -signals directly and subsequently compared with measured S -values. It is assumed that any (systematic) discrepancy in the outcomes of computations and measurements thus must be due to the effect of the depth-integrated correlation component S_{corr} . This method will be used to give some additional justification of the procedure for cross-shore transport computation in the case of breaking waves as derived later in this chapter (see Section 4.6 for more details).

4.2.5 Analytical and mathematical approximations

In order to assess the (relative) magnitude of both transport contributions, viz. the mean component $s_{mean}(z)$ or S_{mean} and the correlation component $s_{corr}(z)$ or S_{corr} , the results of three different types of assessments are discussed next. With an increasing state of complexity the following effects will be considered:

- Effects of harmonic fluctuations (at a specific level);
- Depth-integrated effects using an analytical approximation;
- Depth-integrated effects using a mathematical model.

It is noted that the objective of these explorations is to support and to give additional evidence to the later proposed schematization of the basic cross-shore transport formulation of Equation (4.2.1). However, into the framework of this research project, this is done in a concise approach, although dealing with this fundamental problem would be worth a complete thesis, see e.g. (Chen, 1992b).

Effects of harmonic fluctuations

A first, relatively simple derivation for the nett transport rate s which is only valid for a certain height z above the bottom (thus $s(z)$) is given for a series of combined harmonic fluctuations for both the velocity and concentration term, this according to (see also Equation (4.2.4) and (4.2.5)):

$$u(t) = \sum_{i=0}^{\infty} \hat{u}_i \cos(i\omega t - \alpha_i) = \bar{u} + \sum_{i=1}^{\infty} \hat{u}_i \cos(i\omega t - \alpha_i) \quad (4.2.8)$$

$$C(t) = \sum_{i=0}^{\infty} \hat{C}_i \cos(i\omega t - \beta_i) = \bar{C} + \sum_{i=1}^{\infty} \hat{C}_i \cos(i\omega t - \beta_i) \quad (4.2.9)$$

where:

- \bar{u}, \bar{C} the time-averaged value of the velocity- and concentration-signal, with $\bar{u} = \hat{u}_0$ and $\bar{C} = \hat{C}_0$ respectively;
- \hat{u}_i, \hat{C}_i the amplitude of the i^{th} harmonic component of each fluctuation;
- ω the (basic) angular frequency ($= 2\pi/T$);
- α_i, β_i the phase shift of the i^{th} harmonic component of velocity- and concentration-fluctuation respectively, with $\alpha_0 = 0$ and $\beta_0 = 0$.

It should be noted that this method is applicable for every arbitrary signal, since the components can be obtained by expanding each time signal into Fourier series.

Elaboration of the nett transport rate s (at a certain level z) according to Equation (4.2.6) yields:

$$s = \bar{u} \bar{C} + \frac{1}{T} \int_{t=0}^T \left[\sum_{i=1}^{\infty} \hat{u}_i \cos(i\omega t - \alpha_i) \sum_{i=1}^{\infty} \hat{C}_i \cos(i\omega t - \beta_i) \right] dt \quad (4.2.10a)$$

which, after some further elaborations, can be shown to result in:

$$s = \bar{u} \bar{C} + \frac{1}{2} \sum_{i=1}^{\infty} \hat{u}_i \hat{C}_i \cos(\alpha_i - \beta_i) \quad (4.2.10b)$$

This relative simple result is due to the fact that because of time-averaging the product of all sinusoidal components having no identical angular frequency can be deleted. Consequently, the first term on the right-hand side equals the (local) mean transport component s_{mean} , whereas the correlation component can be described by:

$$s_{corr} = \frac{1}{2} \sum_{i=1}^{\infty} \hat{u}_i \hat{C}_i \cos(\alpha_i - \beta_i) \quad (4.2.11)$$

As discussed before, the relative magnitude of both terms is essential.

This relative magnitude ($=s_{mean}/s_{corr}$), denoted further as R_s , can be expressed as:

$$R_s = \frac{1}{2} \sum_{i=1}^{\infty} \frac{\hat{u}_i}{\bar{u}} \frac{\hat{C}_i}{\bar{C}} \cos(\alpha_i - \beta_i) \quad (4.2.12)$$

and consists basically of the product out of three terms for each harmonic.

From this expression it can be observed that for a particular harmonic component i , the relative magnitude of the correlation component depends on the relative amplitude of the fluctuations of both the $u(t)$ - and $C(t)$ -signal, as well as on the phase shift between both signals ($\alpha - \beta$).

Consequently, if the relative magnitude (\hat{u}_i/\bar{u}) or (\hat{C}_i/\bar{C}) equals near zero, or the mutual phase shift will be about $\pi/2$ rad and thus $\cos(\alpha_i - \beta_i) \approx 0$, the magnitude of the contribution of this harmonic to the total correlation component, is negligible. If this is the case for all relevant harmonics (say $i=1, \dots, n$), the total effect of the correlation component of the nett transport rate (at the level of interest) may be neglected. In this case, only a limited number of components is of interest, namely up to the order of the velocity-signal (e.g. up to $n=2$ for second-order Stokes' waves). The effects of any high(er)-order concentration fluctuations on the nett transport rate are cancelled since for $i=3, 4, \dots$ each amplitude \hat{u}_i and thus (\hat{u}_i/\bar{u}) equal zero by definition.

If this holds for every individual level, the total contribution of the correlation component to the total nett depth-integrated cross-shore transport rate S will also be insignificant, although a negligible magnitude may also be the result of the summation of opposite magnitudes of individual s_{corr} -magnitudes present at different levels, as can be seen from the depth-integrated nett transport formulation.

This total nett transport S can be computed from:

$$S = \int_d \bar{u}(z) \bar{C}(z) dz + \frac{1}{2} \sum_{i=1}^{\infty} \int_d \hat{u}_i(z) \hat{C}_i(z) \cos(\alpha_i(z) - \beta_i(z)) dz \quad (4.2.13)$$

in which the two terms on the right side denote the mean transport component S_{mean} and the correlation component S_{corr} respectively.

The complexity of the latter term is obvious:

$$S_{corr} = \frac{1}{2} \sum_{i=1}^{\infty} \int_d \hat{u}_i(z) \hat{C}_i(z) \cos(\alpha_i(z) - \beta_i(z)) dz \quad (4.2.14)$$

although some preliminary remarks can be made.

The magnitude of the concentration amplitude $\hat{C}_i(z)$ will probably decrease in upward direction due to damping effects. From this point of view, the contribution to S_{corr} will diminish upward. Moreover, the impact of the *cos*-term may lead to an upward altering sign and thus to an additional reduction in the total S_{corr} -magnitude.

A more fundamental attempt to get some additional insight in the latter expression and thus in the (relative) magnitude of the corresponding transport components, is made in the following.

Depth-integrated effects using analytical approximations

The former assessment was basically related to a particular height above the bottom. Next, more or less the same approach is followed for the depth-integrated components of the nett transport rate, this being based on the suspension of solids due to a periodical motion in horizontal direction according to (Ribberink, 1987; Steetzel, 1990a). The solution involved is derived for a simplified version of the ordinary (1D-vertical) non-stationary, convection-diffusion equation (see Section 3.3 for more details) according to:

$$\frac{\partial C}{\partial t} = w_s(z) \frac{\partial C}{\partial z} + \frac{\partial}{\partial z} \left(\varepsilon_s(z) \frac{\partial C}{\partial z} \right) \quad (4.2.15)$$

in which both a constant particle fall velocity $w_s(z) = w_s$ and a constant, spatially uniform, vertical diffusivity $\varepsilon_s(z, t) = \varepsilon_s(z) = \varepsilon_s$ have to be assumed in order to achieve an analytical solution. So a solution has to be derived for:

$$\frac{\partial C}{\partial t} = w_s \frac{\partial C}{\partial z} + \varepsilon_s \frac{\partial^2 C}{(\partial z)^2} \quad (4.2.16a)$$

or, in a re-arranged order:

$$\frac{\partial^2 C}{(\partial z)^2} + \frac{w_s}{\varepsilon_s} \frac{\partial C}{\partial z} - \frac{1}{\varepsilon_s} \frac{\partial C}{\partial t} = 0 \quad (4.2.16b)$$

Its solution, viz. the assessment of $C(z, t)$, requires boundary conditions at both the bed level $z=0$ and at an infinite elevation $z = \infty$, according to:

$$C(0, t) = C_0(t) \quad (4.2.17)$$

and

$$C(z \rightarrow \infty, t) = 0 \quad (4.2.18)$$

respectively. For example, the lower boundary condition, thus $C_0(t)$, has been represented by an energetics-based power-law according to:

$$C_0(t) = M |u(t)|^N \quad (4.2.19)$$

in which, for the sake of convenience $M=1$ is chosen. Moreover, the power N needs to be even ($N=2, 4, \dots$) in order to achieve an analytical solution of Equation (4.2.16b).

For a spatially uniform (no x - and z -dependency), the horizontal periodic velocity according to:

$$u(t) = \sum_{i=0}^n \hat{u}_i \cos(i \omega t) = \bar{u} + \sum_{i=1}^n \hat{u}_i \cos(i \omega t) \quad (4.2.20)$$

with $\bar{u} = \hat{u}_0$, the related $C_0(t)$ -signal can be determined from the combination of former two equations according to:

$$M \left[\sum_{i=0}^n \hat{u}_i \cos(i \omega t) \right]^N = \sum_{i=0}^{nN} \hat{C}_{0,i} \cos(i \omega t) \quad (4.2.21)$$

resulting in:

$$C_0(t) = \sum_{i=0}^{nN} \hat{C}_{0,i} \cos(i \omega t) = \bar{C}_0 + \sum_{i=1}^{nN} \hat{C}_{0,i} \cos(i \omega t) \quad (4.2.22)$$

in which the number of components thus is restricted to $i_{max} = nN$ and $\hat{C}_{0,i}$ for $i = 0, 1, \dots, nN$ can be elaborated from Equation (4.2.21). As will be shown later in this thesis, only the $\hat{C}_{0,i}$ -magnitudes for harmonics $i = 0, 1, \dots, n$ are of interest for the assessment of the nett transport rate.

From this, a periodic solution with $C(z, t) = C(z, t + T)$, for the instantaneous concentration profile $C(z, t)$ can be derived (after (Nielsen, 1979)).

A general solution, using a separation of variables, can be represented by:

$$C(z, t) = \sum_{i=0}^{\infty} \hat{C}_{0,i} f_{\hat{e}i}(z) f_{c'i}(t|z) = \bar{C}_0 f_c(z) + \sum_{i=1}^{\infty} \hat{C}_{0,i} f_{\hat{e}i}(z) f_{c'i}(t|z) \quad (4.2.23)$$

in which:

- $\hat{C}_{0,i}$ the basic amplitude of the i^{th} harmonic, with $\bar{C}_0 = \hat{C}_{0,0}$;
- $f_{\hat{e}i}$ a shape function describing the time-averaged distribution of the concentration fluctuations for each harmonic, with $\{0 < f_{\hat{e}i} \leq 1\}$;
- $f_{c'i}$ a time function describing both the fluctuation and time shift for a specific level z and harmonic i , with $\{-1 \leq f_{c'i} \leq 1\}$.

The first term on the right side denotes the stationary part, describing the vertical profile of the time-averaged concentration according to Equation (4.3.1) and is examined in more detail in Section 4.3.

After further elaboration, the specific solution of Equation (4.2.16b) can be shown to yield:

$$C(z, t) = \sum_{i=0}^{\infty} \hat{C}_{0,i} \exp\left(-\frac{w_s}{\epsilon_s} P_i z\right) \cos\left(i \omega t - \frac{w_s}{\epsilon_s} Q_i z\right) \quad (4.2.24)$$

with:

$$P_i = \frac{1}{2} + \sqrt{\frac{1}{16} + (i\Lambda)^2} \cos(\alpha_i/2) \quad (4.2.25)$$

$$Q_i = \sqrt{\frac{1}{16} + (i\Lambda)^2} \sin(\alpha_i/2) \quad (4.2.26)$$

and: $\alpha_i = \text{atan}(4i\Lambda)$ (4.2.27)

in which the concentration fluctuations at higher levels are controlled by the dimensionless P_i and Q_i parameters. The dimensionless parameter Λ in the latter expression denotes the so-called time-lag parameter which relates the response time of the suspended concentration to the concentration variation at the bed level. This time-lag parameter is defined as:

$$\Lambda = \frac{\omega \varepsilon_s}{w_s^2} = \frac{\omega r_c}{w_s} \quad (4.2.28)$$

in which r_c ($= \varepsilon_s/w_s$) denotes the concentration decay length-scale (see Section 4.3.2 for more details).

For storm surge conditions as observed in a large-scale model test (see Section 4.3 for more details), the magnitude of the time-lag parameter is in the range of $\Lambda \approx 5 \dots 100$, with $\Lambda \approx 30$ as a characteristic value (as estimated from characteristic values $\varepsilon_s \approx 0.004 \dots 0.03$ m²/s, $w_s \approx 0.020 \dots 0.025$ m/s, $r_c \approx 0.15 \dots 1.5$ m and $T \approx 5 \dots 8$ s respectively; see Section 4.3). The magnitude increases in upward direction due to the spatially non-uniform mixing processes (upward increasing ε_s -magnitudes due to effects of wave breaking; see Section 4.3.3).

The shape (or distribution) function $f_{\hat{\varepsilon}i}$ in Equation (4.3.23) is thus defined as:

$$f_{\hat{\varepsilon}i} = \exp\left(-\frac{w_s}{\varepsilon_s} P_i z\right) \quad (4.2.29)$$

from which can be seen that $\{0 < f_{\hat{\varepsilon}i} \leq 1\}$ and that the upward decrease is proportional to the magnitude of P_i , where $P_0 = 1$ and $P_i > 1.0$ for $i = 1, 2, \dots$ and moreover $P_{i+1} > P_i$.

The time function $f_{c'i}$ is represented by:

$$f_{c'i} = \cos\left(i\omega t - \frac{w_s}{\varepsilon_s} Q_i z\right) \quad (4.2.30)$$

with $Q_0 = 0$, showing that the phase lag is a linear function of the elevation above the bed. The level at which the phase lag with respect to the bottom equals π rad ($= (\pi \varepsilon_s)/(Q_i w_s)$) decreases for increasing Q_i -values, since $Q_i > 0$ for $i = 1, 2, \dots$ and $Q_{i+1} > Q_i$.

Re-writing of Equation (4.2.24), by separation of the steady $i = 0$ (and thus $\alpha_0 = 0$, $P_0 = 1$ and $Q_0 = 0$) and fluctuating components $i = 1, 2, \dots$, yields:

$$C(z, t) = \bar{C}_0 \exp\left(-\frac{w_s}{\varepsilon_s} z\right) + \sum_{i=1}^{\infty} \hat{C}_{0,i} \exp\left(-\frac{w_s}{\varepsilon_s} P_i z\right) \cos\left(i\omega t - \frac{w_s}{\varepsilon_s} Q_i z\right) \quad (4.2.31)$$

showing the mean (time-averaged) concentration profile as the first term on the right-hand side, which equals the ordinary negative exponential concentration distribution based on a first-order (constant) mixing distribution, this according to Equation (4.3.18) in Section 4.3.

As stated, the magnitude of Λ has a great impact on the instantaneous concentration profile and thus on the nett transport rate as will be shown in the following.

For the special case of $\Lambda \downarrow 0$ (e.g. very coarse sediment, large periods, gentle mixing) and thus $\alpha_i \approx 0$, $P_i \approx 1$ and $Q_i \approx 0$ for $i = 1, 2, \dots$, no time lag is present and the concentration distribution approaches an equilibrium profile based on the instantaneous bed concentration, viz.:

$$C(z, t) = \sum_{i=0}^{\infty} \hat{C}_{0,i} \exp\left(-\frac{w_s}{\varepsilon_s} z\right) \cos(i \omega t) \quad (4.2.32)$$

For the other extreme, viz. $\Lambda \rightarrow \infty$ (thus fine sediment and intensive mixing), and thus $\alpha_i \approx \pi/2$, $P_i \approx (1 + \sqrt{2i\Lambda})/2 \approx (\sqrt{2i\Lambda})/2$ and $Q_i \approx (\sqrt{2i\Lambda})/2$, the significant fluctuations of the concentration profile are only restricted to a small layer near the bottom, this especially due to the large damping effect, since $P_i \gg 1$ for $i = 1, 2, \dots$ in this case.

The instantaneous sediment transport rate through a vertical plane $S(t)$, can be computed by combining horizontal particle velocities $u(z, t)$ and local concentrations $C(z, t)$ according to:

$$S(t) = \int_{z=0}^{\infty} u(z, t) C(z, t) dz \quad (4.2.33a)$$

For a velocity which is independent of the elevation, viz. $u(z, t) = u(t)$, this leads to:

$$S(t) = u(t) \int_{z=0}^{\infty} C(z, t) dz = u(t) L_s(t) \quad (4.2.33b)$$

in which L_s denotes the so-called sediment load as described in more detail in Section 4.3.6. Elaboration of the involved depth-integral yields:

$$\begin{aligned} L_s(t) &= \sum_{i=0}^{\infty} \hat{C}_{0,i} \frac{\varepsilon_s}{w_s} \frac{1}{P_i^2 + Q_i^2} (P_i \cos(i \omega t) + Q_i \sin(i \omega t)) \\ &= \bar{C}_0 \frac{\varepsilon_s}{w_s} + \sum_{i=1}^{\infty} \hat{C}_{0,i} \frac{\varepsilon_s}{w_s} \frac{1}{P_i^2 + Q_i^2} (P_i \cos(i \omega t) + Q_i \sin(i \omega t)) \end{aligned} \quad (4.2.34)$$

in which the first term represents the time-averaged part of the sediment load, this conform Equation (4.3.25b).

From this, the total nett (time-averaged) transport rate can be assessed from:

$$S = \frac{1}{T} \int_{t=0}^T S(t) dt = \frac{1}{T} \int_{t=0}^T u(t) L_s(t) dt \quad (4.2.35)$$

which, after further elaboration, can be shown to result in:

$$S = \bar{u} \bar{C}_0 \frac{\varepsilon_s}{w_s} + \frac{1}{2} \sum_{i=1}^{\infty} \hat{u}_i \hat{C}_{0,i} \frac{\varepsilon_s}{w_s} \left(\frac{P_i}{P_i^2 + Q_i^2} \right) \quad (4.2.36)$$

The second term on the right-hand side in this expression represents the desired depth-integrated correlation component:

$$S_{corr} = \frac{1}{2} \sum_{i=1}^{\infty} \hat{u}_i \hat{C}_{0,i} \frac{\varepsilon_s}{w_s} \left(\frac{P_i}{P_i^2 + Q_i^2} \right) \quad (4.2.37)$$

as presented earlier in its fundamental form in Equation (4.2.14). The combined depth-integrated effect of both the vertical damping and elevation-dependent time shift is given by the right term between the brackets.

According to Equation (4.2.20), the number of relevant harmonics is limited to $i_{max} = n$, since the amplitude $\hat{u}_i = 0$ for $i > n$. Consequently, the ratio R_S between the depth-integrated contribution of the correlation component and the depth-integrated contribution of the mean component can be expressed as:

$$R_S = \frac{S_{corr}}{S_{mean}} = \frac{1}{2} \sum_{i=1}^n \frac{\hat{u}_i}{u} \frac{\hat{C}_{0,i}}{C_0} \Omega_i \quad (4.2.38)$$

in which the Ω_i -parameter depends on both the P_i - and Q_i -parameter as defined in Equation (4.2.25) and (4.2.26) and is thus a unique function of the former introduced time-lag parameter Λ :

$$\Omega_i(\Lambda) = \frac{P_i}{P_i^2 + Q_i^2} \quad (4.2.39)$$

In Figure 4.1, this Ω -relation is presented as a function of Λ for the harmonics $i = 1, 2, 3$ and 5 , whereas the specific range of relevant Λ -values is also presented.

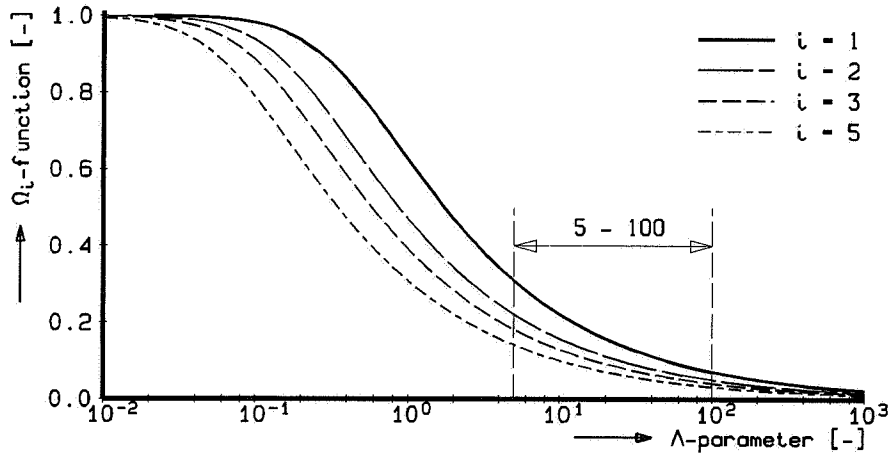


Figure 4.1 Magnitude of reduction parameter Ω as a function of the time-lag parameter Λ for a number of harmonics.

The reduction parameter Ω depends largely on the time-lag parameter Λ and shows, apart from the relative amplitudes of the harmonics, whether the correlation component has a large impact on the nett transport rate. For high Λ -values, say $\Lambda \gg 10$, the asymptotic magnitude of $\Lambda \approx 1/\sqrt{2i\Lambda}$ is reached, yielding low Ω -values. For lower Λ -values, say $\Lambda \ll 1$, viz. mild to moderate hydraulic conditions, this contribution is of the same order

as the mean component and thus the effect of both contributions to the total nett transport has to be accounted for. However, for the conditions with intensive breaking waves as studied here, this is definitely not the case.

Next the relative magnitude of the correlation component according to Equation (4.2.38) can be assessed for the actual magnitude of the governing parameters, viz. (\hat{u}_i/\bar{u}) , $(\hat{C}_{0,i}/\bar{C}_0)$ and Ω_i for $i = 1, 2, \dots, n$. It should be noted that the first-order component of the concentration, viz. $\hat{C}_{0,1}$, is probably not significant in most of the cases. Moreover, the correlation with the basic velocity amplitude \hat{u}_1 will result in a major second-order concentration component (so $\hat{C}_{0,2} > \hat{C}_{0,1}$).

For a second-order Stokes' wave (so $n = 2$), with $(\hat{u}_1/\bar{u}) \approx 5$ and $(\hat{u}_2/\bar{u}) \approx 1$, relative concentration amplitudes of $(\hat{C}_{0,2}/\bar{C}_0) \approx 0.5$ (half of \bar{C}_0 , being an upper limit probably) and $(\hat{C}_{0,1}/\bar{C}_0) \approx 0.25$ (half of the former ratio as a maximum) respectively and a characteristic time-lag parameter $\Lambda \approx 30$ (and thus $\Omega_1 \approx 0.15$ and $\Omega_2 \approx 0.10$), the relative contribution of the correlation component to the total depth-integrated nett transport rate R_g equals:

$$R_g = \frac{1}{2} (5 \cdot 0.25 \cdot 0.15 + 1 \cdot 0.5 \cdot 0.10) \approx 0.119 = 11.9\%$$

Even for a lower Λ -value (say $\Lambda = 5$), the relative contribution to the nett transport rate is about 20 % at most.

From this, it can be concluded that for the special case of intensively breaking waves and neglecting the contribution of the correlation component S_{corr} , it will probably lead to only a secondary error in the nett transport rate S .

Depth-integrated effects using a mathematical model

The mathematical version of the former approach allows for both the input of non-harmonic signals, non-constant mixing as well as for a special treatment of the bottom boundary (Steetzel, 1990a), see also (Bakker, 1974; Fredsøe et al., 1983).

As an example, the non-stationary diffusion equation according to Equation (4.2.15) is resolved mathematically for a velocity signal according to:

$$u(z, t) = u(t) = \bar{u} + \hat{u}_1 \cos(\omega t) + \hat{u}_2 \cos(2\omega t - \beta_2) \quad (4.2.40)$$

in which $\bar{u} = -0.10$ m/s, $\hat{u}_1 = 1.00$ m/s, $\hat{u}_2 = 0.40$ m/s, $\beta_2 = \pi/8$ and $\omega = 2\pi/T$ in which the wave period equals $T = 5$ s. Furthermore, the constant though spatially non-uniform vertical mixing distribution was schematized according to:

$$\varepsilon_s(z, t) = \varepsilon_s(z) = \varepsilon_0 + \mu z \quad (4.2.41)$$

in which $\varepsilon_0 = 0.003$ m²/s and $\mu = 0.04$ m/s (see Section 4.3.3 for more details).

It is remarked that the assumption of a time-varying mixing coefficient yields comparable results. Consequently, a time-invariant mixing assumption seems sufficient to model the interaction of waves and currents. This finding agrees with the results of analysis by You et al. (1991).

The magnitude of the concentration at $z=0$ m, was assumed to be related to the instantaneous (near-bed) velocity according to:

$$C_0(t) = M|u(t)|^N \quad (4.2.42)$$

with $M=1$ and $N=2$. In Figure 4.2 the computed equilibrium fluctuation of the near-bottom concentration is presented and denoted by the lower dashed line (direct response).

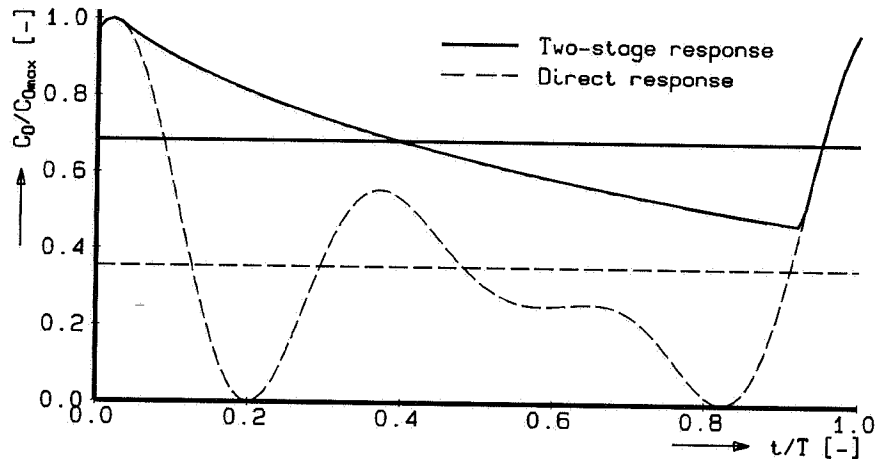


Figure 4.2 Example of active/passive behaviour of near-bottom concentration.

The fall in magnitude of C_0 to even a zero concentration seems rather absurd since the concentrations at a somewhat higher level are still significant. Based on this argument, it was assumed that during time intervals with decreasing concentrations (according to a direct response), the concentration near the bottom is determined by the amount of suspended sediment at higher elevations (it takes time to fall). If during a small computational time step Δt , the reference concentration is decreasing due to a decrease in the forcing near-bottom velocity (thus according to a direct response function as presented in Equation (4.2.42)), the 'new' lower magnitude of this concentration (at $t = t + \Delta t$) is compared with the maximum drop in the concentration magnitude which can be obtained by settling of the suspended sediment (present just above this level) during this time step. If the latter yields a smaller magnitude of the concentration, than the original direct response magnitude is accepted. If the drop in the concentration magnitude can not be obtained, then the actual concentration will exceed the direct response magnitude (Steetzel, 1990a). Figure 4.2 shows the effect of this two-stage behaviour on the fluctuations during the wave period also.

Due to this behaviour, viz. the two-stage response, the suspension will almost solely be determined by the maximum velocities. Consequently, the time-averaged concentration (denoted by the horizontal lines in the former figure) will be of a greater magnitude.

Figure 4.3 shows the computed development of the concentration profile during a wave cycle. Apart from the time-averaged concentration profile, four momentary $C(z)$ -profiles are presented.

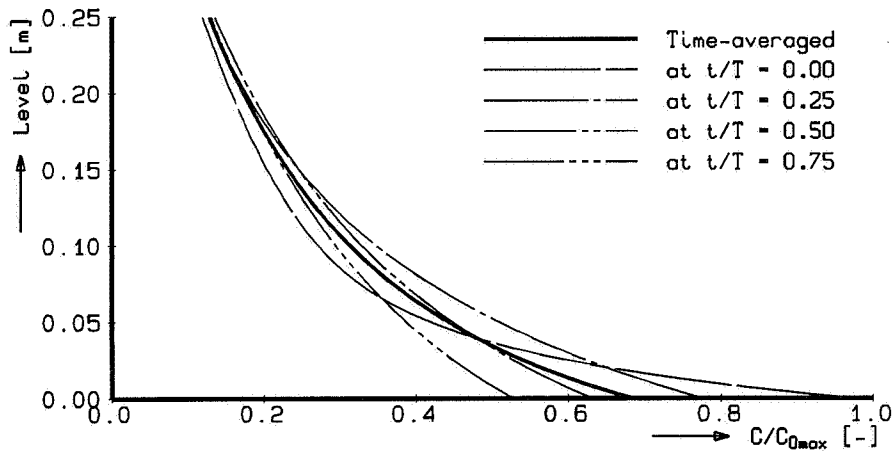


Figure 4.3 Example of computed concentration profiles during a wave cycle.

These momentary $C(z)$ -relations oscillate around the time-averaged values, this according to previously derived analytical solutions.

The computed development of the local concentration $C(t)$ at three different elevations above the bottom is shown in Figure 4.4.

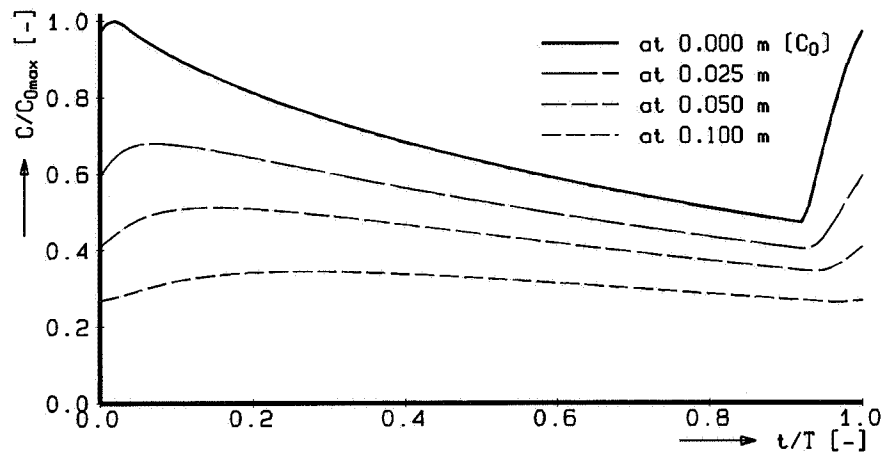


Figure 4.4 Example of computed development of concentrations at different levels.

From this, both the upward increasing phase lag and the decreasing amplitude of the fluctuations can be seen. It is noted that former results are in agreement with the conclusions of Frødsø et al. (1983) and Ifuku and Kakinuma (1988).

The effect on the instantaneous transport distributions can now be assessed by computation of the product of the instantaneous velocity (profile) $u(z,t)$ and the instantaneous concentration profile $C(z,t)$. By integrating the former results over the wave period T , the nett transport profile $s(z)$ can be determined. The product of time-averaged concentration profile $\bar{C}(z)$ and time-averaged velocity profile \bar{u} forms the mean contribution $s_{mean}(z)$, whereas the residual difference equals the vertical profile of the correlation component $s_{corr}(z)$. The vertical profiles of these transport contributions are shown in Figure 4.5.

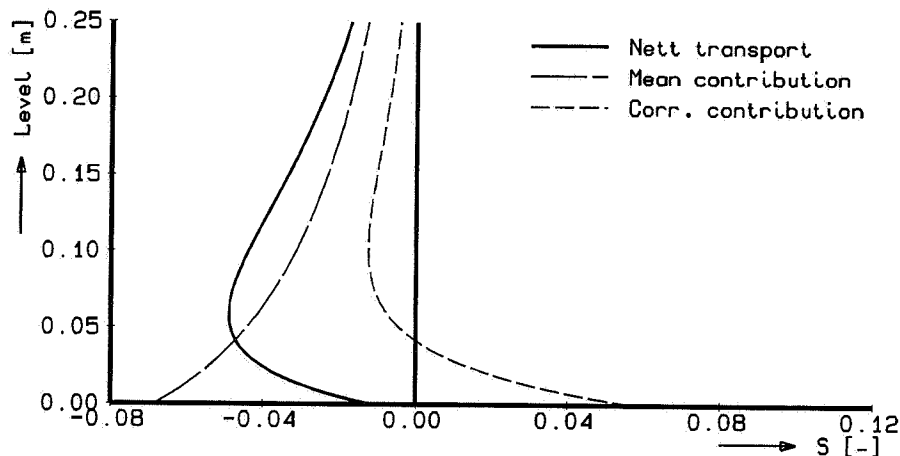


Figure 4.5 Example of computed profiles of the transport contributions.

Due to the reverse current (negative \bar{u} -value) a negative nett transport is found. The effect of the correlation component is shown by the dashed line on the right side in this figure. Near the bottom this results in an additional positive transport rate in the wave direction. At higher levels the direction is altered due to the phase shift. Consequently, the nett effect of this component is almost eliminated.

For this case, the depth-integrated magnitudes of the mean transport contribution $s_{mean}(z)$ is almost equal to the nett transport rate S .

It is noted that the former example was presented to illustrate the character of the transport contributions and to obtain some insight in the major related effects on the nett transport rate. Besides, from a more extensive elaboration of governing parameters it was concluded that the former presented example indeed did represent characteristic results.

4.2.6 Results of relevant measurements

Some interesting results on the fundamental problem of cross-shore transport modelling are presented by Chen (1992a, 1992b), shown in Figure 4.6, who conducted series of experiments under non-breaking waves and superimposed opposing current in a small-scale wave flume. Measurements of local time-varying sediment concentrations and velocities were obtained using an optical concentration meter and an electro-magnetic flow meter at a number of elevations above the bottom.

From a comparison between the behaviour of the time-variations of the concentration and the velocity, it appeared that variations in the concentrations show large random components (which do not contribute to the nett transport rate!). Furthermore, the test results indicate that a significant phase lag exists between velocity and concentration fluctuations which changes in vertical direction. With a relatively strong mean flow the phase lag near the bottom amounts to almost 90 degrees and the effect on the nett sediment rate is negligible.

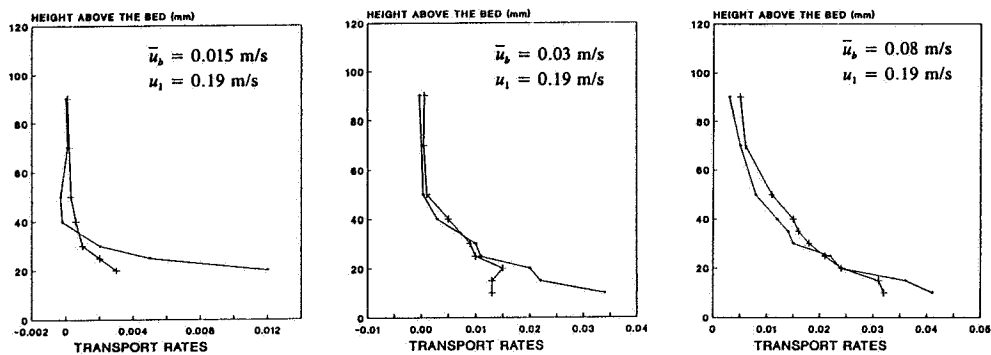


Figure 4.6 Vertical distributions of sediment transport rate over the water depth (Chen, 1992a).

In Figure 4.6 the vertical profile of both the nett transport s ($=\overline{u C}$; denoted by the dots) and the mean contribution s_{mean} ($=\overline{u C}$; denoted by the +symbols) are given for three mean near-bed velocities (denoted by \overline{u}_b). Especially for a relatively strong mean flow rate (right-hand figure) both profiles are almost comparable. Their mutual deviation is caused by the effect of the s_{corr} -component ($=\overline{u' C'}$) of the transport, which is relatively small and changes in upward direction resulting in a negligible depth-integrated transport contribution.

In summary, the test results indicate that in principle the contribution of the fluctuations of sediment concentration should be accounted for in cross-shore transport computations. However, under some specific conditions (for example in a surfzone where the mean flow is relatively strong due to wave breaking), the contributions of the fluctuations may be neglected as a first order of approximation.

Other interesting results were obtained by Van Rijn who conducted tests on the transport process of fine sands in combined current and wave conditions in a flume (Van Rijn et al., 1993). Time-averaged fluid velocities were measured by an electromagnetic current meter, whereas time-averaged concentrations were measured by a pump sampler. The net transport rate was obtained by integration of the product of velocity and concentration over the water depth. Apart from the finding that a larger wave height leads to both larger concentrations and a steeper (more uniform) concentration profile, (probably as a result of an increase of the wave-related mixing), the relative importance of the correlation contribution to the net transport was also discussed. Although based on only three experiments it was concluded that for a limited ratio between the near-bed orbital velocity and mean velocity (say < 2), the correlation component seemed to be of less importance to the net transport. Neglecting this contribution may lead to a systematic error of about 30 % at most.

Former conclusions are in accordance with earlier presented outcomes of the theoretical assessment of relative transport contributions.

4.2.7 Conclusions on relative contributions

Summarizing the results of formerly presented assessments and relevant measurements, some preliminary conclusions with respect to the relative contribution of the correlation component to the net transport can be made, as outlined in the following.

With respect to the *amplitude* of the (concentration) fluctuations it can be assumed that:

- The fluctuations of the concentration near the bed level are damped due to the delayed settlement of sediment in the case of 'steep' concentration profiles;
- Due to the opposing current which occurs with undertow, the effects of wave asymmetry on the 'near-bed' sediment concentrations will be reduced (or even minimized);
- The concentration fluctuations well above the bed are relatively small and do not hardly correlate with the velocity fluctuations (more or less random);
- The concentration fluctuations at higher altitudes are even smaller (due to damping) and probably not correlated with the velocity fluctuations (more or less random).

The *phase shift* of the (concentration) fluctuations:

- In upward direction the phase shift between concentration fluctuations and velocity fluctuations increases;
- At higher elevations the shift results in a reverse sign of the transport component.

The actual *magnitude* of correlation component of transport:

- Due to small fluctuations the contribution of the correlation component s_{corr} at a specific level will be relatively small;
- The magnitude of $s_{corr}(z)$ will decrease in upward direction;
- At higher levels, the direction of the local component s_{corr} will be opposite to that at the bottom;
- Consequently, the total depth-integrated nett transport contribution S_{corr} will be small.

Based on former considerations it is postulated that the magnitude of the depth-integrated correlation component S_{corr} is relatively small compared to the depth-integrated mean component S_{mean} . Consequently, the ratio $R_S (= S_{corr}/S_{mean})$ is small:

$$|R_S| \ll 1 \quad (4.2.43)$$

Consequently, the total nett transport rate S , elaborated as:

$$S = S_{mean} + S_{corr} = S_{mean} (1 + R_S) \quad (4.2.44)$$

can be assessed from the mean component:

$$S \approx S_{mean} \quad (4.2.45)$$

and is just determined by the time-averaged velocities and time-averaged sediment concentrations.

It should be noted that not neglecting the effect of a non-zero R_S -parameter, according to Equation (4.2.38), will of course lead to a more advanced transport model. In fact, the incorporation of this contribution is one of the possible improvements of the model, as will be discussed in Section 9.3.

4.2.8 Implications for transport computation

Since in the special case of intensive breaking waves the nett contribution of the correlation component is relatively small, as a first order of approximation the amount of vertically integrated nett cross-shore transport can be computed from the following equation:

$$S(x) \approx \int_{z=z_b(x)}^{\eta_{max}} \bar{u}(x,z) \bar{C}(x,z) dz \quad (4.2.46a)$$

or in position x (with reference to the mean bottom level):

$$S \approx \int_{z=0}^{\eta_{max}} \bar{u}(z) \bar{C}(z) dz \quad (4.2.46b)$$

in which η_{max} is the maximum water level of the wave crest.

This approach is only valid within the breaker zone. In the swash zone this approximation

is probably not correct due to the effect of increasing correlation between water motion and sediment concentrations. However, it is noted that this kind of transport formula is used also for the assessment of longshore transport rates in an adjusted form (see Section 4.8).

In order to compute the local net transport rate according to Equation (4.2.46b), the vertical distributions of both (time-averaged) flow field (undertow) $\bar{u}(z)$ and sediment concentrations $\bar{C}(z)$ must be known.

This would be of course, a tremendous advantage, since knowledge on the intra-wave fluctuations of both the velocity and sediment concentration to assess the magnitude of the correlation component is not necessary any more.

It should be noted that this approach has already been proposed by the author in 1985. However, at that time this hypothesis was solely based on a limited number of preliminary elaborations of less reliable time-averaged flow and concentration profiles (Steetzel, 1985). Apart from the outcomes of several laboratory experiments as described in Section 4.2.6, more arguments demonstrating the fairness of this simplification of the transport process are provided by the results of Kuriyama's analysis of an extensive field measurement campaign (Kuriyama, 1991).

4.2.9 Approach to transport model development

In order to be more specific about the transport formulation of Equation (4.2.46b), the time-averaged profiles of the suspended sediment concentration and the flow velocity have to be examined.

A start was made with the investigation of the suspended sediment distributions because of the availability of a large amount of reliable data from measurements and successive employment of the results of this analysis (mixing) for the description of the time-averaged velocity profile. Moreover, it must be remarked that the cross-shore transport rate is merely controlled by the amount of suspension rather than by the secondary flow. The fluctuations in the mean current are restricted to a factor of about two, whereas the magnitude of the (depth-averaged) concentrations may vary over a range of ten. Consequently, the advantage of detailed knowledge on the sediment suspension is obvious.

The results of the analysis into suspended sediment concentrations and secondary flow profiles are presented in Section 4.3 and 4.4 respectively, whereas in Section 4.5 the final computation of net cross-shore transport is described. For the sake of convenience the overbar (denoting time-averaging), will be omitted in the following.

Ensuing, in Section 4.6 a comparison between measured (from profile development) and computed (using derived equations) transport rates is presented in order to justify this approach.

The opportunity to have an 'internal' check on the transport model results can be seen as an additional advantage of this method. Next to this an overall 'external' check of the transport model is, of course, also possible (see Section 5.1.1 for more details). If use is made of a quite different calculation method, e.g. the energetics-based approach as described in Section 3.5.7, such a second verification would be impossible.

4.3 Sediment concentration

4.3.1 Introduction

As already noted in Section 4.2.5, the vertical profile of the (time-averaged) suspended sediment concentration above a sandy bed can basically be described by its magnitude and vertical distribution and, consequently, can be written as a product of a reference concentration C_0 and a dimensionless sediment distribution function $f_c(z)$, according to:

$$C(z) = C_0 f_c(z) \quad (4.3.1)$$

this representing the stationary part of Equation (4.2.23).

This basic description of the time-averaged suspended sediment profile is shown schematically in Figure 4.7. The exact shape has to be related to a set of measured concentrations (denoted by the boxes) which will be studied in the following.

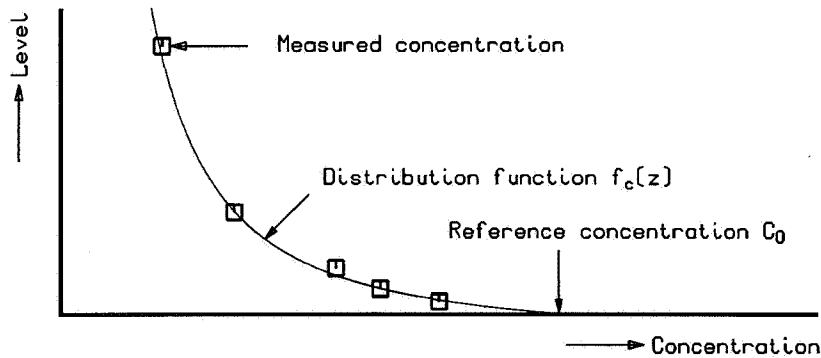


Figure 4.7 Schematic description of the time-averaged concentration profile.

It should be noted that in this expression the reference concentration at the bottom level C_0 is only used to fix this concentration profile to a specific level, viz. $z=0$. For this reason, the widely used, though misleading term 'bottom concentration' is avoided in this thesis, since it indeed suggests a specific concentration at this level.

The range of $f_c(z)$ is restricted to $0 < f_c(z) \leq 1$, since it seems a reasonable thought that even for breaking wave conditions the magnitude of the time-averaged concentration decreases with increasing distance from the bottom. It is, however, envisaged that momentary concentration profiles may show upward increasing values.

In order to calculate the magnitude of the reference concentration for one particular measurement (consisting of several data points as indicated in the figure), the vertical profile of the sediment concentration, viz. the distribution function $f_c(z)$, has to be

determined first.

The procedure which has been followed to achieve this goal is presented in Figure 4.8 and consists of five successive steps, namely:

- 1) analyse concentration profile (measurements);
- 2) determine apparent, inherent mixing profile;
- 3) describe mixing profile;
- 4) describe and fit concentration profile;
- 5) compute reference concentration.

More details about this procedure are presented in the following sections.

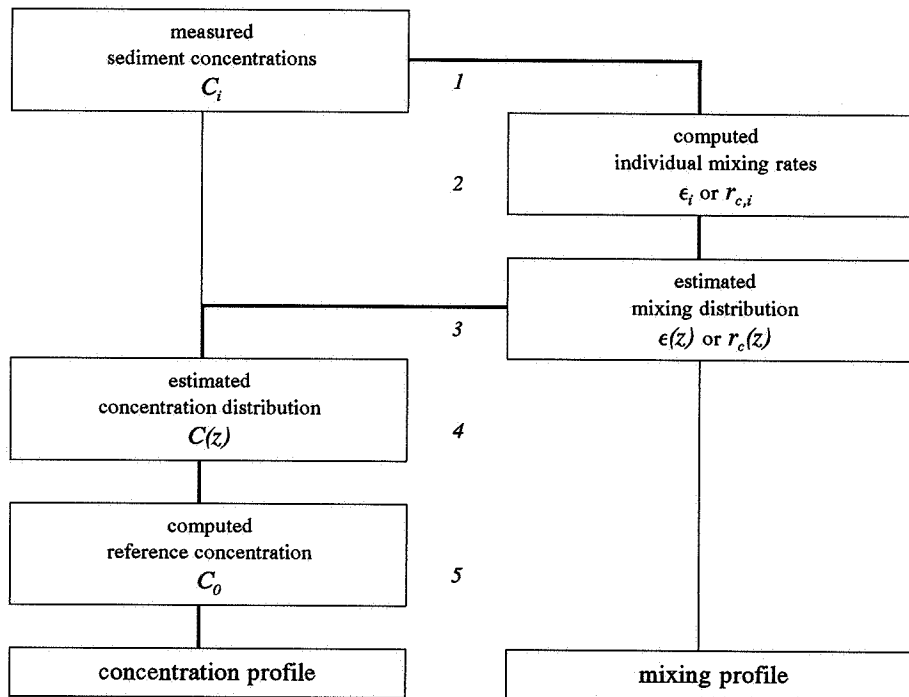


Figure 4.8 Procedure for the examination of concentration profiles.

As already indicated in Section 2.7, the distribution of suspended sediment in breaking wave conditions has been investigated by analysis of a large number of concentration measurements which were conducted in the large Deltaflume (Steetzel, 1987b).

The concentrations were measured using a transverse suction method according to Bosman et al., resulting in a set of time-averaged values of the suspended sediment concentration (Bosman and Steetzel, 1986; Bosman et al., 1987). The measurement device mounted on the measurement carriage as can be observed in Figure 4.9.

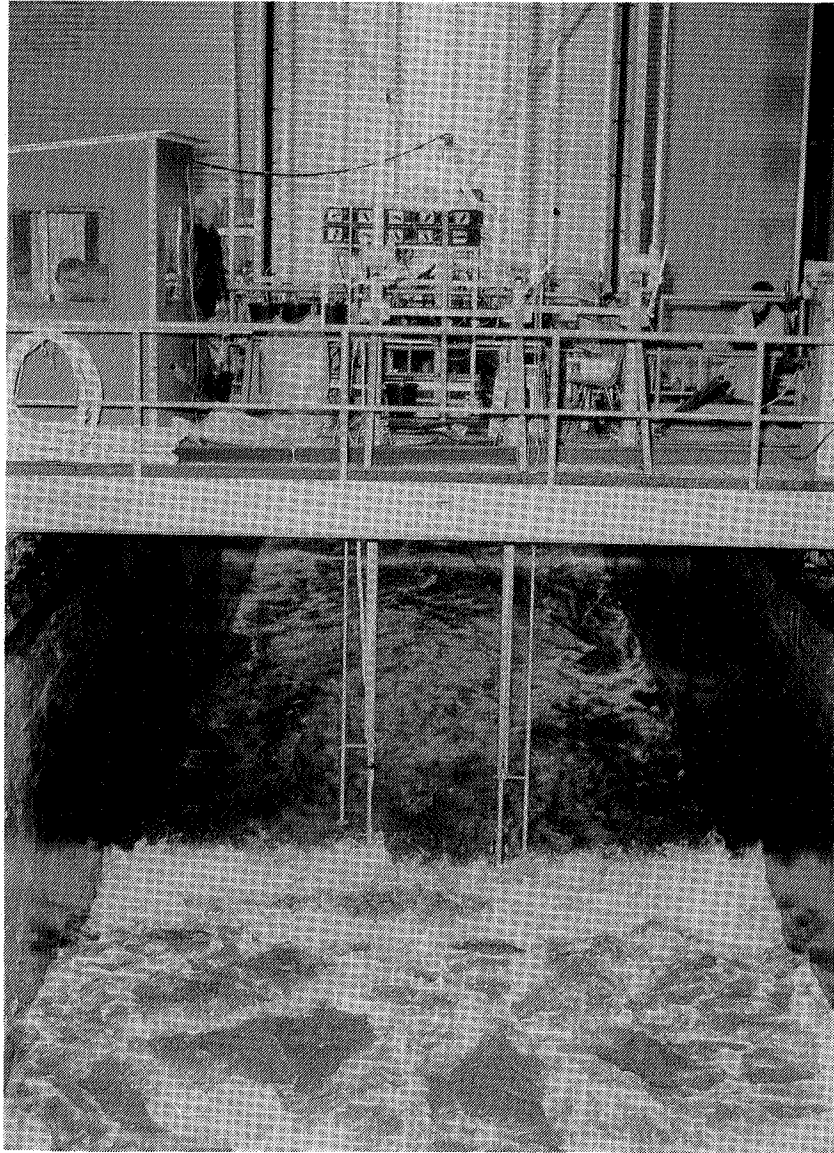


Figure 4.9 *Photo of the measurement carriage equipped with concentration measurement device (left) and velocity measurement devices (right) in the Deltaflume.*

Data on the velocity profile were obtained by using four electromagnetic velocity meters (EMF's), see Section 4.4 for more information.

Each individual concentration measurement consists of maximal 10 points at different levels above the sandy bed with upward increasing mutual distances. A typical example of some of these measured suspended sediment concentrations is shown in Figure 4.10. The lines through the data points are the final result of the analysis to be explained in the following sections.

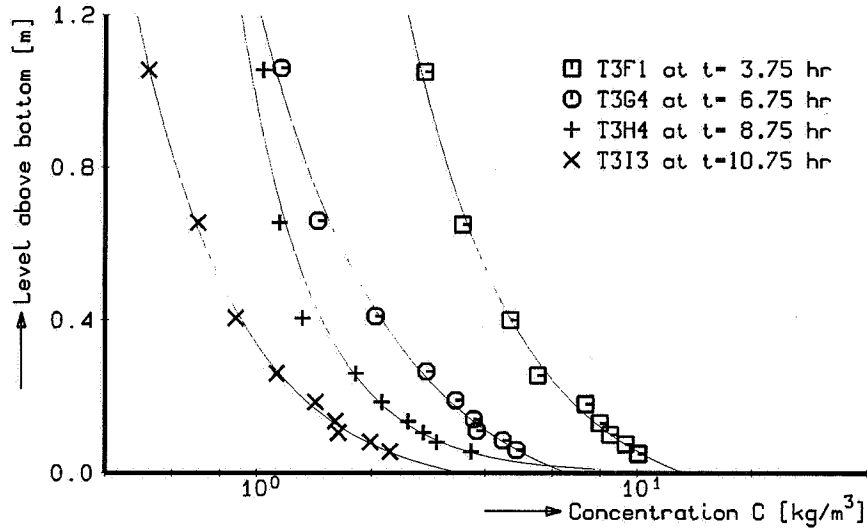


Figure 4.10 Example of some measured suspended sediment concentration profiles; test T3 of H298-I-series, position $x = 187$ m.

4.3.2 General distribution function

The suspension of solids in a fluid is described by the non-stationary, diffusion equation according to:

$$\frac{\partial C}{\partial t} = w_s(z) \frac{\partial C}{\partial z} + \frac{\partial}{\partial z} \left(\varepsilon_s(z) \frac{\partial C}{\partial z} \right) \quad (4.3.2a)$$

in which the particle fall velocity is denoted by w_s and the turbulent exchange factor or diffusion coefficient equals ε_s . In this equation the horizontal diffusion coefficients are neglected as these, relative to the vertical gradients, are irrelevant. For the present case, viz. the description of time-averaged concentrations, the time derivative $\partial C/\partial t$ should equal zero, so:

$$w_s(z) \frac{\partial C}{\partial z} + \frac{\partial}{\partial z} \left(\varepsilon_s(z) \frac{\partial C}{\partial z} \right) = 0 \quad (4.3.2b)$$

After integration and using a proper boundary condition, the one-dimensional stationary diffusion equation (often referred to as the Rouse-equation) is found, according to:

$$\varepsilon_s(z) \frac{dC(z)}{dz} + w_s(z) C(z) = 0 \quad (4.3.2c)$$

in which:

$$\begin{aligned} \varepsilon_s & \text{ the mixing coefficient for the sediment} & (\text{m}^2/\text{s}) \\ w_s & \text{ the fall velocity of the bed material} & (\text{m/s}) \end{aligned}$$

It should be remarked that the mixing coefficient in Equation (4.3.2c) is originally denoted as the diffusion coefficient. However, since in (breaking) waves the exchange of sediment particles over the water depth seems mainly caused by large-scale convection processes rather than by small-scale diffusion, the more universal term 'mixing coefficient' will be used in this thesis.

In this case, a local vertical equilibrium between the upward mixing-related and downward gravity-related transport occurs. From this, a general expression describing the vertical profile of the time-averaged sediment concentration can be derived, since some re-arranging and further elaboration of the former equation yields:

$$\frac{d \ln[C(z)]}{dz} = -\frac{w_s(z)}{\varepsilon_s(z)} \quad (4.3.3a)$$

or:

$$\ln[f_c(z)] = -\int_0^z \frac{w_s(z)}{\varepsilon_s(z)} dz \quad (4.3.3b)$$

Consequently, the concentration distribution function $f_c(z)$ can in general terms be described by:

$$f_c(z) = \exp \left[-\int_0^z \frac{w_s(z)}{\varepsilon_s(z)} dz \right] \quad (4.3.4a)$$

and simplified to:

$$f_c(z) = \exp[\sigma] \quad (4.3.4b)$$

in which:

$$\sigma = -\int_0^z \frac{w_s(z)}{\varepsilon_s(z)} dz \quad (4.3.5a)$$

or:

$$\sigma = -\int_0^z [r_c(z)]^{-1} dz \quad (4.3.5b)$$

The concentration decay length scale r_c (in m) used in the latter equation, is defined by Bosman and Steetzel according to:

$$r_c = \frac{\varepsilon_s}{w_s} \quad (4.3.6)$$

The magnitude of r_c represents the vertical distance along which the concentration is altered by a factor $1/e$. It denotes the absolute value of the local tangent of the concentration profile in a linear-logarithmical plot as can be seen readily from Equation (4.3.3a) (Bosman and Steetzel, 1986).

Assuming the sediment characteristics, represented by the fall velocity w_s , to be independent on the elevation above the bottom (so $w_s(z) = w_s$), the σ -function can be simplified to:

$$\sigma = -w_s \int_0^z [\varepsilon_s(z)]^{-1} dz \quad (4.3.5c)$$

This σ -function, and thus the distribution function $f_c(z)$, mainly depends on the vertical distribution of the (sediment) mixing coefficient ε_s , which will be examined in the next section by analyzing the apparent mixing profile. For the sake of simplicity, the subscript s (for sediment) in the notation will be further omitted, so in the following $\varepsilon(z) = \varepsilon_s(z)$.

4.3.3 Mixing coefficient distribution

Corresponding to the general formulation of the vertical distribution of the suspended sediment concentration, the mixing coefficient distribution $\varepsilon(z)$ can be written as a product of a reference mixing coefficient at the bed level (say ε_0) as well as a distribution function also.

In order to describe this mixing coefficient distribution, a great number of measured sediment concentrations sets have been analyzed.

From each of the (about 70) available data sets, the r_c -distribution was estimated from measured concentrations. Assuming a constant fall velocity $w_s(z) = w_s$, the accompanying ε -distribution can be determined next also by using Equation (4.3.6).

Assessment of individual r_{ci} -values

Since the concentration decay length scale according to Equations (4.3.3a) and (4.3.6) is defined as:

$$r_c = - \left[\frac{d \ln C}{dz} \right]^{-1} = \frac{-dz}{d \ln C} \quad (4.3.7)$$

in a first approximation, the r_{cj} -value for $j = i$ can be estimated from measured C_j -values at the levels z_j for $j = i-1$ and $j = i+1$, using a simple linear fit, according to:

$$r_{ci} = \frac{z_{i+1} - z_{i-1}}{\ln[C_{i-1}] - \ln[C_{i+1}]} \quad (4.3.8a)$$

Figure 4.11 shows an example of the result of this fit procedure.

This first-order fit procedure is in fact only applicable for a (local) equidistant vertical grid with $z_{i+1} - z_i = z_i - z_{i-1} = \Delta z$.

This particular situation yields:

$$r_{ci} = \frac{2 \Delta z}{\ln[C_{i-1}] - \ln[C_{i+1}]} \quad (4.3.8b)$$

Since concentration measurements have been conducted on a non-equidistant vertical grid with upward increasing grid size, this fit procedure has been slightly modified. Because the vertical gradients of the concentration profile are relatively small in a linear-logarithmical

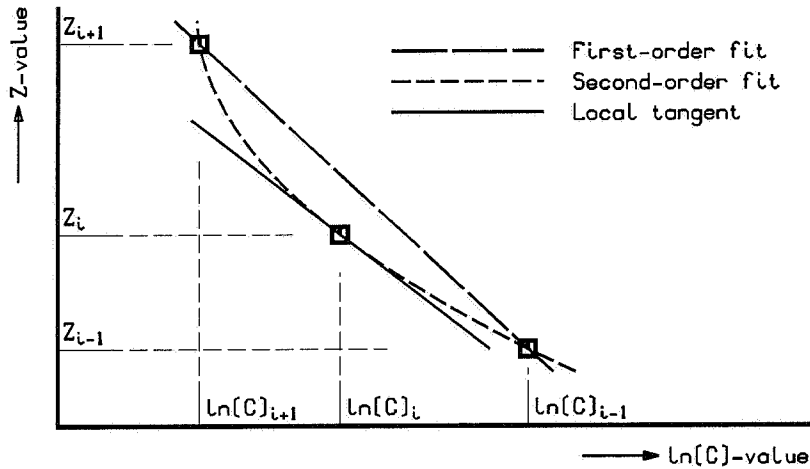


Figure 4.11 Illustration of the fit procedure to compute the best estimate of the local tangent.

plot according to $z = F\{\ln C\}$, the local (that is near the level of interest) concentration distribution can be adequately described by a second-order equation, according to:

$$\ln C = k_0 + k_1 y + k_2 y^2 \quad (4.3.9)$$

with $y = z - z_i$ being the vertical ordinate with respect to the level of interest. The non-zero k_2 -value in this expression accounts for the dissimilarity from the linear fit result. Equation (4.3.9) is now used to fit the C_j -values at levels z_j for $j = i-1, i$ and $i+1$, in order to compute the r_{ci} -value for $j = i$. Differentiation of the former expression yields:

$$\frac{d \ln C}{dy} = k_1 + 2k_2 y \quad (4.3.10)$$

Taking into account Equation (4.3.7), the local magnitude of r_{ci} at z_i (with $y = y_i = z_i - z_i = 0$) equals:

$$r_{ci} = \frac{-1}{k_1} \quad (4.3.11)$$

Since $y_i = 0$ and consequently $k_0 = \ln C_i$, the k_1 -value can be derived from the next set of equations:

$$\begin{cases} \ln C_{i+1} = \ln C_i + k_1 y_{i+1} + k_2 (y_{i+1})^2 \\ \ln C_{i-1} = \ln C_i + k_1 y_{i-1} + k_2 (y_{i-1})^2 \end{cases} \quad (4.3.12)$$

After some elaboration the k_f -value can be derived. The local estimate of the concentration decay length scale, using Equation (4.3.11), equals:

$$r_{ci} = \frac{(z_{i+1} - z_i)(z_{i-1} - z_i)(z_{i+1} - z_{i-1})}{(z_{i+1} - z_i)^2 \ln[C_{i-1}/C_i] - (z_{i-1} - z_i)^2 \ln[C_{i+1}/C_i]} \quad (4.3.13)$$

For the special case of $z_{i+1} - z_i = z_i - z_{i-1} = \Delta z$, this equation reduces to the more simple formulation as presented earlier in Equation (4.3.8b). The additional terms account for effects of the non-equidistant vertical grid size.

In Figure 4.11 the result of this fit procedure is also illustrated, showing both the results of the second-order fit and the local tangent. The absolute magnitude of the latter ($= \Delta z / \Delta \ln C$) represents the local concentration decay length-scale r_{ci} .

Results of individual r_{ci} -fits

Finally, the former described fit-procedure results in $(n-2)$ r_{ci} -values for every (n) C_i -values.

Figure 4.12 shows an example of the intermediate and final results of the fit procedure for one particular measurement, as outlined originally in Figure 4.8. From the 9 measured concentrations C_i (boxes in the figure), 7 r_{ci} -values (crosses) have been computed in this case.

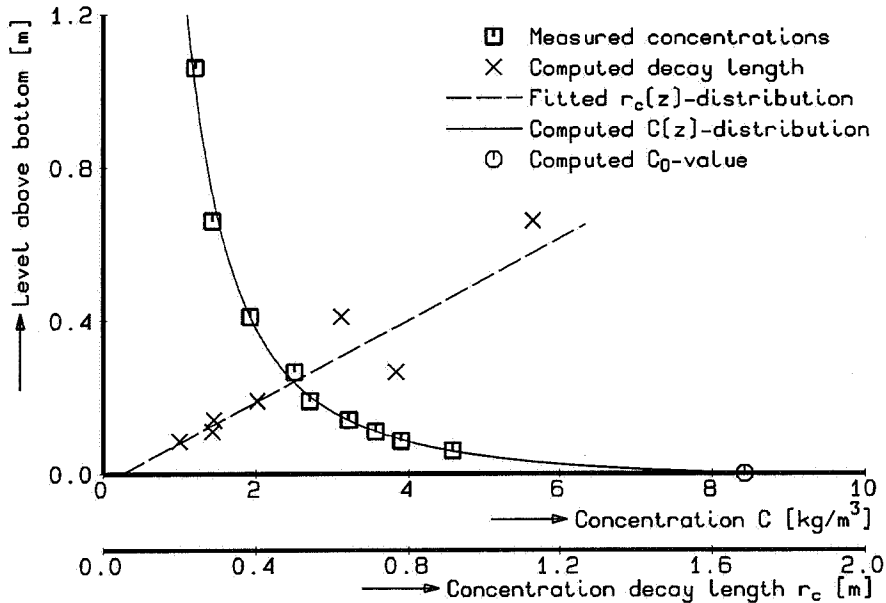


Figure 4.12 Example of $C(z)$ -fit procedure; test T1F1 of H298-I-series.

Shape of r_c -distribution

Mixing in breaking wave conditions is due to two major sources, namely wave-generated turbulence originated near the mean water level and bottom-generated turbulence initiated at the bottom boundary (Deigaard et al., 1991; Tsuchiyata et al., 1988). In the case of intensive wave breaking it is likely that the first one will be the predominant source. Effects of the bottom-generated turbulence will decrease (fast) in upward direction, whereas turbulence intensity due to wave breaking decreases downward in a manner which will probably depend on the way the individual waves break. Consequently, the idea that the total effect will be a downward decreasing rate of turbulence as indicated by the individual fit results seems fair. So, the amount of mixing increases with increasing elevation above the bottom.

The local magnitude of the concentration decay length scale r_c is comparable to the order of magnitude of the amplitude of the vertical water motion at the level of interest (e.g. ripple height near the sandy bed and wave height near the mean water level), see e.g. (Nielsen, 1979; Steetzel, 1984b; Ribberink and Al-Salem, 1990, 1991). However, a firm argumentation for this finding cannot (yet) be presented. Probably the dominating convection processes are accountable for this phenomenon (Steetzel, 1984a; Nielsen, 1985, 1992).

The rough shape of the derived mixing distribution is in accordance with the results of investigations carried out by other researchers even for non-breaking waves, see e.g. (Ifuku and Kakinuma, 1988; Van de Graaff, 1988; Van Rijn, 1989) (see also (DELFT HYDRAULICS, 1986b)).

A first attempt to characterize the mixing distributions for the test data used here was made by Ras and Amesz (1989). Their research, however, did not result in a description of the vertical distribution of the apparent mixing profile.

Description of r_c -distribution

A deliberate fit of computed individual r_{ci} -values will result in a relation for the $r_c(z)$ -distribution and ultimately in an $\varepsilon(z)$ -distribution (for constant w_s -value) for each measurement, at least over the depth interval in which the concentration measurements have been conducted.

For each measurement, the individual r_{ci} -values are fitted using a least-squares regression technique (Draper and Smith, 1966). From mutual comparison between various optional distributions it was concluded that the most acceptable fit was obtained by a simple linear relation with the elevation above the bed (first-order fit) according to:

$$r_c(z) = r_{c,0} + p z \quad (4.3.14)$$

in which:

$$\begin{array}{ll} r_{c,0} & \text{the reference decay length scale at the bed level } z=0 \text{ m} & (\text{m}) \\ p & \text{the (vertical) gradient of the } r_c(z)\text{-distribution } (= \Delta r_c / \Delta z) & (-) \end{array}$$

For the reference decay length scale r_{c0} the same comments hold as those for the reference concentration C_0 .

In the example of Figure 4.12, this first-order $r_c(z)$ -relation is shown by the dashed line. The derived r_{c0} -value equals 0.051 m, whereas the dimensionless mixing increase rate p ($= \mu/w_s$) amounts to 1.815.

Final $\varepsilon(z)$ -distribution

As a final result of the former fit procedure for $r_c(z)$, the $\varepsilon(z)$ -distribution is also represented by a linear function of the elevation above the bed.

So, the first-order $\varepsilon(z)$ -distribution is described by:

$$\varepsilon(z) = \varepsilon_0 + \mu z \quad (4.3.15)$$

where:

$$\begin{array}{ll} \varepsilon_0 & \text{the reference mixing coefficient at the bed level } z=0 \text{ m} \quad (\text{m}^2/\text{s}) \\ \mu & \text{the (vertical) gradient of the } \varepsilon(z)\text{-distribution } (= \Delta \varepsilon / \Delta z) \quad (\text{m}/\text{s}) \end{array}$$

Both ε_0 and μ depend on the local hydraulic conditions which will be examined in the next chapter.

A schematic mixing coefficient distribution is shown in Figure 4.13.

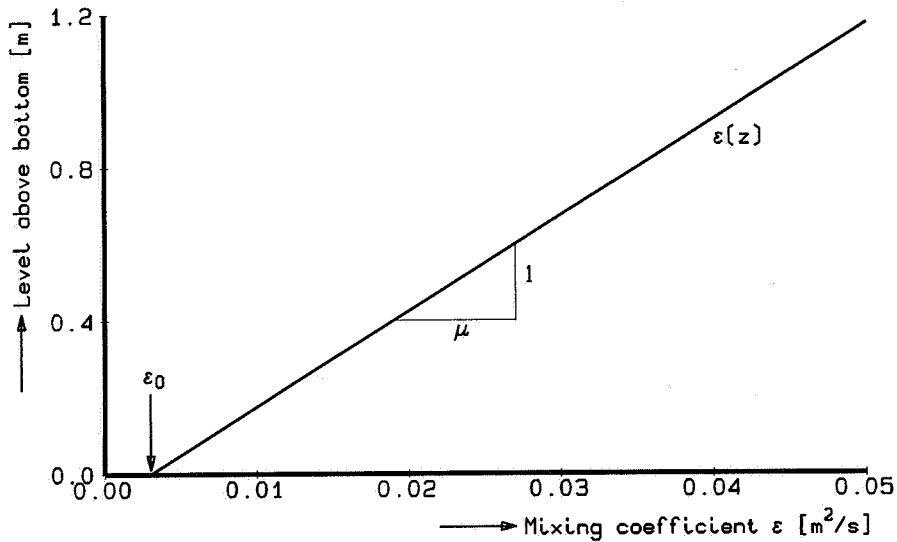


Figure 4.13 Schematic description of the vertical distribution of the mixing coefficient.

The intercept with the $z=0$ level equals ε_0 , whereas the tangent ($= \Delta \varepsilon / \Delta z$) is defined as the μ -value. Characteristic values derived from the analysis of concentration profiles are

$\varepsilon_0 = 0.003 \text{ m}^2/\text{s}$ and $\mu = 0.04 \text{ m/s}$.

A linear relationship for $\varepsilon_s(z)$ is also suggested by Songvissessomja and Samarasinghe (1988), who compared different $\varepsilon(z)$ -profiles, viz. constant, parabolic and linear relations, by analyzing concentration data obtained by Nielsen (1984). However, they assumed the reference mixing coefficient ε_0 to be zero.

4.3.4 Suspended sediment distribution

Substitution of the derived $\varepsilon(z)$ -relation of Equation (4.3.15) in the σ -expression of Equation (4.3.5c) yields:

$$\sigma = -w_s \int_0^z \frac{1}{(\varepsilon_0 + \mu z)} dz \quad (4.3.16a)$$

which after further elaboration results in:

$$\sigma = \frac{-w_s}{\mu} \ln(\varepsilon_0 + \mu z) \Big|_0^z = \frac{-w_s}{\mu} \ln \left[1 + \frac{\mu z}{\varepsilon_0} \right] \quad (4.3.16b)$$

Finally, the suspended sediment distribution function $f_c(z)$ can be described by:

$$f_c(z) = \exp(\sigma) = \left[1 + \frac{\mu z}{\varepsilon_0} \right]^{(-w_s/\mu)} \quad (4.3.17)$$

The shape of this function depends on the magnitude of the reference mixing ε_0 , the mixing gradient parameter μ and the fall velocity of the bed material w_s .

Next the influence of the actual magnitude of these parameters on the concentration distribution will be elaborated in more detail. The sensitivity is assessed relative to some characteristic values, namely $\varepsilon_0 = 0.003 \text{ m}^2/\text{s}$, $\mu = 0.04 \text{ m/s}$ and $w_s = 0.02 \text{ m/s}$.

Effect of ε_0 -parameter

The influence of the magnitude of the reference mixing coefficient ε_0 on the shape of the concentration distribution is shown in Figure 4.14.

Relative to low mixing rates, an increase in near bottom mixing results in a steeper concentration distribution. In comparison to the effect of an increased μ -value (see next item), especially the amount of suspended sediment near the bottom is affected.

For $\varepsilon_0 \downarrow 0$, the concentration, even at a very low level above the bed, is almost nihil. Modelling of a concentration distribution for $\varepsilon_0 = 0 \text{ m}^2/\text{s}$ requires a higher reference level.

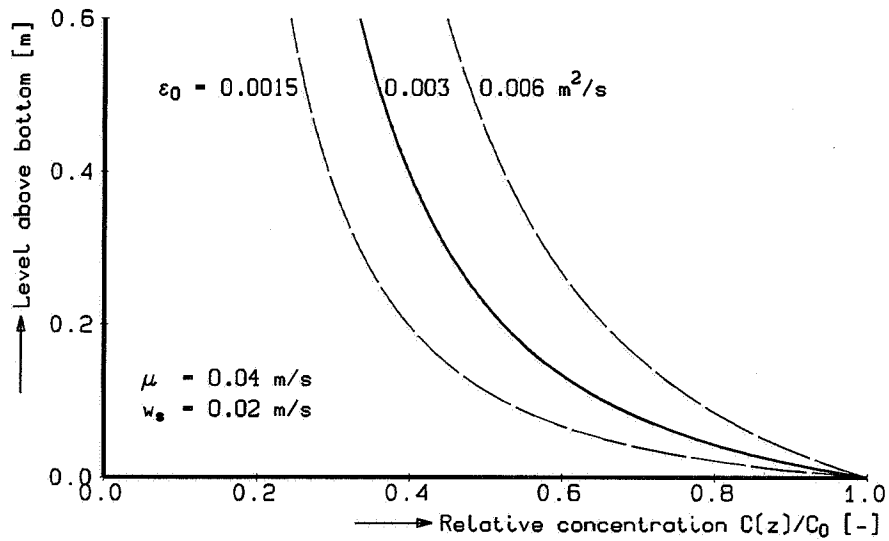


Figure 4.14 Influence of near-bottom mixing rate on the concentration profile.

Effect of μ -parameter

The influence of the gradient parameter on the concentration distribution is shown in Figure 4.15 for a range of μ -values.

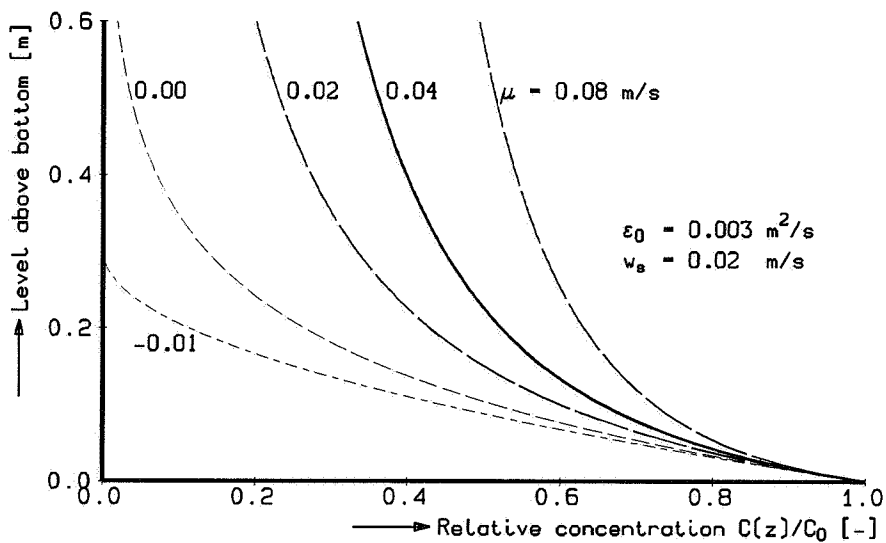


Figure 4.15 Influence of the μ -parameter on the concentration profile.

As could be expected, an increase of μ results in a steeper distribution.

In the special case of $\mu = 0$ m/s, mixing is constant over the depth, viz. $\varepsilon(z) = \varepsilon_0$ (zero-order mixing distribution). The inherent consequence for the distribution function $f_c(z)$ can be assessed from:

$$\ln[f_c(z)] = \frac{-w_s}{\mu} \ln \left[1 + \frac{\mu z}{\varepsilon_0} \right]$$

The expression on the right side can be elaborated in a series expansion according to:

$$\frac{-w_s}{\mu} \ln \left[1 + \frac{\mu z}{\varepsilon_0} \right] = \frac{-w_s}{\mu} \left[\left(\frac{\mu z}{\varepsilon_0} \right) - \frac{1}{2} \left(\frac{\mu z}{\varepsilon_0} \right)^2 + \frac{1}{3} \left(\frac{\mu z}{\varepsilon_0} \right)^3 - \dots \right]$$

which for $\mu \downarrow 0$ m/s can be shown to result in:

$$\frac{-w_s}{\mu} \ln \left[1 + \frac{\mu z}{\varepsilon_0} \right] = \frac{-w_s z}{\varepsilon_0}$$

Finally, the accompanying distribution function is described by:

$$f_c(z) = \exp \left[\frac{-w_s z}{\varepsilon_0} \right] \quad (4.3.18)$$

As could be expected, the well-known negative exponential distribution is found for this case, see e.g. (Steetzel, 1984b). This relation is shown in Figure 4.15 by the line (small dashes) in the upper left.

For negative μ -values, mixing decreases in upward direction. This might be a feasible description for conditions with dominating bottom-generated turbulence, but this is definitely not the case here. An example for $\mu = -0.01$ m/s is shown in Figure 4.15 also. The $f_c(z)$ -function of Equation (4.3.17) is now only valid for $z \leq (-\mu/\varepsilon_0)$ (sort of boundary layer), since the concentration at the upper level amounts to $C=0$ and at higher elevations $\varepsilon(z)$ would be negative! For this example the zero level equals $z=0.30$ m.

As can be seen from the plotted concentration distribution functions, the constant mixing approach, viz. $\mu = 0$, seems a fair first-order estimation for the suspended sediment distribution near the bottom. For a wide range of μ -values, the concentration profile is hardly affected in this lower zone (say below $z=0.1$ m level). For conditions with low, or even without waves and especially in wave tunnel experiments (with no wave-breaking induced turbulence), the accompanying negative exponential concentration decay formulae have indeed been proved to give an accurate description of measured time-averaged concentration profiles, see e.g. (Steetzel, 1984b; Ribberink and Al-Salem, 1991).

Effect of w_s -parameter

The effect of the fall velocity w_s on the shape of the concentration profile is shown in Figure 4.16.

Finer sediment, with a smaller fall velocity, will result in a steeper distribution with more sediment in suspension. For non-uniform bottom material the mixing will yield a vertical sorting of suspended material. So, the relative portion of finer material will increase in upward direction. This is in accordance with the results of measurements in which bottom

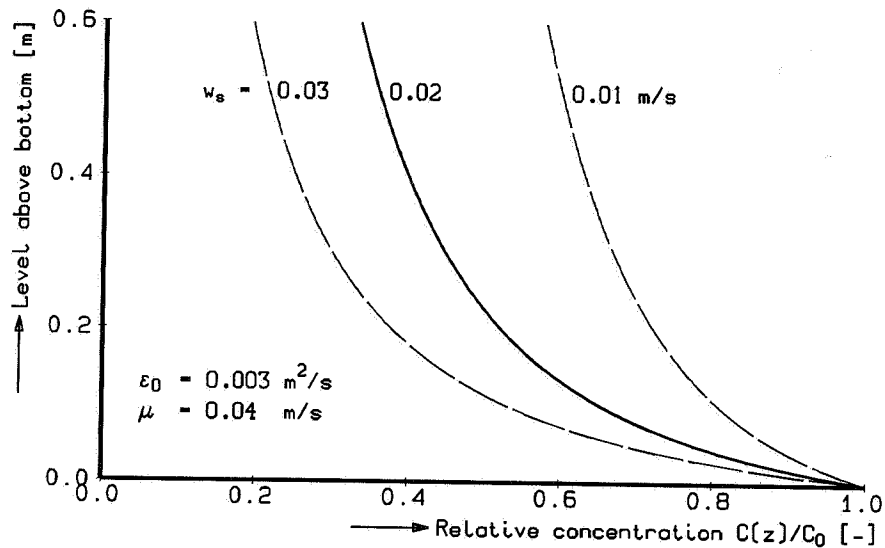


Figure 4.16 Influence of the fall velocity on the concentration profile.

samples were compared with suspended sediment data.

More details on the effect of grading on the vertical distribution of suspended sediment are presented by Van de Graaff (1988).

Effect of (μ/w_s) -ratio

In Figure 4.17 the influence of the dimensionless (μ/w_s) -quotient (p -value in Equation (4.3.14)) on the concentration distribution is shown for a range of (μ/w_s) -values.

As could be expected, a larger mixing increase rate will result in a greater amount of suspended sediment. Moreover, a smaller fall velocity, or finer sediment, yields a larger (μ/w_s) -ratio and thus a steeper concentration profile. This finding is in agreement with the outcomes of test series carried out in DELFT HYDRAULICS' large oscillating water tunnel, see (Ribberink and Al-Salem, 1992; Ribberink and Chen, 1983).

4.3.5 Concentration profile

Using the expression for the $f_c(z)$ -function, the required vertical distribution of the time-averaged sediment concentration can be described by:

$$C(z) = C_0 \left[1 + \frac{\mu z}{\epsilon_0} \right]^{(-w_s/\mu)} \quad (4.3.19)$$

It is noted that for sheetflow conditions in an oscillating water tunnel a negative power function was shown to yield also an appropriate fit.

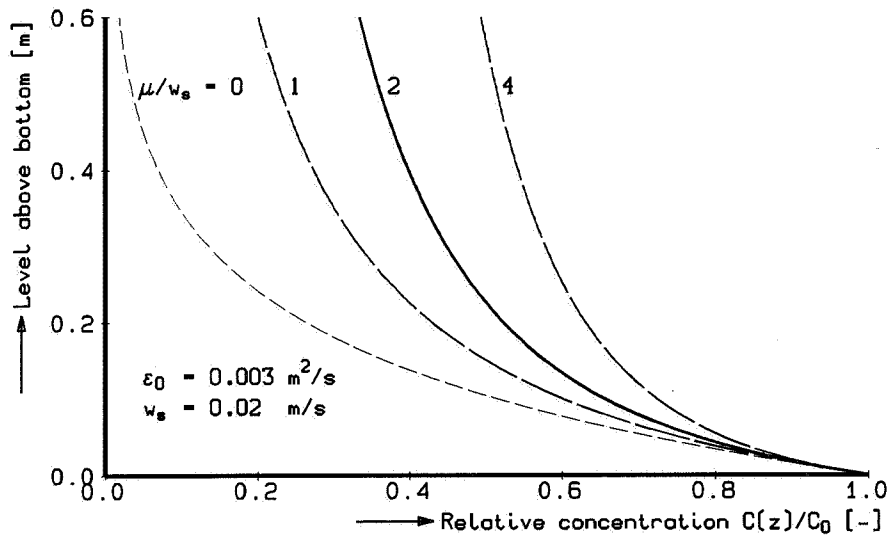


Figure 4.17 Influence of the (μ/w_s) -ratio on the concentration profile.

The power itself was found to be almost constant for the tests carried out with one sediment grain size (Ribberink and Al-Salem, 1992). The qualitative impact of the sediment diameter was discussed above.

Reference concentration C_0

As being the last step of the applied fit procedure, the magnitude of the reference concentration at the bed level C_0 can be obtained by a least-squares fit of measured C -values using Equation (4.3.19). The final result of this procedure is shown in the example in Figure 4.12 by the solid line. The magnitude of the reference concentration C_0 for this particular measurement amounts to 8.43 kg/m^3 .

It is noted once more that the thin lines through the data points in the concentration profiles in Figure 4.10 on page 51 are also the result of the former described fit procedure.

4.3.6 Sediment load

The total amount of suspended sediment is characterized by the so-called sediment load. This sediment load L_s (expressed in kg/m^2) can be computed from a depth integration according to:

$$L_s = \int_{z=0}^d C(z) dz \quad (4.3.20)$$

Substitution of the former derived concentration profile, viz. Equation (4.3.19), yields:

$$\begin{aligned}
L_s &= \int_{z=0}^d C_0 \left[1 + \frac{\mu z}{\varepsilon_0} \right]^{(-w_s/\mu)} dz \\
&= C_0 \frac{\varepsilon_0}{\mu} \frac{1}{1-w_s/\mu} \left(\left[1 + \frac{\mu d}{\varepsilon_0} \right]^{(1-w_s/\mu)} - 1 \right)
\end{aligned} \tag{4.3.21a}$$

This formula can also be presented in a more simple form:

$$L_s = C_0 I_1 \tag{4.3.21b}$$

in which the I_1 -parameter (expressed in m; see also Section 4.5.2 and the Appendix) equals:

$$I_1 = \frac{\varepsilon_0}{\mu} \frac{1}{K_1} \left[K_2^{K_1} - 1 \right] \tag{4.3.22a/4.5.5}$$

The two additional, dimensionless constants K_1 and K_2 used in this equation are defined by:

$$K_1 = 1 - w_s/\mu \tag{4.3.23/4.5.8}$$

$$K_2 = 1 + (\mu/\varepsilon_0) d \tag{4.3.24}$$

As will be shown later, the latter two constants will also be used to quantify the nett sediment transport rate (see Section 4.5 for more details). It should be remarked that the K_2 -value is related to the mean water depth d , whereas in Section 4.5 the water depth below the trough level d_t has been used.

In the following, some special cases are considered.

For the (very) special case of $(w_s/\mu) = 1$ and consequently $K_1 = 0$, the I_1 -parameter yields:

$$I_1 = \frac{\varepsilon_0}{\mu} \ln[K_2] \tag{4.3.22b}$$

For a constant mixing case, viz. spatially uniform mixing with $\mu = 0$ m/s and thus $\varepsilon_s(z) = \varepsilon_0$, the equation describing the sediment load can be shown to result in:

$$L_s = C_0 \frac{\varepsilon_0}{w_s} \left(1 - \exp \left[\frac{-w_s d}{\varepsilon_0} \right] \right) \tag{4.3.25a}$$

For large $(w_s d/\varepsilon_0)$ -values (say $d \gg (\varepsilon_0/w_s)$, deep water) this reduces to:

$$L_s = C_0 \frac{\varepsilon_0}{w_s} = C_0 r_{c0} \tag{4.3.25b}$$

whereas for small $(w_s d/\varepsilon_0)$ -values (strong mixing in shallow water):

$$L_s = C_0 d \tag{4.3.25c}$$

viz. a near-uniform concentration profile is found.

4.3.7 Summary and conclusions

As a result of the analysis of series of measured suspended sediment distributions, both the descriptions of the time-averaged concentration profile and the apparent mean mixing distribution for breaking wave conditions are determined.

The concentration profile in the case of breaking waves can be described by:

$$C(z) = C_0 \left[1 + \frac{\mu z}{\varepsilon_0} \right]^{(-w_s/\mu)} \quad (4.3.19)$$

whereas the accompanying mixing profile is characterized by:

$$\varepsilon(z) = \varepsilon_0 + \mu z \quad (4.3.15)$$

The latter equation will also be used as a starting-point for the description of the detailed secondary current profile as outlined in the next section.

For more details on specific data reference is made to relevant research reports, viz. (Steetzel, 1987b, 1990a).

The magnitude of each of the introduced parameters (reference concentration C_0 , reference mixing coefficient ε_0 and mixing increase rate μ) is assessed for every test. The relation with local hydraulic conditions will be determined in the calibration phase of the model development as described in Chapter 5.

4.4 Secondary flow

4.4.1 Introduction

In water motion, two kinds of local mean (time-averaged) flow patterns can be recognized, namely primary and secondary currents. In the case of a primary current there is indeed a nett transport of water which occurs in the case of wave-generated or tidal longshore currents. Under breaking waves in a pure two-dimensional case secondary currents (with no nett transport of water) are present caused by the landward directed mass transport due to the waves near the mean water level. This secondary flow will be shown to be essential for the cross-shore transport computation.

In the following it is assumed that the onshore directed wave-generated mass transport of water is restricted to a narrow zone above the level of the mean wave troughs, say down to $\bar{H}/2$ below the mean water level. Consequently, there since is no nett transport, this mass transport results in a compensating (seaward directed) transport of water below this level which is known as undertow.

The definition of the accompanying time-averaged velocity profile $u(z)$ will be formulated for two different zones, viz. for an upper and a lower zone. The detailed description of the secondary flow profile, as discussed in the next sections, is restricted to the lower zone with $0 \leq z \leq d_t$ in which d_t denotes the level of the mean wave trough. As will be shown later, a similar description of the mean flow in the upper zone is not required for the assessment of the nett transport rate (see Section 4.5.3).

It should be remarked that the elaboration of the secondary flow profile was mainly carried out in order to achieve a consistent transport model (see Section 4.4.4). In a first version of the mathematical model the (slightly different) formulations according to De Vriend and Stive (1987) were used.

4.4.2 Shear stress distribution

The description of the time-averaged velocity profile $\bar{u}(z)$ below the wave trough level $z=d_t$ is based on the vertical distribution of the time-averaged shear stress $\bar{\tau}(z)$ (in N/m^2). Omitting the overbar which indicates time-averaging, the shear stress distribution is defined according to:

$$\tau(z) = \rho \varepsilon_f(z) \frac{du}{dz} \quad (4.4.1)$$

in which ε_f denotes the (time-averaged) mixing coefficient for the fluid.

It should be noted that this shear stress equation originally was valid for uniform flows only, where in that case u refers to the time-average flow profile.

In order to be more specific about $\tau(z)$, it is assumed that a constant vertical gradient in this shear stress is present. This has been proved on an experimental basis by several

researchers to be a fair description, see e.g. (Stive and Wind, 1986; Stive, 1988b; Okayasu et al., 1988):

$$\frac{d\tau}{dz} = \rho \frac{d}{dz} \left(\varepsilon_f(z) \frac{du}{dz} \right) = \rho \alpha \quad (4.4.2)$$

Integration of this expression yields a linear τ -profile according to:

$$\tau(z) = \rho \alpha z + \rho \beta \quad (4.4.3)$$

with:

$$\beta = \frac{\tau_0}{\rho} \quad (4.4.4)$$

in which β is expressed in m^2/s^2 and τ_0 denotes the (negative) mean shear stress (in N/m^2) at the reference level $z = 0$ (see Section 4.4.6).

A schematic example of this mean shear stress distribution is shown in Figure 4.18.

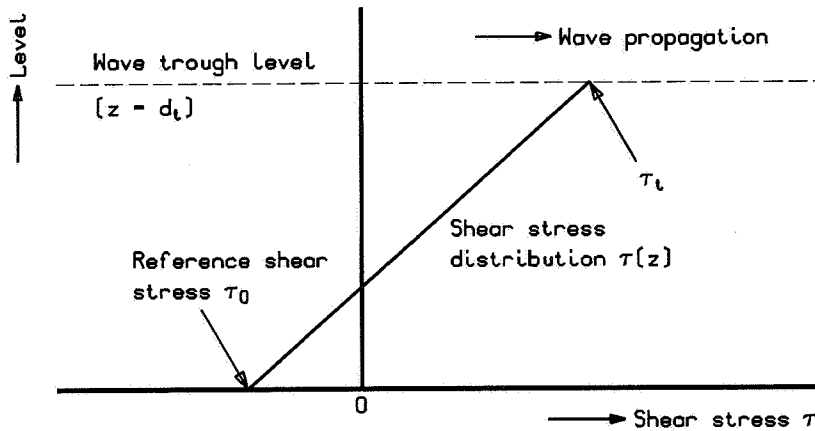


Figure 4.18 Schematic description of the mean shear stress distribution.

The (negative) reference shear stress at the lower boundary τ_0 is due to the interaction between near-bed water motion and the bottom boundary (sandy bed).

The (positive) shear stress τ_t at the upper boundary $z = d_t$ is generated by waves and equals:

$$\tau_t = \tau_0 + \alpha \rho d_t \quad (4.4.5)$$

Consequently, the (positive) shear stress gradient α (in m/s^2) is defined by:

$$\alpha = \frac{1}{\rho} \frac{\tau_t - \tau_0}{d_t} \quad (4.4.6)$$

In the following, the basic flow profile formulation will be presented. For more details about the shear stress distribution reference is made to (Deigaard and Fredsøe, 1989).

4.4.3 Basic flow profile formulation

The formulation of the secondary velocity profile $u(z)$ can be resolved by combining Equations (4.4.1) and (4.4.3) yielding:

$$\varepsilon_f(z) \frac{du}{dz} = \alpha z + \beta \quad (4.4.7a)$$

So:

$$\frac{du}{dz} = \alpha \frac{z}{\varepsilon_f(z)} + \beta \frac{1}{\varepsilon_f(z)} \quad (4.4.7b)$$

Integration of this equation yields the basic flow profile formulation:

$$u(z) = \alpha \int_0^z \frac{z}{\varepsilon_f(z)} dz + \beta \int_0^z \frac{1}{\varepsilon_f(z)} dz + \gamma \quad (4.4.8)$$

in which the third right-hand term, viz. the integration constant γ , represents the mean velocity at the reference level $u(0) = u_0$ (in m/s) and the constants α and β are defined by Equation (4.4.6) and (4.4.4) respectively.

Conform to the comments made about the use of the reference concentration C_0 (see Section 4.3.1), the u_0 -parameter is only used to fix the vertical velocity profile to a particular level and does not implicate a specific velocity at the bed level.

As can be readily seen from Equation (4.4.8), the exact shape of this secondary flow profile depends on the actual vertical distribution of the time-averaged mixing coefficient $\varepsilon_f(z)$.

4.4.4 Present formulation

To define the secondary flow profile, the vertical distribution of the mixing coefficient for the fluid has to be known. Since in the case of intensive turbulence due to breaking waves, mixing processes acting on sediment and water particles are mutually comparable, this fluid-related mixing distribution $\varepsilon_f(z)$ is taken equal to the former derived sediment mixing distribution $\varepsilon_s(z) (= \varepsilon(z))$ as described in Section 4.3.3:

$$\varepsilon_f(z) = \varepsilon(z) = \varepsilon_0 + \mu z \quad (4.4.9/4.3.15)$$

Consequently, the time-averaged velocity profile below the wave trough level of Equation (4.4.8) can be described by:

$$u(z) = u_0 + \alpha \int_0^z \frac{z}{\varepsilon_0 + \mu z} dz + \beta \int_0^z \frac{1}{\varepsilon_0 + \mu z} dz \quad (4.4.10)$$

being composed out of three terms, namely a uniform component and two depth-integrals.

It is interesting to note that the shape of this mixing profile differs from the assumption used by several other researchers in the field of flow modelling, since often the standard assumption of a constant or quasi-constant shape is used, see e.g. (De Vriend and Stive, 1987; Nielsen, 1985; You et al., 1991). However, it seems obvious that the turbulence due to breaking of waves yields an downward spreading and an inherent decay of the turbulence intensity and, consequently, requires the mixing coefficient to be a decreasing function of the distance from the surface, see e.g. (Svendsen, 1984b).

An attempt to quantify this mixing rate distribution, is made by Deigaard et al. (1991), who combine the knowledge of the shear-stress distribution in the surf zone with a one-equation turbulence model.

Before returning to the present formulation, it is also interesting to note that the results of laboratory experiments carried out by Okayasu et al. (1988) showed similar outcomes. Analysis of the signals from a two-component Laser-Doppler velocity meter showed that the mixing coefficient in the surf zone could be schematized by a linear function of the elevation.

The first integral (in the second term on the right side of former equation) can be shown to result in:

$$\begin{aligned} \int_0^z \frac{z}{\varepsilon_0 + \mu z} dz &= \frac{1}{\mu^2} \left([\varepsilon_0 + \mu z] - \varepsilon_0 \ln[\varepsilon_0 + \mu z] \right) \Big|_0^z \\ &= \frac{1}{\mu^2} \left(\mu z - \varepsilon_0 \ln \left[1 + \frac{\mu z}{\varepsilon_0} \right] \right) \end{aligned} \quad (4.4.11)$$

whereas elaboration of the second integral (as present in the third right-hand term) yields:

$$\begin{aligned} \int_0^z \frac{1}{\varepsilon_0 + \mu z} dz &= \frac{1}{\mu} \ln[\varepsilon_0 + \mu z] \Big|_0^z \\ &= \frac{1}{\mu} \ln \left[1 + \frac{\mu z}{\varepsilon_0} \right] \end{aligned} \quad (4.4.12)$$

Substitution of former results in Equation (4.4.10) yields, after some re-arranging of terms:

$$u(z) = u_0 + \left(\frac{\alpha}{\mu} \right) z + \left(\frac{\beta}{\mu} - \frac{\alpha}{\mu^2} \varepsilon_0 \right) \ln \left[1 + \frac{\mu z}{\varepsilon_0} \right] \quad (4.4.13)$$

Consequently, the time-averaged velocity profile $u(z)$ can be described by an apparent simpler formula according to:

$$u(z) = u_0 + K_{lin} z + K_{log} \ln \left[1 + \frac{\mu z}{\varepsilon_0} \right] \quad (4.4.14)$$

with profile constants K_{lin} (in s^{-1}) and K_{log} (in m/s) which are defined by:

$$K_{lin} = \alpha / \mu \quad (4.4.15)$$

$$K_{log} = \frac{1}{\mu} \left(\beta - \frac{\alpha}{\mu} \varepsilon_0 \right) \quad (4.4.16)$$

Since $\alpha > 0$ and $\mu > 0$, K_{lin} is positive also, whereas the constant K_{log} is negative since $u_0 < 0$ and so $\beta < 0$. The derived secondary flow profile below the trough level therefore consists of three contributions, namely:

- a negative, uniform part : u_0 ;
- a positive, linear part : $K_{lin} z$;
- a negative, logarithmical part : $K_{log} \ln[1 + (\mu/w_s)z]$.

Figure 4.19 shows a schematic outline of the composition of the secondary flow profile.

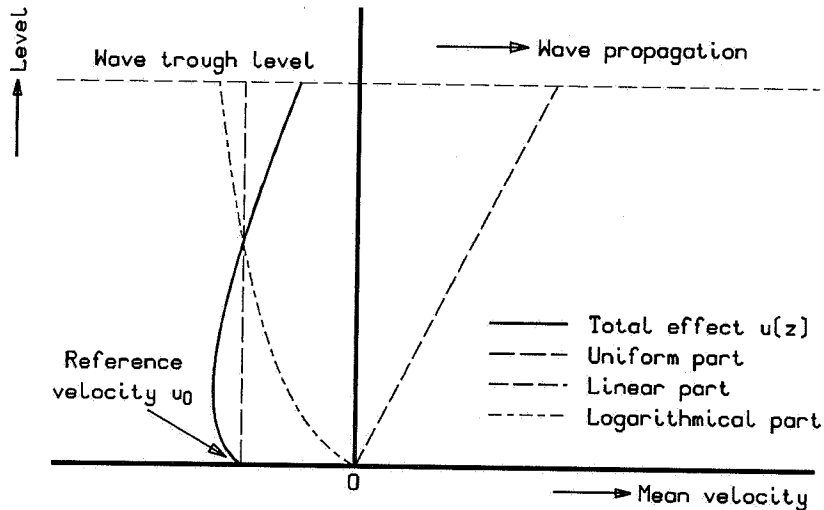


Figure 4.19 Composition of the secondary flow profile.

The form and magnitude of this velocity distribution depend principally on the magnitude of the three basic integration constants, namely α , β and γ , in which the latter represents the reference velocity near the bed u_0 and the others depend on the shear stress magnitude at both the reference level τ_0 and the trough level τ_t .

Influence of μ -parameter

Rather new in this formulation is the fact that the effect of the spatially non-uniform mixing coefficient is taken into account. A spatially uniform mixing coefficient, $\varepsilon(z) = \varepsilon$ and thus $\mu = 0$ m/s, is still widely used to model a secondary current. Svendsen and Hansen (1988) state that the use of constant mixing distribution is certainly not correct, although it has great advantages in modelling. In order to compare the formulations, the transition of the former derived expression to the constant mixing case will be outlined in the following.

For small values of $\mu z/\varepsilon_0$ the \ln -term in Equation (4.4.13) can be elaborated using a series expansion according to:

$$u(z) = u_0 + \frac{\alpha}{\mu} z + \frac{1}{\mu} \left(\beta - \frac{\alpha}{\mu} \varepsilon_0 \right) \left[\left(\frac{\mu z}{\varepsilon_0} \right) - \frac{1}{2} \left(\frac{\mu z}{\varepsilon_0} \right)^2 + \frac{1}{3} \left(\frac{\mu z}{\varepsilon_0} \right)^3 - \dots \right] \quad (4.4.13a)$$

Consequently for $\mu \ll 0$ (constant mixing) this equation describing the velocity profile reduces to:

$$u(z) = u_0 + \frac{\beta}{\varepsilon_0} z + \frac{1}{2} \frac{\alpha}{\varepsilon_0} z^2 \quad (4.4.17)$$

This formulation is applied by De Vriend and Stive and used in the energetics-based cross-shore transport model CROSTRAN (De Vriend and Stive, 1987; Stive, 1988a). This holds also for this model's successor UNIBEST-TC (Roelvink and Stive, 1989). They introduce a schematic non-uniformity of the mixing coefficient by using former expression for two separate layers, viz. a (small) boundary layer and a middle layer.

4.4.5 Continuity condition

Since in the case of a secondary current (in a two-dimensional case) no nett transport of water is present by definition, the vertical velocity profile for $0 \leq z \leq d_t$ has to satisfy the continuity condition according to:

$$\int_{z=0}^{d_t} u(z) dz = \int_{z=d_t}^{\infty} u(z) dz = -\frac{m}{\rho} \quad (4.4.18a)$$

in which m denotes the mass flux (in kg/m/s) above the mean wave trough level.

Substitution of Equation (4.4.14) yields:

$$-\frac{m}{\rho} = \int_{z=0}^{d_t} \left[u_0 + K_{lin} z + K_{log} \ln \left(1 + \frac{\mu z}{\varepsilon_0} \right) \right] dz \quad (4.4.18b)$$

whereas integration of the right-hand term results in:

$$-\frac{m}{\rho} = u_0 d_t + \frac{1}{2} K_{lin} d_t^2 + K_{log} I_0 \quad (4.4.19)$$

The outcome of the depth-integral I_0 (expressed in m) can be shown to be equal to:

$$\begin{aligned} I_0 &= \int_{z=0}^{d_t} \ln \left(1 + \frac{\mu z}{\varepsilon_0} \right) dz \\ &= \frac{\varepsilon_0}{\mu} \left[\left(1 + \frac{\mu d_t}{\varepsilon_0} \right) \left[\ln \left(1 + \frac{\mu d_t}{\varepsilon_0} \right) - 1 \right] + 1 \right] \end{aligned} \quad (4.4.20)$$

A complete derivation of this equation is presented in the Appendix. This basic constant I_0 is a function of three known parameters, namely the reference mixing coefficient ε_0 , the mixing gradient μ and the water depth below the wave trough level d_t .

4.4.6 Boundary conditions and solution procedure

A unique solution of both the former derived secondary flow formula according to Equation (4.4.14) and the continuity condition of Equation (4.4.19) requests, apart from the mass flux m , three additional boundary conditions (basically to deal with the three constants in Equation (4.4.8), viz. α , β and γ).

It is noted that both the magnitudes of the ε_0 - and μ -parameter describing the mixing profile, as well as the water depth d_t are supposed to be known already.

The first additional boundary condition is formed by the mean shear stress at the trough level τ_t . Together with the mass flux m these two conditions can be seen as the external boundary conditions acting from above on the lower zone $0 \leq z \leq d_t$.

The other two boundary conditions are present at the lower boundary ($z=0$), describing the reference velocity u_0 and the reference shear stress τ_0 .

Since these parameters are mutually dependent, instead of two boundary conditions one additional 'internal boundary relation' can be used, relating the mean reference shear stress τ_0 to the near-bed velocity field (including reference velocity u_0).

External parameters

The mean water motion below the wave trough level is affected by quantities of the water motion in the upper zone such as wave energy and dissipation.

The actual two governing parameters are the mass flux in this upper zone and the shear stress at trough level. Both are based on relations which have been presented by De Vriend and Stive (1987), see also (Svendsen, 1984b).

The mass flux m (in kg/m/s) which occurs above the mean trough level is described by:

$$m = \frac{E}{c} + P_{br} K_r \rho \frac{H_{rms}^2}{T_p} \quad (4.4.21)$$

in which:

E	the wave energy ($= \frac{1}{8} \rho g H_{rms}^2$)	(J/m ²)
c	the wave propagation velocity	(m/s)
P_{br}	the portion of breaking waves	(-)
K_r	the dimensionless quotient of roller area and H_{rms}^2	(-)
ρ	mass density of the fluid	(kg/m ³)
H_{rms}	the rms-wave height	(m)
T_p	the peak wave period	(s)

In this equation, the additional term on the right side is due to the effects of wave breaking. For K_r , a value of 0.9 has been used according to Svendsen and Hansen (Svendsen, 1984b; Svendsen and Hansen, 1988).

The shear stress at the mean trough level τ_t (in kg/m/s²) can be based on linear wave theory and can, consequently, be described as (see (Stive and Wind, 1986; De Vriend and Stive, 1987)):

$$\tau_t = \frac{1}{2} \frac{D_{br}}{c} \quad (4.4.22)$$

in which:

D_{br}	the dissipation due to wave breaking ($\approx dE/dx$)	(J/m ¹)
c	the wave propagation velocity	(m/s)

Internal boundary relation

At the lower boundary three optional types of boundary conditions can be recognized, namely:

- A 'free slip' condition, with $\tau_0 = 0$ and so $u_0 \neq 0$;
- A 'no slip' condition, with $\tau_0 \neq 0$ and so $u_0 = 0$;
- A 'partial slip' condition, with both $u_0 \neq 0$ and $\tau_0 \neq 0$.

From a preliminary examination of the apparent vertical distribution of measured time-averaged velocities it was concluded that the last intermediate condition is present, since the velocities well near the bottom surface are certainly not insignificant (so no 'no-slip' condition) and, moreover, a vertical gradient appears to occur (either upward increasing or decreasing velocities) so the 'free slip' condition could be cancelled as well. This agrees with the laboratory results as reported by Okayasu et al. (1988).

For the intermediate 'partial slip' condition the mean shear stress at the reference level τ_0 can be related to both the mean velocity u_0 at this level and the local u_{rms} -velocity, this according to a relation which reads in general terms as:

$$\tau_0 = F\{u_0, u_{rms}, \dots\} \quad (4.4.23a)$$

It is remarked that the previous approach, viz. taking into account the total water motion of waves and currents, was also suggested by Bijker (1967) and Svendsen and Hansen (1986, 1988).

In the present model formulation an adjusted form of the stationary flow equation has been used according to:

$$\tau_0 = \rho \frac{g}{C^2} u_0 \sqrt{u_0^2 + u_{rms}^2} \quad (4.4.23b)$$

in which:

ρ	mass density of the fluid	(kg/m ³)
g	the gravitational constant	(m/s ²)
C	the Chézy coefficient	(m ^{1/2} /s)
u_{rms}	the wave-generated rms-velocity at the bed level	(m/s)
u_0	the reference velocity for $u(z)$ -profile	(m/s)

Final solution procedure

The final expression for the velocity profile $u(z)$ below the wave trough level is based on the equation which describes the continuity condition, viz.:

$$-\frac{m}{\rho} = u_0 d_t + \frac{1}{2} K_{lin} d_t^2 + K_{log} I_0 \quad (4.4.19)$$

Substitution of the profile constants K_{lin} and K_{log} and basic constants α and β , yields a relation between the four governing parameters, namely the reference velocity u_0 , the reference shear stress τ_0 , the shear stress at the trough level τ_t and the mass flux m , this according to:

$$u_0 = \frac{-1}{\rho d_t} [K_0 \tau_0 + K_t \tau_t + m] \quad (4.4.24)$$

in which the boundary-related constants K_0 and K_t (both expressed in s) are defined as:

$$K_0 = \frac{I_0}{\mu} - K_t \quad (4.4.25)$$

and:

$$K_t = \frac{1}{\mu} \left(\frac{d_t}{2} - \frac{\varepsilon_0}{\mu d_t} I_0 \right) \quad (4.4.26)$$

These constants, in which I_0 is defined by Equation (4.4.20), are a function of three known parameters, namely ε_0 , μ and d_t .

Applying the additional (internal) relation between the reference shear stress τ_0 and the reference velocity near the bed u_0 according to Equation (4.4.23a), the magnitude of the unknown reference velocity can be computed from:

$$u_0 = \frac{-1}{\rho d_t} [K_0 \mathbf{F}\{u_0, \dots\} + K_t \tau_t + m] \quad (4.4.27a)$$

or:

$$\rho d_t u_0 + K_0 \mathbf{F}\{u_0, \dots\} = -1 (K_t \tau_t + m) \quad (4.4.27b)$$

The reference velocity u_0 as present in the terms on the left side is now related to the external parameters, namely the shear stress at the trough level τ_t and the mass flux above this level m .

It should be noted that for the special case that the reference shear stress is defined as a second-order relation (or of lower magnitude), say for example $\tau_0 = k_0 + k_1 u_0 + k_2 u_0^2$, the u_0 -magnitude can be elaborated from Equation (4.4.27b) in a direct way. In other cases as present here the u_0 -magnitude has to be assessed using an iterative mathematical procedure.

4.4.7 Fit procedure

In order to assess a best fit for the individual magnitude of the governing parameters (the reference velocity u_0 , the reference shear stress τ_0 , the shear stress at the trough level τ_t ,

and the mass flux m) for each measurement, a distinctive procedure has been followed.

First the mass flux is estimated from the measured time-averaged velocities by sketching a preliminary velocity contour and subsequent depth-integration of this profile over the lower zone (up to mean trough level).

Next, the shear stress distribution (so both the reference shear stress and the shear stress at the trough level, determining in fact the α - and β -parameter) has been chosen in such a way that a proper resemblance between computed and measured velocities was obtained.

A characteristic example of measured time-averaged velocities and an estimated flow profile is shown in Figure 4.20, in which the reference velocity u_0 equals -0.272 m/s.

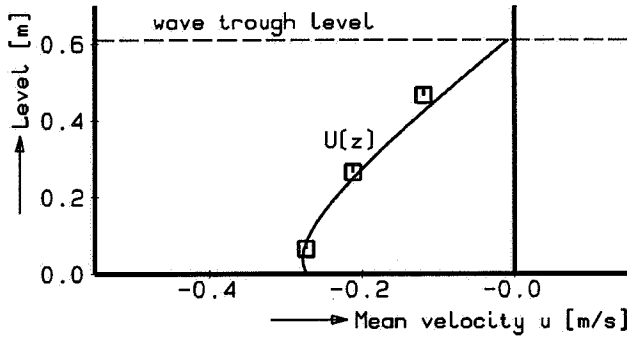


Figure 4.20 Example of measured velocities and accompanying computed flow profile.

For the specific data on the (secondary) flow reference is made to the relevant research reports, viz. (Steezel, 1987b, 1990a).

In addition, it is noted that the shape of the undertow profile is in agreement with the results of some impressive field measurement campaigns, see e.g. (Kuriyama, 1991; Greenwood and Osborne, 1990).

4.4.8 Summary and conclusions

As a result of the former described approach the time-averaged velocity profile below the wave trough can be characterized by the equation:

$$u(z) = u_0 + K_{lin} z + K_{log} \ln \left[1 + \frac{\mu z}{\varepsilon_0} \right] \quad (4.4.14)$$

In order to assess the magnitude of K_{lin} and K_{log} in this equation, first the I_0 -constant has to be computed using Equation (4.4.20). Subsequent determination of K_0 and K_t using Equations (4.4.25) and (4.4.26) and assessment of the reference velocity u_0 and thus τ_0 from Equation (4.4.27), give the α and β parameters from which K_{lin} and K_{log} can be

computed from Equation (4.4.15) and (4.4.16) respectively.

The suspended sediment concentration profile, as specified in the previous Section 4.3, is transported by this time-averaged velocity profile. The resulting equations for the final nett cross-shore transport computation will be elaborated in the next section.

4.5 Nett cross-shore transport computation

4.5.1 Introduction

In principle, the major part of the nett local cross-shore transport rate should be derived from a time and a depth integration of instantaneous velocities and concentrations according to Equation (4.2.1). However, based on arguments presented in Section 4.2.7, it is postulated here that a reliable estimate of the nett amount of cross-shore sediment transport can be obtained from the depth-integrated product of the time-averaged velocity profile $\bar{u}(z)$ and the time-averaged sediment concentration profile $\bar{C}(z)$, this according to:

$$S = \int_{z=0}^{\eta_{max}} \bar{u}(z) \bar{C}(z) dz \quad (4.5.1)$$

in which η_{max} denotes the maximum water level with respect to the bottom.

Due to the definition of the secondary current $\bar{u}(z)$ as presented in Equation (4.4.14) (see Section 4.4 for more details), the depth-integration has to be split up into two parts, namely:

$$S = \int_{z=0}^{d_t} \bar{u}(z) \bar{C}(z) dz + \int_{z=d_t}^{\eta_{max}} \bar{u}(z) \bar{C}(z) dz = S_l + S_u \quad (4.5.2)$$

resulting in a lower (below the mean wave trough level $z=d_t$) and an upper transport contribution (above this level): S_l and S_u respectively.

These transport contributions will be elaborated further in the next two sections. The overbar, denoting time-averaging, will further be omitted. Some additional justifications for the application of the presented procedure will be given in Section 4.6.

4.5.2 Transport below the mean trough level

The nett seaward-directed sediment transport below the mean wave trough level $z=d_t$ (lower contribution) is computed from the depth-integration according to:

$$S_l = \int_{z=0}^{d_t} u(z) C(z) dz \quad (4.5.3)$$

This integration can be split up into three different parts conform to the description of the

secondary flow profile. Substitution of the formulations for both the time-averaged velocity profile $u(z)$ as presented in Equation (4.4.14) and the mean concentration profile $C(z)$ of Equation (4.3.19), yields the next expression after some elaboration:

$$S_I = C_0 u_0 \left[\int f_c(z) dz \right]_1 + C_0 K_{lin} \left[\int z f_c(z) dz \right]_2 + C_0 K_{log} \left[\int \ln(1 + (\mu/\varepsilon_0)z) f_c(z) dz \right]_3 \quad (4.5.4)$$

in which $f_c(z)$ denotes the concentration distribution function according to Equation (4.3.17).

Elaboration of the three depth-integrals (in between rectangular brackets) ultimately results in three basic parameters I_1 (expressed in m), I_2 (in m²) and I_3 (in m) according to respectively:

$$I_1 = \frac{\varepsilon_0}{\mu} \frac{1}{K_1} \left[K_2^{K_1} - 1 \right] \quad (4.5.5/4.3.22a)$$

$$I_2 = \frac{\varepsilon_0}{\mu} \frac{1}{K_1} \left[K_2^{K_1} \left(d_t - \frac{\varepsilon_0}{\mu} \frac{K_2}{K_1+1} \right) + \frac{\varepsilon_0}{\mu} \frac{1}{K_1+1} \right] \quad (4.5.6)$$

$$I_3 = \frac{\varepsilon_0}{\mu} \frac{1}{(K_1)^2} \left[K_2^{K_1} (K_1 \ln(K_2) - 1) + 1 \right] \quad (4.5.7)$$

in which two additional, dimensionless constants K_1 and K_2 are defined as:

$$K_1 = 1 - w_s/\mu \quad (4.5.8)$$

$$K_2 = 1 + (\mu/\varepsilon_0)d_t \quad (4.5.9)$$

The complete derivation of these three basic constants is given in the Appendix. Moreover, it is noted that the I_1 -parameter has also been used in the sediment load formulation in Section 4.3.6, although in that case the vertical integration interval was not restricted to the level below the wave trough (d instead of d_t) and consequently the K_2 -definition of Equation (4.3.24) and (4.5.9) are slightly different.

In summary, the transport rate for $0 \leq z \leq d_t$ can be computed from an apparently rather simple expression:

$$S_I = C_0 \left[u_0 I_1 + K_{lin} I_2 + K_{log} I_3 \right] \quad (4.5.10)$$

using the basic constants as defined in Equation (4.5.5...9). This formula consists of three contributions of which the first one is the most important, namely the transport of the sediment load ($= C_0 I_1$) by a uniform flow profile ($u(z) = u_0$).

4.5.3 Transport above the mean trough level

Above the mean trough level (for $z > d_t$) the landward directed transport S_u (upper contribution) should actually be computed from:

$$S_u = \int_{z=d_t}^{\eta_{max}} u(z) C(z) dz \quad (4.5.11)$$

This, however, requires knowledge of both the flow profile $u(z)$ and the distribution of suspended sediment $C(z)$ in this zone.

Since the vertical gradients in the suspended sediment concentrations near the mean water level are relatively small, viz. $\Delta C / \Delta z \approx 0$, the former integral can be simplified to:

$$S_u \approx C(d) \int_{z=d_t}^{\eta_{max}} u(z) dz \quad (4.5.12)$$

in which $C(d)$ denotes the time-averaged sediment concentration at the (mean) water level $z = d$.

Since the right-hand integral by definition is related to the mass flux (see Section 4.4.6) according to:

$$\int_{z=d_t}^{\eta_{max}} u(z) dz = \frac{m}{\rho} \quad (4.5.13/4.4.20)$$

an estimate of the nett landward upper component of the transport S_u can be obtained using Equation (4.4.19) yielding:

$$\begin{aligned} S_u &\approx C_0 f_c(d) \frac{m}{\rho} \\ &= -C_0 f_c(d) \left[u_0 d_t + \frac{1}{2} K_{lin} d_t^2 + K_{log} I_0 \right] \end{aligned} \quad (4.5.14)$$

in which $f_c(d)$ denotes the relative concentration at mean water level $z=d$ according to Equation (4.3.17).

So, the landward transport above the mean trough level (upper contribution) is described by the product of the time-averaged concentration at the mean water level and the nett amount of water, moving landward.

In this approach, the detailed description of the secondary flow profile in this zone is not relevant.

It is noted that in the case of breaking waves with sediment in suspension over the whole water depth, the onshore transport component is definitely not insignificant. Moreover, omitting this compensating transport rate will lead to a significant over-estimation of the offshore transport rate.

4.5.4 Total nett transport formulation

After specifying the transport in the two zones, the total nett transport S can now simply be computed from Equation (4.5.2) by substitution of Equation (4.5.10) and (4.5.14), yielding:

$$S = C_0 \left[u_0 (I_1 - f_c(d) d_t) + K_{lin} \left(I_2 - f_c(d) \frac{1}{2} d_t^2 \right) + K_{log} (I_3 - f_c(d) I_0) \right] \quad (4.5.15)$$

in which $f_c(d)$ denotes the time-averaged concentration at $z = d$ according to Equation (4.3.17):

$$f_c(d) = \left[1 + \frac{\mu d}{\epsilon_0} \right]^{(-w_s/\mu)} \quad (4.5.16)$$

and I_0 is defined according to Equation (4.4.20).

As can be observed, the nett transport consists of three contributions which are related to the uniform, linear and logarithmic part of the secondary flow profile, respectively. It is noted that increasing mixing rates will not always result in a larger nett transport rate. Moreover, a near-uniform concentration profile will even result in no nett cross-shore transport at all, although there may be a large amount of longshore transport (if any longshore current is present).

4.5.5 Example of nett transport computation

An example of the result of a nett transport computation is shown in Figure 4.21. The right side of this figure shows the measured and best-fit concentration distribution, whereas the left part shows the measured and best fit nett velocity profile below the mean wave trough level.

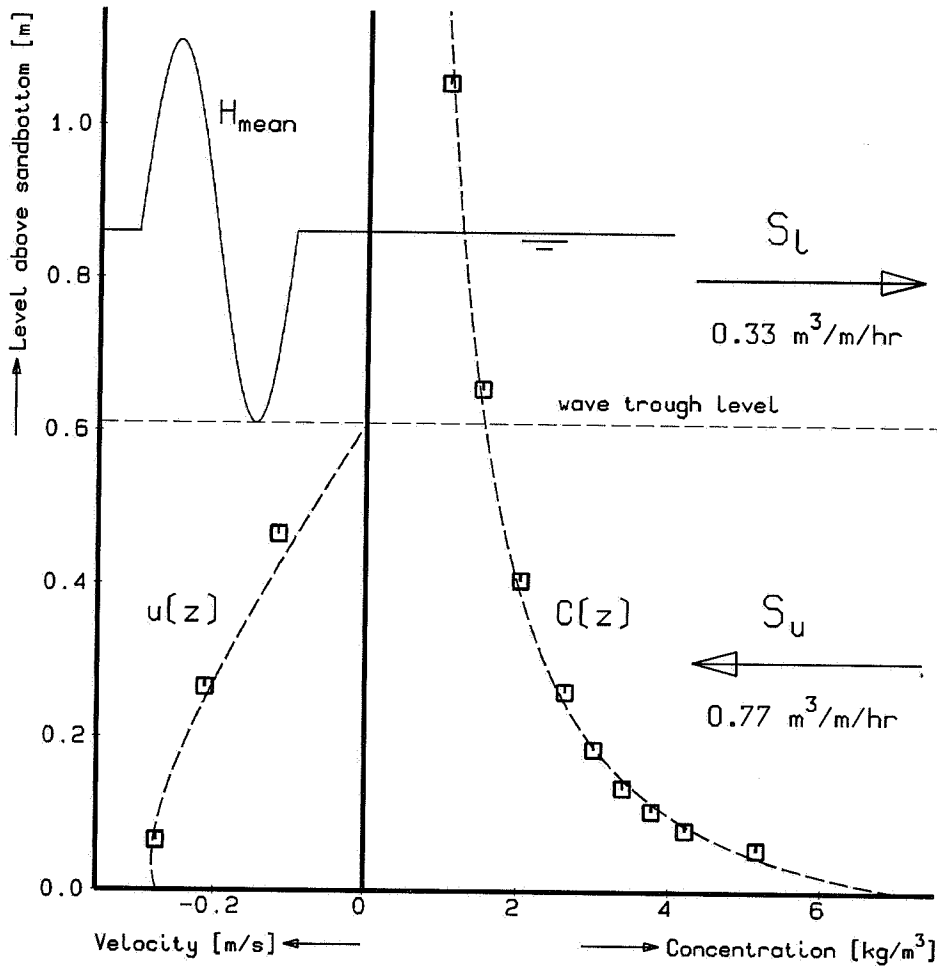


Figure 4.21 Example of nett transport computation based on velocity and concentration profile; test T314 at location $x = 181$ m.

The seaward directed transport (including pores; below the wave trough) equals $0.77 \text{ m}^3/\text{m/hr}$. The partially compensating transport above the trough level amounts to $0.33 \text{ m}^3/\text{m/hr}$, so the nett result is an offshore transport of $0.44 \text{ m}^3/\text{m/hr}$. In this elaboration a specific mass density of the sand of $\rho_s = 2650 \text{ kg/m}^3$ has been used. In order to compute the transport rate (including pores) a porosity of $p = 0.38$ has been assumed (see Section 4.6.3).

4.6 Justification of the proposed computation method

4.6.1 Introduction

In order to give some justification for the former derived nett cross-shore transport computation, the instantaneous transport rate (computed by integration of the product of time-averaged velocity profile and time-averaged concentration profile over the water depth according to Equation (4.5.1) or (4.5.15)), has been compared with transports which have been determined from the (frequently) measured bottom profiles of the H298-I-test series (Steetzel, 1987b).

4.6.2 Measured transport rates

The actual transport rates are derived from the measured development of the cross-shore profile. By levelling of the bed surface before and after a limited number of flow and concentration measurements, the actual local transport rate (including pores) can be derived from the integrated sediment volume balance according to:

$$S_x(t) = \frac{dA_x(t)}{dt} \quad (4.6.1)$$

in which the accumulated transport $A_x(t)$ equals the landward, time-integrated loss of volume according to:

$$A_x(t_j) = \int_x^{\infty} (z_b(x|t=t_j) - z_b(x|t=t_0)) dx \quad (4.6.2)$$

in which $z_b(x|t)$ denotes the bottom level in position x at a specific moment t .

It is clear that these integrated volumes are only available at the moment the soundings took place, viz. $A_x(t_j)$, $j=0, 1, 2, \dots, j_{max}$. An example of a computed development of this accumulated transport, viz. the observed erosion rate, is shown in Figure 4.22.

In the case of a model test with constant hydraulic conditions, the development of this volume near $t=t_j$ can be adequately characterized by a logarithmical relationship, according to:

$$A_x(t) = A_x(t_j) + B \ln(t/t_j) \quad (4.6.3)$$

in which a local best estimate for $t \approx t_j$ of the B -value (the tangent of the relation on a linear-logarithmical plot as shown in Figure 4.22) can be computed from:

$$B = \frac{A_x(t_{j+1}) - A_x(t_j)}{\ln(t_{j+1}/t_0) - \ln(t_j/t_0)} \quad (4.6.4)$$

The local estimate of the transport rate (including pores) is computed from Equation (4.6.1)

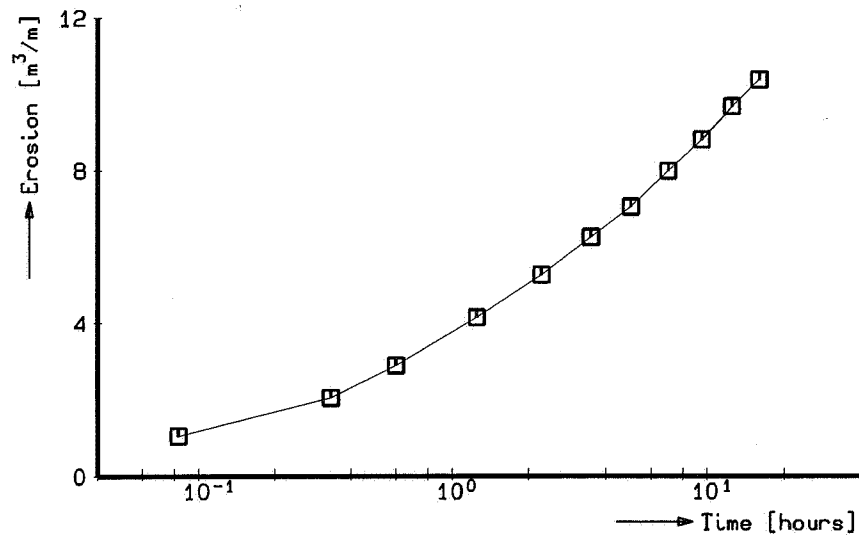


Figure 4.22 Example of the development of erosion rates; test T3 of H298-I-series.

by substitution of Equation (4.6.3), yielding:

$$S_x(t) = \frac{dA_x(t)}{dt} = B \frac{1}{t} \quad (4.6.5)$$

Consequently, the instantaneous estimate of the rate at $t=t^*$ for $t_j \leq t^* \leq t_{j+1}$ can be assessed by combining Equation (4.6.4) and (4.6.5), yielding:

$$S_x(t^*) = \frac{A_x(t_{j+1}) - A_x(t_j)}{t^* \ln(t_{j+1}/t_j)} \quad (4.6.6)$$

Figure 4.23 shows an example with the momentary profiles for a partly protected dune (test T3 of H298-I-series) after wave attack of 9.5 and 12.5 hours (DELFT HYDRAULICS, 1987a).

The nett transport at the time interval of the analyzed measurements ($t=11.25$ hr, as used in Figure 4.21) equals $0.398 \text{ m}^3/\text{m}/\text{hr}$ (including pores). This deviates only 10 % from the former computed value of $0.440 \text{ m}^3/\text{m}/\text{hr}$ (see Section 4.5.5).

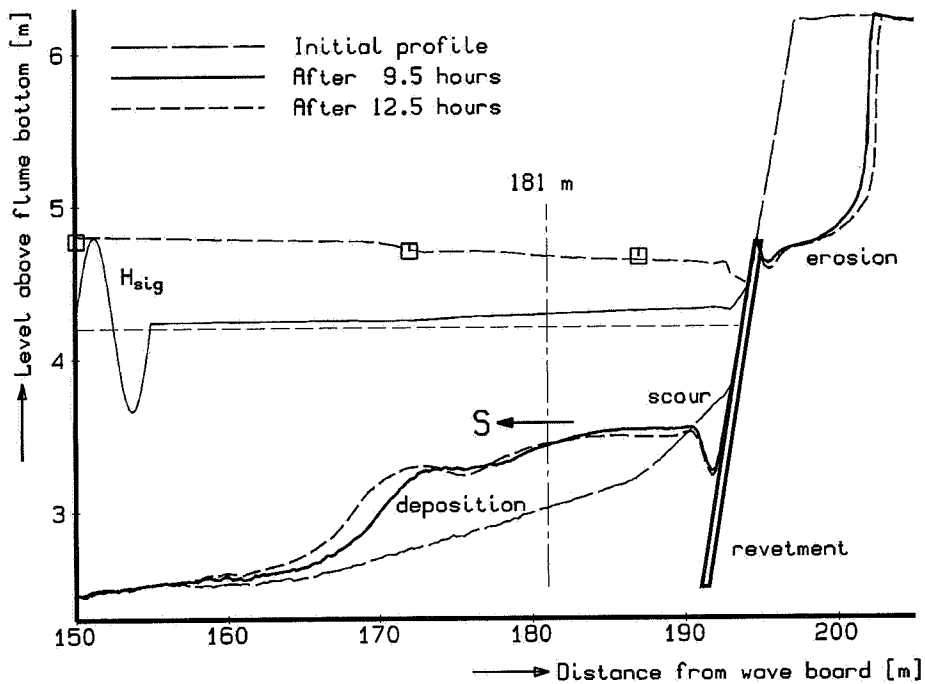


Figure 4.23 Example of transport computation based on measurement of an observed profile development; test T3 of H298-I-series.

4.6.3 Comparison of estimated transport rates

For a decent comparison between the computed (cf. Section 4.5) and measured transport rates of the previous section a distinction has been made for mutually different sectors in the cross-shore profile: on the erosion profile and foreshore, above the revetment (above a non-erodible structure) as well as several locations in the scour hole. Moreover, the effect of significantly varying bottom slopes (upward or downward) has to be accounted for also.

The overall comparison between measured and computed transport rates is shown in Figure 4.24. Figure 4.25 presents a detail using linear scales.

The dashed best-fit relation is restricted to positions on both the erosion profile and the foreshore, although for other groups a similar relation is found.

The exact ratio between measured (profile) transports S_p and computed transports S_{uc} equals:

$$(S_{uc}/S_p) = 1.029 \pm 0.395$$

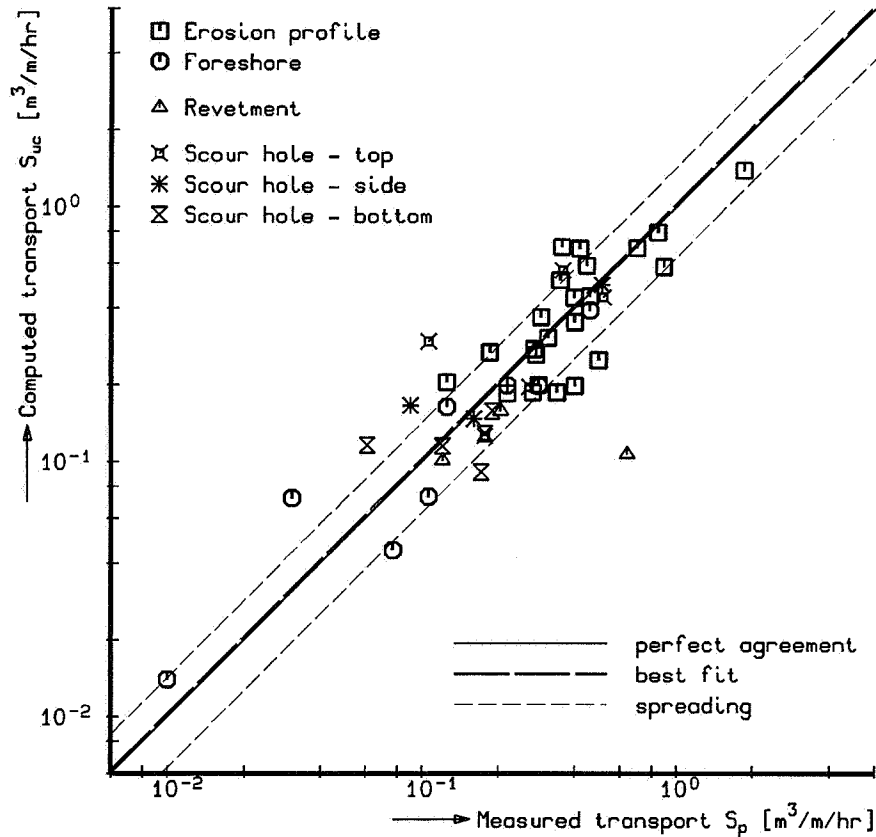


Figure 4.24 Comparison between computed and measured transport rates.

Since the mean ratio between measured and computed transport is similar, viz. $S_{uc}/S_p \approx 1$, and the deviations from these are random, the method to compute the transport rates seems to provide reliable results.

If all presented data points are taken into account, a ratio of $(S_{uc}/S_p) = 1.055 \pm 0.512$ will be found, viz. a similar relationship though with a larger spreading.

The effect of the bottom slope, viz. an increase in the (seaward) transport rate for a positive slope and a slight decrease in the opposite case, has to be accounted for an additional correction factor for the computed transport rate (see Section 4.7.6 for more details).

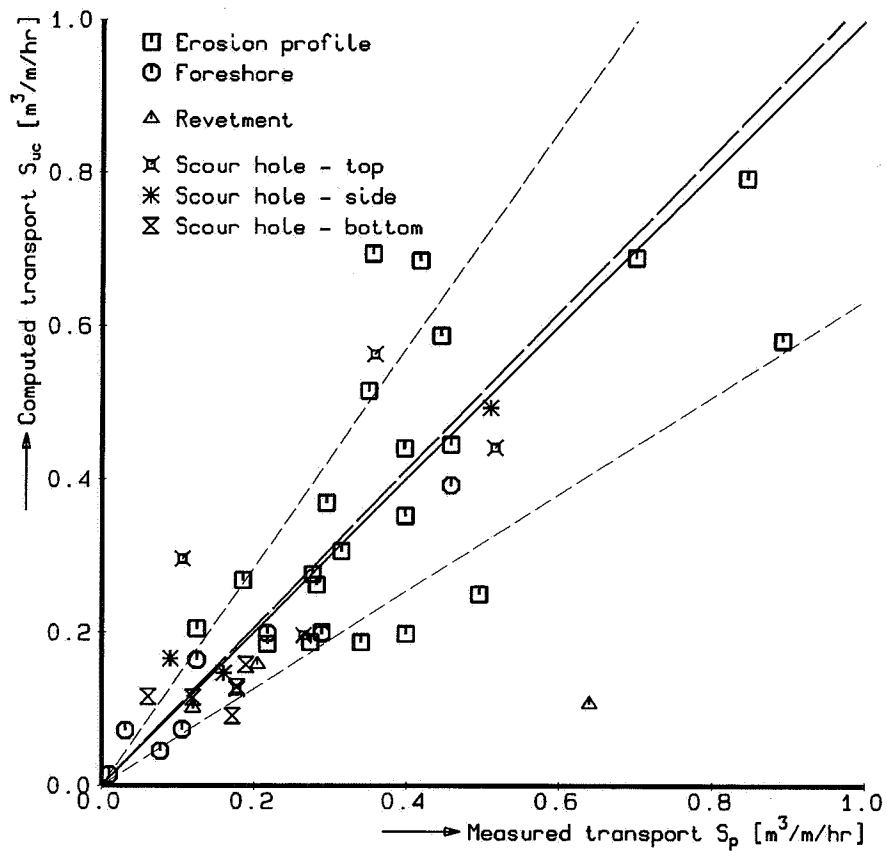


Figure 4.25 Detailed comparison between computed and measured transport rates on linear scales.

4.6.4 Conclusion

From the comparison between measured and computed transport rates it is concluded that, although a large amount of (random) scatter occurs, the transport computation based on the derived equations, viz. time-averaged concentration times time-averaged velocity profile, provides indeed a fair estimate of the measured transport rates for the tested conditions (breaking waves).

This conclusion confirms the findings presented in Section 4.2.

The set-up of a mathematical model using this idea is presented in the next section.

4.7 Set-up of computational model

4.7.1 Introduction

In this section a brief outline of the computational model is presented. In addition, some remarks are presented about some model components. The described procedures and routines are brought together in the form of a user-friendly PC-model: DUROSTA-1.11 (DELFT HYDRAULICS, 1991).

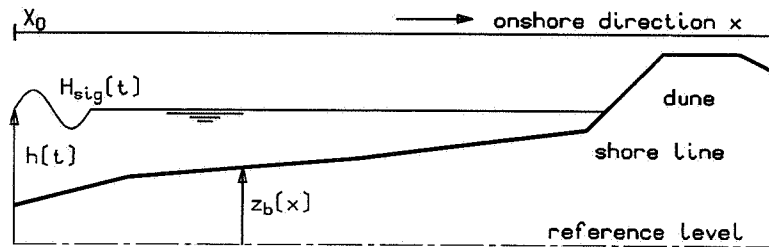


Figure 4.26 *Definitions and coordinate system used in the computational program.*

The coordinate system used is shown Figure 4.26. The hydraulic conditions (mean water level and wave conditions) are prescribed on the seaward boundary, viz. $x = X_0$.

4.7.2 Input data

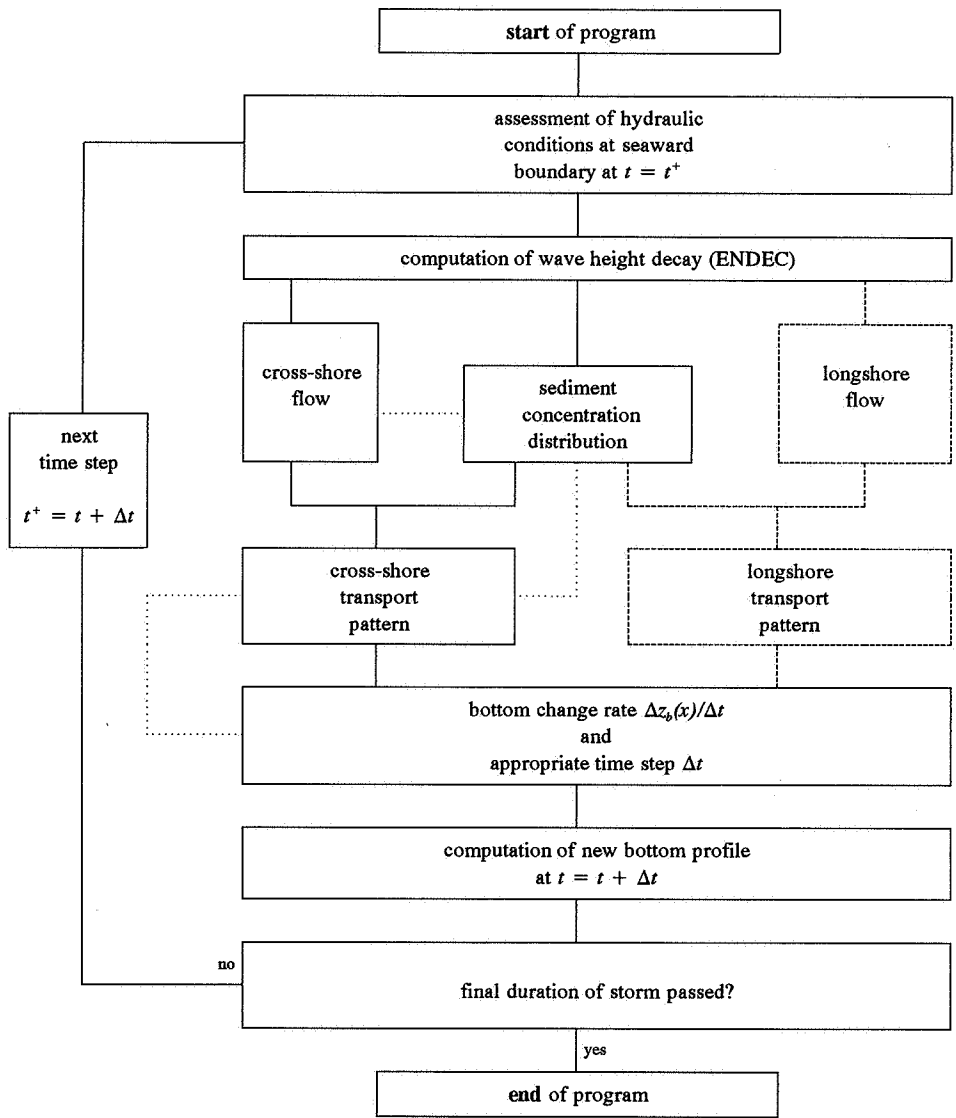
The input data for the computational model consist of three sets of information, namely:

- General data;
- Ray data;
- Time functions.

The general data consists of bed material characteristics, time intervals and time step restrictions.

The ray data describe the initial bottom profile and the computational grid to be used, whereas the time functions describe the pattern of the hydraulic conditions during a storm surge.

In the present version of the model a user-friendly pre-processor is available to create the required data file (DELFT HYDRAULICS, 1991).



Remarks: - dashed lines indicate model extension
 - dotted lines refer to backward correction procedures

Figure 4.27 Aggregate flow-chart of the computational model.

4.7.3 Flow-chart

An aggregate flow-chart of the computational model is presented in Figure 4.27.

The different phases of the dynamical model are obvious. On the initial bottom profile the momentary offshore hydraulic conditions determine the local wave heights by using the wave height decay model ENDEC as described in the next section (Battjes and Janssen, 1978).

From this the relevant parameters (e.g. cross-shore secondary current and sediment concentrations) are computed resulting in local cross-shore transport rates. This procedure has been thoroughly described in Section 4.3 to 4.5. The additional computation of both longshore flow and longshore transport pattern (as denoted by the dashed part of the diagram) is discussed in the next section.

Finally the bottom changes are computed through application of the mass balance equation of the sediment. The new bottom profile is computed after which the procedure for a next time step is restarted.

Some of the relevant phases are described in more detail in the next sections.

4.7.4 Computation of wave height decay

For each computational time step the local hydraulic conditions across the momentary profile are resolved. Starting with the conditions at the seaward boundary, the momentary wave height decay is computed using the procedure as described in (Battjes and Janssen, 1978).

The basic equations describing this wave height decay while taking account of the wave-induced cross-shore water level set-up are the wave action equation and the cross-shore momentum equation, according to:

$$\frac{d}{dx} (c_g E) + D_b + D_f = 0 \quad (4.7.1)$$

$$\frac{dS_{xx}}{dx} + \rho g (d + \bar{\eta}) \frac{d\bar{\eta}}{dx} = 0 \quad (4.7.2)$$

where:

$$E = \frac{1}{8} \rho g H_{rms}^2 \quad (4.7.3)$$

$$S_{xx} = \left(2n - \frac{1}{2}\right) E \quad (4.7.4)$$

$$n = \frac{1}{2} kd / \sinh(2kd) \quad (4.7.5)$$

and:

$$\omega^2 = gk \tanh(kd) \quad (4.7.6)$$

The energy dissipation due to wave breaking D_b and bottom friction D_f is described by respectively:

$$D_b = \frac{1}{4} \rho g \alpha Q_b (\omega/2\pi) H_m^2 \quad (4.7.7)$$

$$D_f = \frac{1}{8} \rho f_w \pi^{-\frac{1}{2}} (\omega H_{rms} / \sinh(kd))^3 \quad (4.7.8)$$

in which Q_b denotes the fraction of breaking waves.

The maximum wave height is described by:

$$H_m = (2 \pi S_{max} / k) \tanh(\gamma kd / 2 \pi S_{max}) \quad (4.7.9)$$

where S_{max} denotes the maximum wave steepness (see also Section 5.2).

It is remarked that former equations, viz. Equation (4.7.1...9) are just presented for the sake of completeness. More background on these (basic) equations and the ENDEC-model is given in (Stive and Dingemans, 1984; Stive and Battjes, 1985).

4.7.5 Averaging procedures

In order to allow for an orderly development of the coastal profile, the governing individual parameters are subjected to a smoothing routine. Especially the effect of the breaking wave fraction Q_b (which is extremely sensitive to small bottom irregularities) yields, for example, a spatially unlikely varying mass flux m . Since this mass flux has a great impact on the cross-shore distribution of the sediment transport, a spatially local averaged mass flux has been used instead.

The advantage of this procedure is that the amount of numerical smoothing needed at the time of the new bottom computation can be significantly reduced. Furthermore, it harmonizes probably more with the physical processes involved. More information can be found in (Steetzel, 1993).

4.7.6 Local modification of transport rates

In order to obtain a better agreement between the cross-shore distribution of the computed and observed transport, the transport computation has been modified to take into account the effects of both swash-induced transports and local bed slope.

Swash zone

Since the standard computed transport rates are not valid in the swash zone (the correlation component can not be ignored!; see Section 4.2), the transport in this area is determined in a special manner.

This is done by the use of a function which relates the relative magnitude of the transport rate in this zone to its position and altitude with reference to the 'beach boundary'. The latter is defined as the position where the distance up to the computed water line is equal to a quarter of the local wave length. In this position the original procedure is assumed to be still valid (Steetzel, 1993).

Bed slope effects

As mentioned earlier in Section 4.6.3, the offshore-directed transport rate is slightly affected due to a non-horizontal bed slope.

Based on a comparison between computed and measured transport rates for positions with a significant mean bed slope, it was concluded that this effect could be schematized by:

$$S'_x = \left[1 + K_{sl} \left(\frac{\Delta z_b}{\Delta x} \right) \right] S_x \quad (4.7.10)$$

in which S'_x the new estimate of the transport rate. This common procedure of incorporating bed slope effects is also presented by Horikawa (1988). For the assessment of the slope factor, with $K_{sl} \geq 0$, see Section 5.5.3.

4.7.7 Bottom changes and time step assessment

Bottom changes are computed using the conservation equation of sediment mass, according to:

$$\frac{dz_b(x)}{dt} = \frac{-I}{(1-p)} \left[\frac{dS_x(x)}{dx} \right] \quad (4.7.11)$$

in which p denotes the porosity of the settled bed material.

In order to eliminate optional irregularities in the next bottom profile first the across-shore 'bottom change velocity' (the left-hand term) is computed. Based on this distribution, an acceptable computational time step Δt is assessed. In this way initial irregularities are reduced. Furthermore, the mitigating effects of the next time step will inhibit their further growth which would otherwise result in a saw-tooth shaped bottom profile.

The final new bottom profile at time $t + \Delta t$ is computed using a modified numerical LAX-scheme according to (see e.g. (Horikawa, 1988)):

$$z_b(x, t + \Delta t) = z_b(x, t) - \frac{\Delta t}{2(1-p)\Delta x} [S_x(x + \Delta x, t) - S_x(x - \Delta x, t)] \\ + \frac{1}{2} \gamma [z_b(x + \Delta x, t) - 2z_b(x, t) + z_b(x - \Delta x, t)] \quad (4.7.12)$$

in which γ denotes a numerical smoothing factor which determines to what extent the bed levels of the surrounding points of $z_b(x)$ at time t are taken into account for the computation of the new bed level at time $t + \Delta t$. This causes numerical smoothing at sharp transitions of the bed profile. From trial computations it was concluded that $\gamma = 0.05$ provided the anticipated result.

4.8 Additional extension of the model

4.8.1 Introduction

In order to extend the applicability of the computational model as indicated in Table 2.1 both the effect of structures and longshore transports on the cross-shore profile development are incorporated by adjusting and adding computational routines.

4.8.2 Effect of structures

A structure (for example a dune revetment or a longshore dam) is schematized as a non-erodible part of the cross-shore profile.

To determine the impact of such a non-erodible section on the development of the cross-shore profile the computational procedure for the assessment of the new bottom profile (see Section 4.7.7) is modified.

In fact, the cross-shore gradient of the initially computed cross-shore transport distribution is adjusted in such a way that no erosion will occur in a non-erodible part of the profile. In addition, the computational time step is reduced to such an extent that the remaining local transport gradient results in an erosion magnitude up to the protected bottom contour.

The effect of an adjusted (reduced) transport rate is assumed to have no effect on the secondary flow profile so that this affects only the amount of suspended sediment. Consequently, the latter is changed by a proportional correction of the reference concentration C_o . This backward correction procedure is indicated in the flow-chart of Figure 4.27 by the dotted lines.

In this way the presence of a structure will obstruct the normal cross-shore transport distribution and will, for example, lead to the formation of local scour holes in front of a structure, see e.g. (Steetzel, 1987a, 1988).

A large number of comparisons of computed and measured profile developments for situations with structures is presented in Section 6.6, whereas in Section 8.5 some related applications of the model are given.

4.8.3 Longshore transport

For the assessment of the longshore transport rate (in Y -direction) it is assumed that both the local magnitude and the vertical shape of the suspended sediment concentration field $C(x,z)$ are fully due to the effects of the cross-shore transport processes. However, it is stressed that the presence of waves is assumed to have a large effect on both the magnitude and the shape of the primary longshore current (see also (You et al., 1991)). The longshore current acts just as a transport medium for the sediment suspension generated by the intensive breaking waves. The additional increase in the longshore transport rate due to longshore current-induced shear stresses is neglected.

For more details reference is made to the research report (Steetzel, 1990c).

The longshore transport computation is basically comparable with the computation of the cross-shore transport below the wave trough level as presented in more detail in Section 4.5.2.

However, since the local time-averaged transport rate S_y has to be computed from:

$$S_y = \int_{z=0}^d \bar{v}(z) \bar{C}(z) dz \quad (4.8.1)$$

knowledge of both the time-averaged flow profile $\bar{v}(z)$ and time-averaged concentration profile $\bar{C}(z)$ is needed.

Consequently, to assess $S_y(x)$ (and omitting the overbar indicating time-averaging), first the cross-shore distribution of the mean longshore current, denoted as $\bar{v}(x)$, and the vertical distribution of the accompanying flow profile $v(z|x)$ has to be described in detail.

Cross-shore distribution of (mean) longshore current

The local, mean (depth-averaged) longshore current, denoted as \bar{v} (overbar denoting depth-averaged value), can be composed out of tidal-driven \bar{v}_c and wave-driven currents \bar{v}_w . The total nett current rate can be computed from the alongshore momentum equation according to:

$$\frac{dS_{yx}}{dx} + \rho g d \frac{d\zeta}{dy} + \overline{\tau_{by}} = 0 \quad (4.8.2)$$

in which $d\zeta/dy$ denotes the alongshore water level gradient (if present).

The radiation stress S_{yx} and bottom shear stress $\overline{\tau_{by}}$ are defined by:

$$S_{yx} = E(n \cos\theta \sin\theta) \quad (4.8.3)$$

and:

$$\overline{\tau_{by}} = \rho c_f \bar{v} |\bar{v}| \quad (4.8.4)$$

in which θ denotes the wave angle with respect to the shore normal and $c_f (=g/C^2)$ is a dimensionless alongshore friction factor.

Vertical distribution of longshore flow

The derivation of the local (viz. position x on the cross-shore profile) vertical distribution of the mean longshore flow $v(z)$ is based on an analogous argumentation as followed for the assessment of the vertical distribution of the time-averaged cross-shore flow below the wave trough level $u(z)$. In order to mark related, though dissimilar formulations, some of the 'longshore related parameters' are supplied with an accent for the sake of convenience. Consequently, the vertical gradient in the (time-averaged) shear stress (denoted as $\tau'(z)$) is assumed to be constant, according to Equation (4.4.2):

$$\frac{d\tau'}{dz} = \rho \frac{d}{dz} \left(\varepsilon(z) \frac{dv}{dz} \right) = \rho \alpha' \quad (4.8.5)$$

Since the mean shear stress at the upper boundary (water level $z = d$) equals zero, the shear stress gradient for longshore flow (in m/s^2) is defined by:

$$\alpha' = \frac{1}{\rho} \frac{-\tau_0'}{d} \quad (4.8.6)$$

in which τ_0' denotes the reference shear stress at the bottom level (in Y -direction).

A similar elaboration of the shear stress equation, using the same mixing distribution as elaborated in Section 4.3.3 and 4.4.4, ultimately yields:

$$v(z) = v_0 + K_{lin}' z + K_{log}' \ln \left[1 + \frac{\mu z}{\varepsilon_0} \right] \quad (4.8.7)$$

in which the profile constants K_{lin}' (in $1/\text{s}$) and K_{log}' (in m/s) are defined as:

$$K_{lin}' = \frac{-\tau_0'}{\rho \mu} \frac{1}{d} \quad (4.8.8)$$

$$K_{log}' = \frac{\tau_0'}{\rho \mu} \left(1 + \frac{\varepsilon_0}{\mu d} \right) \quad (4.8.9)$$

In order to solve Equation (4.8.1), the continuity condition has to be satisfied:

$$\int_{z=0}^d v(z) dz = d \bar{v} \quad (4.8.10)$$

in which \bar{v} denotes the depth-averaged velocity as derived from the alongshore momentum equation.

Substitution of the derived $v(z)$ -profile, viz. Equation (4.8.7), and subsequent integration yields:

$$v_0 d + \frac{1}{2} K_{lin}' d^2 + K_{log}' I_0' = d \bar{v} \quad (4.8.11)$$

in which the depth-integral I_0' (in m) equals (see Appendix for complete derivation):

$$\begin{aligned} I_0' &= \int_0^d \ln \left[1 + \frac{\mu z}{\varepsilon_0} \right] dz \\ &= \frac{\varepsilon_0}{\mu} \left[\left(1 + \frac{\mu d}{\varepsilon_0} \right) \left(\ln \left[1 + \frac{\mu d}{\varepsilon_0} \right] - 1 \right) + 1 \right] \end{aligned} \quad (4.8.12)$$

Substitution of the profile constants K_{lin}' and K_{log}' as defined in Equation (4.8.8) and (4.8.9) results in:

$$v_0 d + \frac{\tau_0'}{\rho \mu} \left[\frac{-d}{2} + \left(1 + \frac{\varepsilon_0}{\mu d} \right) I_0' \right] = d \bar{v} \quad (4.8.13a)$$

or:

$$v_0 + \frac{\tau_0'}{\rho \mu} K_0' = \bar{v} \quad (4.8.13b)$$

with the dimensionless lower boundary-related constant K'_0 defined as:

$$K'_0 = \left(1 + \frac{\varepsilon_0}{\mu d} \right) \frac{I'_0}{d} - \frac{1}{2} \quad (4.8.14)$$

For the final solution of the governing equations, three types of boundary conditions can be identified, namely a 'no-slip', a 'free-slip' and a 'partial slip' condition.

For a 'no-slip' condition, with $v_0 = 0$ m/s, the magnitude of the reference shear stress τ'_0 can be computed from Equation (4.8.13b):

$$\begin{aligned} \frac{\tau'_0}{\rho \mu} K'_0 &= \bar{v} \\ \text{so: } \tau'_0 &= \frac{\rho \mu \bar{v}}{K'_0} \end{aligned} \quad (4.8.15)$$

whereas for a 'free-slip' condition with consequently $\tau'_0 = 0$ N/m², Equation (4.8.13b) yields $v_0 = \bar{v}$ and thus, since for both $K'_{in} = 0$ and $K'_{log} = 0$, a vertical uniform flow profile with $v(z) = \bar{v}$ is found.

In the case of a realistic intermediate 'partial-slip' boundary, the reference shear stress τ'_0 can be described by:

$$\tau'_0 = \rho c_f v_0^2 \quad (4.8.16)$$

The reference velocity v_0 can, consequently, be computed from Equation (4.8.13b):

$$v_0 + \frac{c_f}{\mu} K'_0 v_0^2 = \bar{v} \quad (4.8.17a)$$

or for $c_f \neq 0$:

$$v_0 = \frac{\mu}{2 c_f K'_0} \left(\sqrt{1 + 4 c_f K'_0 \frac{\bar{v}}{\mu}} - 1 \right) \quad (4.8.17b)$$

Figure 4.28 shows an example of a longshore current profile for these three types of boundary conditions for $\mu = 0.04$ m/s, $\varepsilon_0 = 0.003$ m²/s, $d = 1$ m, $c_f = 0.02$ and $\bar{v} = 0.5$ m/s. The computed reference shear stresses amount to $\tau'_0 = 3.0$ N/m² for the 'partial slip' condition and the maximum of $\tau'_0 = 13.3$ N/m² for the 'no-slip' condition.

This plausible 'partial-slip' case yields a profile that considerably differs from the one that is found from a 'no-slip' assumption, although the latter might be used in analogy with open channel flow, see e.g. (Van Rijn, 1990). However, the presence of breaking waves makes that the assumption of a uniform profile over the water depth is much closer to reality than a 'no-slip' profile (Svendsen and Lorentz, 1989). The results of some detailed measurements by Visser suggest that this method yields velocity profiles that are qualitatively correct (Visser, 1984).

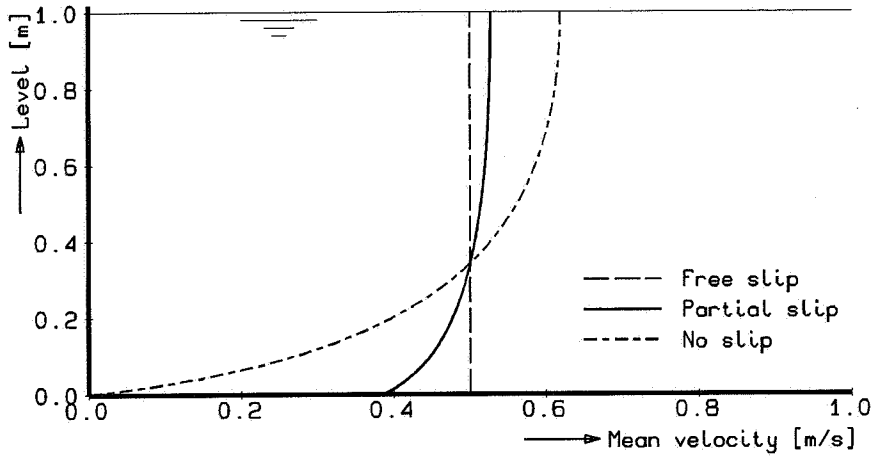


Figure 4.28 Example of longshore flow profile for three types of boundary conditions.

It is noted that the combination with the local cross-shore flow profile yields a three-dimensional profile, see e.g. (De Vriend and Ribberink, 1988; Svendsen and Lorentz, 1989).

Local longshore transport rate

The local longshore transport rate S_y at position x in the cross-shore profile can be computed from:

$$S_y = \int_{z=0}^d v(z) C(z) dz \quad (4.8.18)$$

in which $C(z)$ denotes the (time-averaged) sediment concentration profile as described thoroughly in Section 4.3.

In a first approach, assuming $v(z) = \bar{v}$, this transport rate can be assessed from:

$$S_y \approx \bar{v} \int_{z=0}^d C(z) dz = \bar{v} L_s \quad (4.8.19)$$

in which L_s denotes the total sediment load according to Equation (4.3.21). However, taking account of the vertical profile of $v(z)$, the precise magnitude of the transport can be computed by substitution of (4.8.7) and (4.3.19) in (4.8.18) and successive integration. Corresponding to the elaboration as presented in Section 4.5.4, this results in a longshore transport formulation according to:

$$S_y = C_0 [v_0 I_1' + K_{lin}' I_2' + K_{log}' I_3'] \quad (4.8.20)$$

in which C_0 denotes the reference concentration and the profile constants K_{lin}' and K_{log}'

are defined in Equation (4.8.8) and (4.8.9) respectively. The three integration constants I_1' (in m), I_2' (in m²) and I_3' (in m) are now defined according to (see Appendix):

$$I_1' = \frac{\varepsilon_0}{\mu} \frac{1}{K_1} \left[K_2'^{K_1} - 1 \right] \quad (4.8.21)$$

$$I_2' = \frac{\varepsilon_0}{\mu} \frac{1}{K_1} \left[K_2'^{K_1} \left(d - \frac{\varepsilon_0}{\mu} \frac{K_2'}{K_1+1} \right) + \frac{\varepsilon_0}{\mu} \frac{1}{K_1+1} \right] \quad (4.8.22)$$

$$I_3' = \frac{\varepsilon_0}{\mu} \frac{1}{K_1^2} \left[K_2'^{K_1} (K_1 \ln(K_2') - 1) + 1 \right] \quad (4.8.23)$$

in which the dimensionless constants K_1 and K_2' are defined by:

$$K_1 = 1 - w_s/\mu \quad (4.8.24)$$

$$K_2' = 1 + (\mu/\varepsilon_0)d \quad (4.8.25)$$

respectively.

4.8.4 Longshore transport gradients

An alongshore variation in longshore transport rate can be due to several causes, for example:

- Wave attack on a non-straight (curved) coastline;
- Alongshore variations in (longshore) currents in the case of a straight or non-straight coastline (gradients in tidal currents);
- Alongshore variations in wave attack on a straight or non-straight coastline (e.g. due to significant variations in cross-shore profiles);
- Transitions between different types of coastal structures (dikes, dunes).

The presence of these gradients will affect the cross-shore profile development and so have an effect on the ultimate amount of dune erosion. It is remarked that a preliminary assessment of such an effect is reported in (DELFT HYDRAULICS, 1983b). More details on the present elaboration are provided in (DELFT HYDRAULICS, 1990c).

Approach

In the following, the consequences of the first two causes for longshore transport gradients will be elaborated in more detail. Since a (positive) alongshore transport gradient is associated with a (positive) alongshore current gradient, this alongshore gradient is due to respectively:

- Increasing angle of wave attack (due to coastline curvature), resulting in increasing wave-driven longshore currents;
- Increasing alongshore water level gradient, resulting in increasing tide-driven longshore currents.

The magnitude of the longshore transport gradient is assessed by performing computations on a principal main ray as well as on a supplementary second ray. In the latter the angle of wave attack θ_0 or the alongshore water table gradient $d\zeta/dy$ (affecting the local alongshore tidal currents) could be mutually different from the conditions in the main ray. Consequently, the cross-shore distribution of the mean longshore current in these two rays will be different also.

Figure 4.29 shows an outline of this double-ray approach for a curved coastline as explained in the following.

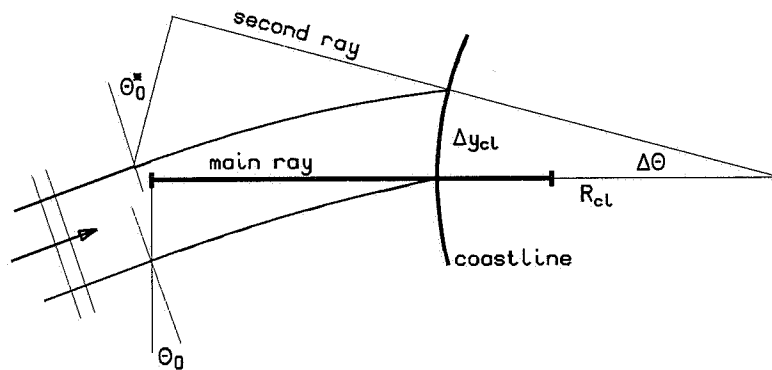


Figure 4.29 Schematic outline of double-ray approach for a uniform curved coastline.

Coastline curvature

The rate of coastline curvature is expressed in the rate of change in coastline orientation $\Delta \alpha$ (in degrees) per alongshore distance Δs .

The coastline radius R_{cl} is related to both $\Delta \alpha$ and length Δs of a specific coastline section, according to:

$$R_{cl} = \frac{360}{2\pi} \frac{\Delta s}{\Delta \alpha} \quad (4.8.26)$$

The magnitude of $\Delta \alpha$ should be determined for a coastline section with a length of about 100 m (TAW, 1984, 1990).

Consequently, the cross-shore distribution of the alongshore velocity in the supplementary second ray has to be computed for the hydraulic conditions which are valid in a coastline position which is situated at a coastline location $\Delta s = 100$ m further. The standard mutual distance between both rays is thus defined as $\Delta y_{cl} = 100$ m at cross-shore position $x = x_{cl}$.

In the case of a curved coastline, the local distance (being a function of the cross-shore position x) between both rays $\Delta y(x)$ can be computed from:

$$\Delta y(x) = \Delta y_{cl} \left(1 + \frac{x_{cl} - x}{R_{cl}} \right) \quad (4.8.27)$$

For a positive curvature, the mutual distance between both rays increases in offshore direction, whereas for straight coastline, with $R_{cl} = \infty$, this yields $\Delta y(x) = \Delta y_{cl}$. The shift in the angle of wave attack $\Delta \theta_0$ (at the seaward boundary) equals:

$$\Delta \theta_0 = \frac{360}{2\pi} \frac{\Delta y_{cl}}{R_{cl}} \quad (4.8.28)$$

and equals the shift in the coastline angle $\Delta \alpha$ by definition.

Longshore flow gradient

Using previously introduced double-ray approach, the local alongshore flow gradient $d\bar{v}/dy$ can now be estimated from:

$$\frac{d\bar{v}}{dy}(x) = \frac{\bar{v}^*(x) - \bar{v}(x)}{\Delta y(x)} \quad (4.8.29)$$

in which:

\bar{v}	mean alongshore velocity (in position x)	(m/s)
\bar{v}^*	mean alongshore velocity in the supplementary ray	(m/s)
Δy	the local distance between both rays	(m)

Longshore transport gradient

The actual longshore transport gradient could, according to Equation (4.8.29), be computed from:

$$\frac{dS_y}{dy}(x) = \frac{d\bar{v}}{dy}(x) L_s \quad (4.8.30)$$

in which L_s denotes the suspended sediment load as defined in Equation (4.3.25). However, a better estimate is obtained by:

$$\frac{dS_y}{dy}(x) = \frac{S_y^*(x) - S_y(x)}{\Delta y(x)} \quad (4.8.31)$$

in which:

S_y	longshore transport (in position x)	(m ³ /m/s)
S_y^*	longshore transport in the second ray	(m ³ /m/s)
Δy	the mutual local distance between both rays	(m)

The latter approach is used in the computational program.

Sediment balance equation

In order to calculate the bottom profile developments, the continuity equation for the sediment has to be satisfied. Elaboration of the complete balance equation for a curved coast can be shown to result in:

$$\frac{dz_b(x)}{dt} = \frac{-1}{(1-p)} \left[\frac{dS_x(x)}{dx} + \frac{S_x(x)}{R_{cl} \left(\frac{x-x_{cl}}{R_{cl}} - 1 \right)} + \frac{dS_y(x)}{dy} \right] \quad (4.8.32)$$

in which R_{cl} denotes the coastline radius and x_{cl} the position till where this radius is measured.

The second term on the right side is due to the 'pie effect'. Since its contribution is negligible in most cases, Equation (4.8.32) can be simplified to:

$$\frac{dz_b(x)}{dt} = \frac{-1}{(1-p)} \left[\frac{dS_x(x)}{dx} + \frac{dS_y(x)}{dy} \right] \quad (4.8.33)$$

For $dS_y(x)/dy = 0$ the original sediment balance equation, viz. Equation (4.7.11), is found.

Incorporating above described relations in the computational program yields the opportunity to compute the impact of longshore transport gradients on the profile development. Some examples of related applications are presented in Section 8.6.

4.8.5 Summary and conclusions

By incorporating a best estimate of the physical processes accountable for the effects of storm surge conditions on the development of the cross-shore profile in a mathematical model, the extension of the model for related processes seems allowable.

Structures

The impact of a structure in the coastal profile is modelled by an adaption of the computational routine for the assessment of the bottom changes per time step. Various examples of the impact of revetments on the development of the cross-shore profile will be presented in Chapter 7, giving a comparison between measured and computed results.

Longshore transport

The direct coupling of cross-shore and longshore processes follows in fact the basic approach for longshore transport computation. In Section 6.7 a comparison is given between the outcome of both the present model and some other longshore transport formulae (Bijker, Van Rijn and Bailard).

Longshore transport gradients

The effect of an alongshore gradient on the transport rate is determined using a double ray approach. The accompanying effect on the local sediment balance equation is computed from the local mutual transport deviation and ray spacing. Some examples of the results of computations are presented in Section 8.6.

5 CALIBRATION

5.1 Introduction

5.1.1 Internal and external process parameters

For calibration and verification purposes, two groups of process parameters have been identified, namely:

- Internal process parameters;
- External process parameters.

The first group forms the basic input for the transport computation module of the mathematical model, whereas the second set is essentially related to specific process results. Examples of internal parameters are the sediment concentration at the reference level and the vertical distribution of turbulent mixing. The amount of erosion above storm surge level after a specific storm event can be seen as an example of an external result of the process involved.

It is noted that verification of the model, as will be discussed in Chapter 6, will be essentially based on a number of 'external' process results, such as profile development and the amount of dune erosion above the maximum surge level.

In the following, the calibration of the transport model, viz. the specification of parameters introduced in Chapter 4, will be elaborated in more detail. However, prior to this the calibration phases and procedure will be outlined briefly.

5.1.2 Calibration phases

Calibration of the cross-shore transport model is divided into two successive steps, namely:

- Initially, a basic calibration;
- Finally, an overall calibration.

Firstly, the basic calibration of the dynamical model is carried out for the 'internal' process parameters, in order to calibrate the parameters which determine the rate of local transport according to the formulations as derived in the previous sections, viz. Section 4.3 through 4.5. The basic idea behind this approach is that one should 'penetrate' as deep as possible in the transport process by describing the basic parameters involved, viz. by tuning its governing parameters ('low-level' tuning). It is noted that the assessment of the relations

describing the dependency of the hydraulic conditions required the development of some additional formulations. For the sake of convenience, nevertheless, these elaborations are denoted as calibration also.

The overall calibration ('high-level' tuning) is restricted to an additional tuning of the effect of the integrated cross-shore transport distribution. This actual calibration is performed in order to adjust the ultimate profile development.

5.1.3 Calibration procedure

The two-phase calibration procedure which has been followed is presented schematically in Figure 5.1. The sections in which the successive calibration phases will be discussed, are given on the left hand side in this figure also for the sake of convenience.

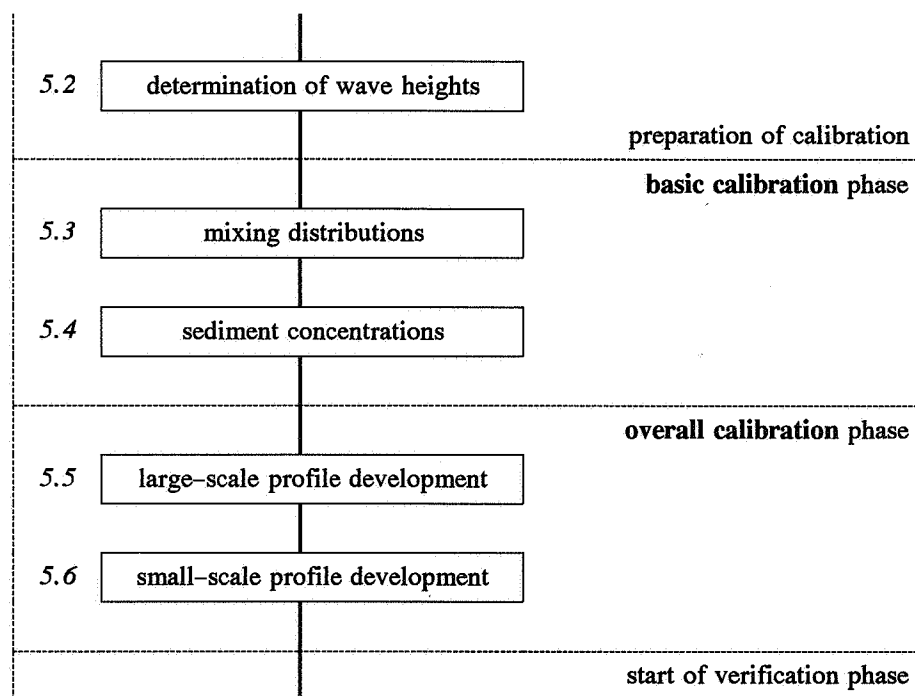


Figure 5.1 Outline of the applied calibration procedure.

The internal transport formulations as described in Chapter 4 are calibrated by the use of a great number of simultaneously measured concentration and velocity profiles during storm surge conditions which were conducted in large-scale model tests, viz. the H298-I-test series (DELFT HYDRAULICS, 1987a).

Since for this initial basic calibration the relevant parameters (for example the concentration C_0 and mixing gradient μ) have to be related to the local hydraulic conditions in some way,

these conditions have to be assessed first. The hydraulic conditions are determined by the use of the mathematical wave-height decay model ENDEC. Conclusively, the preceding step has to be the additional calibration of the wave-height decay model as described briefly in Section 4.7. The outcome of this phase are summarized in Section 5.2.

Next the internal process parameters are related to the computed hydraulic conditions in the first basic calibration stage. The proposed relations and accompanying calibration results on the mixing rates and suspended sediment concentration are provided in Section 5.3 and 5.4 respectively. The derived relations cover a great range of hydraulic and geometric conditions, although the bottom material unfortunately is the same in all cases.

The final calibration consists basically of the addition of an overall transport factor which reduces or increases the computed transport rate by a certain factor. In the case of successful former calibration phases, this additional correction should in principle be minor. Initially, this transport correction factor is assessed for a large-scale model test as discussed in Section 5.5.

Since the large-scale tests have been conducted only for one particular sediment diameter, the assumed relative effect of divergent sand characteristics is calibrated separately by mutual comparison of computed and measured profile developments in a similar small-scale model test (see Section 5.6).

A preliminary validation of the formulations is presented in Section 5.7, by comparing computed and measured concentration profiles and secondary flow profiles. A more comprehensive verification is elaborated in Chapter 6.

5.2 Wave heights

5.2.1 Introduction

The wave heights in the flume used, viz. DELFT HYDRAULICS' Scheldeflume or Deltaflume, have been measured for each of the tests performed. These measurements have been conducted in a number of distinct positions, viz. near the wave board and in several positions on the near-shore in the flume.

This wave height decay along the flume has to be assessed in more detail in order to determine the local hydraulic conditions present during the execution of a particular measurement at a specific position (see Section 5.3 and 5.4).

This assessment is also needed in order to obtain an accurate estimate of the wave height at the wave board position. The latter will be used as a boundary condition for the verification runs of the transport model (see Chapter 6).

5.2.2 Objective and approach

The objective of this calibration procedure is to:

- Determine the best fit of the wave height decay along the flume;
- Assess an optimal calibration of parameters which control the wave-height decay process;
- Compute the pertaining deep water condition (or wave height near the wave board);
- Compute the local hydraulic conditions at the time of a particular measurement.

More details on subsequent items are presented in the following.

5.2.3 Fit of wave-height decay

The wave-height decay along the flume depends both on the input on the seaward boundary and the loss in energy during wave propagation in the flume. For a particular wave height at the 'seaward' boundary, the accompanying wave height decay has been compared with the results of measured wave heights. From this a modified incoming wave height at deep water can be derived.

A schematic overview of the profiles is presented in Figure 5.2.

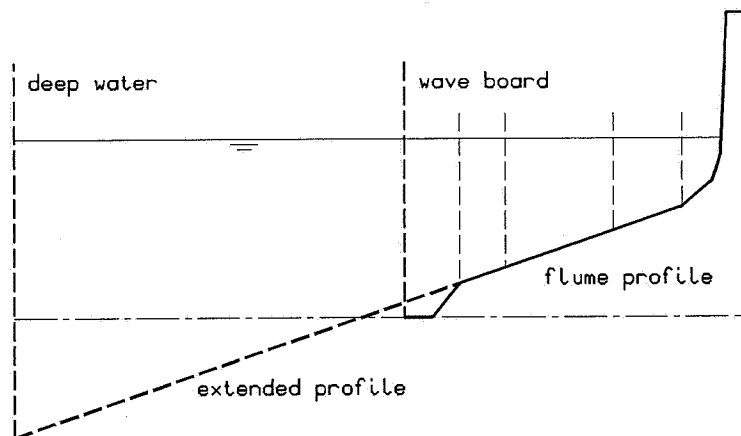


Figure 5.2 Schematic example of profiles used for the wave-height decay fit procedure.

The following successive steps were performed:

- 1) Extrapolate the uniform foreshore slope up to very deep water, say -30 m below reference level in prototype (in this way a decent adjustment of the individual wave heights to the actual bottom slope is guaranteed);
(It is noted that this step is only required if the apparent deep water condition has to be assessed);
- 2) Assess a first (or revised) estimate of the incoming (input) wave height at the seaward boundary H_{s0} ;
- 3) Compute the accompanying wave height decay along the (extended) flume;
- 4) Determine the relative deviation R_i of measured and computed wave heights ($H_{sm,i}$ and $H_{sc,i}$ respectively) for each measurement according to:

$$R_i = \frac{H_{sc,i} - H_{sm,i}}{H_{sc,i}} \quad (5.2.1)$$

- 5) Compute the squared sum of R_i of all N measurements;
- 6) Repeat from step 2) until a minimum for this sum is found;
- 7) Compute for this best fit both the average relative deviation \bar{R} and the standard deviation σ according to:

$$\bar{R} = \frac{1}{N} \sum_{i=1}^N |R_i| \quad (5.2.2)$$

and:

$$\sigma^2 = \left[\sum_{i=1}^N (R_i)^2 - \frac{1}{N} \left(\sum_{i=1}^N R_i \right)^2 \right] / (N - 1) \quad (5.2.3)$$

respectively, this to quantify the goodness of the fit.

An example of the result of this fit procedure (using standard values for the calibration constants as discussed in the next section) for a large-scale model test is given in Figure 5.3. The average relative deviation for all the tests used for the model development amounts to only 3.1 % (Steetzel, 1990b).

It is remarked that the actual deep water wave height (at 20 m below datum) is 2.24 m in the model and $H_{s20} = 11.2$ m in prototype and is well over the original meant value of $H_{s20} = 7.0$ m at the -20 m depth contour (COW, 1982). For more details on this dilemma, reference is made to (Steetzel, 1990b).

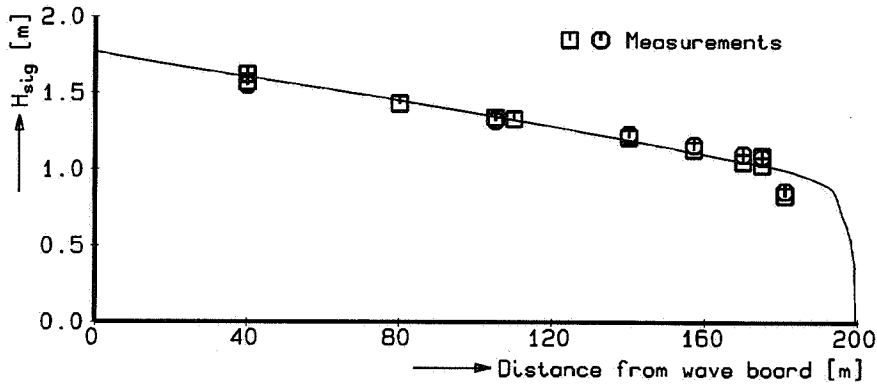


Figure 5.3 Result of the fit procedure for test T2 of the M1263-III-test series.

5.2.4 Assessment of optimal calibration

As noted before, the actual computed wave height decay depends also on the local breaking process. As presented in Section 4.7.4, the formulations for wave breaking depend on four parameters, namely:

- The factor α ;
- The breaker index γ ;
- The maximum wave steepness S_{max} ;
- The friction factor c_f .

The first three parameters control the energy loss due to wave breaking D_b , see also Equation (4.7.7), since:

$$D_b = \frac{1}{4} \rho g \alpha Q_b f_p H_m^2 \quad (5.2.4)$$

in which Q_b denotes the portion of breaking waves, f_p the peak frequency ($= 2\pi/T_p$) and H_m the maximum breaking wave height (see also Equation (4.7.9)), according to:

$$H_m = \frac{2\pi S_{max}}{k} \tanh \left[\gamma \frac{kd}{2\pi S_{max}} \right] \quad (5.2.5)$$

For shallow water, viz. $kd \downarrow 0$, the maximum H_m -value of $H_m = \gamma d$ is found, whereas for deep water ($kd \rightarrow \infty$) this maximum wave height is limited by the maximum wave steepness, viz. $H_m = (2\pi/k)S_{max}$.

In this section, the sensitivity of these constants is investigated by comparing the computed wave height decay for a specific setting with a series of measured wave heights. For

comparison the comparable results of three small-scale model tests have been used, viz. test T04, T11 and T12 of research programme M1819-I (DELFT HYDRAULICS, 1982d).

The α -factor in the breaker function

Basically, the α -factor which is of the order of 1, corrects for the inadequacy of the theoretical wave-breaking model. As can be seen from Equation (5.2.3), a larger magnitude results in an increased dissipation rate and so in a reduced wave height in the breaker zone. The computed standard deviation for a range of α -values is presented in Figure 5.4.

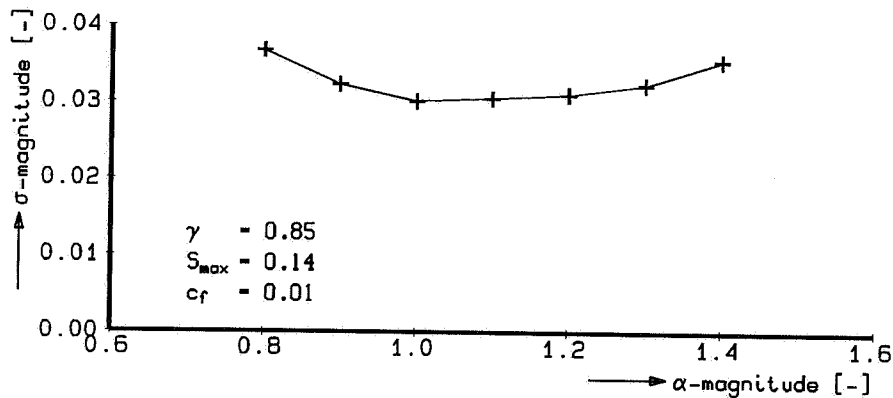


Figure 5.4 Standard deviation for a range of α -values.

Apparently, $\alpha \approx 1.0$ provides the best correlation.

Breaker index γ

The breaker index γ controls the actual wave height in the breaker zone to a large extent. A larger magnitude implies a larger (H_{sig}/d) -ratio and thus a higher wave. The computed standard deviation for a range of γ -values is presented in Figure 5.5.

The standard value of $\gamma = 0.85$ provides the best result (for $S_{max} = 0.14$).

Maximum wave steepness S_{max}

As can be readily seen from Equation (5.2.2), the breaker index and the maximum wave steepness are mutually related. In Figure 5.5 both the results for $S_{max} = 0.12$ and 0.14 are presented, whereas the latter provides the best results, viz. the lowest σ -magnitudes.

Friction factor c_f

Basically, the friction factor is definitely not a calibration factor. Besides, the effect on the wave height decay in the breaker zone is rather small, since energy losses are merely controlled by the dominant wave breaking processes for the conditions studied.

The results for a range of c_f -values are presented in Figure 5.6, showing hardly any differences in the computed standard deviation. Apparently the best fit is of the order of 0.01 to 0.02.

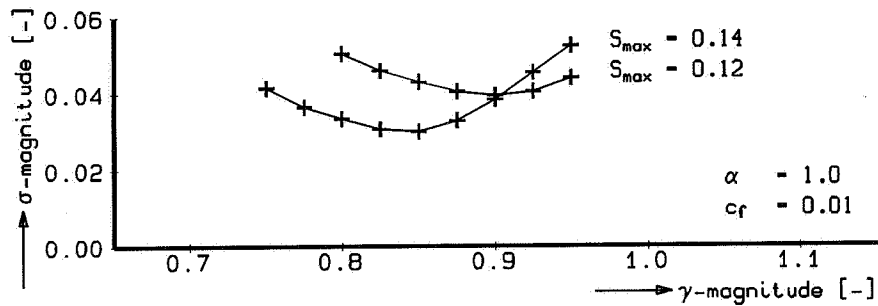


Figure 5.5 Standard deviation as a function of breaker index for two friction factors.

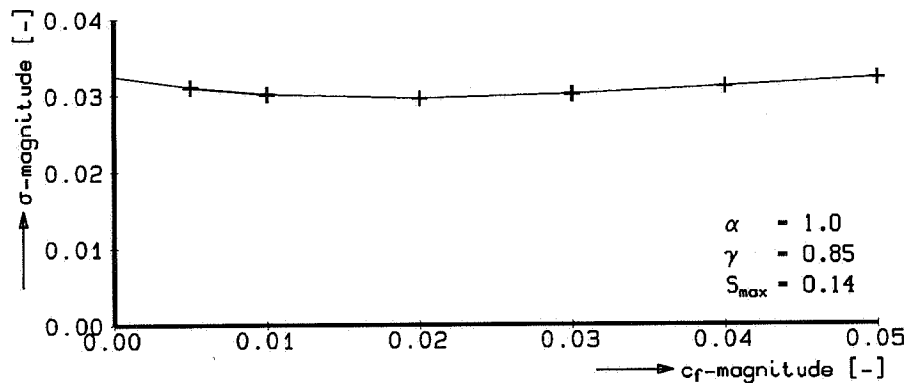


Figure 5.6 Standard deviation for a range of friction factors.

The results of the calibration indicate that the standard values of the constants related to the wave breaking process indeed provide the best results. A more comprehensive elaboration of previous calibrations is presented in (Steetzel, 1990b).

5.2.5 Accompanying deep water conditions

As a result of the fit procedure a reliable estimate is obtained of the apparent deep water condition for each of the model tests performed, viz. the actual wave input at the position of the wave board.

From all the dune erosion tests considered it was concluded that the actual wave input, especially in the large-scale model tests, was far beyond the maximum condition which

could be expected in nature. This contradiction was due to the assumption from former days that the wave height decay could be described adequately by linear wave theory. For more details on the latter contradiction reference is made to (Steetzel, 1990b).

5.2.6 Local hydraulic conditions

By following the previously described procedure a reliable estimate of the cross-shore distribution of the hydraulic conditions can be obtained, by using the deep water or wave board wave height as a boundary condition.

In this way these local hydraulic conditions come available for every combined concentration and flow measurement, yielding an opportunity to relate a measured quantity to the (computed) governing hydraulic condition. A thorough attempt to do so for the parameters describing the mixing distribution and the reference concentration is presented in the following sections.

5.3 Mixing distribution

5.3.1 Introduction

The local vertical distribution of the suspended sediment and the shape of the time-averaged velocity profile depend both on the vertical distribution of a mixing coefficient $\varepsilon(z)$. Here it is assumed that the mixing coefficients for sediment and fluid are the same.

Based on the analyses presented in Section 4.3.3, this mixing profile can, at least for the special case of intensive breaking waves studied here, be characterized by:

$$\varepsilon(z) = \varepsilon_0 + \mu z \quad (5.3.1)$$

in which both the reference mixing coefficient at the bed level ε_0 and the accompanying vertical mixing gradient μ have to be related to the local hydraulic conditions.

An additional, related parameter, is mixing at the mean trough level (at $z = d_t$), which is defined as:

$$\varepsilon_t = \varepsilon_0 + \mu d_t \quad (5.3.2)$$

It should be remarked that the mixing rate is commonly expressed in terms of a product of a characteristic velocity scale U and a characteristic length scale L , viz. $\varepsilon = UL$.

5.3.2 Reference mixing coefficient

In the case of non-breaking waves, the mixing rate near the bed level is related to the size of the bottom irregularities and the near bottom velocity (say u_{rms} -velocity). If this also holds for this case, the reference mixing coefficient at the bed level would follow an

analogous relation according to:

$$\varepsilon_0 = \mathbf{F}\{D_{50}\} u_{rms} \quad (5.3.3)$$

however, based on the available data, a rather crude relation according to $\varepsilon_0 = \mathbf{F}\{D_{50}\}$ seems just as good as Equation (5.3.3). Moreover, applying traditional formulations to estimate the ε_0 -magnitude yields a significant under-estimation of former determined values.

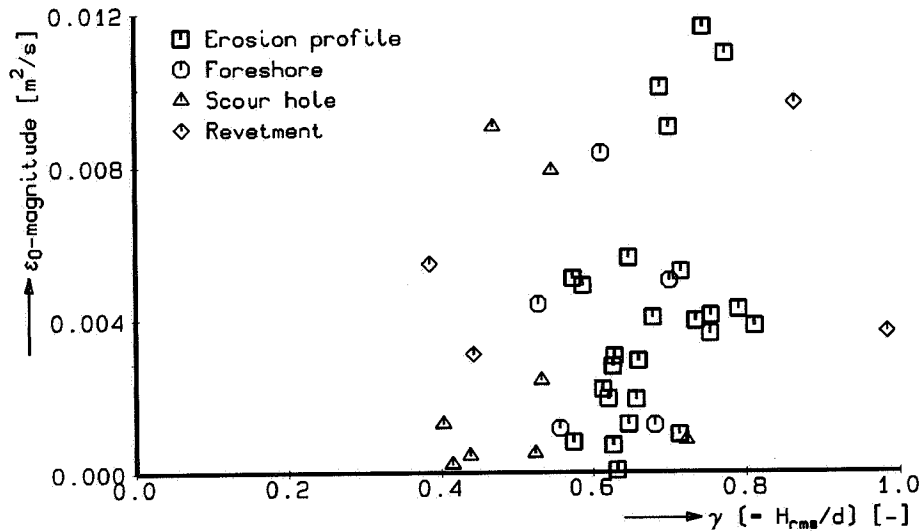


Figure 5.7 Computed reference mixing as a function of estimated breaker index.

Figure 5.7 shows the relation between the estimated reference mixing coefficient ε_0 and local breaker index γ or (H_{rms}/d) -ratio.

Although, again, no outstanding correlation is found the ε_0 -magnitude is assumed to be described by:

$$\varepsilon_0 = \mathbf{F}\{D\} \mathbf{F}\{\gamma\} u_{rms} \quad (5.3.4)$$

in which $\mathbf{F}\{\gamma\}$ denotes a dimensionless function describing the (additional) relative impact of the breaker index.

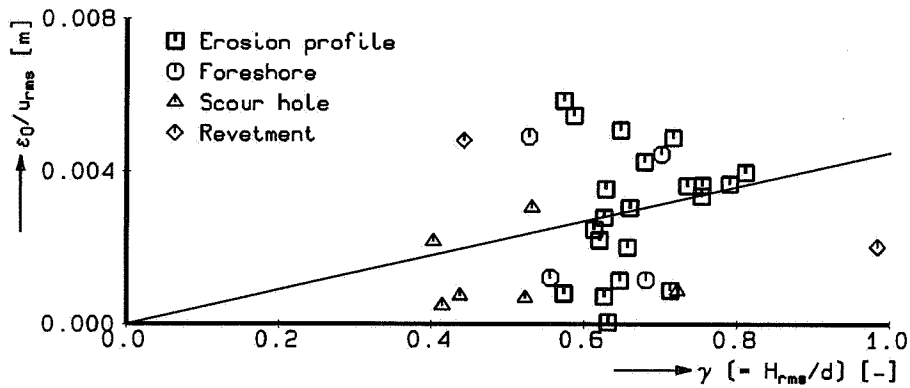


Figure 5.8 Computed reference mixing/velocity ratio as a function of estimated breaker index.

From Figure 5.8, showing the (ε_0/u_{rms}) -ratio as a function of the estimated breaker index, is was concluded that:

$$(\varepsilon_0/u_{rms}) = \mathbf{F}\{D\} \gamma \quad (5.3.5)$$

seems a feasible relation.

Since in the case of breaking waves the sand bottom in the breaker zone will be more or less flat (sheetflow conditions) and the thickness of the bottom layer is related to the present sand material, the $\mathbf{F}\{D\}$ -function is chosen to be proportional to the sediment diameter according to:

$$\mathbf{F}\{D\} = K_e D_{50} \quad (5.3.6)$$

in which K_e denotes a dimensionless constant. Its magnitude is derived from a data fit yielding $K_e = 21.9$ (using $D_{50} = 225 \mu\text{m}$).

Finally, the reference mixing at the bed level ε_0 is defined by:

$$\varepsilon_0 = K_e D_{50} u_{rms} \gamma \quad (5.3.7)$$

It is noted that this relation is apart from the introduced specific effect of the breaker index comparable with the relations presented by other researchers in the field of modelling (Van Rijn, 1989).

5.3.3 Mixing gradient parameter

The vertical profile of the mixing coefficient largely depends on the mixing gradient parameter μ . With Equation (5.3.2) the mixing rate ε_t can be seen as a measure for mixing at the wave trough level. Figure 5.9 shows the dependency of this ε_t -magnitude according to Equation (5.3.2) of the breaker index γ .

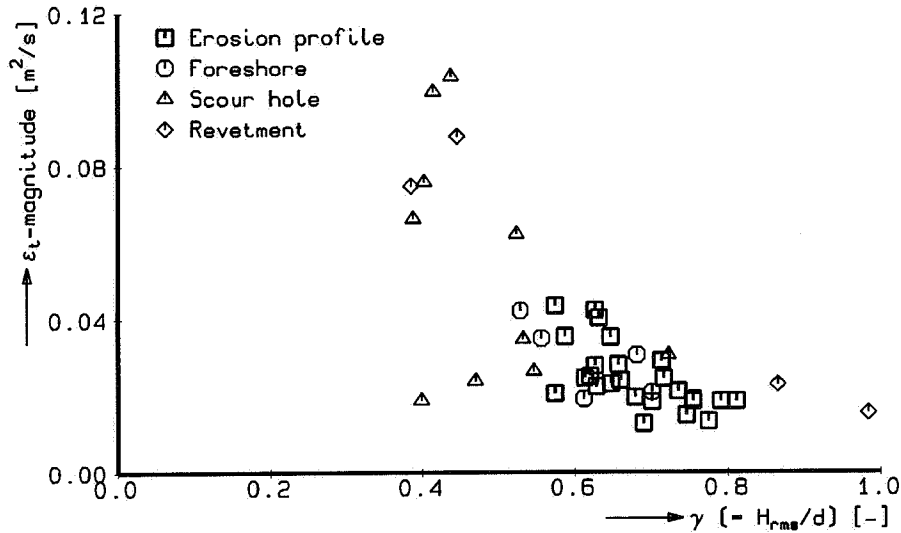


Figure 5.9 Computed mixing rate at trough level as a function of estimated breaker index.

As can be seen, increased breaking (i.e. larger H_{rms}/d -values) leads to decreased mixing rates at the trough level.

The relation for the mixing increase rate μ itself shows a similar tendency as can be seen from Figure 5.10.

Mixing under waves is commonly assumed to be proportional to the product of wave celerity c and water depth d , viz. $\varepsilon :: cd$ (Stive and Wind, 1986).

Using $\mu \approx \varepsilon/d$ yields $\mu :: c$, leading to the relation between the μ/c -ratio and the breaker index γ to be examined, namely:

$$\mu = \mathbf{F}\{\gamma\} c \quad (5.3.8)$$

in which $\mathbf{F}\{\gamma\}$ denotes a function which accounts for the impact of the breaker index.

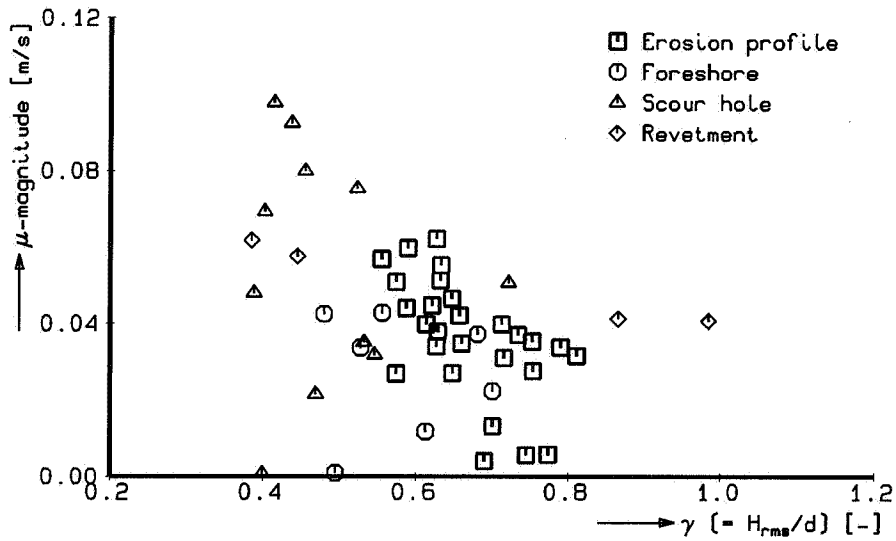


Figure 5.10 Computed mixing increase rate μ as a function of estimated breaker index.

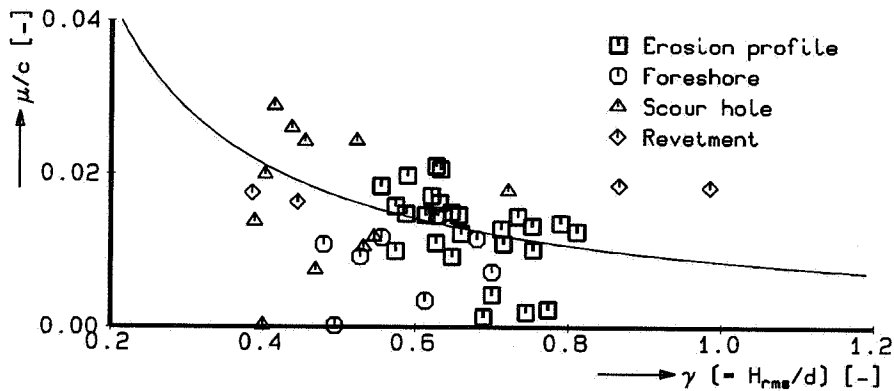


Figure 5.11 Computed μ/c -ratio as a function of estimated breaker index.

From Figure 5.11 it was concluded that a feasible relation for this breaking index effect may be:

$$F\{\gamma\} = K_{\mu} / \gamma \quad (5.3.9)$$

in which K_{μ} denotes a dimensionless constant to be derived from the available data, yielding $K_{\mu} = 8.5 \cdot 10^{-3}$ as a final result.

This dependency, i.e. Equation (5.3.9) showing $\mu \propto \gamma^{-1}$, is also found by elaboration of the $\varepsilon(z)$ -relations presented by Songvisessomja and Samarasinghe (1988). They re-analyzed concentration measurements carried out by Nielsen (1984) (see (Steetzel, 1990a) for more details).

Conclusively, the mixing gradient parameter μ is defined by:

$$\mu = K_{\mu} c / \gamma \quad (5.3.10)$$

in which the dimensionless constant equals $K_{\mu} = 8.5 \cdot 10^{-3}$.

5.3.4 Conclusions

It is admitted that, due to a considerable scatter in the available data, previous relations are not based on solid arguments, i.e. an outstanding data fit. However, the overall tendency which corresponds more or less with traditional relations, is assumed to be sufficiently reliable to be used for the (initial) calibration of the transport model.

Furthermore, it is clear that if additional data on mixing in breaking waves become available a re-calibration may be considered. For the time being, however, the presented relations have been used for the construction and utilization of the cross-shore transport model.

5.4 Sediment concentrations

5.4.1 Introduction

Although the mechanisms responsible for the process of sediment suspension under intensive breaking waves are already qualitatively described by numerous researchers, no workable formulae for its quantification appeared to be present, see e.g. (Kana, 1979).

In the case of non-breaking waves the sediment concentration is often associated with the near-bottom velocity and the accompanying bottom shear stresses. For breaking waves, however, the amount of suspension and thus the reference concentration also is probably for the greater part related to the turbulence level generated from the breaking waves, see e.g. (Horikawa et al., 1982; Nadaoka and Kondah, 1982; Sato et al., 1990).

5.4.2 General considerations

Based on detailed field observations Nadaoka et al. (1988) presented a qualitative description of the processes involved in the processes of sediment suspension. Due to the wave breaking process a certain amount of turbulent kinetic energy is released from the

upper zone. Depending on the way of breaking (say the magnitude of the local breaker index) a specific fraction of this energy reaches the bottom and causes an increase in the near bottom sediment suspension quantity. Moreover, in spilling and intermediate breakers the amount of suspended sediment is relatively small compared to the case of plunging waves (Sato et al., 1990).

Finally, the amount of suspension (i.e. the reference concentration) has to be related to both the intensity of wave breaking (energy loss due to wave breaking) and the way the individual waves break (breaker index). An attempt to do so is elaborated in the following.

5.4.3 Effect of wave breaking intensity

A thorough analysis of a large number of imaginable relations, as reported in more detail in (Stetzel, 1990a), showed that the most promising correlation with the reference concentrations C_0 was found by using the intensity of wave breaking as a governing parameter. A relation with the near-bed orbital (peak) velocity for example, did not account for the large spreading in the concentration magnitudes.

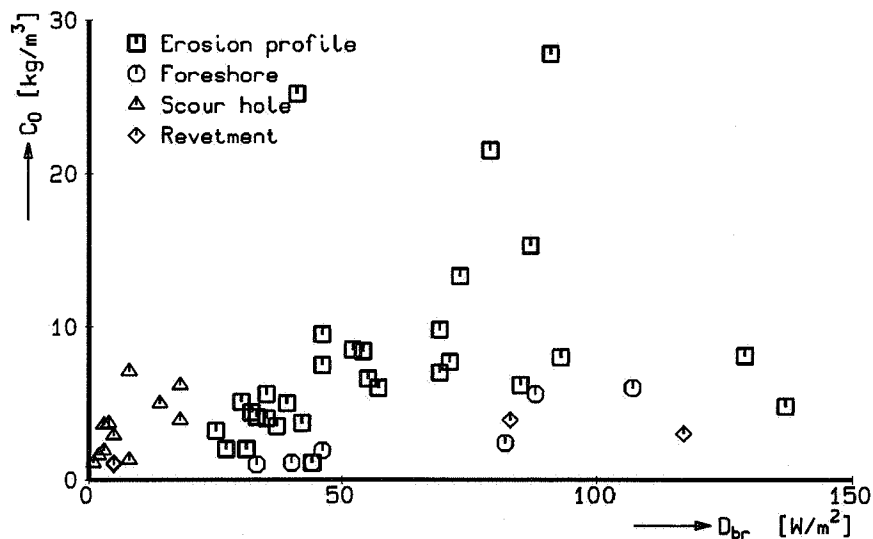


Figure 5.12 Relation between measured reference concentration and computed (breaking) dissipation rates.

Figure 5.12 shows the relation between calculated reference concentration from the measurements (see Section 4.3 for more details about its assessment) and the computed dissipation rate (due to wave breaking). The latter is computed from the best fit of the measured wave-height decay (see Section 5.2.6).

Although the correlation is far better than was found by using local u_{rms} - or u_{sig} -velocities, some improvement seemed welcome. This was achieved by using a modified dissipation rate and by introducing the effect of the breaker index.

In the case of the dissipation term, a distinction has been made between the dissipation source term in the wave energy balance equation due to wave breaking, i.e. D_{br} , and the dissipation of the turbulent kinetic energy D_t .

Consider the (simplified) wave energy balance equation, viz.:

$$\frac{dP}{dx} + D_{br} = 0 \quad (5.4.1)$$

in which D_{br} denotes the energy dissipation due to wave breaking (in $W/m^2 = kg/s^3$) and P ($= E c_g$) the energy flux (in $J/s/m = kg/m^3s$). The dissipation term in this equation can be regarded as a production term for the turbulent energy. It takes some time to convert the organized potential and kinetic energy generated from the breaking waves into a more small-scale dissipative turbulent motion. The turbulent energy dissipation lags behind the large-scale dissipation accountable for the wave height decay.

Considering the mean turbulent energy flux P_t according to:

$$\frac{dP_t}{dx} + D_t = D_{br} \quad (5.4.2)$$

in which the production term on the right side equals the energy loss according to Equation (5.4.1). The turbulent dissipation itself is described by, see e.g. (Launder and Spalding, 1972):

$$D_t = \rho \bar{K}^{3/2} \quad (5.4.3)$$

in which \bar{K} denotes the depth-averaged, turbulent energy per unit of mass (in $J/kg = m^2/s^2$).

The mean turbulent energy flux P_t is computed from:

$$\frac{dP_t}{dx} = \rho \frac{d}{dx}(c d \bar{K}) \quad (5.4.4)$$

where c denotes the wave celerity and d the water depth.

Combination of former equations and successive elaboration in an iterative computational procedure yields a cross-shore distribution of the turbulent dissipation term. More details about this can be found in (Steetzel, 1990a; Roelvink and Stive, 1989).

A relation of the reference concentration C_0 with the computed turbulent dissipation is presented in Figure 5.13. As can be observed from a mutual comparison between former two figures, a rather correct correlation is found in the latter case (so $C_0 \propto D_t$). As mentioned before, some further improvement is found by incorporation the effect of the way of breaking as elaborated in the next section.

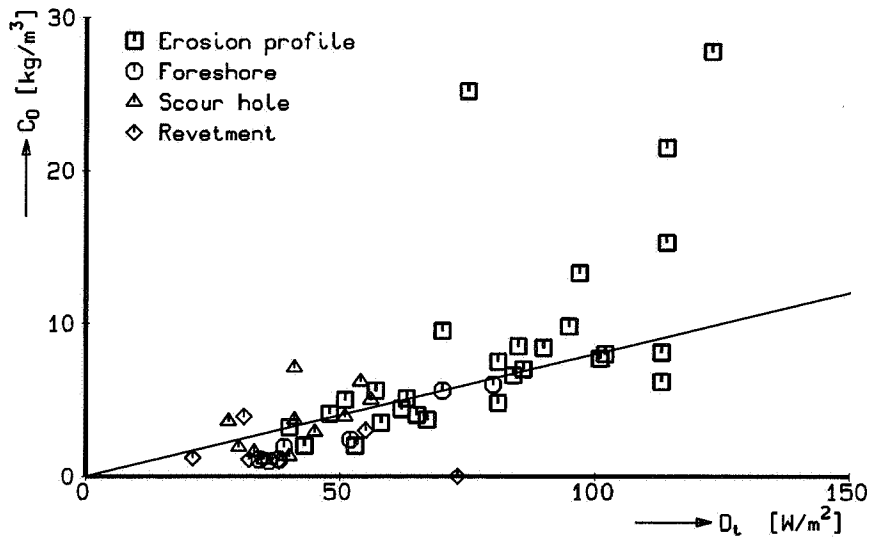


Figure 5.13 Relation between measured reference concentration and computed (turbulent) dissipation rates.

5.4.4 Effect of way of wave breaking

Individual waves can break in a different manner, ranging from spilling (for low γ) to plunging (for large γ -magnitudes). It is obvious that plunging waves provide a relatively larger impact on the process of sediment suspension.

The magnitude of the depth- and time-averaged turbulent energy per unit of mass \bar{K} (in m^2/s^2) can be computed from Equation (5.4.3), yielding:

$$\bar{K} = \left(\frac{D_t}{\rho} \right)^{2/3} \quad (5.4.5)$$

In order to take account for the effects of the way the waves are breaking, a relation between the near-bottom magnitude of the turbulent energy k_0 (in m^2/s^2) and the total turbulent energy \bar{K} is assumed, according to:

$$k_0 = \bar{K} F_k(\gamma) \quad (5.4.6)$$

in which the $F_k(\gamma)$ -function has to be specified.

Although the vertical distribution of the turbulent energy $k(z)$ is not known in detail, a negative exponential distribution is assumed to provide a feasible first-order characterization, see e.g. (Perigrine and Svendsen, 1978). So:

$$k(y) = k_d \exp\left(\frac{-y}{y^*}\right) \quad (5.4.7)$$

in which y denotes the level with respect to the mean water level (y positive downward with $y = 0$ at the mean water level and $y = d$ at the bottom).

In this expression k_d denotes the magnitude of k at the mean water level and y^* symbolizes a characteristic penetration depth. This penetration depth is assumed to be proportional to the local wave height according to:

$$y^* = \alpha_k H_{rms} \quad (5.4.8)$$

in which α_k is a dimensionless constant.

Since the depth-integrated magnitude of $k(y)$ should agree with the depth-averaged value \bar{K} , viz.:

$$\bar{K} = \frac{1}{d} \int_d k(y) dy \quad (5.4.9)$$

the accompanying $F_k(\gamma)$ -function can, using $d/y^* = (\alpha_k \gamma)^{-1}$, be shown to result in:

$$F_k(\gamma) = \left[\alpha_k \gamma \left(\exp\left(\frac{1}{\alpha_k \gamma}\right) - 1 \right) \right]^{-1} \quad (5.4.10)$$

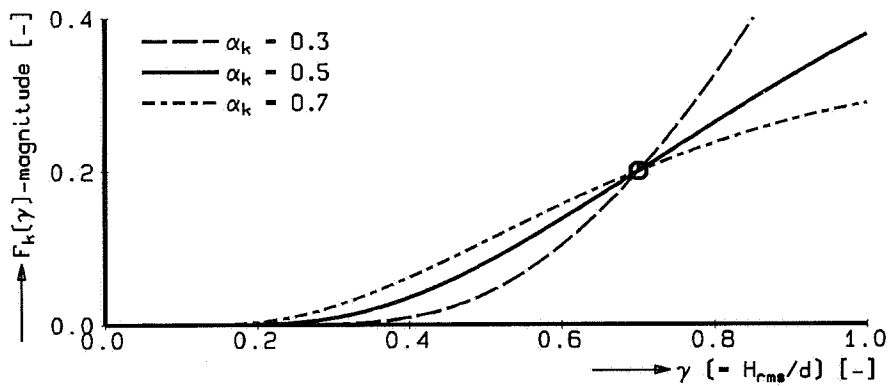


Figure 5.14 Assumed behaviour of breaking-function.

Figure 5.14 shows the behaviour of this relation for a number of α_k -values.

In the case of spilling breakers (say $\gamma < 0.3$), wave breaking does not contribute to the reference concentration, since $F_k(\gamma) \downarrow 0$ in that case.

Figure 5.15 shows a comparison with the actual measurements.

Apart from the scour hole data, the overall tendency is explained roughly for $\alpha_k \approx 0.5$ (the solid line).

It should be remarked that using former relations will yield an under-estimation of the

concentrations in the scour hole.

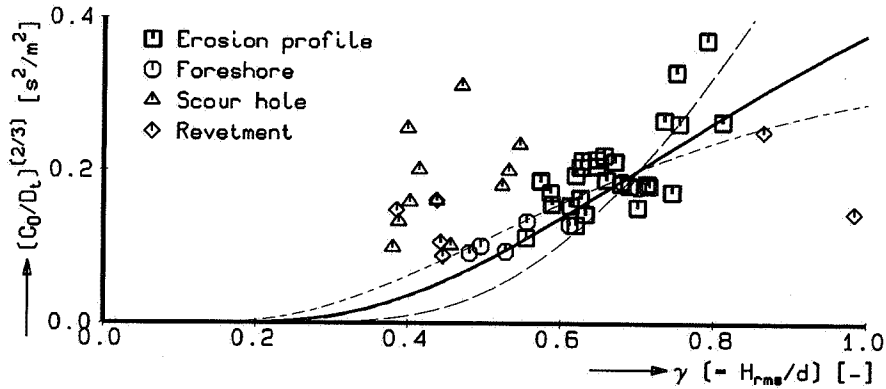


Figure 5.15 Dependency of estimated breaker index.

5.4.5 Final formulation

The reference concentration C_0 is related to both the intensity of breaking and the way of breaking (spilling or plunging) according to:

$$C_0 = \rho_s K_c F_D \left(\frac{\rho}{\tau_{cr}} \right)^{\frac{3}{2}} F_k (\gamma | \alpha_k)^{\frac{3}{2}} \left(\frac{D_t}{\rho} \right) \quad (5.4.11)$$

in which:

- K_c a dimensionless constant (-)
- F_D a dimensionless function related to the sediment diameter (-)
- τ_{cr} the critical shear stress (N/m²)
- F_k a function which describes the effect of the way the waves break (-)
- D_t the dissipation of turbulent kinetic energy (W/m²)

The critical shear stress is defined according to:

$$\tau_{cr} = \Theta_{cr} (\Delta - 1) \rho g D_{50} \quad (5.4.13)$$

in which the critical Shields parameter amounts to $\Theta_{cr} \approx 0.05$.

Apart from the dimensionless calibration coefficient K_c and the dimensionless F_D -function, the parameters come from previous elaboration and consistency of dimensions.

It is undeniably true that the dependency on the sediment diameter is probably not yet taken into account correctly (or at least completely) in this expression. Since the data used here are only valid for one specific diameter, viz. $D_{50} = 225 \mu\text{m}$, this seems to be a problem.

In order to avoid this, an additional dimensionless F_D -function is introduced in Equation (5.4.11) which is described by:

$$F_D = \left(\frac{0.000225}{D_{50}} \right)^{\alpha_D} \quad (5.4.12)$$

and takes into account the effect of the sediment diameter as far it is as not incorporated in the other formulations. The magnitude of the power α_D in this equation will be discussed later (see Section 5.6). For the moment, however, the precise power is not important since for the present test series the governing ratio equals 1 by definition and thus $F_D = 1$ also. It is assumed that possible errors introduced by this manoeuvre are minor since the characteristic sand diameter of most of the (Dutch) prototype beaches is of the same order of magnitude.

The dimensionless calibration constant was estimated from the data, yielding $K_c = 1.2 \cdot 10^{-6}$, see (Steezel, 1990a).

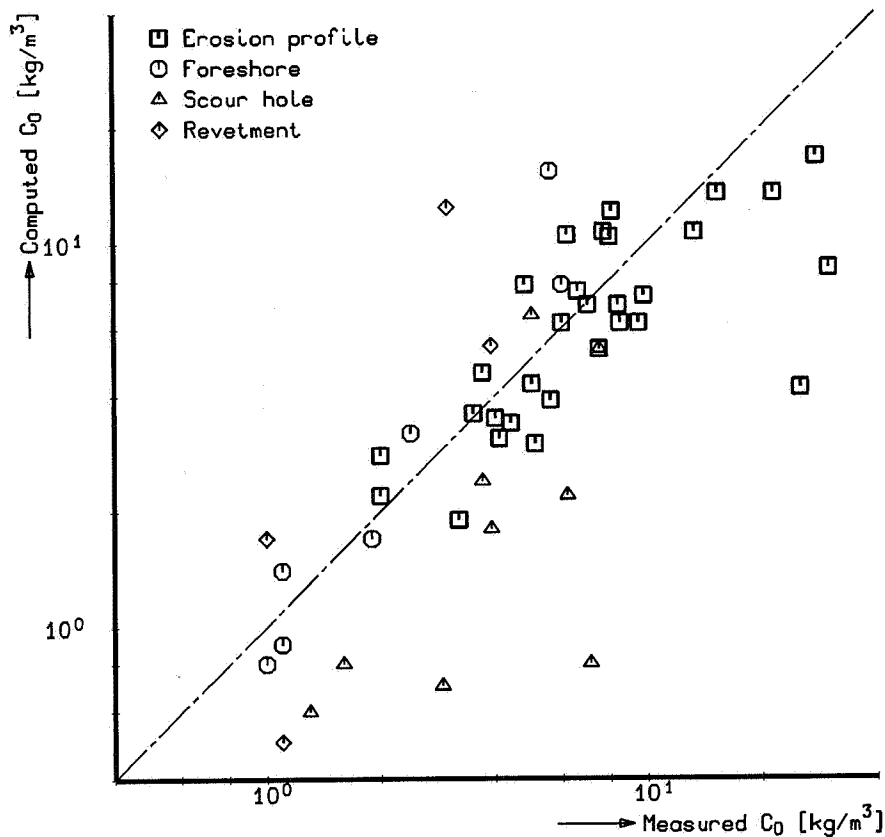


Figure 5.16 Comparison between measured and computed reference concentrations.

5.4.6 Verification/justification

Figure 5.16 shows a comparison between measured and computed reference concentrations. With respect to most of the 'non-scour hole' data, the agreement between measurements and computations was found to be satisfactory.

It is noted that the under-prediction of the concentrations on the erosion profile (as situated in the upper right corner of this figure) is partly due to an over-estimation of the measured concentrations.

The same figure using linear scales and leaving out these doubtful data is given in Figure 5.17.

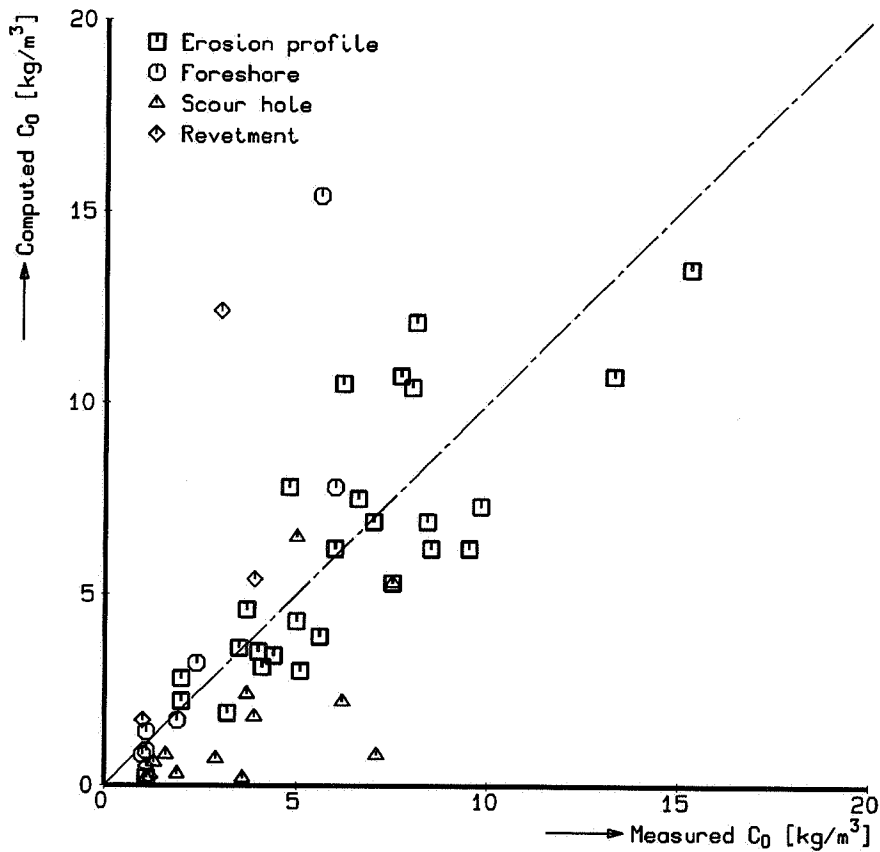


Figure 5.17 Comparison between measured and computed reference concentrations on linear scales.

5.4.7 Summary and conclusions

Although a large amount of scatter is present a useful formulation for the reference concentration has been derived.

The dependency with the sediment characteristics is not yet correct. An additional correction will be made in the second calibration phase, as elaborated in Section 5.6.

5.5 Overall large-scale calibration

5.5.1 Introduction

In the previous sections an attempt has been made to correlate the parameters describing the mixing and the reference concentration to local hydraulic conditions.

Assuming all other parameters to be sufficiently accurate described by their generally-accepted expressions, the basic 'internal' calibration phase as outlined in Figure 5.1 has finished.

The mathematical model itself can now be employed for the final overall 'external' calibration.

In order to fine-tune the accompanying profile development a detailed comparison between measured and computed profile development has been made using the results of a large-scale model test.

From this, the optimal magnitude of three transport correction factors have been assessed, namely:

- A correction factor $K_{sl} \neq 0$ to deal with the effects of the bottom slope;
- A beach/swash factor $K_{sw} \neq 1$ to cope with the effects of numerical instability in the swash zone;
- An overall correction factor on the transport rate K_{cor} with presumably $K_{cor} \approx 1$ to correct for the inadequacy of the transport model.

It is noted that the effect of the sediment diameter (the dimensionless F_D -function in the formulation of the reference concentration C_0) will be dealt with in Section 5.6.

5.5.2 Large-scale profile development

Test T2 of research programme M1263-III has been used for the final calibration of the transport model. The measured profile development is presented in Figure 5.18.

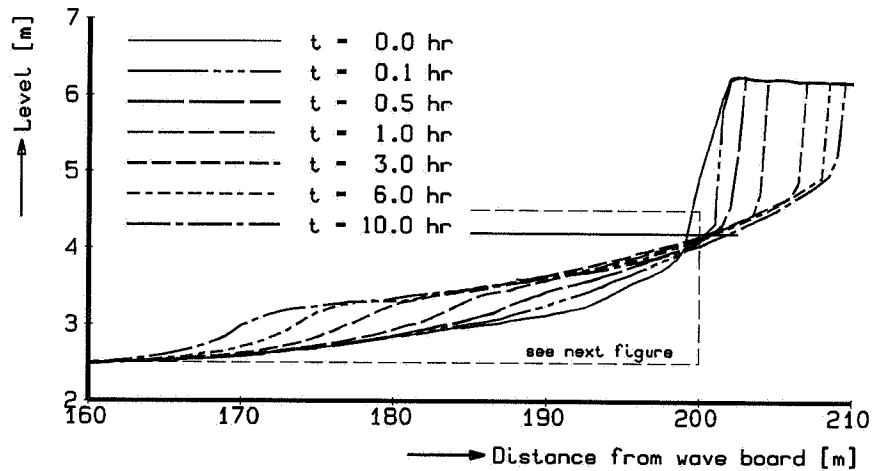


Figure 5.18 Measured profile development for test T2 of the M1263-III-series.

A detail of this part of the profile development is shown in Figure 5.19, since especially the under water processes have been examined so far.

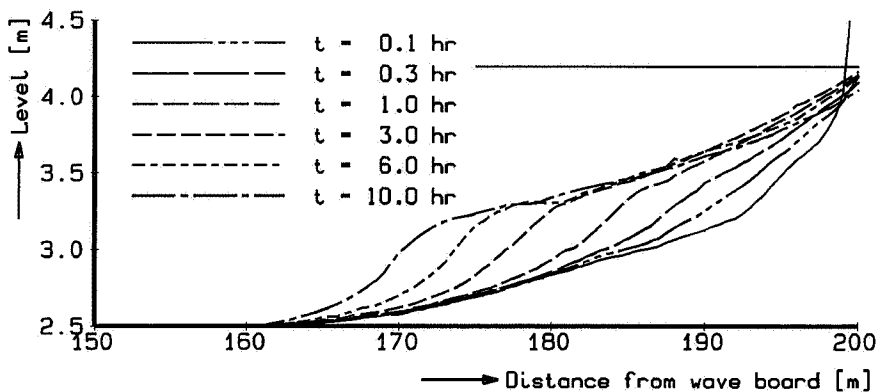


Figure 5.19 Detail of measured profile development for test T2 of the M1263-III-series.

5.5.3 Slope correction factor

The expression used to incorporate the bed slope effects was already presented in Section 4.7.6. In order to account for the additional impact of the bottom slope on the transport rate, a correction factor $K_{sl} \neq 0$ has to be applied in:

$$S'_x = \left[1 + K_{sl} \left(\frac{\Delta z_b}{\Delta x} \right) \right] S_x \quad (4.7.10/5.5.1)$$

From a comparison between measured and computed transport rates for non-horizontal bed slopes it was concluded that $K_{sl} = 4$ provided a fair description of the dependency that was found.

5.5.4 Swash factor

In the transition zone between shallow water and duneface, the mathematical model tends to generate unacceptable bottom irregularities. In order to cope with this numerical effect, an additional numerical smoothing procedure has been incorporated. This was realized by intensifying the standard numerical diffusion due to the γ -factor in Equation (4.7.12) by adding a multiplication factor $K_{sw} \geq 1$ in this region. So:

$$\gamma' = K_{sw} \gamma \quad (5.5.2)$$

From a number of trial computations it was concluded that in order to obtain a satisfying profile development in this zone, a 'swash factor' $K_{sw} = 2$ has to be used.

5.5.5 Transport correction factor

The transport rate is basically computed from the expressions presented in Section 4.5. In order to enable the final tuning of the model using the observed development of the erosion profile, the outcome of Equation (4.5.15) has been multiplied by a dimensional calibration constant, viz. the transport correction factor K_{cor} :

$$S' = K_{cor} S \quad (5.5.3)$$

From a comparison of the outcome of model runs for a range of K_{cor} -values, it was concluded that the employment of a correction factor for the transport according to $K_{cor} = 1.6$ gives the best result. The accompanying computed profile development is presented in Figure 5.20 (see also Figure 6.8).

It is noted that a re-analyses of the outcome of this calibration as carried out in the course of the writing of this thesis showed that this value is probably slightly too small. For the time being, this initial magnitude has been used in the computations as presented in the following chapters, viz. Chapter 6 through 8. This discrepancy has to be considered in a

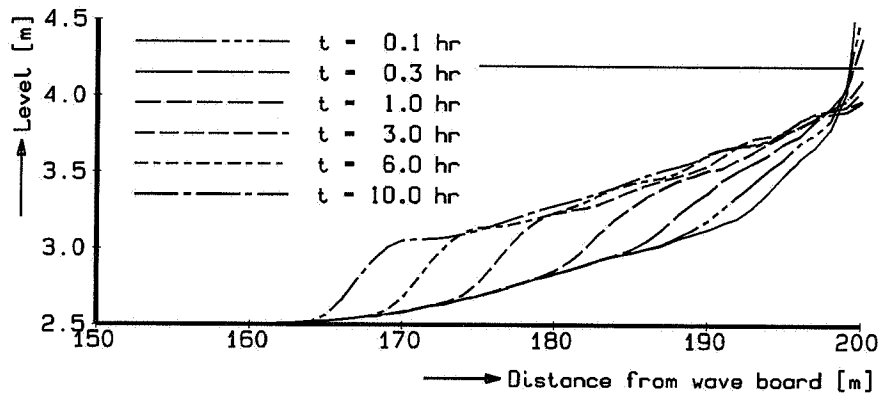


Figure 5.20 Detail of computed profile development for test T2 of the M1263-III-series.

next version of the computational model in which also additional calibration data can be taken into account (see Section 9.3 in which recommendations are made).

5.5.6 Summary and conclusions

From the confrontation of the observed profile development in a large-scale model test with numerous runs with the mathematical model, the appropriate magnitude of the correction factors has been assessed.

For the slope effect a correction factor of $K_{st} = 4$ was found to be appropriate, yielding a transport correction of 10% in the case of a rather steep 1:40 bed slope.

Furthermore, it was found that in order to obtain a decent profile development in the swash zone, a (numerical) swash factor $K_{sw} = 2$ has to be used.

Finally, the tuning of the erosion profile resulted in an overall transport correction factor. For the latter $K_{cor} = 1.6$ has been found to be appropriate.

5.6 Additional small-scale calibration

5.6.1 Introduction

If it is assumed that all parameters related to the hydraulic conditions, give reliable results also when using other model scales, then the impact of sediment material still will be an unknown factor.

As can be seen from the related function, viz.:

$$F_D = \left(\frac{0.000225}{D_{50}} \right)^{\alpha_D} \quad (5.6.1)$$

for the large-scale test with $D_{50} = 225 \mu\text{m}$ as discussed in Section 5.5, $F_D = 1$ is found.

Since the cross-shore transport rate is proportional to the reference concentration, see Section 5.5.4, viz. Equation (4.5.15), the actual magnitude of α_D will determine the additional correction of transport rate as far as this is related to the influence of the sediment diameter.

A larger α_D -magnitude implies a larger F_D -value and so a larger reference concentration and, consequently, an increased transport rate.

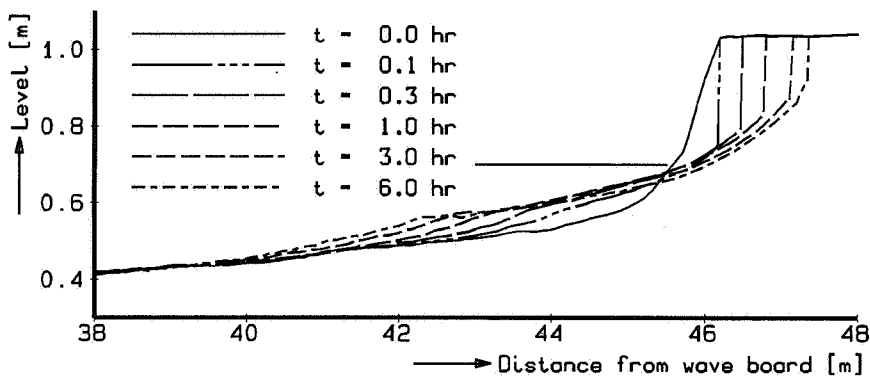


Figure 5.21 Measured profile development for test T04 of the M1819-III-series.

5.6.2 Small-scale profile development

Test T04 of research programme M1819-I, being a small-scale replicate of the previously used large-scale calibration test, has been used for the final calibration of the transport model. The measured profile development is presented in Figure 5.21.

The particle size was $D_{50} = 90 \mu\text{m}$ in this test.

5.6.3 Results

By successively performing computations of the profile development for a range of enforced F_D -values, viz. $F_D = 1, 2, \dots, 5$, the best feasible agreement between the measured and computed profile development could be selected.

From this it was concluded that $F_D \approx 3$ provided the best agreement.

The accompanying computed profile development is presented in Figure 5.22.

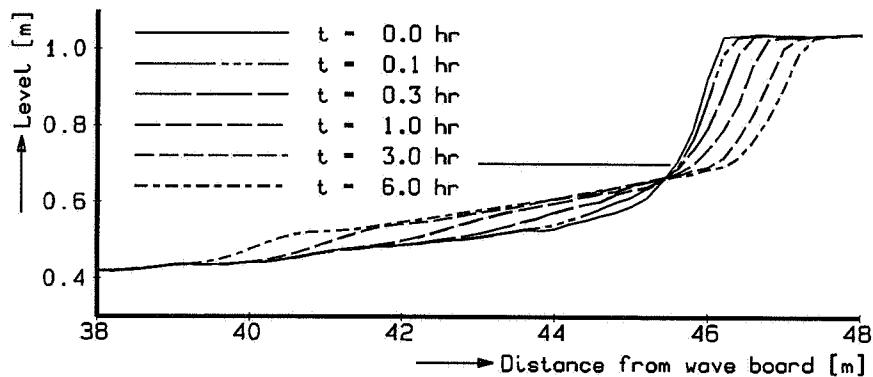


Figure 5.22 Computed profile development for test T04 of the M1819-III-series.

Conclusively for the sand diameter $D_{50} = 90 \mu\text{m}$ used in this test, the accompanying α_D -magnitude can be obtained from:

$$F_D = \left(\frac{0.000225}{0.000090} \right)^{\alpha_D} = (2.5)^{\alpha_D} \approx 3 \quad (5.6.2)$$

yielding $\alpha_D = 1.2$ as the requested magnitude.

5.6.4 Summary and conclusions

An additional confrontation of the mathematical model with a physical test result with a different grain size provided the α_D -power in the F_D -function. As a result $\alpha_D = 1.2$ was found.

5.7 Preliminary validation

5.7.1 Introduction

Although the model should be used to predict the development of the cross-shore profile and the major verification will be based on this, in the next some results of a brief check on the predicted internal parameters will be presented. Both the computed cross-shore and computed vertical distribution of time-averaged concentrations and time-averaged velocities will be compared with measured data. For this purpose computations have been carried out for test T3 of the H298-I-test series as presented in Figure 5.23.

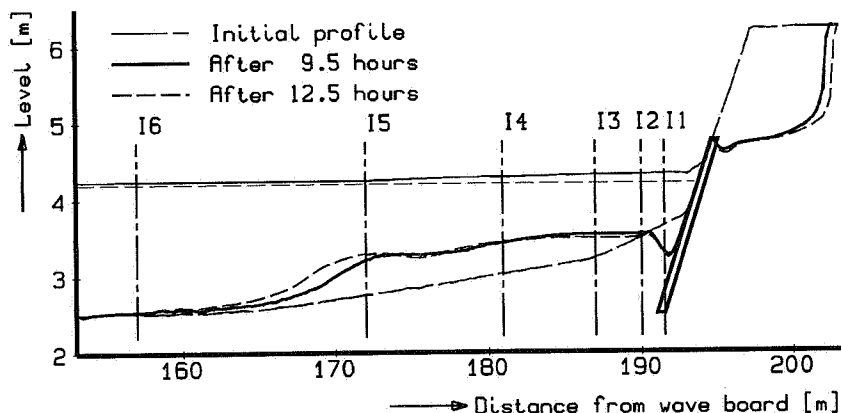


Figure 5.23 Location of measurements; test T3 of the H298-I-test series, phase I, viz. 9.5 - 12.5 hrs).

The results with respect to the sediment concentrations and the secondary flow will be discussed in the following.

5.7.2 Sediment concentrations

A comparison for computed (for both 9.5 and 12.5 hrs) and the estimated reference concentration C_0 is presented in Figure 5.24.

From this it can be observed that the computed distribution agrees rather well with the measurements.

The comparisons between the vertical profiles at positions $x = 157$, 181 and 190 m are shown in Figure 5.25. Apart from the outcome for the scour-hole position, viz. test T3I2, a fair agreement is found.

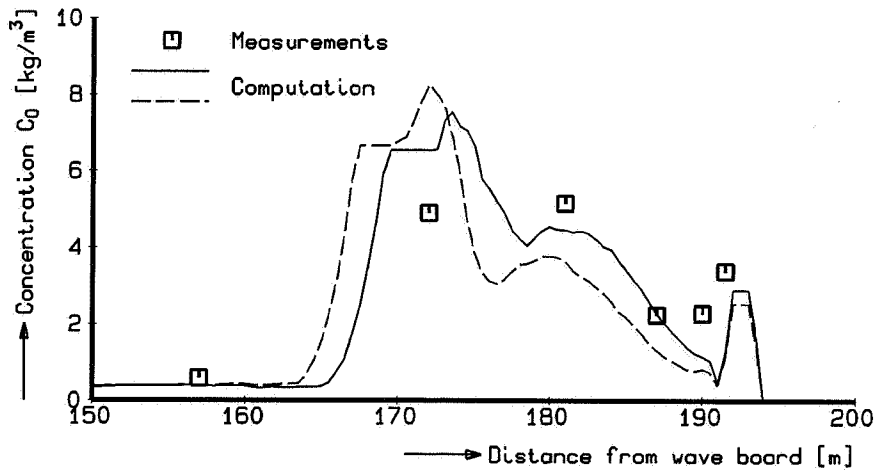


Figure 5.24 Computed cross-shore distribution of reference concentration compared with measured magnitudes.

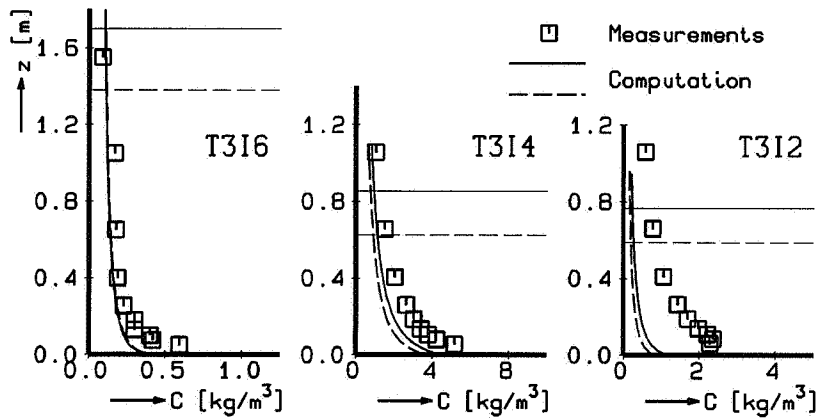


Figure 5.25 Computed vertical distribution of suspended sediment concentration compared with measured profiles for three data sets.

5.7.3 Secondary flow

Comparable figures are presented for the secondary flow. Figure 5.26 shows a comparison between the computed cross-shore distribution of the reference velocity u_0 (for both 9.5 and 12.5 hrs) and the measured time-averaged magnitude at both 0.05 m and 0.25 m

above the bottom.

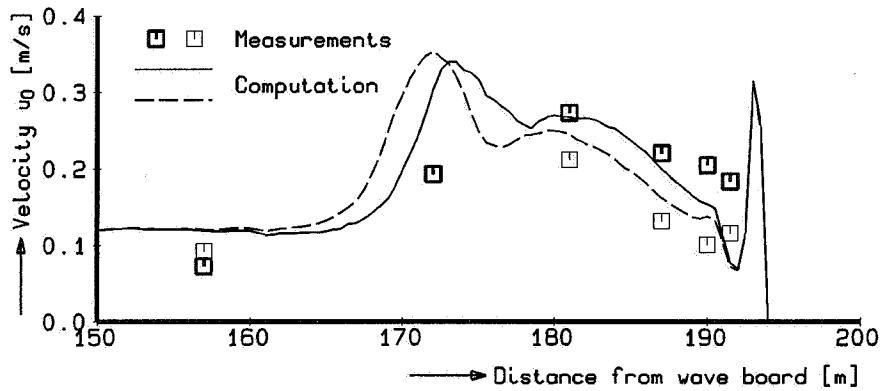


Figure 5.26 Comparison between computed and measured time-averaged velocities.

The comparison between the accompanying vertical profiles is provided in Figure 5.27 showing a fair agreement also.

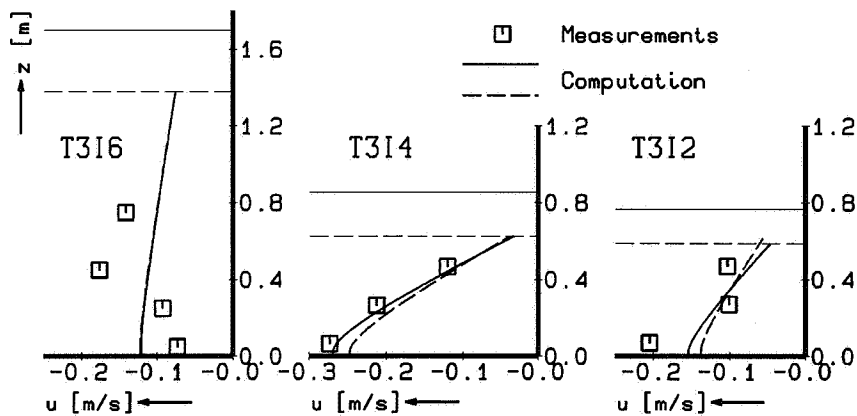


Figure 5.27 Comparison between computed and measured secondary flow profiles.

5.7.4 Conclusions

In summary an encouraging agreement is found between measured and computed data. A more comprehensive check of the mathematical model is elaborated in Chapter 6.

6 VERIFICATION

6.1 Introduction

6.1.1 General

This chapter summarizes the results of a comprehensive comparison between observed and computed profile changes. This final verification of the model is accomplished by comparing measured and computed quantities for a large number of model tests and a number of prototype data.

As already noted in Section 5.1, this verification of the cross-shore transport model is merely based on the 'external' process results, such as the shape of the post-storm profile and the ultimate amount of dune erosion above the (maximum) surge level.

With reference to the first mentioned process result, it is noted that although it is easy to state that computed and measured profiles show satisfactory agreement, the degree of similarity is hard to quantify and thus always the result of a subjective judgement.

By comparing the amount of accretion in a particular part of the cross-shore profile or the rate of erosion above a certain level, e.g. storm surge level, this quantification problem does not exist since we are dealing with actual quantities in this cases.

6.1.2 Approach

In the next three sections, viz. 6.2 through 6.4, the impact of both constant and varying storm surge conditions on (almost) unprotected coastal profiles will be studied first.

A number of cases will be dealt with, namely:

- A detailed comparison of measured and computed post-storm profiles, based on a large number of tests carried out in both large-scale and small-scale model facilities;
- A limited number of well-documented prototype cases;
- A systematic verification of the impact of several principal erosion governing parameters on the amount of dune erosion above the storm surge level.

Finally, the conclusions on the performance of the cross-shore transport model in the case of unprotected dunes are summarized and its accuracy is quantified in Section 6.5.

Whereas previous comparisons refer only to the basic formulation of the model (see Table 2.1), the following two sections focus on the reliability of the so-called model extensions as elaborated in Section 4.8. To be more specific:

- The verification of the profile development in the case of the presence of non-erodible parts, viz. structures, particularly in the active part of the cross-shore profile (Section 6.6);
- A preliminary verification of computed longshore effects (Section 6.7).

Finally, the overall performance of the cross-shore transport model is briefly discussed in Section 6.8.

It is noted that the data used for verification purposes are not yet used for the calibration of the model. Moreover, the data used can be referred to as additional new data.

6.1.3 Sediment balance

One of the basic assumptions of the present (and probably any other) cross-shore transport model is that the amount of material (in terms of weight) in the coastal profile of interest remains unchanged. Since a both time and space non-varying, constant porosity p is assumed, this balance holds also for the volumes involved. So, in order to allow for a fair comparison of model results with any model or prototype data, the measured viz. observed volumes present in the coastal profile should not vary during the test period.

These volumes, or in fact areas since we are dealing with cross sections only, can be computed from:

$$A = \int_{x=X_1}^{x_2} \Delta z(x) dx \quad (6.1.1)$$

with:

$$\Delta z(x) = \begin{cases} z(x) - Z_0 & \text{for } \{z(x) > Z_0\} \\ 0 & \text{for } \{z(x) \leq Z_0\} \end{cases} \quad (6.1.2)$$

resulting in the volume of sand A in zone $X_1 \leq x \leq X_2$ above the level $z = Z_0$.

As will be shown in the following, the amount of sediment expressed in volumes in a flume seems to decrease during most of the test programmes studied. This is caused by the fact that there is a significant difference present between the initial compaction of the sand in the duneface and the final compaction present in the erosion profile.

6.2 Laboratory data for unprotected dunes

6.2.1 Introduction

Series of data on cross-shore profile development from both large-scale and small-scale model tests conducted at DELFT HYDRAULICS are discussed in Section 6.2.2 and 6.2.3 respectively. Subsequently, the verification using some well-documented other, say 'non-Delft', data is outlined in Section 6.2.4. Section 6.2.5 summarizes the main findings. An overview of the laboratory data used is presented in Table 6.1.

Research programme	number of tests used	facility, reference
Large-scale data		Deltaflume
M1797	test T1 (out of 2)	see (DELFT HYDRAULICS, 1982b)
M1811	1 test	see (DELFT HYDRAULICS, 1982c)
M1263-III-series	all 5 tests	see (DELFT HYDRAULICS, 1984a)
H298-I-series	test T5 out of 5	see (DELFT HYDRAULICS, 1987a)
Small-scale data		Scheldeflume
M1819-I-series	29 tests in total	see (DELFT HYDRAULICS, 1982d)
M1819-III-series	test T1 (out of 4)	see (DELFT HYDRAULICS, 1983d)
Other data		Große Wellen Kanal
SFB 205/TP A6	six tests	see (Dette and Uliczka, 1988)

Table 6.1 Overview of (model) test-series used for verification.

It is noted that using test results from several model scales does not imply that the mathematical model is developed using scale relations. The result of each test is considered to be a prototype one, although much smaller waves and finer sand have been applied. It is for that reason that the use of large-scale data is most favourable. Relatively to small-scale test results these 'near-prototype' data are very useful, since the actual conditions in the flume are almost comparable with the conditions to be met under (at least moderate) prototype conditions.

6.2.2 Large-scale data

In the following, some well-documented large-scale model tests are used for a comparison with the outcome of the cross-shore transport model. All tests mentioned hereafter have been carried out in DELFT HYDRAULICS' Deltaflume. This flume has a length of 233 m, the depth and width are 7 and 5 m respectively. The facility is equipped with a programable vertical wave board, presently provided with wave active reflection compensation, which is able to generate random waves up to $H_{sig} = 2$ m in the wave period range of 2 to 10 s.

M1797-series, test T1

In order to determine the impact of an existing dune revetment at a coastal section of the Noorderstrand at Schouwen on the ultimate amount of dune erosion during a specific design storm surge, both a test with and a test without a revetment have been conducted in the Deltaflume (DELFT HYDRAULICS, 1982b). The outcome of the test without a structure, viz. test T1, are discussed in the following.

The hydraulic conditions, viz. water level $h(t)$, (significant) wave height $H_{sig}(t)$ and (peak) wave period $T_p(t)$ present during both tests are shown in Figure 6.1.

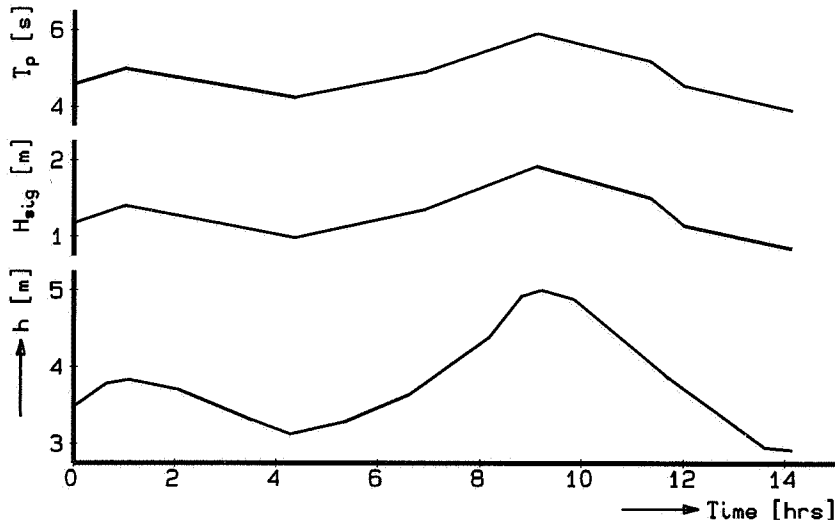


Figure 6.1 Hydraulic conditions used in test T1 (and T2) of the M1797-series.

Figure 6.2 shows a comparison between the measured (observed) and computed cross-shore profile after 14.1 hours of wave attack for test T1.

The two horizontal lines in this figure denote the maximum and minimum surge level, viz. +5.0 and +2.9 m above the flume bottom. Although a decent resemblance is present between the measured and computed final profile for say $x < 160$ m, the final profile near the duneface shows less agreement. Moreover, the amount of dune erosion above the maximum surge level was computed to be $26.2 \text{ m}^3/\text{m}^1$, whereas $32.0 \text{ m}^3/\text{m}^1$ was estimated from the measured post-storm profile. The deviation of $5.8 \text{ m}^3/\text{m}^1$, being 18% of the observed value, is partly due to a significant difference between the compaction of the settled sand on the beach and foreshore and the eroded sand from the dune. A comparison between pre- and post-storm profiles showed that about $4.1 \text{ m}^3/\text{m}^1$ of the total volume is missing.

Relative to the measured total erosion rate of $35.6 \text{ m}^3/\text{m}^1$, the volume loss amounts to about 12%. Consequently, the corrected erosion rate above the maximum storm surge level amounts $(1 - 0.12) 32.0 = 28.2 \text{ m}^3/\text{m}^1$. Relative to the computed volume there is a shortage

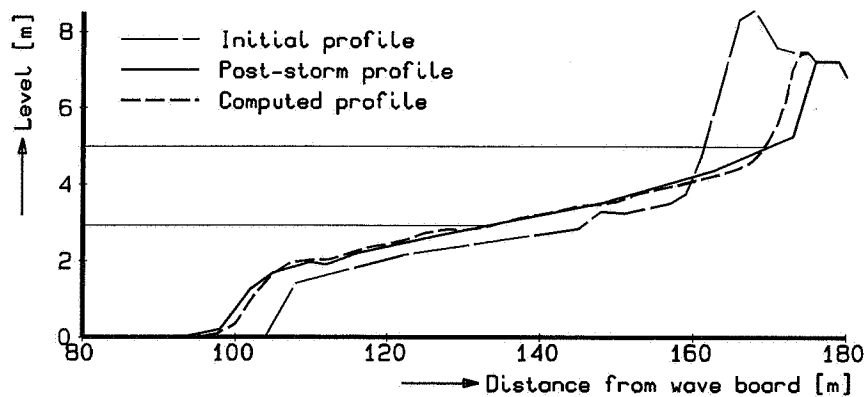


Figure 6.2 Comparison between measured and computed post-storm profiles for test T1 of the M1797-series.

of only $2.0 \text{ m}^3/\text{m}^1$. The latter is due to a still inappropriate computation procedure for the net cross-shore transport distribution in the swash zone.

For the sake of completeness, it is noted that the results for test T2, viz. the protected dune, are presented in Section 6.6.2 (see Figure 6.85).

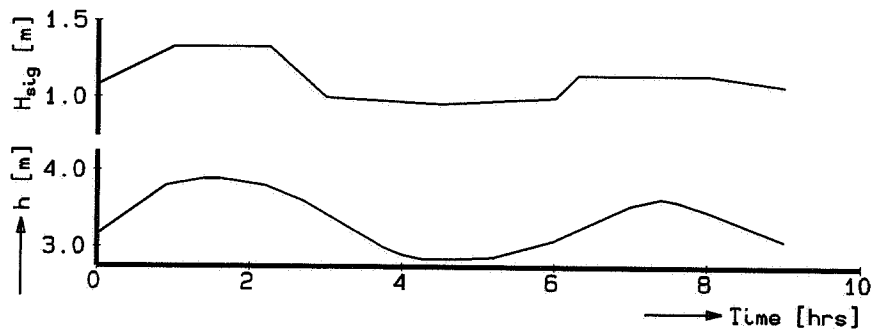


Figure 6.3 Hydraulic conditions used in the M1811-series.

M1811-series

This large-scale model test was conducted to gain insight into the effect of the presence of blockhouses on the dune erosion processes, see (DELFT HYDRAULICS, 1982c).

The hydraulic conditions used during this test are shown in Figure 6.3. The wave period was constant, namely $T_p = 4.8 \text{ s}$.

Figure 6.4 shows a comparison between the measured and computed profile development.

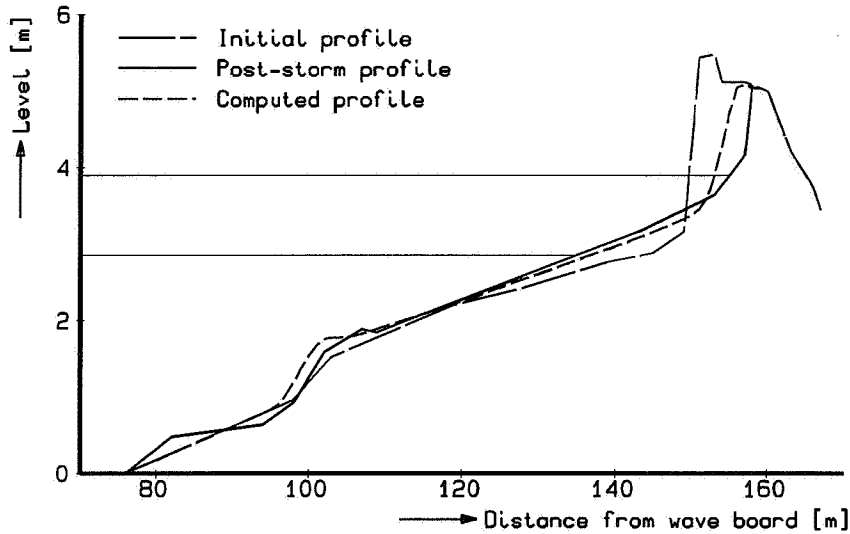


Figure 6.4 Comparison between the measured and computed post-storm profiles for the M1811-series.

As can be observed a fair resemblance is present for the 'seaward' part of the final profile. The amount of erosion above the storm surge level of +3.9 m is under-estimated. The computed (predicted) amount is $6.3 \text{ m}^3/\text{m}^1$, whereas the test result yields $9.4 \text{ m}^3/\text{m}^1$. Analyzing the measured cross-shore profiles shows that about $2.1 \text{ m}^3/\text{m}^1$ is missing, this being almost 20% of the total eroded volume ($11.8 \text{ m}^3/\text{m}^1$). From this it can be concluded that the mutual difference between computed and measured dune erosion ($3.1 \text{ m}^3/\text{m}^1$) for about 60% is caused by porosity effects.

M1263-III-series

This test programme was conducted in order to verify the scale relations and the reliability of the existing dune erosion model (as described in Section 2.5 in more detail) (DELFT HYDRAULICS, 1984a). In total five different tests were carried out.

Two tests, viz. test T1 and T2, were conducted using constant hydraulic conditions, whereas a third test was performed to investigate the relative effect of the naturally varying water level. In test T4, the storm surge of 1953 was reproduced with a depth scale factor of $n_d = 3.27$, while the last test can be considered as a full scale replica of a moderate storm in nature.

A brief description of all tests is presented in Table 6.2.

test	hydraulic conditions	h [m]	H_{sig} *) [m]		T_p [s]	brief description
T1	constant	4.20	1.50	1.72	5.4	steep profile (1 : 60)
T2	constant	4.20	1.50	1.70	5.4	less steep (1 : 90); reference test
T3	varying	< 4.20	< 1.50	-	< 5.4	as test T2 with varying conditions
T4	varying	< 4.20	< 1.85	-	< 5.0	'Delfland'-profile for 1953-surge
T5	constant	5.00	2.00	2.86	7.6	arbitrary profile

*) Second number refers to estimated actual condition.

Table 6.2 Overview of the tests of the M1263-III-series.

The second wave height is the actual wave height at the location of the wave board, as determined from a large number of wave height measurements in the flume. The procedure followed to obtain this number is presented in Section 5.2.3, see also (Steetzel, 1990b). It will be obvious that this magnitude has been used as a boundary condition for the subsequent verification of the mathematical model.

For the moulding of the profile dune sand with $D_{50} = 225 \mu\text{m}$ has been used, having an estimated fall velocity of $w_s = 0.0268$ m/s. More details on the individual tests are summarized hereafter.

An overview of the flume for Test T1 is shown in Figure 6.5. The slope of the foreshore is 1 : 60 which is about three times as steep as the average prototype slope, being 1 : 180 on an average. The test duration was 10 hours. Wave generation was stopped at $t = 0.1$, 0.3, 1.0, 3.0, 6.0 and 10.0 hours for profile recording by echo sounding in three parallel rays along the flume. The latter result, viz. the post-storm profile present at $t = 10.0$ hours, is also shown in the figure.

The detailed comparison between the computed (dashed) and measured (solid line) post-storm attack profile is shown in Figure 6.6.

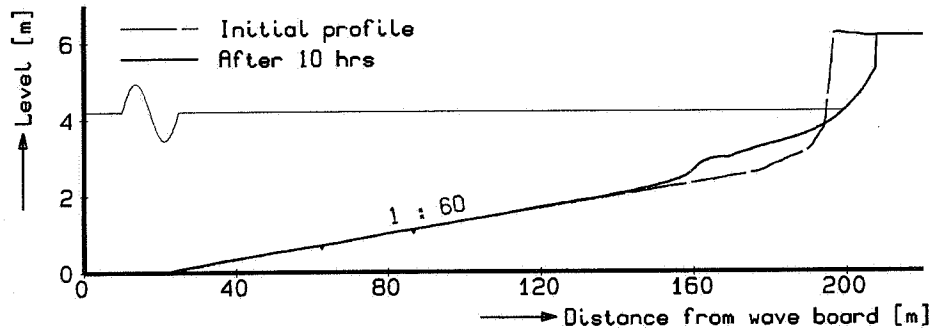


Figure 6.5 Overview of profiles for test T1 of the M1263-III-series.

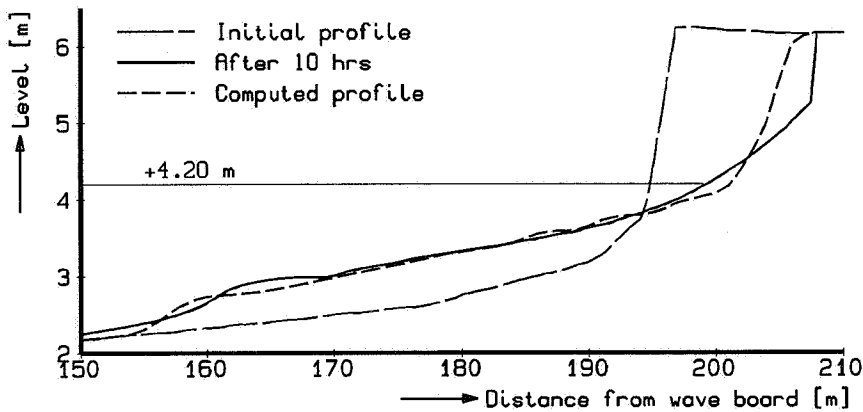


Figure 6.6 Comparison between measured and computed post-storm profiles for test T1 of the M1263-III-series.

As can be observed the 'seaward' part of the profile agrees well. With respect to the amount of erosion and accretion the results of both the measurement and the computation are summarized in Table 6.3. In this table A_d denotes the erosion rate above the maximum water level, A_{er} and A_{ac} denote the total volume of erosion and accretion respectively. For the computations the latter are equal, viz. $A_{er} = A_{ac}$, whereas in the case of the physical model the mutual difference, viz. $(A_{er} - A_{ac})$, is a measure for the apparent loss in sediment volume, see Section 6.1.3 and (Steezel, 1993). As can be seen from the results the latter equals $1.6 \text{ m}^3/\text{m}^1$ for this specific test.

The profile development of test T2 has already been used for calibration of the transport correction factor, as described in Section 5.5.5.

An overview of the flume including the final profile at $t = 10.0$ hours is shown in Figure 6.7.

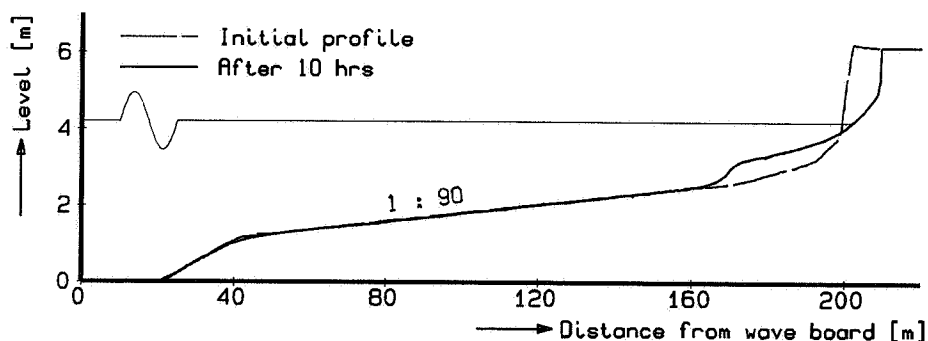


Figure 6.7 Overview of profiles for test T2 of the M1263-III-series.

Both the measured and computed final profiles are presented in Figure 6.8.

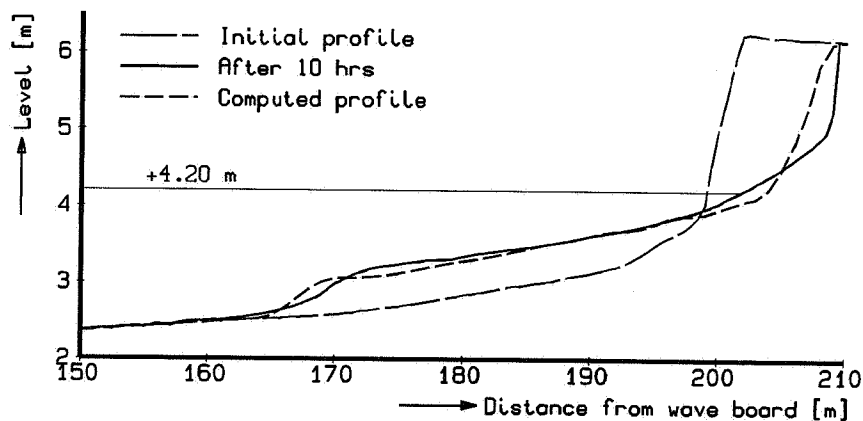


Figure 6.8 Comparison between measured and computed post-storm profiles for test T2 of the M1263-III-series.

It is noted that the agreement in the final volumes present in the under water profile is the result of the calibration.

The erosion quantities are summarized in Table 6.3. For the sake of convenience, the result of the comparable test T5 of the H298-I-series, is given also.

test	time [hrs]	Measurement					Computation	
		A_d [m ³ /m ¹]	A_{er} [m ³ /m ¹]	A_{ac} [m ³ /m ¹]	$(A_{er} - A_{ac})$ [m ³ /m ¹]	$(\Delta A / A_{er})$ [%]	A_d [m ³ /m ¹]	$A_{er} = A_{ac}$ [m ³ /m ¹]
T1	10.0	19.8	20.7	19.1	1.6	7.7	16.9	18.3
T2	10.0	14.8	15.1	14.1	1.0	6.6	12.7	13.5
T5 ^{a)}	(9.5)	(15.9)	(16.4)	(15.0)	(1.4)	(8.5)	(11.3)	(12.4)
T3	19.25	9.6	9.7	9.3	0.4	4.1	7.3	9.5
T4	17.0	7.6	7.6	7.3	0.3	4.0	5.0	6.3
T5	6.0	49.4	51.3	43.8	7.5	14.6	55.3	61.1

^{a)} Refers to results for test T5 of the H298-I-series.

Table 6.3 Summary of ultimate dune erosion quantities for model tests of the M1263-III-series.

Although for both test T1 and T2 the rough shape of the erosion profile is reproduced correctly, the discrepancies near the duneface are obvious. As noted, these differences were also present in the first two test cases, viz. the M1797- and M1811-case. As will be seen in the following, comparable remarks can be made for all the other results also.

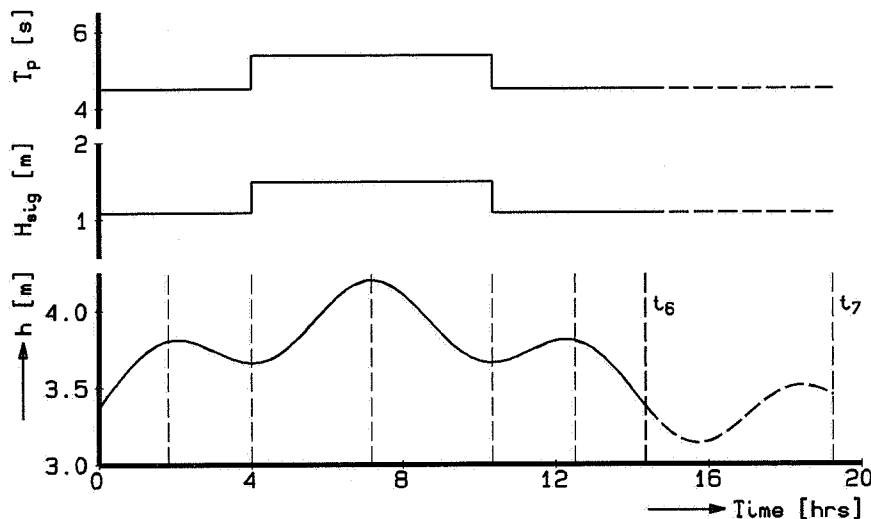


Figure 6.9 Hydraulic conditions used for test T3 of the M1263-III-series.

In test T3, the initial profile of test T2 was tested again but now with a natural storm surge hydrograph and naturally varying wave height and wave period instead of fixed hydraulic conditions. The water level and wave conditions present during this test are shown in Figure 6.9.

As can be observed, an additional storm phase has been introduced, ranging from t_6 to t_7 . An overview of the flume including the cross-shore profile after 19.25 hours ($= t_7$) is shown in Figure 6.10.

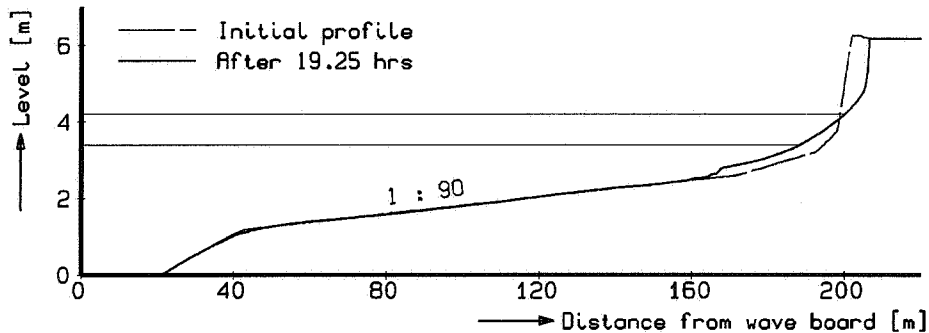


Figure 6.10 Overview of profiles for test T3 of the M1263-III-series.

During the latter stage of the surge, viz. from t_6 to t_7 , some onshore transport occurs. Figure 6.11 shows a comparison between the measured and computed profile development after the complete surge, viz. up to $t = 19.25$ hours.

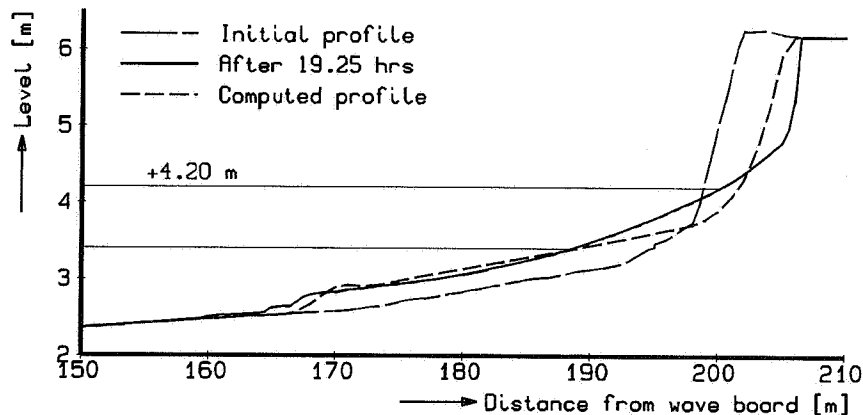


Figure 6.11 Comparison between measured and computed post-storm profiles for test T3 of the M1263-III-series.

As can be observed, similar remarks with respect to the model performance can be made.

Some quantitative data concerning the volumes involved are summarized in Table 6.3. From the physical model tests it was concluded that the effect of a period of about 2.0 to 2.5 hours of constant (maximum) surge conditions is equivalent to the effect of a naturally varying storm surge hydrograph. Figure 6.12 presents a comparison between measured and computed erosion rates (above the +4.20 m level) for both test T2 and T3. From this it can be observed that this is also the case for the outcome of the mathematical model.

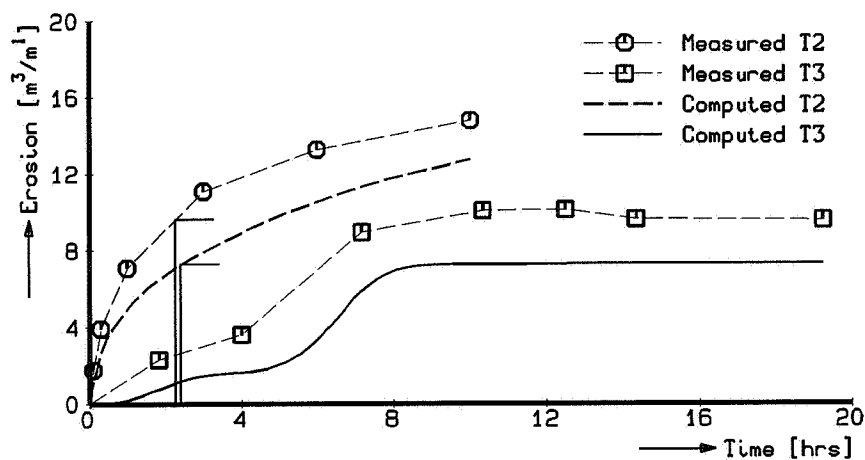


Figure 6.12 Development of erosion quantity for both constant and varying conditions.

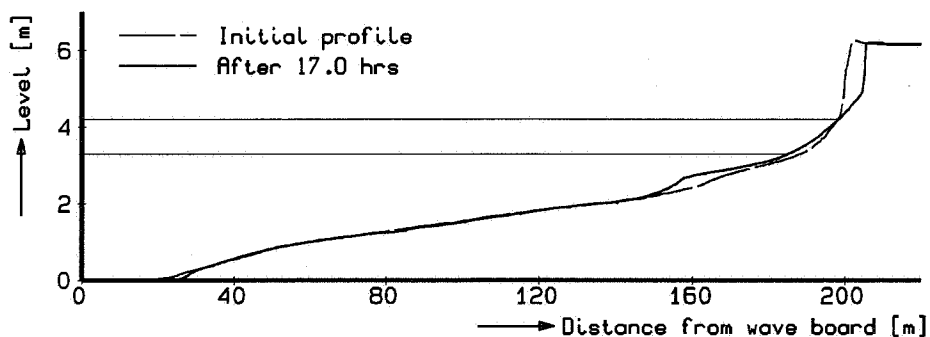


Figure 6.13 Overview of profiles for test T4 of the M1263-III-series.

The hydraulic conditions present during test T4 are shown in Figure 6.14, whereas an overview of the initial 'Delfland'-profile is shown in Figure 6.13.

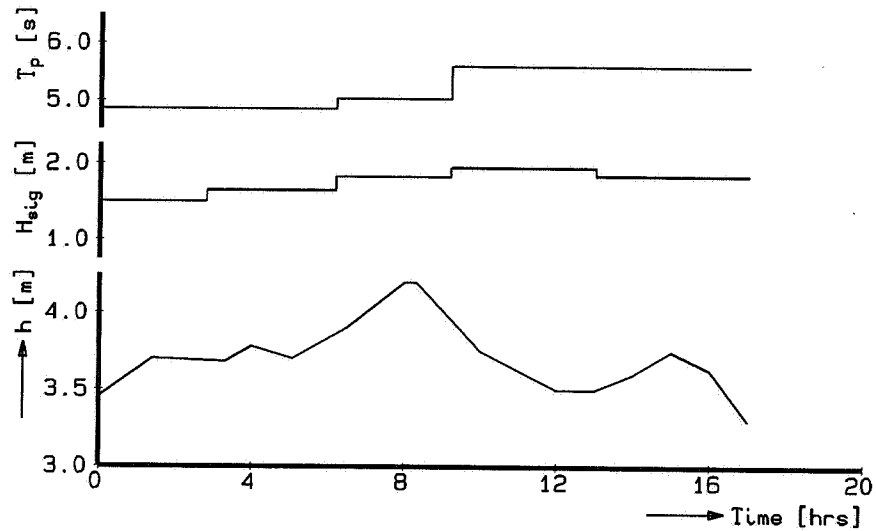


Figure 6.14 Hydraulic conditions used for test T4 of the M1263-III-series.

Figure 6.15 shows a comparison between the measured and computed profile development for this test, while the volumes involved are summarized in Table 6.3.

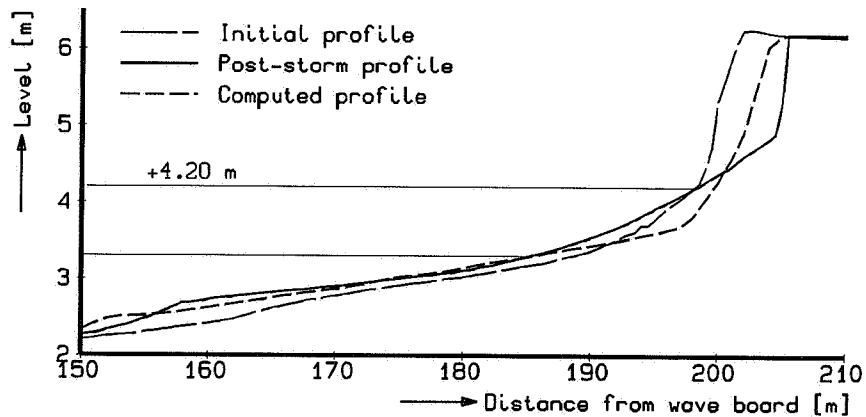


Figure 6.15 Comparison between measured and computed post-storm profiles for test T4 of the M1263-III-series.

It is noted that the (relative) apparent sediment loss for test T1 to T4 reduces systematically due to an overall increased compaction of the sand in the flume.

In the last test, viz. test T5, a 'full scale' reproduction of the conditions during a moderate storm surge in situ was investigated.

An overview of the flume, including the profiles after 1.0 and 6.0 hours, is shown in Figure 6.16.

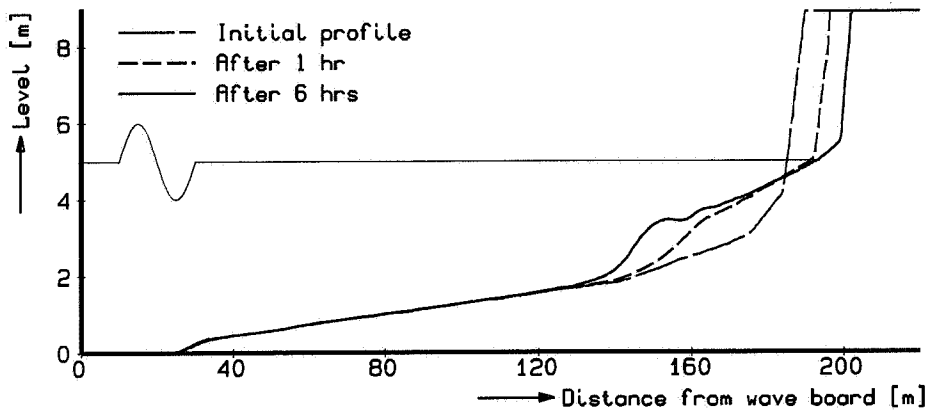


Figure 6.16 Overview of profiles for test T5 of the M1263-III-series.

The comparison between measured and computed cross-shore profiles is shown in Figure 6.17.

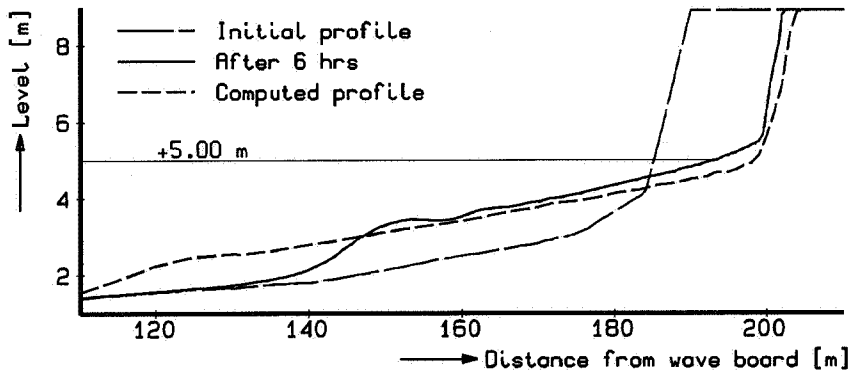


Figure 6.17 Comparison between measured and computed post-storm profiles for test T5 of the M1263-III-series.

The amounts of erosion involved are summarized in Table 6.3. Since a significant amount of extra sand was added for this test, the apparent sediment loss did increase dramatically.

H298-I-series, test T5

The objective of this test-series was to gain insight in the relative effect of dune revetments on the development of the cross-shore profile (Steetzel, 1987b). The initial profile is based on the profile as used in test T2 of previously presented M1263-III-series (see Figure 6.7).

Several degrees of protection were studied (see Table 6.11). The last test, viz. test T5, was a reference test in which the complete revetment was removed, in fact being a full-scale replicate of test T2 of the M1263-III-series.

An overview of the initial, the profile after 3.5 hours and the final profile at $t = 16.0$ hours is shown in Figure 6.18.

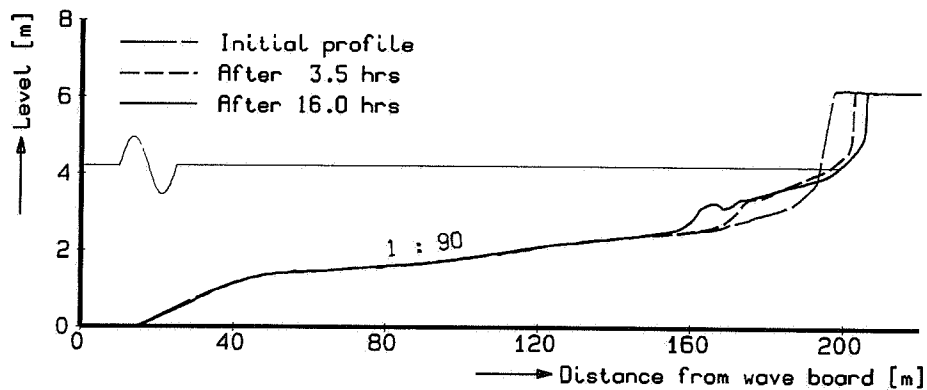


Figure 6.18 Overview of profiles for test T5 of the H298-I-series.

The detailed comparison between measured and computed cross-shore profiles is shown in Figure 6.19.

The amount of dune erosion is under-estimated by the computational model, although the seaward profiles agree well.

With respect to the model's performance near the duneface, the formerly given arguments are valid also for this test.

It is noted that the erosion quantities are summarized in Table 6.3. As can be seen they agree well with the result of test T2 of the M1263-II-series.

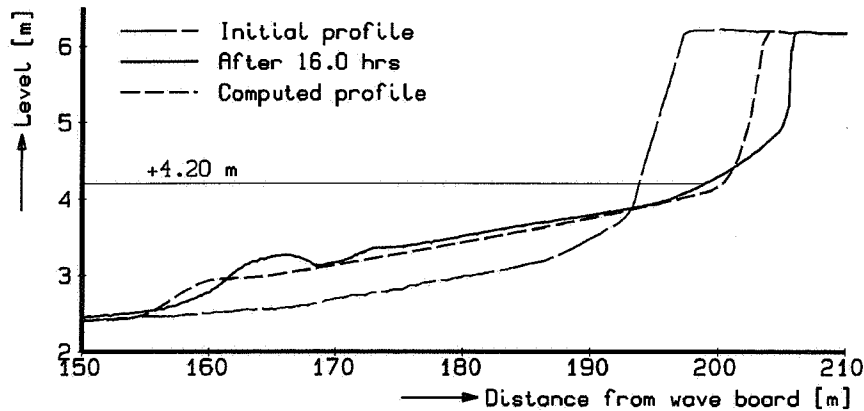


Figure 6.19 Comparison between measured and computed post-storm profiles for test T5 of the H298-I-series.

6.2.3 Small-scale data

In the following some results for small-scale model tests will be presented. These tests have all been carried out in the 50 m long Scheldeflume of DELFT HYDRAULICS. It is noted that results from preceding small-scale test programmes will not be taken in account since even larger depth scales were used, see e.g. (Van der Meulen and Gourlay, 1968; DELFT HYDRAULICS, 1981a).

M1819-I-series

Indisputably one of the most extensive small-scale test series into dune erosion and cross-shore profile development has been carried out in 1982, see (DELFT HYDRAULICS, 1982d). The objective was to determine the relative impact of all the dune-erosion governing parameters on the erosion rate.

An overview of the tests performed is given in Table 6.4.

For tests T21 through T28 varying hydraulic conditions have been applied, whereas for the other tests, viz. test T01 through T20 and test T29 a constant hydraulic condition has been used.

In the repetition tests, viz. test T14 through T20, the effect of wave groups, sand porosity and wave spectrum on the amount of dune erosion has been studied. It is remarked that the results of these tests are not taken into account here. More details are presented in (DELFT HYDRAULICS, 1982d).

test	hydraulic conditions	brief description / goal
T01-T13	constant, though variable	tests for different hydraulic conditions
T14-T20	constant	various repetitions of basic test T04
T21-T28	varying	effect of bars and gullies
T29	constant	see test T01-T13

Table 6.4 Overview of the tests of the M1819-I-series.

It should be remarked that relative to the results of the large-scale test series, the wave attack on the duneface consisting out of fine sediment did result in a significant loss of sediment volume from the active zone. For this reason the tuning of the mathematical model on the amount of accretion was troublesome (see Section 5.6).

However, the small-scale tests provided valuable insight in the dependency of the dune erosion rate on the governing hydraulic and geometric conditions. These dependencies will be discussed in more detail in Section 6.4.

In the following, the tests with fixed and varying hydraulic conditions will be discussed in more detail.

Test T01-T13 and T29 (fixed conditions)

An overview of the initial cross-shore profile used in the flume for all tests with constant hydraulic conditions is shown in Figure 6.20.

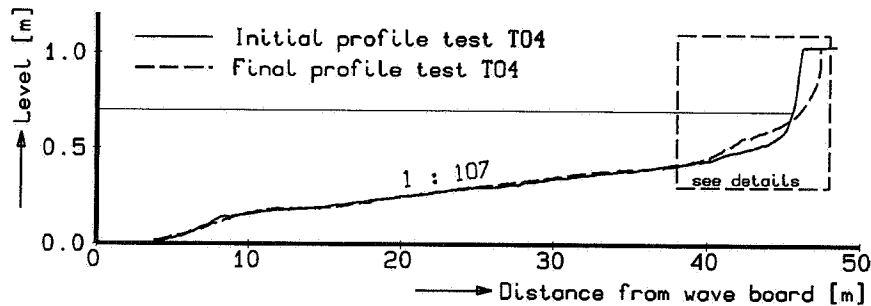


Figure 6.20 Overview of profile used for tests with fixed hydraulic conditions.

This so-called reference profile is related to the initial profile of test T1 and T2 of the M1263-III-series (and T5 of H298-I-series), although the distortion is somewhat lesser, see (Vellinga, 1986).

An overview of the detailed hydraulic and geometric (dune height) conditions for these tests is given in Table 6.5. The second wave height is the wave height which has been assessed from the measured wave height decay in the flume (see Section 5.2 for more details). This magnitude has also been used in the computations also.

test	h [m]	H_{sig} [m] ^{*)}		T_p [s]	z_d [m]	remarks
T01	0.700	0.133	0.164	1.588	1.033	low waves
T02	0.700	0.173	0.220	1.807	1.033	($\gamma = 0.95$)
T03	0.700	0.213	0.272	2.008	1.033	($\gamma = 0.95$)
T04	0.700	0.253	0.297	2.191	1.033	reference test
T05	0.700	0.253	0.305	1.826	1.033	($\gamma = 0.95$)
T06	0.700	0.253	0.304	2.008	1.033	($\gamma = 0.90$)
T07	0.683	0.253	0.282	2.191	1.033	
T08	0.717	0.253	0.280	2.191	1.033	
T09	0.717	0.253	0.295	2.191	1.033	
T10	0.717	0.253	0.299	1.588	1.033	
T11	0.700	0.133	0.163	2.191	1.200	
T12	0.700	0.253	0.294	2.191	0.866	
T13	0.700	0.133	0.163	2.191	1.033	($\gamma = 0.80$)
T29	0.750	0.253	0.321	2.191	1.033	

^{*)} Second number refers to estimated actual condition.

Table 6.5 Overview of model tests with fixed hydraulic conditions of the M1819-I-series.

For the moulding of the profiles so-called 'Asserzand' has been used with $D_{50} = 90 \mu\text{m}$ (and $w_s = 0.0083 \text{ m/s}$). A detailed comparison (see Figure 6.20 for its bounds) between the measured and computed final profiles (both after 6.0 hours of wave attack) for all the tests, viz. test T01 to T13 and T29, is presented in Figure 6.21 through Figure 6.34.

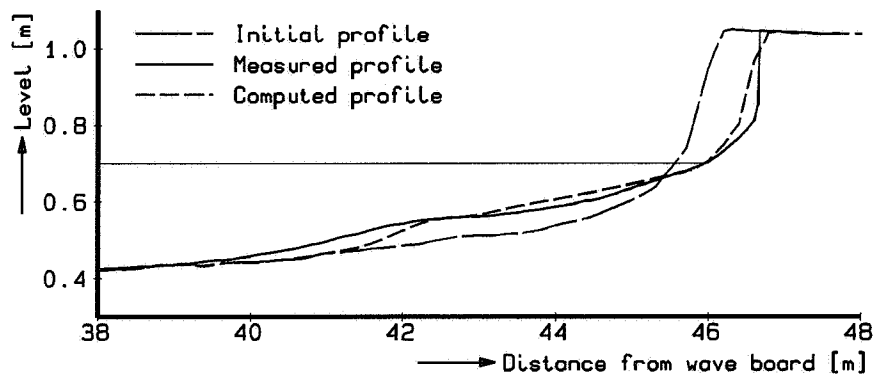


Figure 6.21 Comparison of final profiles for test T01 of M1819-I-series (fixed conditions).

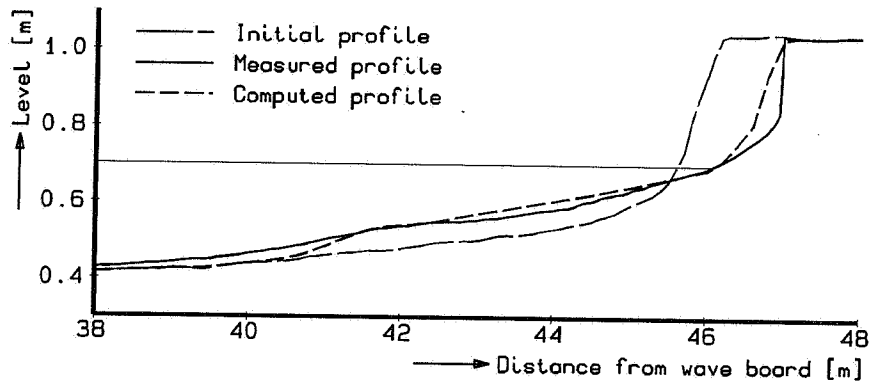


Figure 6.22 Comparison of final profiles for test T02 of M1819-I-series (fixed conditions).

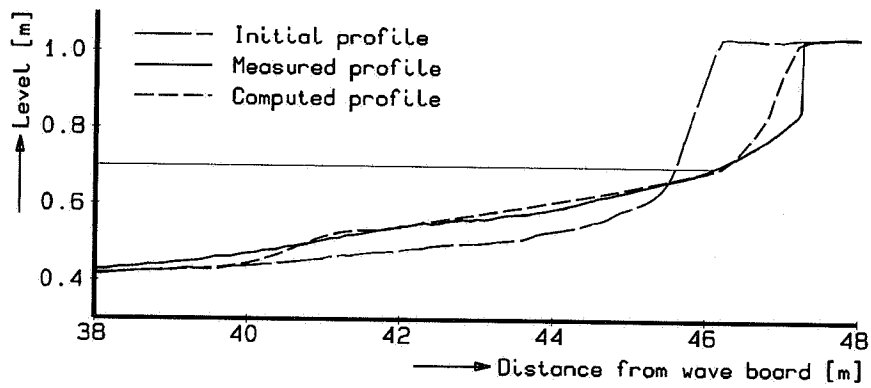


Figure 6.23 Comparison of final profiles for test T03 of M1819-I-series (fixed conditions).

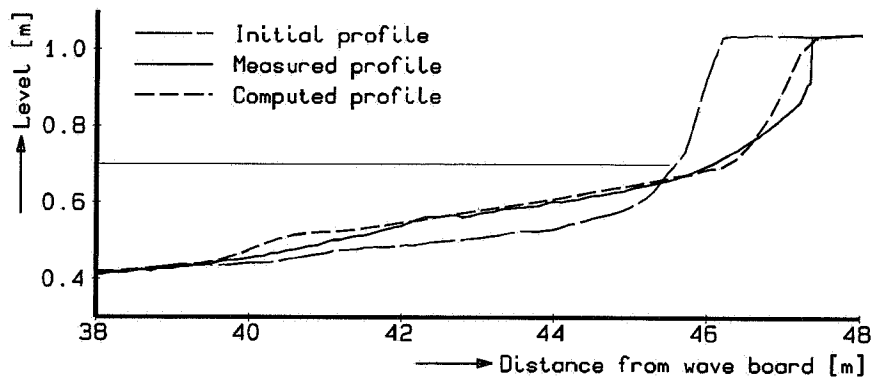


Figure 6.24 Comparison of final profiles for test T04 of M1819-I-series (fixed conditions).

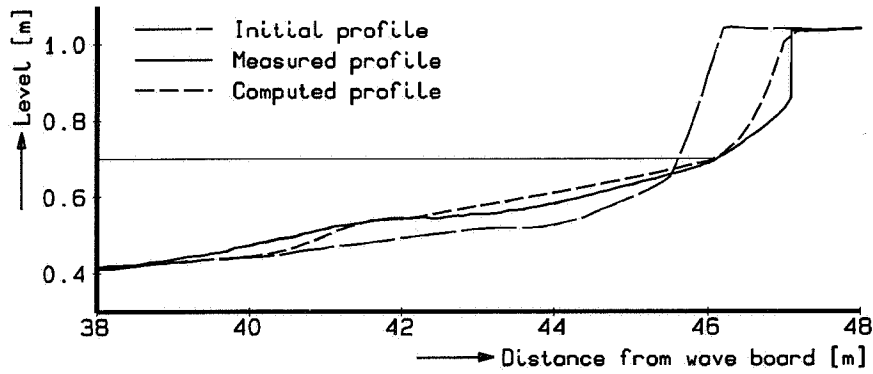


Figure 6.25 Comparison of final profiles for test T05 of M1819-I-series (fixed conditions).

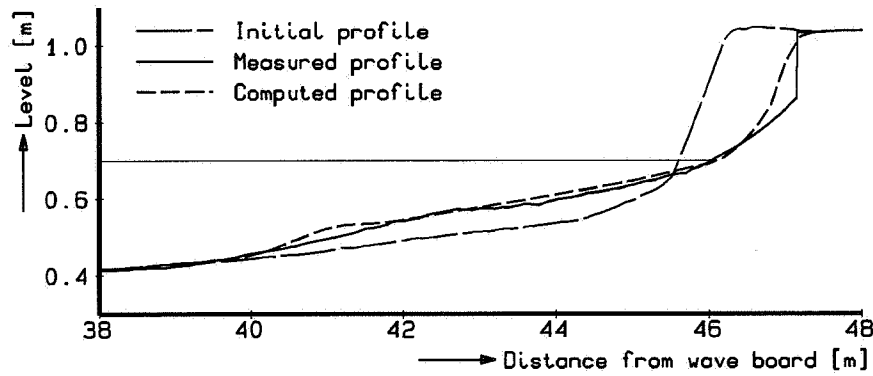


Figure 6.26 Comparison of final profiles for test T06 of M1819-I-series (fixed conditions).

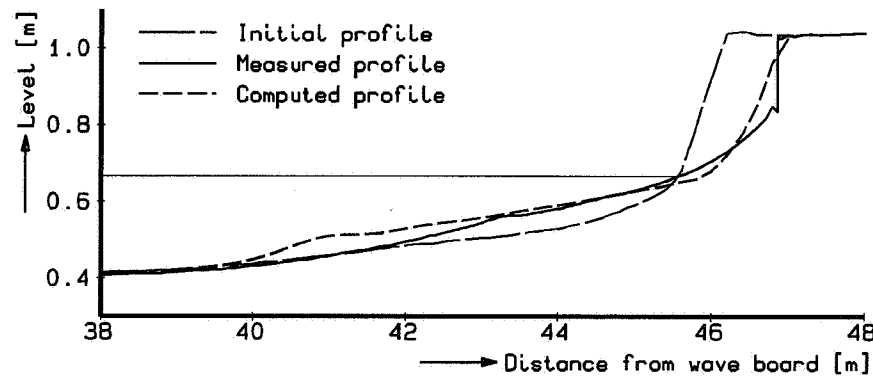


Figure 6.27 Comparison of final profiles for test T07 of M1819-I-series (fixed conditions).

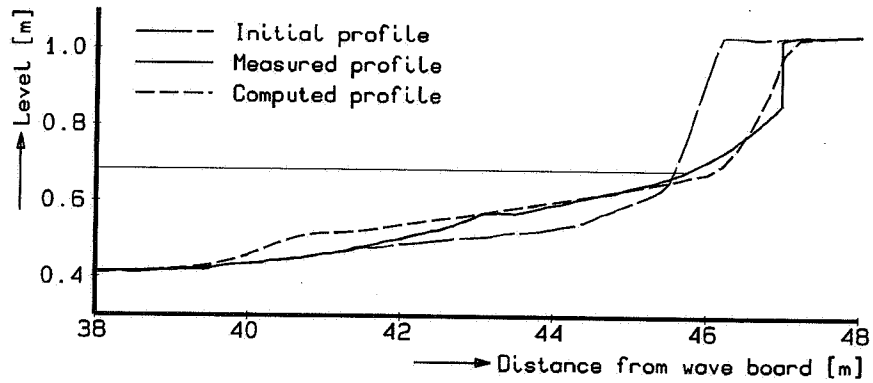


Figure 6.28 Comparison of final profiles for test T08 of M1819-I-series (fixed conditions).

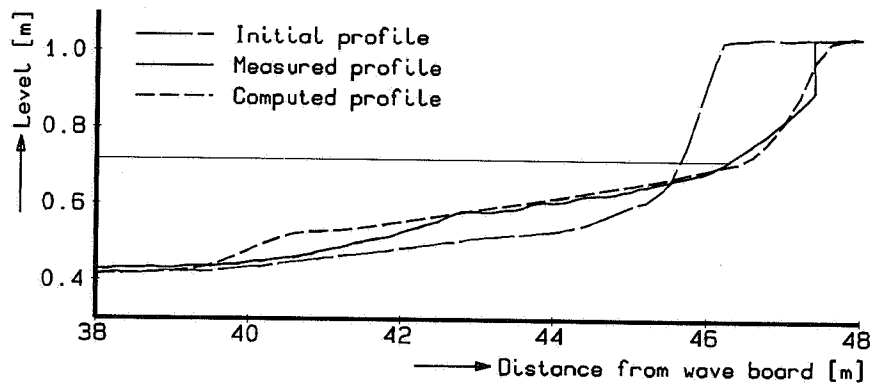


Figure 6.29 Comparison of final profiles for test T09 of M1819-I-series (fixed conditions).

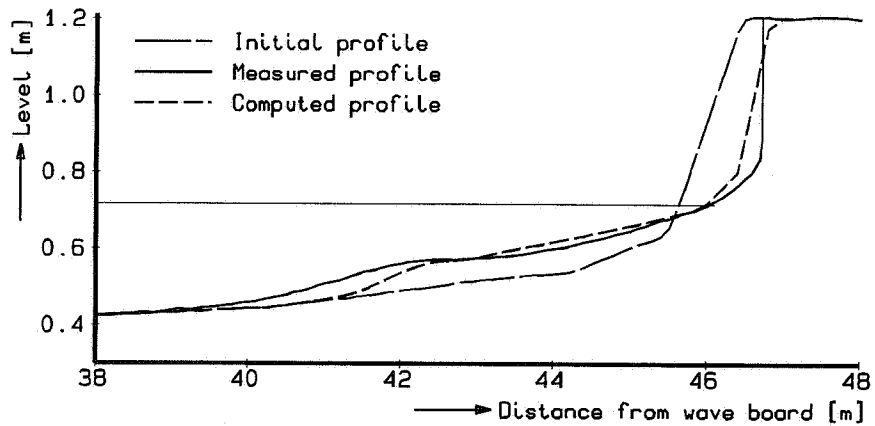


Figure 6.30 Comparison of final profiles for test T10 of M1819-I-series (fixed conditions).

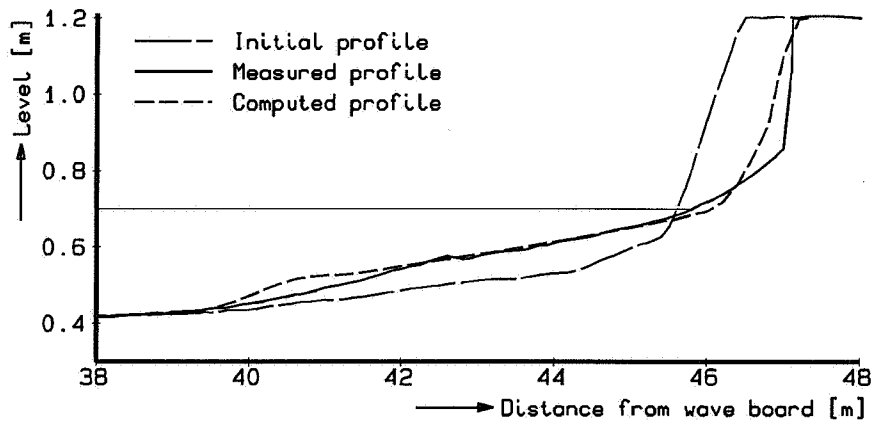


Figure 6.31 Comparison of final profiles for test T11 of M1819-I-series (fixed conditions).

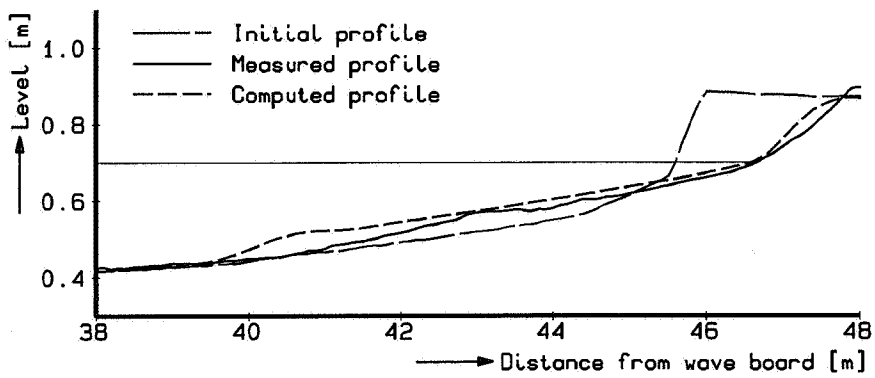


Figure 6.32 Comparison of final profiles for test T12 of M1819-I-series (fixed conditions).

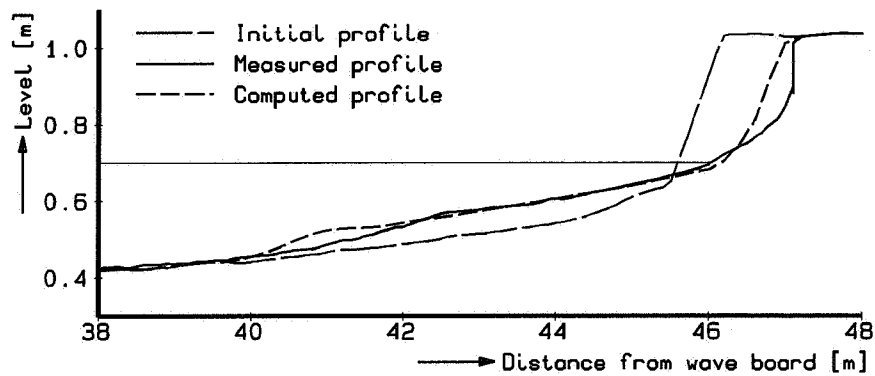


Figure 6.33 Comparison of final profiles for test T13 of M1819-I-series (fixed conditions).

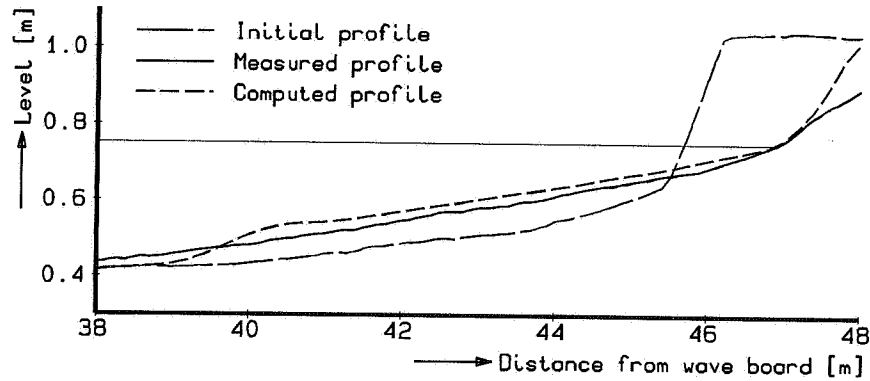


Figure 6.34 Comparison of final profiles for test T29 of M1819-I-series (fixed conditions).

A summary of computed and measured dune erosion quantities is presented in Table 6.6, in which the second number refers to the result of a computation using a different γ -factor (see Section 5.2).

test	A_d [m^3/m^1] after 6.0 hours			remarks
	Measured	Computed ^{*)}		
T01	0.2237	0.1967		
T02	0.3149	0.2626	0.3349	($\gamma = 0.95$)
T03	0.3888	0.3149	0.4009	($\gamma = 0.95$)
T04	0.3687	0.3325		reference test
T05	0.3324	0.2735	0.3305	($\gamma = 0.95$)
T06	0.3378	0.3002	0.3403	($\gamma = 0.90$)
T07	0.2682	0.2486		
T08	0.2874	0.2886		
T09	0.3580	0.3843		
T10	0.2917	0.2453		
T11	0.4303	0.3663		
T12	0.2547	0.2481		
T13	0.3221	0.2648	0.2284	($\gamma = 0.80$)
T29	0.5635	0.4657		

^{*)} Second number refers the result for the divergent γ -magnitude.

Table 6.6 Overview of dune erosion quantities for model tests with fixed hydraulic conditions of the M1819-I-series.

The systematic comparison between computed and measured erosion rates is presented in Section 6.4.

Test T21-T28 (varying conditions)

The varying conditions used for test T21 through T28 are shown in Figure 6.35.

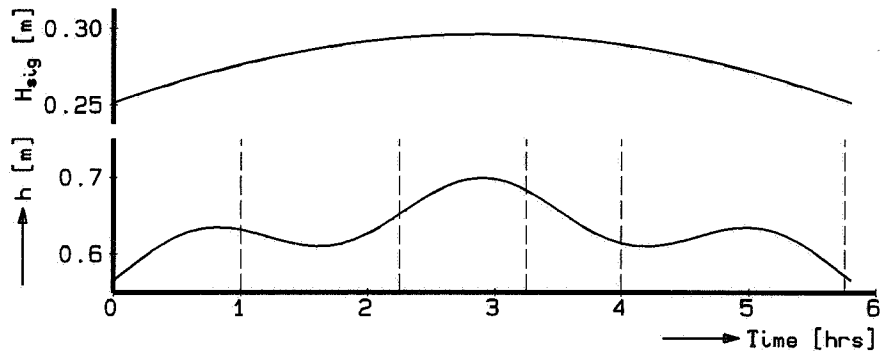


Figure 6.35 Hydraulic conditions used in tests T21-T28 of M1819-I-series.

The initial profiles that were tested are slightly exaggerated versions of actual coastal profiles along the Dutch coast. A brief characterization of each of the profiles is given in Table 6.7.

test	brief description
T21	reference test
T22	profile with a nearshore trough
T23	a very nearshore trough
T24	two bars
T25	two bars with one very close to the shore
T26	one bar
T27	a bar and a trough
T28	a very deep (tidal) gully

Table 6.7 Overview of model tests with varying hydraulic conditions of the M1819-I-series.

A 'nearshore' detail of these profiles is presented in Figure 6.36 also, showing the observed post-storm profile. It is noted that in this figure the cross-section for test T28 has been shifted 'landward' across 2 m to get a better comparison.

For the moulding of the profiles so-called 'Asserzand' has been used with $D_{50} = 90 \mu\text{m}$ (and $w_s = 0.0077 \text{ m/s}$).

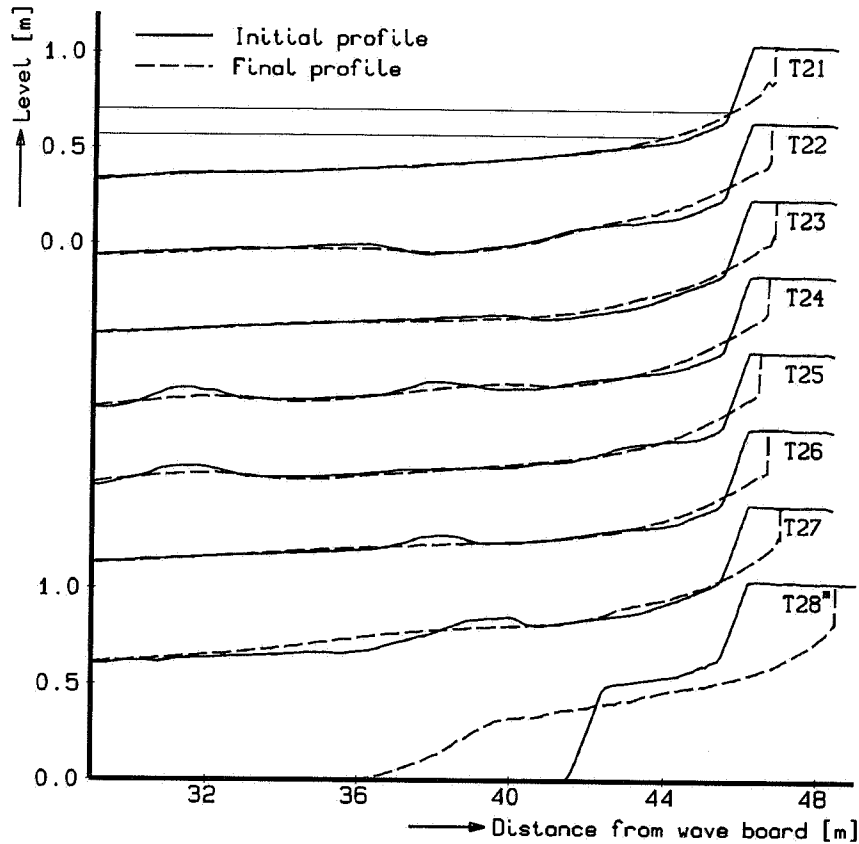


Figure 6.36 Overview of profiles used in the tests with varying hydraulic conditions.

The measured profile development of the reference test T21 (comparable to test T04, apart from the hydraulic conditions) is shown in Figure 6.37.

As can be observed, the amount of nett erosion does alter only slightly during the second phase of the storm surge. A major problem, however, is caused by the apparent sediment loss, since looking in more detail at the ultimate volumes present in the erosion and accretion areas show that a significant deficit is present. Landward of $x = 42$ m, an amount of $0.1411 \text{ m}^3/\text{m}^1$ is missing. This can also be observed from the T21-profile in Figure 6.36.

Since in the mathematical model the sediment balance is obeyed, mutual agreement will not be found by definition, as confirmed by the comparison between computed and measured profiles shown in Figure 6.38.

The development of both the measured and computed erosion quantity (above the maximum surge level) is shown in Figure 6.39.

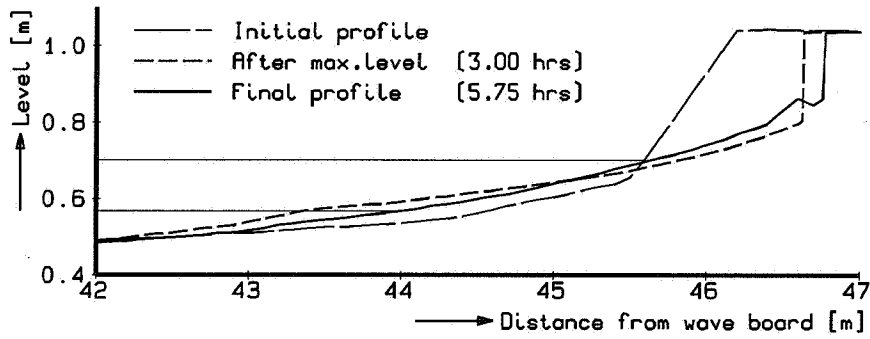


Figure 6.37 Observed profile development during storm surge for test T21 of the M1819-I-series.

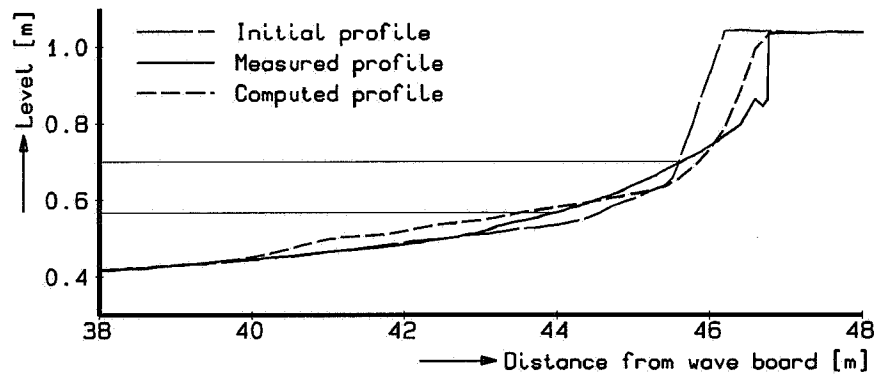


Figure 6.38 Comparison of the final profiles for test T21 of the M1819-I-series (varying conditions).

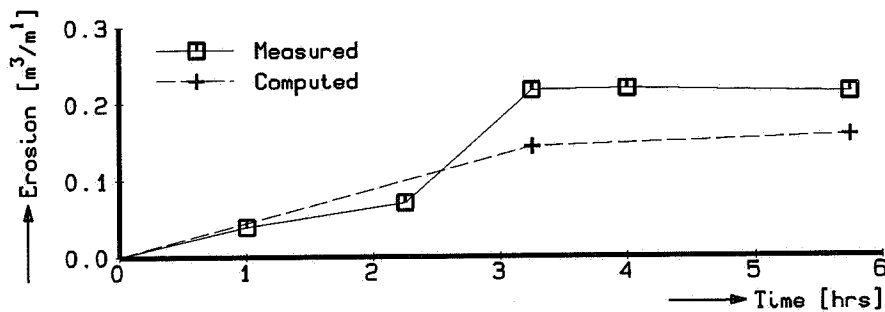


Figure 6.39 Erosion development during test T21 of the M1819-I-series.

As could be expected both the profiles and erosion rates agree moderately.

The detailed comparisons between measured and computed post-storm profiles for all the other tests, viz. test T22 through T28, are presented in Figure 6.40 through Figure 6.46.

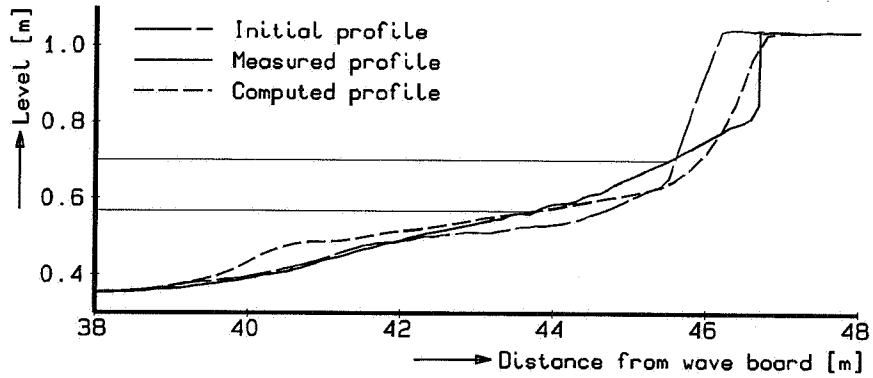


Figure 6.40 Comparison of final profiles for test T22 of M1819-I-series (var. conditions).

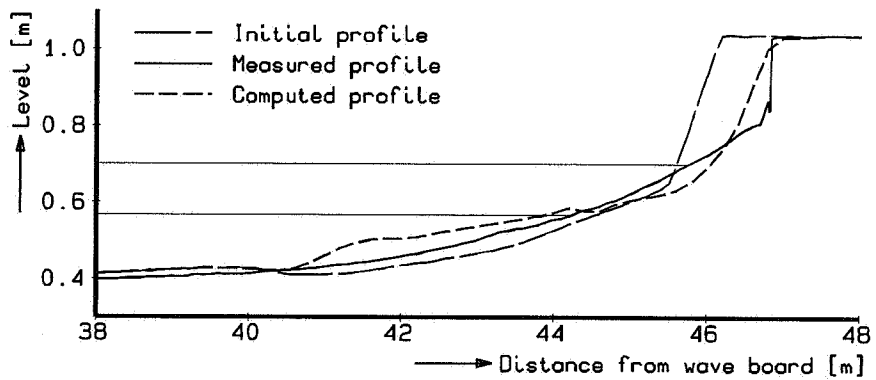


Figure 6.41 Comparison of final profiles for test T23 of M1819-I-series (var. conditions).

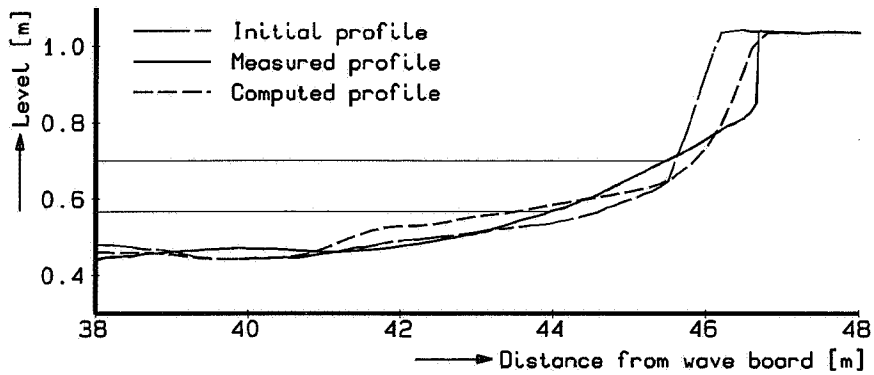


Figure 6.42 Comparison of final profiles for test T24 of M1819-I-series (var. conditions).

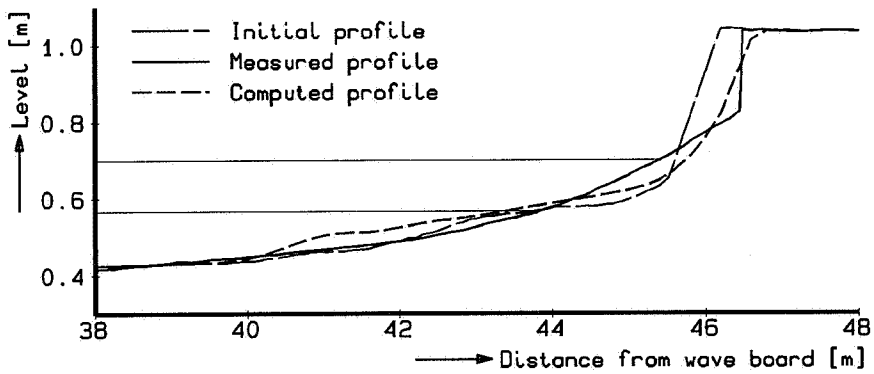


Figure 6.43 Comparison of final profiles for test T25 of M1819-I-series (var. conditions).

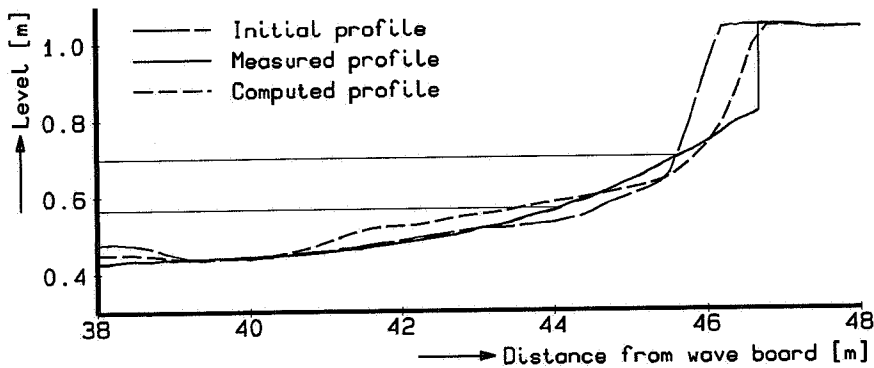


Figure 6.44 Comparison of final profiles for test T26 of M1819-I-series (var. conditions).

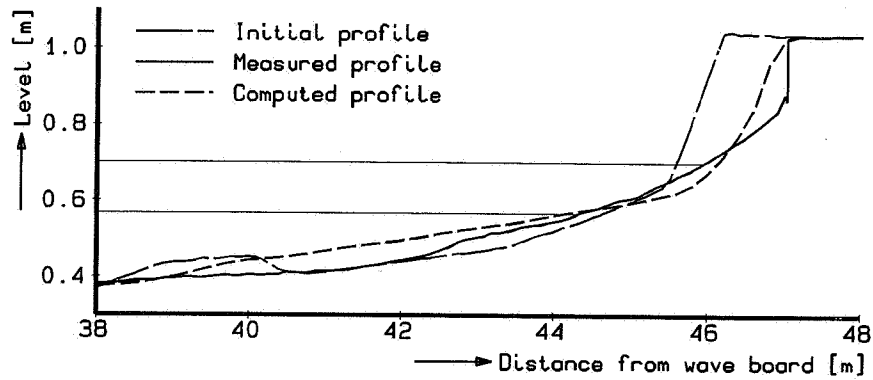


Figure 6.45 Comparison of final profiles for test T27 of M1819-I-series (var. conditions).

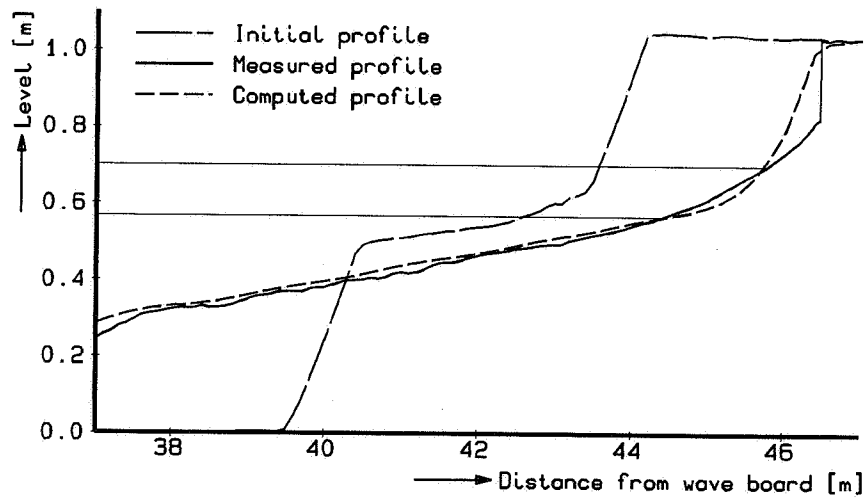


Figure 6.46 Comparison of final profiles for test T28 of M1819-I-series (var. conditions).

An overview of the complete post-storm profiles for test T21 through T27 according to measurements and computations is shown in Figure 6.47 and Figure 6.48 respectively.

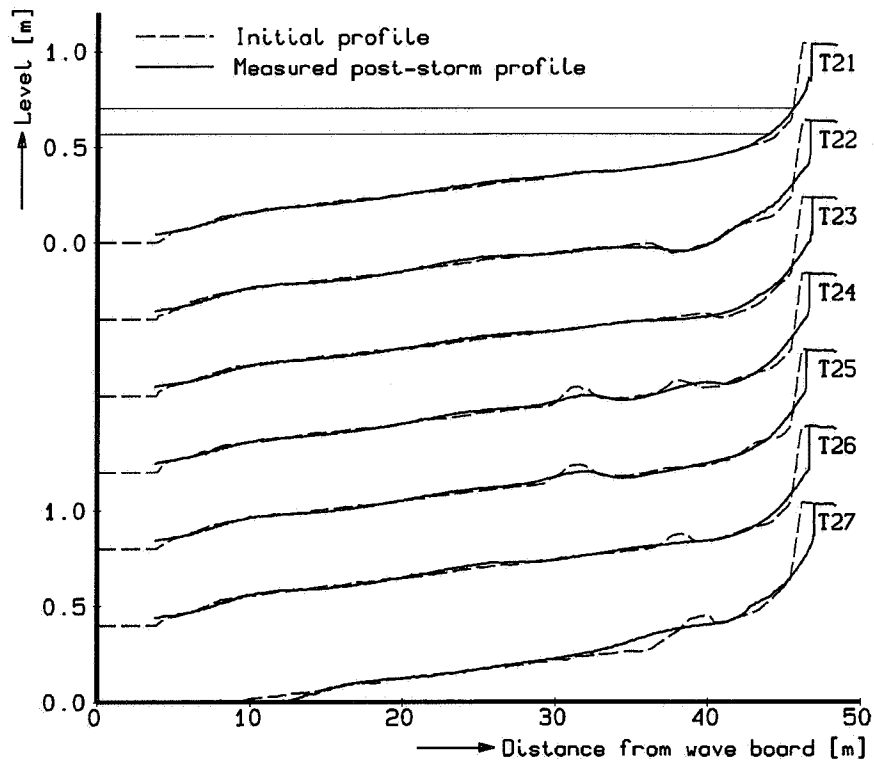


Figure 6.47 Overview of measured post-storm profiles for test T21-T27 of the M1819-I-series.

From this it can be observed that apart from the profile changes near the dune itself also distinct areas of erosion and accretion can be observed on the foreshore, viz. erosion in the $x \approx 15$ m area and accretion in the $x \approx 25$ m area in Figure 6.47. This phenomenon is probably due to the effects of (bound) long waves, see also (Steezel, 1986). Since these effects have not been taken into account in the mathematical model, these zones are absent in Figure 6.48.

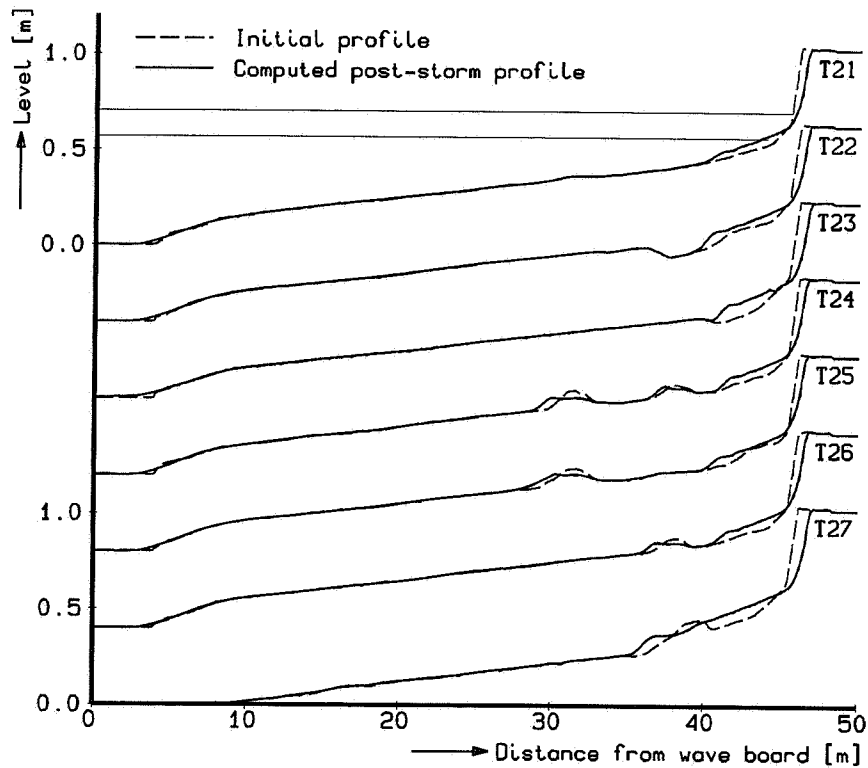


Figure 6.48 Overview of computed post-storm profiles for test T21-T27 of the M1819-I-series.

The flattening of the bars, as present in test T25, T26 and T27 occurs in both the measurements and the computations. Since this will affect the incoming wave height, an effect on the accompanying dune erosion rate will also be present.

A summary of computed and measured dune erosion quantities is presented in Table 6.8.

test	A_d [m^3/m^1] after 5.8 hours		remarks
	Measured	Computed	
T21	0.2096	0.1575	reference test
T22	0.1994	0.1787	
T23	0.2393	0.2128	
T24	0.1721	0.1500	
T25	0.1225	0.1304	
T26	0.1997	0.1578	
T27	0.2982	0.2476	
T28	0.8020	0.7726	

Table 6.8 Overview of dune erosion quantities for model tests with varying hydraulic conditions of the M1819-I-series.

The presence of troughs and bars has a large impact on the amount of dune erosion. Relative to the result of reference test T21 ($0.2096 \text{ m}^3/\text{m}^1$) the actual erosion varies from $0.1225 \text{ m}^3/\text{m}^1$ (test T25) to $0.2982 \text{ m}^3/\text{m}^1$ (test T27), showing a deviation of $\pm 40\%$.

M1819-III-series, test T1

The hydraulic conditions present during this test are shown in Figure 6.49 (DELFT HYDRAULICS, 1983d).

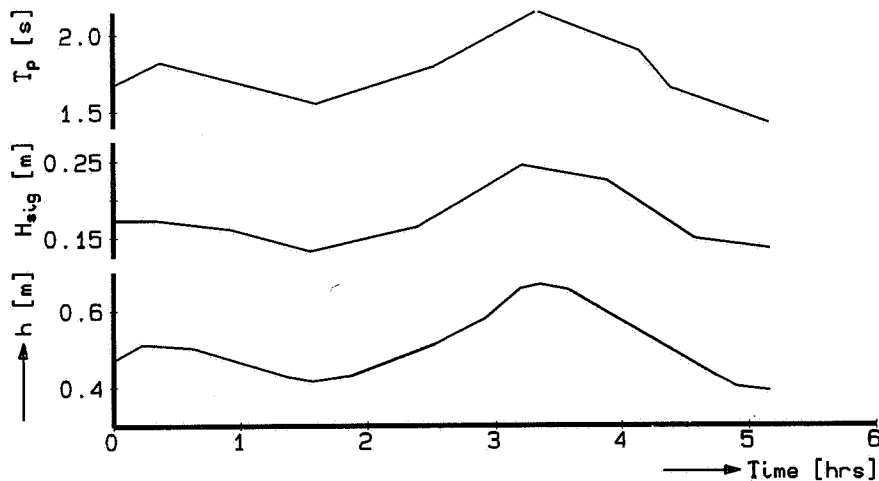


Figure 6.49 Hydraulic conditions used in the M1819-III-series.

Figure 6.50 shows a comparison between the measured and computed profile development, viz. the post-storm profile.

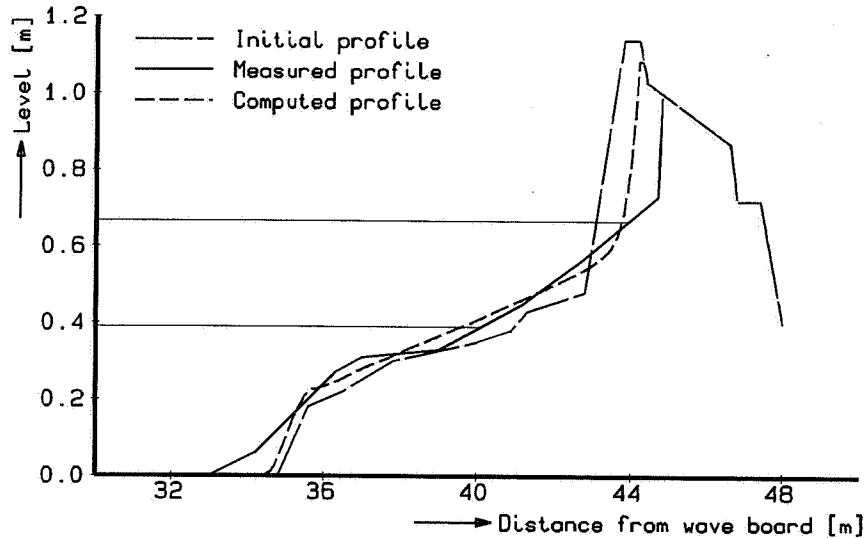


Figure 6.50 Comparison between measured and computed final profiles for test T1 of the M1819-III-series.

Although the average profile in the middle section shows a fair resemblance, overall agreement, especially compared to the results of large-scale tests, is only moderate.

The computed erosion rate of $0.29 \text{ m}^3/\text{m}^1$ under-estimates significantly the measured volume of $0.54 \text{ m}^3/\text{m}^1$.

The loss in sediment volume is estimated to amount to $0.14 \text{ m}^3/\text{m}^1$, being about 25% of the eroded volume. However, this deficit only partially explains the discrepancy in the dune erosion volumes.

6.2.4 Other laboratory data

In the following the comparisons between the outcome of the mathematical model and the results of some non-DELFT HYDRAULICS laboratory tests are presented.

One of the primary test series was carried out by Saville in 1957. These results were used by Larson (see Section 3.4) to develop his SBEACH-model (Larson and Kraus, 1988a). Since this test was carried out using regular waves, no comparison with the present model was made.

For an additional verification of the model's result the data from a test series conducted in 'das Große Wellen Kanal' have been used. More details are provided in the following.

GWK-series

An overview of the hydraulic conditions used in this test series is given in Table 6.9, see also (Dette and Uliczka, 1986, 1988).

test	h [m]	H_{sig} [m]	T_p [s]	t [hrs]	remarks
T1	5.0	1.50	6.0	9.75	erosion up to revetment
T2	3.0	0.50	4.0	5.60	
T3	3.0	1.00	6.0	8.45	
T4	3.0	0.50	4.0	2.40	
T5	3.0	0.50	10.0	2.75	very low wave steepness
T6	4.0	1.40	6.0	4.01	

Table 6.9 Overview of the model tests of the GWK-series.

As can be observed a great range of fixed hydraulic conditions have been used. This, however, provides the opportunity to carry out a decent and valuable verification of the model. The results for each of the six tests are discussed briefly in the following. For the moulding of each of the profiles sand with $D_{50} = 225 \mu\text{m}$ was used.

In the case of test T1, fair agreement between computed and measured final profiles is found, as shown in Figure 6.51. Both the position and level of the 'seaward' end of the erosion profile, at a water depth of approximately $1.2 H_s$, as well as the average slope of the erosion profile agree well. With respect to the amount of erosion above the mean water level, the mathematical model omits to carry off a small amount of material from the upper part of the concrete 1 : 6 slope. The total amount of erosion is therefore somewhat too small, viz. $19.8 \text{ m}^3/\text{m}^1$ instead of $22.0 \text{ m}^3/\text{m}^1$.

The apparent sediment loss amounts $2.2 \text{ m}^3/\text{m}^1$, being 12 % of the total erosion volume ($30.7 \text{ m}^3/\text{m}^1$).

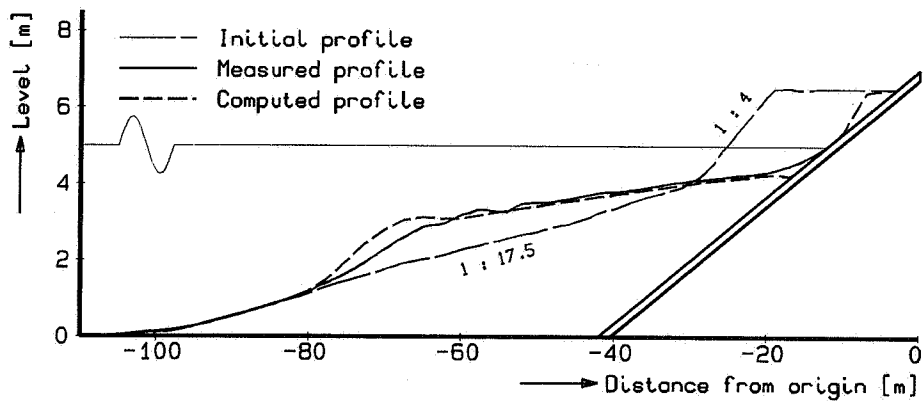


Figure 6.51 Comparison of profile development for test T1 of the GWK-series.

A comparison between the measured and computed post-storm profiles for test T2 is presented in Figure 6.52 and in more detail in Figure 6.53.

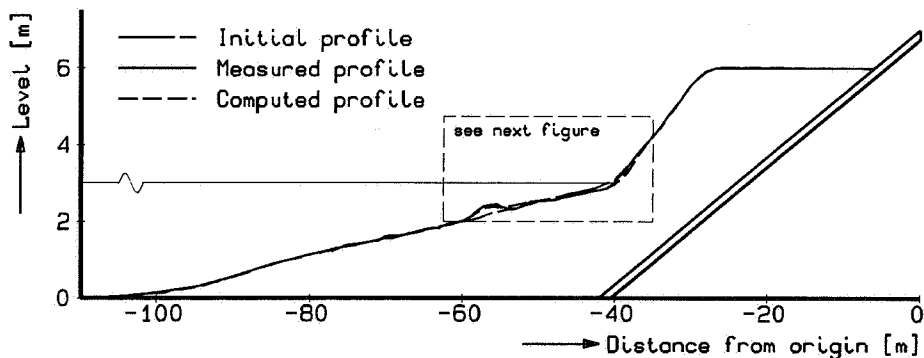


Figure 6.52 Comparison of profile development for test T2 of the GWK-series.

Both in the mathematical model and the physical model only small changes in cross-shore profile are found. This is mainly due to the relative small wave of $H_s = 0.50$ m and the small characteristic wave steepness of about 2.0%. As can be seen from the detail, both the average slope of the erosion profile as well as the position and level of its 'seaward' end are reproduced correctly. For the water depth here, once more a magnitude of about $1.2 H_s$ is found.

The computed dune erosion rate amounts to $0.49 \text{ m}^3/\text{m}^1$ and even exceeds the measured magnitude of $0.13 \text{ m}^3/\text{m}^1$. This rather unexpected fact can, at least for the most part, be

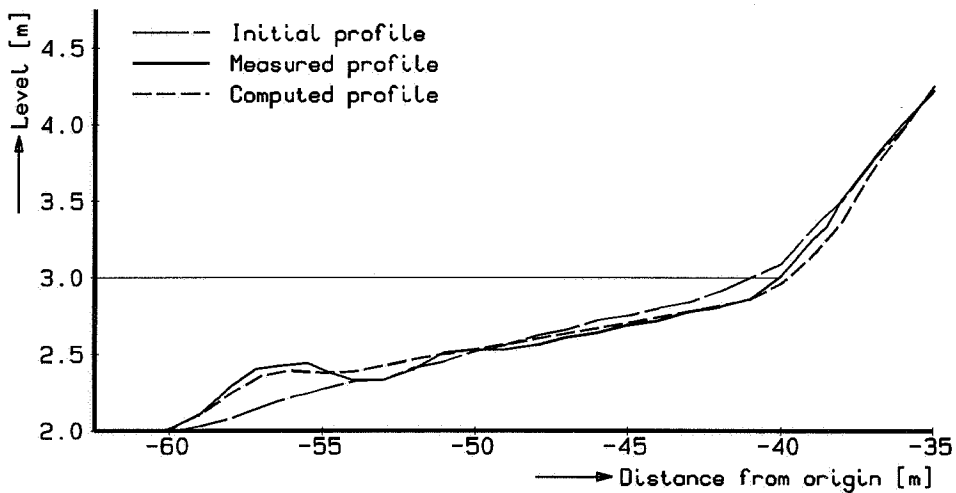


Figure 6.53 Detailed comparison of profile development for test T2 of the GWK-series.

explained from the overall sediment balance, since from this it was found that a gain of $0.13 \text{ m}^3/\text{m}^1$ occurred.

This negative loss is probably due to secondary effects, viz. transports perpendicular to the flume axis. The latter may provide an effect if a test starts with a flat initial bed and the soundings are carried out in only one central ray.

It is noted that this apparently odd dune erosion result is not taken into account in the determination of the model's accuracy (see Section 6.5), although the overall agreement in the accompanying post-storm profiles can be qualified as good.

The comparison between the measured and computed final profile for test T3 is presented in Figure 6.54.

The final shape of the erosion profile shows good resemblance with the measured profile. This holds especially for the 'seaward' part of the profile. Near the duneface considerably larger discrepancies are found. The computed erosion rate amounts to $4.50 \text{ m}^3/\text{m}^1$ and exceed once more the measured magnitude of $3.67 \text{ m}^3/\text{m}^1$, while a gain in sediment volume was also found here, viz. $A_{er} - A_{ac} = 6.57 - 7.15 = -0.58 \text{ m}^3/\text{m}^1$. A fair comparison between the accretion volume for the physical and mathematical model yields $7.15 \text{ m}^3/\text{m}^1$ and $7.09 \text{ m}^3/\text{m}^1$ respectively, providing good agreement.

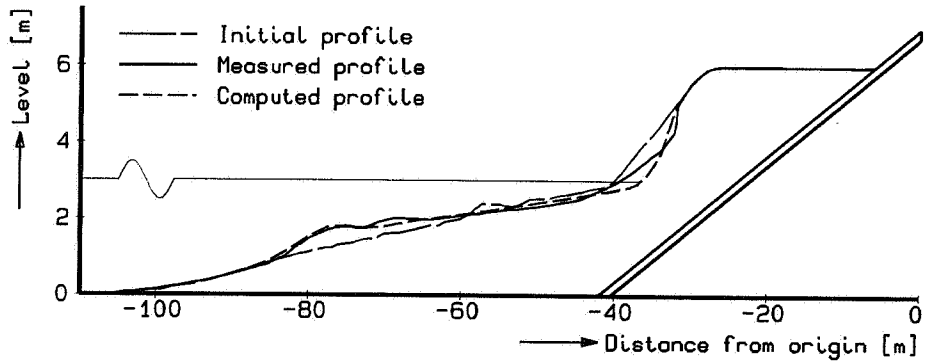


Figure 6.54 Comparison of profile development for test T3 of the GWK-series.

A comparison between the measured and computed profile development for test T4 is presented in Figure 6.55 and Figure 6.56 respectively.

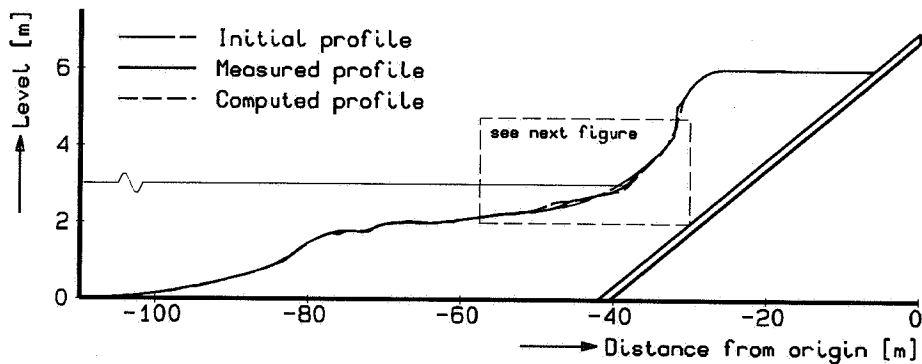


Figure 6.55 Comparison of profile development for test T4 of the GWK-series.

As can be observed a fair resemblance is found. A quantitative judgement with respect to the measured and computed dune erosion volumes of 0.22 and 0.43 m^3/m^1 , is complicated by the not-closed sand balance. A total amount of 0.12 m^3/m^1 is missing, viz. 0.42 m^3/m^1 erosion and only 0.30 m^3/m^1 accretion.

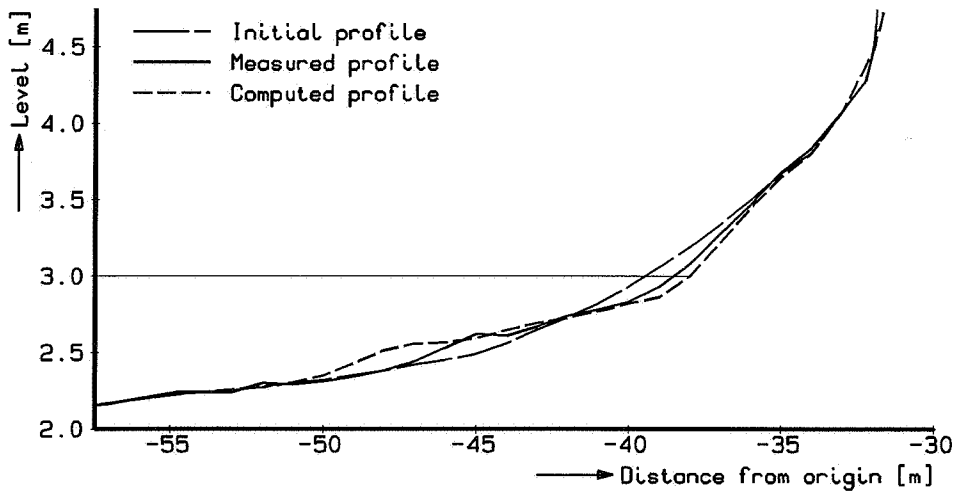


Figure 6.56 Detailed comparison of profile development for test T4 of the GWK-series.

For test T5 the comparisons between the measured and computed profile development is presented in Figure 6.57 and Figure 6.58.

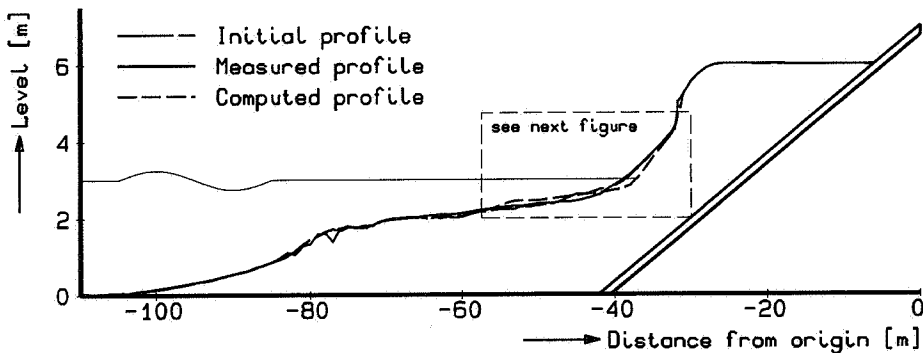


Figure 6.57 Comparison of profile development for test T5 of the GWK-series.

As can be seen from the detail no satisfactory agreement is found. Since waves of very low steepness, viz. 0.3% (small wave height in combination with a long wave period), were used in this test, this is what could be expected. The offshore-directed transport will be partly balanced by the effects of onshore transports. As a consequence, the outcome from the mathematical model for both the erosion and accretion exceeds the volumes found in the physical model. The observed dune erosion value is even negative, demonstrating the

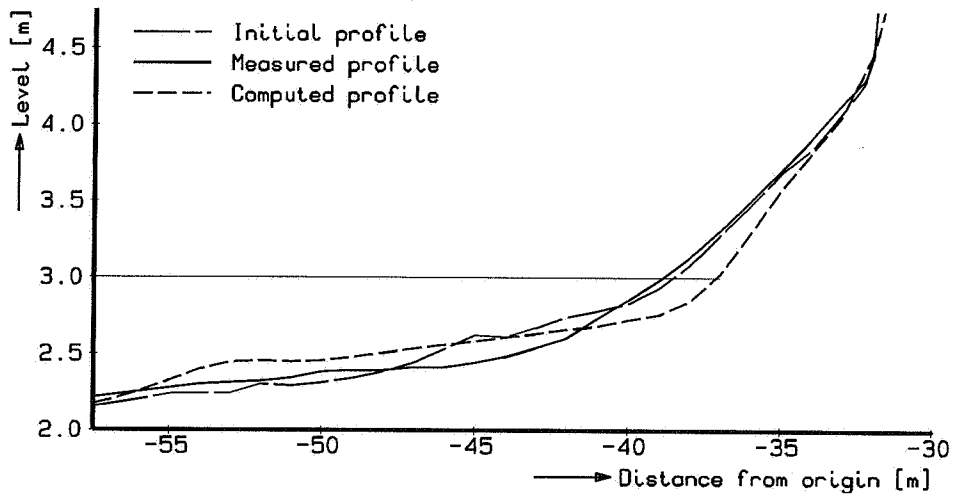


Figure 6.58 Detailed comparison of profile development for test T5 of the GWK-series.

presence of onshore transports.

Since the recovery of a storm profile due to effects of the wave asymmetry is not (yet) accounted for in the model (see also Section 9.3), no agreement will be found for these conditions by definition.

A comparison between the measured and computed post-storm profile for the last test, viz. **test T6**, is given in Figure 6.59.

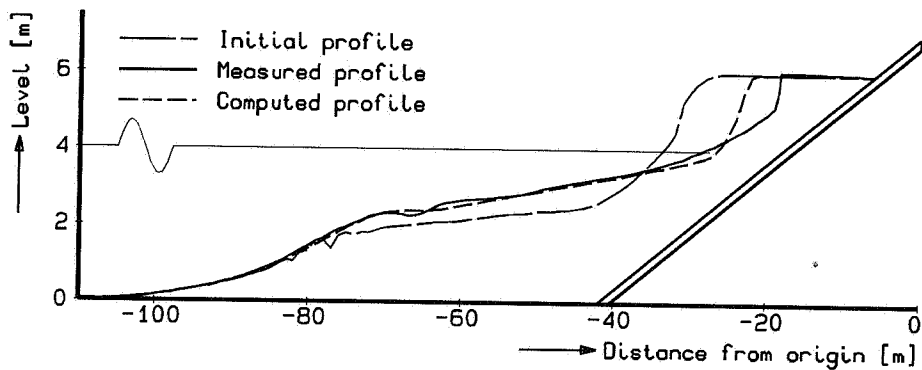


Figure 6.59 Comparison of profile development for test T6 of the GWK-series.

As can be seen good agreement is found here, both for the position and level of the 'seaward' end of the erosion profile (at about $1.2 H_s$ water depth) and the slope of the profile. The amount of dune erosion is, however, under-predicted, yielding $14.29 \text{ m}^3/\text{m}^1$ instead of $19.40 \text{ m}^3/\text{m}^1$. This discrepancy is partly due to a sediment loss of $1.93 \text{ m}^3/\text{m}^1$.

In summary, good agreement is found between the measured and predicted post-storm profiles. The dependency on the governing hydraulic conditions is also found to be good. The level of the seaward end was estimated to be about $1.2 H_s$ below the mean water level. It is noted that the significantly lower ratio, viz. 0.75 as used in the DUROS-model and is found in the M1263-III-tests, is caused by the significant difference in the average slope of the foreshore. In this test series a $1 : 20$ slope was used.

It is noted that the results of test T2, T4 and T5 will not be used for the assessment of the model's accuracy since the effect of a non-closed sediment balance disturbs the related volumes significantly, although apart from the T5-result, the resemblance in the observed and computed final profiles seems rather encouraging.

For more details on the elaborations presented, reference is made to (Steezel, 1992b).

6.2.5 Summary and conclusions

In general good agreement is found between the shape, slope and position of the 'seaward' erosion profiles. This holds especially for the experiments carried out in large-scale facilities, such as DELFT HYDRAULICS' Deltaflume and 'das Große Wellen Kanal'.

Less resemblance is found for the amount of dune erosion above the maximum surge level. The test results indicate that this is for the most part due to the non-constant compaction of the sand in the flume.

The residual error is related to the 'non-perfect' schematization of the transport distribution in the swash zone.

6.3 Additional field data

6.3.1 Introduction

In the following, the estimated profile developments and governing hydraulic conditions for some additional field data are described, followed by a comparison with the outcome of a computation.

It should be noted that, relative to the data from laboratory facilities, both the assessment of the cross-shore profiles (especially the pre-storm profile) and the actual hydraulic conditions cause problems as they are hard to obtain, see e.g. (Steetzel, 1992d).

In spite of the above, in the following is dealt with the impacts of three well-documented, extreme surges.

6.3.2 The 1953 storm surge

As mentioned before, up till now the 1953 storm surge is the most extreme storm which ever attacked the Dutch coastline. Although no information is available on the post-storm erosion profile under water, the amount of dune erosion was recorded in a stretch of the coast called 'Delfland' which showed a large spreading, ranging from 55 to 155 m³/m¹, see e.g. (Vellinga, 1986).

The hydraulic conditions as assumed to be present during the surge at the -20 m depth contour are given in Figure 6.60.

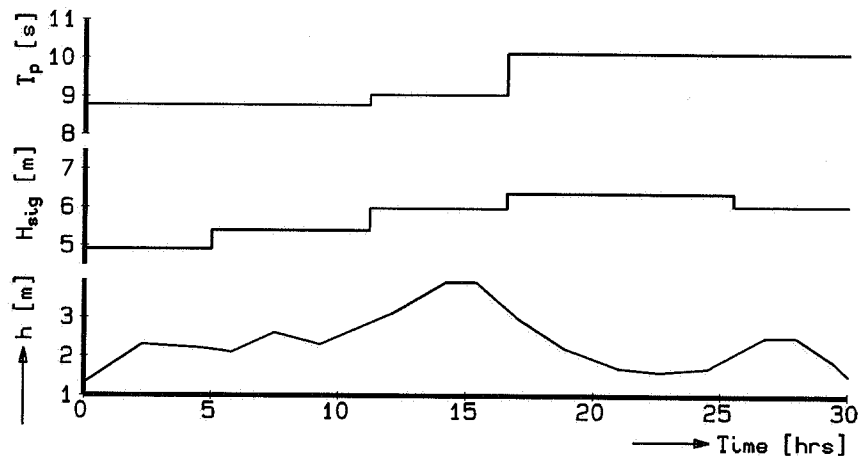


Figure 6.60 Hydraulic conditions during the 1953-storm surge.

The computed profile development is presented in Figure 6.61. The computed amount of dune erosion, viz. 72 m³/m¹, is comparable with the estimated mean value of 90 m³/m¹.

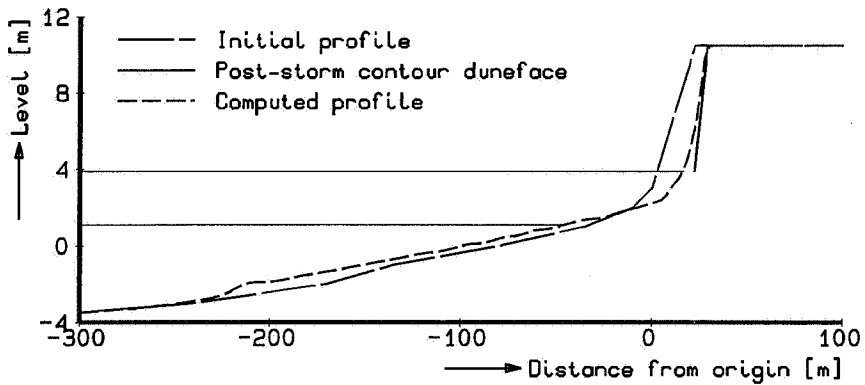


Figure 6.61 Computed erosion due to 1953-storm surge.

6.3.3 Hurricane Eloise

The 'Eloise-case' has been studied by Vellinga (1986) also in order to verify the DUROS-model (DELFT HYDRAULICS, 1983c), see also (Hughes and Chiu, 1981). The hydraulic conditions as assumed to be present during the hurricane are shown in Figure 6.62.

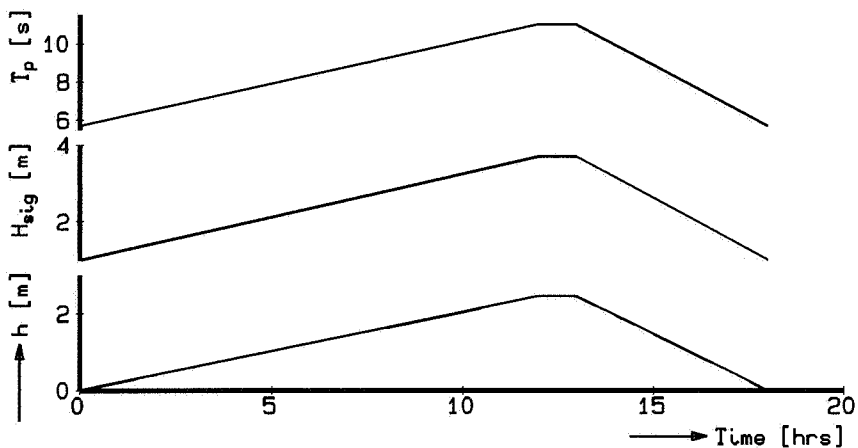


Figure 6.62 Hydraulic conditions during hurricane Eloise.

The computed profile development is presented in Figure 6.63.

There is a decent resemblance between the computed and measured erosion quantity. From

the measured contours the erosion was estimated to be $32.6 \text{ m}^3/\text{m}^1$, whereas a computed measure of $38.3 \text{ m}^3/\text{m}^1$ is found.

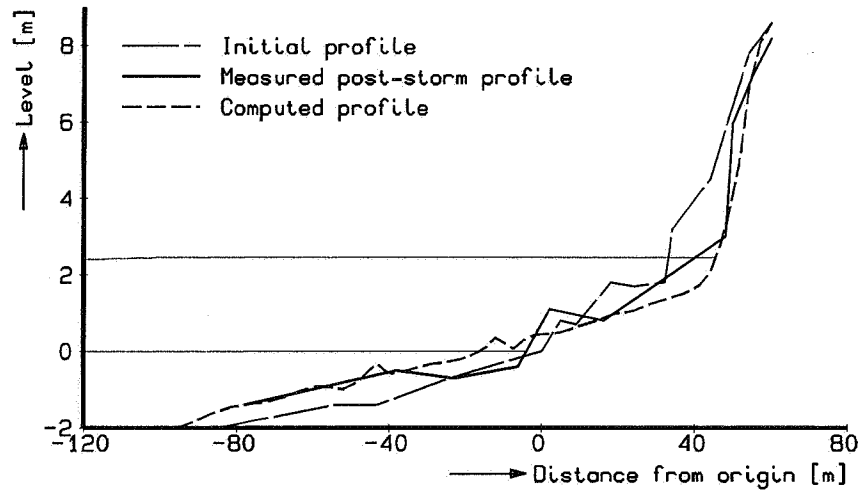


Figure 6.63 *Computed erosion due to the hurricane Eloise.*

It should be noted that the prototype sand balance is not closed, viz. a loss of $10.3 \text{ m}^3/\text{m}^1$ is present for the interval $-78 < x < +60 \text{ m}$.

6.3.4 Extreme event in South Africa

The impact of an extreme condition on an artificial beach in South Africa is described by Möller and Swart (Möller and Swart, 1988; Swart, 1990).

The hydraulic conditions as assumed to be present during this extreme event are shown in Figure 6.64.

The computed profile development is presented in Figure 6.65. The post-storm profile was only measured in three points on the dry beach. The estimated erosion is $54 \text{ m}^3/\text{m}^1$, whereas the mathematical model yields $45.6 \text{ m}^3/\text{m}^1$.

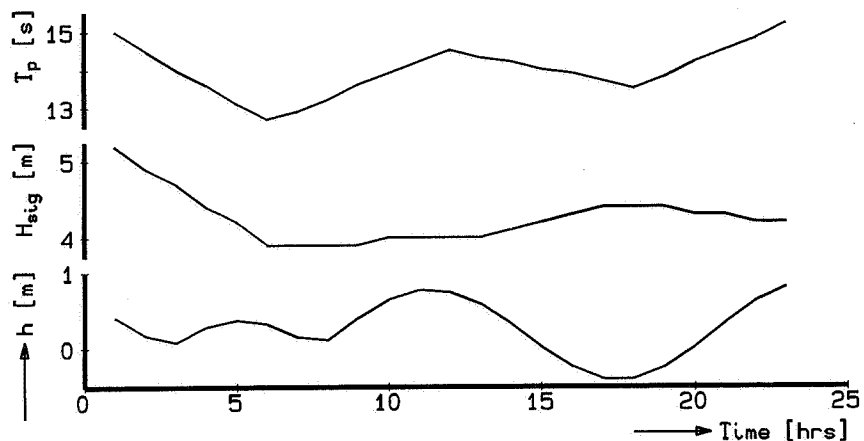


Figure 6.64 Hydraulic conditions during the extreme event.

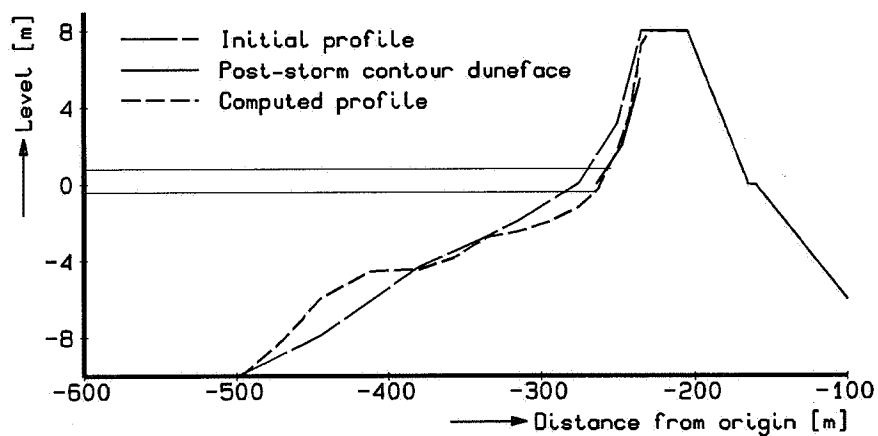


Figure 6.65 Computed erosion due to the extreme event.

6.3.5 Other Dutch storm events

A less severe storm surge took place in January 1976. The surge level only reached a level which was slightly higher than the level of the average dune foot (about NAP+3 m) and, consequently, the amount of erosion was limited. An average value of $32 \text{ m}^3/\text{m}^1$ was found along the whole Dutch coast.

The detailed measurements of the pre- and post-storm profiles for the so-called 'Krokus'-storm surge allowed for a detailed examination of the profile development for three regions along the Dutch coast. However, since this surge was also moderate, the impact of this storm surge was relatively small compared with the profile fluctuations (Steetzel, 1992d). It is noted that the assessment of the hydraulic conditions was studied in more detail for this analysis. Some principal results are presented in Section 8.2.

6.3.6 Summary and conclusions

For the presented cases fair agreement is found between the measured and computed dune erosion quantities, this in spite of the fact that both the pre- and post-storm profiles are not known in detail.

The observed scatter in the results will probably increase if less extreme surges are tested. For that reason, using moderate prototype conditions do not allow for a reliable verification of the mathematical model involved. Moreover, the onshore transport during milder conditions is not accounted for in the model.

6.4 Systematic comparisons

6.4.1 Introduction

In the following sections the actual effect of the hydraulic condition on the amount of dune erosion above maximum surge level will be outlined in more detail. Next the influence of the shape of the initial profile on the erosion quantity will be illustrated.

Use will be made of the results of the M1819-I-test series. For more details on the tests involved, reference is made to Section 6.2.3.

Both the results of model tests and computational model will be given in terms of the amount of erosion above the storm surge level, namely after 6.0 model hours (for constant hydraulic conditions) and after the storm in the case of varying hydraulic conditions.

6.4.2 Effect of the water level

Figure 6.66 shows the influence of the water level on the amount of erosion, using the results of tests T07, T08, T04, T09 and T29 of the M1819-I-series (see Section 6.2.3).

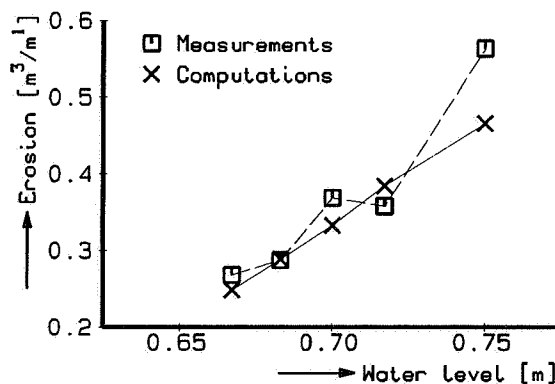


Figure 6.66 *Effect of the water level on the erosion quantity.*

A higher water level causes in both the physical model and computation more erosion, showing a similar trend. An increase of 0.05 m in the surge level results in about 40 % increase in erosion. As will be shown later, the storm surge level is the most relevant parameter with respect to storm surge erosion. See also Section 7.5.

6.4.3 Effect of the wave height

Due to an increase in wave height the amount of erosion above the maximum water level also increases. The results of the four physical and mathematical test runs (tests T01-T04) are shown in Figure 6.67. In the case that computations were carried out for two different γ -values, both the results are given. It should be noted that a comparable wave steepness was used in these tests. A 0.05 m increase in wave attack initially results in 20 to 30 % extra erosion and is therefore not as vital as the surge level.

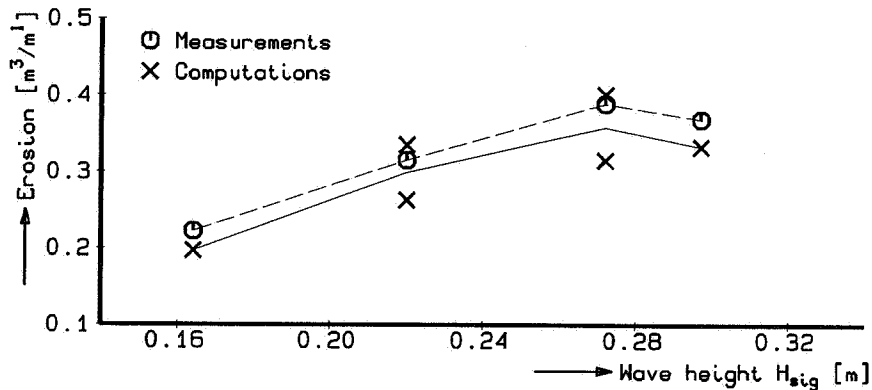


Figure 6.67 Effect of the wave height on the erosion quantity.

It should be remarked that in the case of extreme wave attack with high deep water waves the effects of wave breaking on the foreshore is very effective in decreasing the wave height. This foreshore breaking causes the effective wave height practically not to increase any longer.

The additional increase in erosion for the more extreme wave heights will therefore be partly due to water level rise related to the additional wave set-up, induced from the breaking waves (Steetzel, 1990b).

6.4.4 Effect of the wave period

As for the wave period almost the same arguments are valid. An increase in wave period will allow the incoming wave to reach the dune without too much breaking. An incoming wave with longer wave period will last longer due to the fact that it does not break too fast because of the wave's steepness.

Figure 6.68 shows the comparison between the measured and computed quantities of erosion for two different wave heights, using the test results of T01 and T13 and T05, T06 and T04.

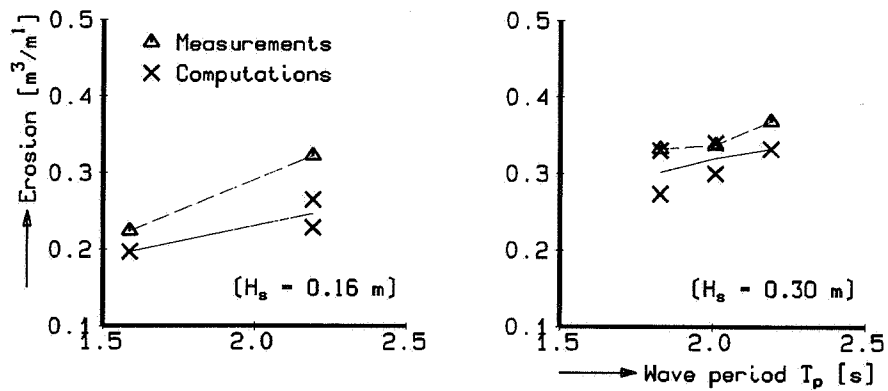


Figure 6.68 Effect of the wave period on the erosion quantity.

The measured and computed trends are similar and show an increased erosion rate for larger wave periods.

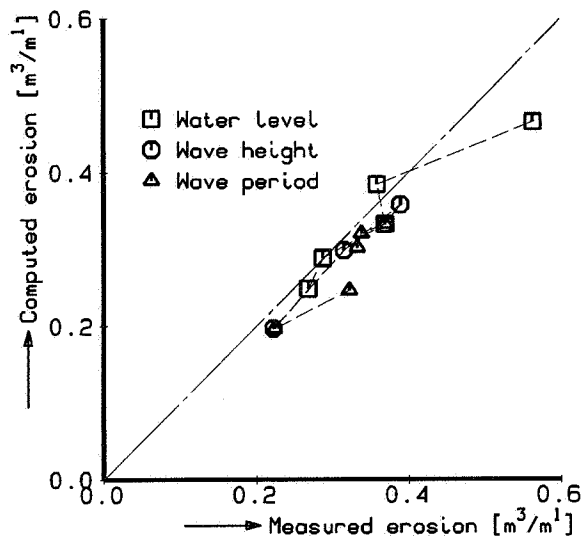


Figure 6.69 Comparison between measured and computed erosion rates for tested hydraulic conditions.

6.4.5 Summary of the tested hydraulic effects

Figure 6.69 summarizes the computed effects of the hydraulic conditions on the amount of erosion above the maximum surge level by a preliminary comparison between measured and computed values.

A quantitative statement about the accuracy of the mathematical model is presented in Section 6.5.

6.4.6 Effect of the dune height

Figure 6.70 shows the influence of the dune height using test T12, T04 and T11 respectively.

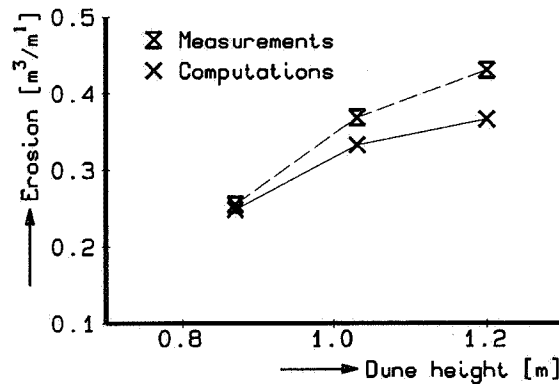


Figure 6.70 Effect of dune height on the erosion quantity.

A higher dune results in an increase in the dune erosion volume. This dependency is also found in the outcome of the mathematical model. A certain shift of a more or less fixed erosion profile in a situation with a relatively high dune, causes more erosion than the same shift in the case of a relatively low dune. So, for geometrical reasons the dune front recession for higher dunes will be smaller, although the erosion quantity (expressed in m³/m³) will be larger than for a low dune. The latter effect is shown in the figure.

6.4.7 Effect of initial cross-shore profile

With respect to the cross-shore profile a number of small-scale tests have been carried out with bars and/or gullies, see Table 6.7 for more details.

Effect of bars

The tests with bars (test T24, T25 and T26) show that a bar may have two effects on the erosion.

If such a bar is situated well outside the active zone, the amount of erosion will decrease due to the reduction in wave heights above this bar. If the bar is situated near the dunefoot the amount of sand which is required from the dune for the development a storm profile will be less and, consequently, will result in less erosion.

Effect of troughs and gullies

In the case of a trough (test T22, T23, and T27) or gully (test T28) near the dune the amount of erosion will increase strongly. If this gully is situated more seaward, then the effect on the amount of dune erosion will be negligible.

The results of both the physical and mathematical test runs are shown in Figure 6.71.

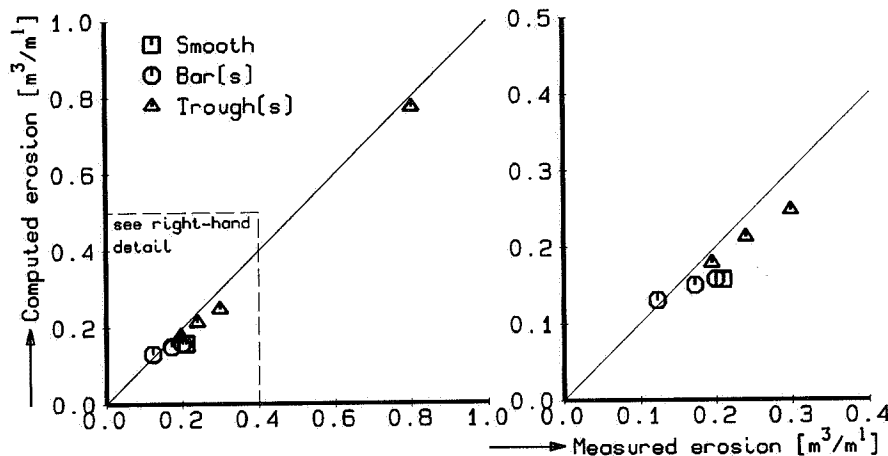


Figure 6.71 Effect of bars and troughs on the erosion quantity.

Relative to the 'smooth' profile (test T21), the presence of bars yields smaller erosion rates, whereas the presence of troughs and gullies has the opposite effect.

6.4.8 Overall summary of tested parameters

Figure 6.72 shows an overall comparison between measured and computed erosion quantities for both constant and varying hydraulic conditions.

The agreement was considered to be rather good which in fact means that the effect of the hydraulic conditions on the dune erosion process was modelled in a reliable way.

A quantification of the model's quality is elaborated in the following.

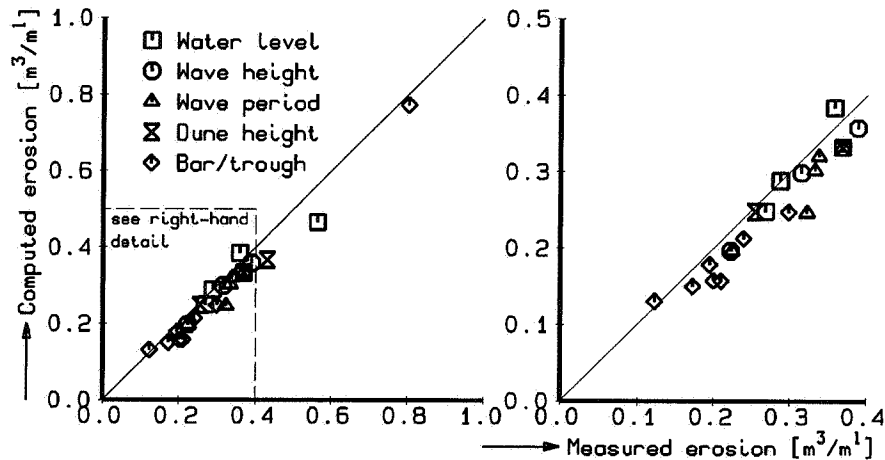


Figure 6.72 Overview of test results for all tested conditions.

6.5 Accuracy of the prediction model

6.5.1 Introduction

In the previous sections an opinion about the performance of the mathematical model was formed on merely qualitative arguments, whereas in the following a quantitative measure will be defined with respect to the model's accuracy.

Since the model has to be used to compute and assess the expected amount of dune erosion, this measure has been used to quantify the correctness.

It should be noted that the formulation and calibration of the model are based on the hydrodynamic and morphodynamic processes acting on the erosion profile (see Chapter 4 and 5). The amount of erosion above the water level is derived from the computed transports in the breaker zone.

For more details, reference is made to (Steetzel, 1992b).

6.5.2 Comparison of dune erosion quantities

For all the tests described in Section 6.2 and 6.3, both the measured and computed amount of erosion above the maximum surge level have been determined.

A comparison between measured and computed erosion rates is presented in Figure 6.73, whereas the pertaining list of used symbols is shown in Table 6.10.

The two dashed lines refer to the spreading in the results around the best fit relation.

□	M1819-I	T1-T13, T29	↑	M1811	T1
○	M1819-I	T21-T28	×	GWK	T1, T4, T6
△	M1819-III	T1	Z	Storm surge	1953
+	M1263-III	T1, T3-T5	Y	Hurricane	Eloise
×	H298-I	T5	⊗	Extreme event	
◇	M1797	T1			

Table 6.10 Overview of symbols used for accuracy assessment.

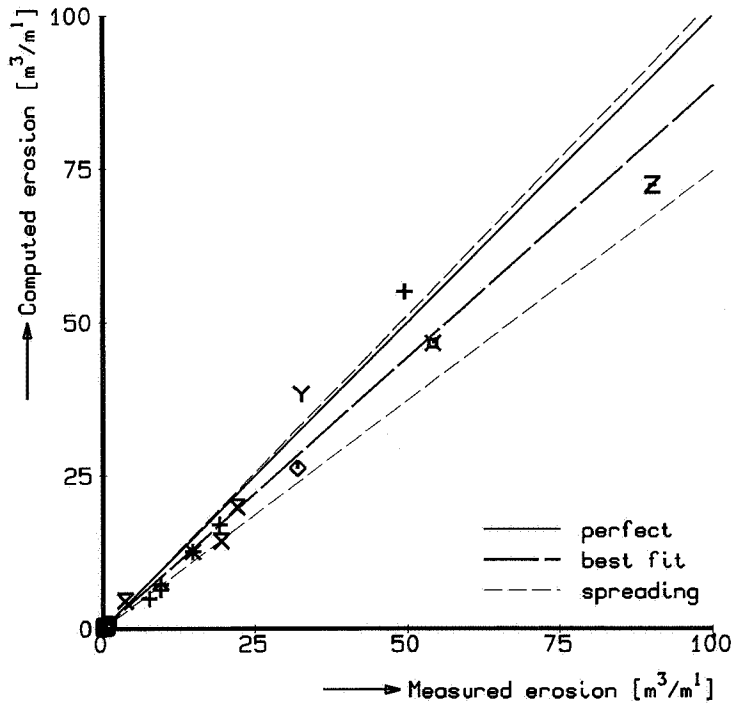


Figure 6.73 Comparison between measured and computed erosion rates; linear scales.

A detail of this figure, showing the small-scale data in more detail is presented in Figure 6.74, whereas Figure 6.75 shows this relation in a log-log-plot.

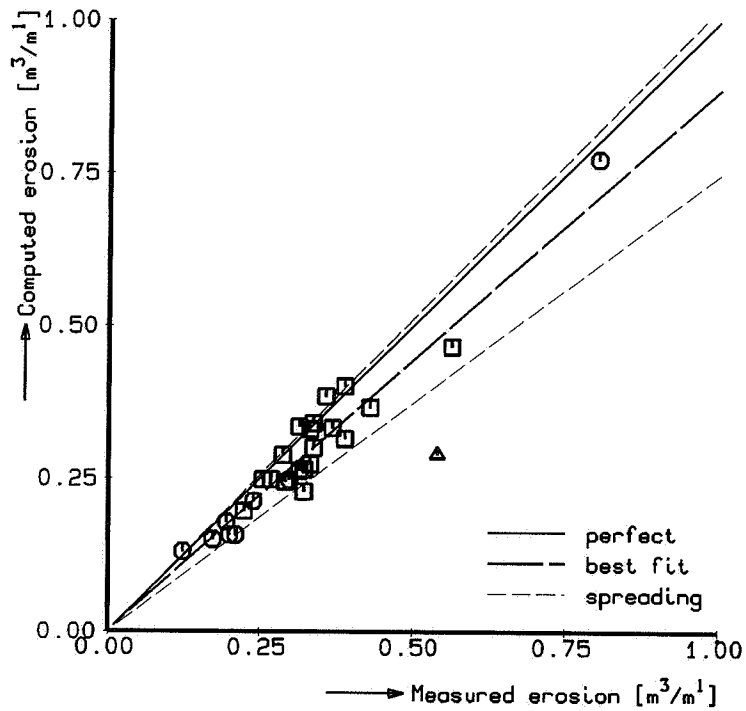


Figure 6.74 Detail of the comparison between measured and computed erosion rates; linear scales.

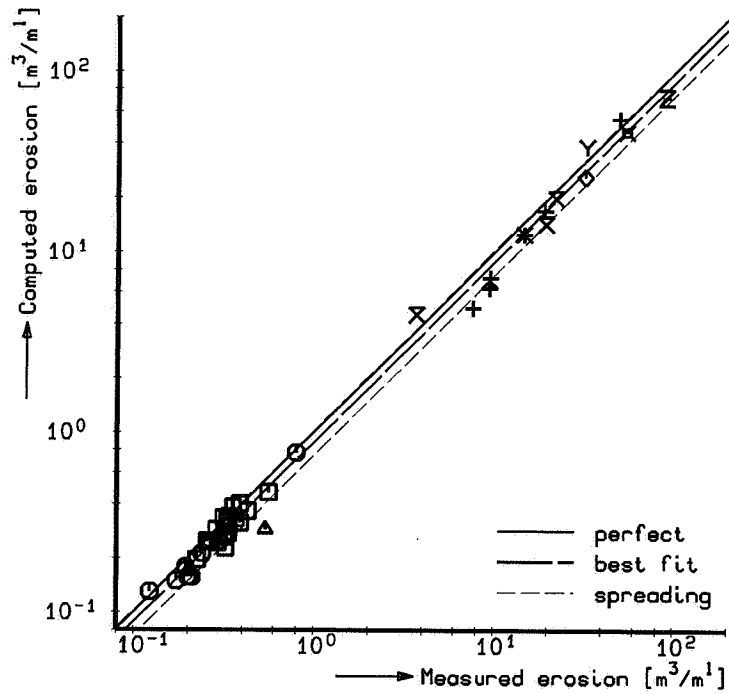


Figure 6.75 Comparison between measured and computed erosion rates; logarithmical scales.

As mentioned earlier, a systematic under-estimation of the observed erosion rates occurs. A detailed analysis between the measured (A_m) and computed erosion rates (A_c), shows that the average under-prediction equals 11.5%, namely:

$$A_c = (0.885 \pm 0.139) A_m \quad (6.5.1)$$

in which the standard deviation σ equals 13.9%.

For the sake of convenience details of the small-scale and large-scale data are presented in Figure 6.76 and Figure 6.77 respectively, using the symbols as shown in Table 6.10.

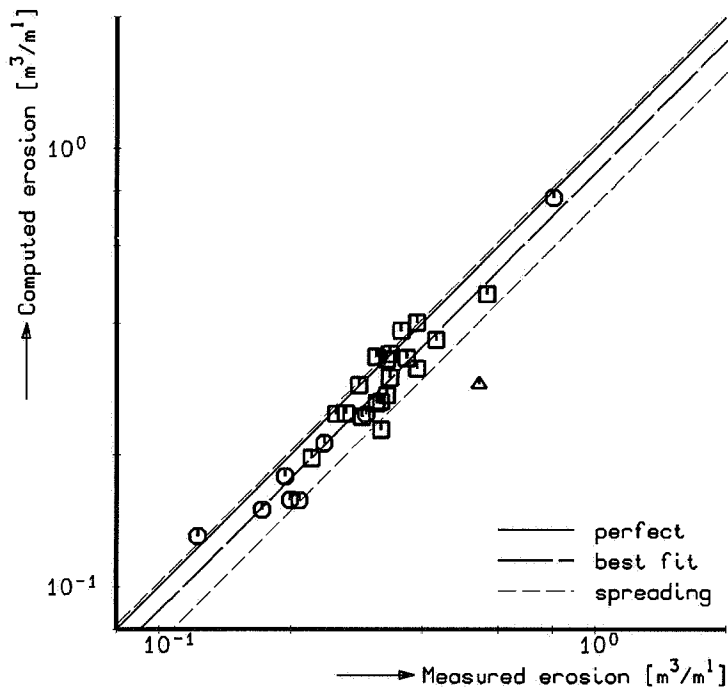


Figure 6.76 Comparison between measured and computed erosion rates for small-scale data.

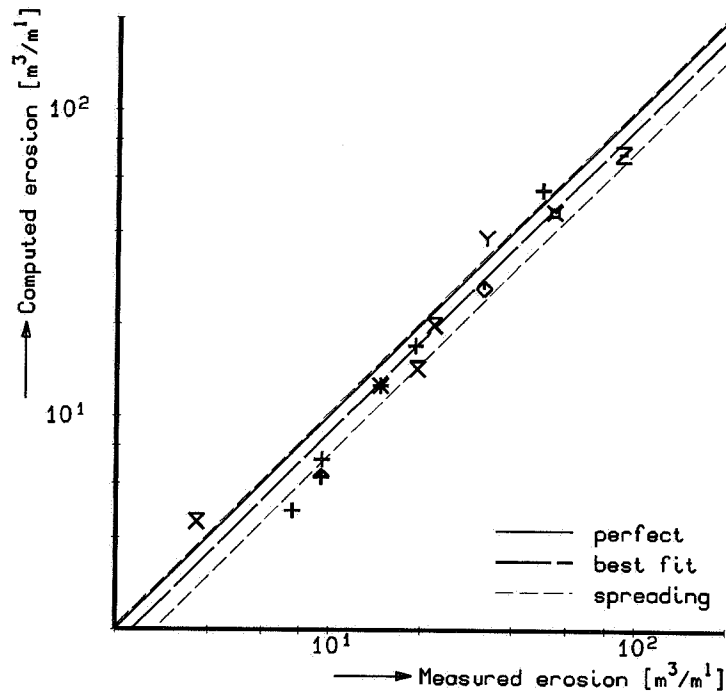


Figure 6.77 Comparison between measured and computed erosion rates for large-scale data.

6.5.3 Summary and conclusions

Perfect agreement, viz. $A_c = (1.0 \pm \sigma) A_m$ (with $\sigma \downarrow 0$) is not reached so far (see Section 9.3 for recommendations).

The effect of a spatially non-constant porosity and the still imperfect assessment of the transport distribution in the swash zone are accountable for these shortcomings.

In order to assess the expected dune erosion quantity A , for the time being the reverse version of Equation (6.5.1) has to be used, namely:

$$A = (1.120 \pm 0.195) A_c \quad (6.5.2)$$

Consequently, the expected erosion rate ranges from 92 to 132 % of the computed value.

6.6 Structures

6.6.1 Introduction

In the following a distinction is made between the profile development that occurs in case of very high revetments and low revetments.

Subsequently, some remarks on scour hole development and the relative effect of dune erosion present for low revetments are made.

6.6.2 High revetments

With a sufficiently high revetment or seawall, dune erosion from the duneface is completely obstructed. Consequently, a scour hole will develop in front of the structure in order to provide material for the moulding of the required 'seaward' profile. In the following some results from laboratory tests as well as the accompanying computational result are presented.

It is noted that some general considerations on scour hole development based on both model investigations and literature review are presented in (Steetzel, 1988).

M1819-III-series, test T4 (DELFT HYDRAULICS, 1983d)

A comparison between the measured and computed profile development is presented in Figure 6.78.

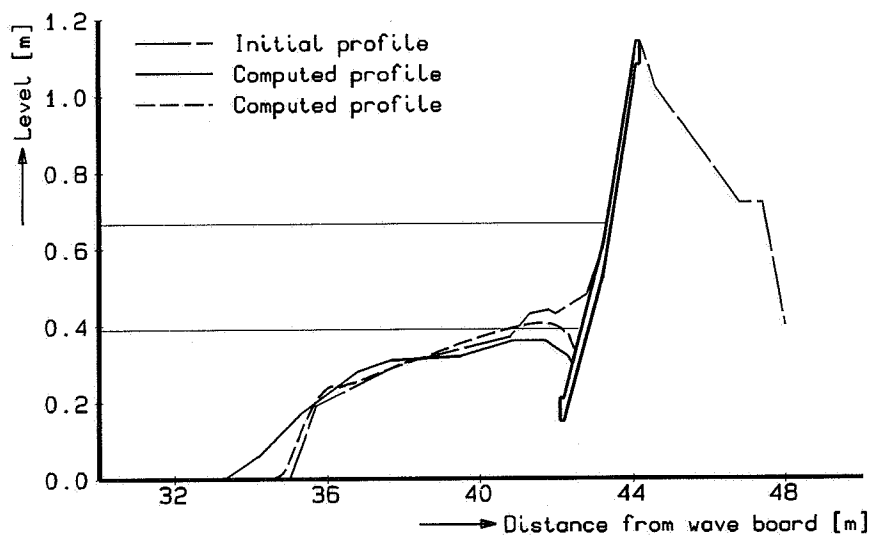


Figure 6.78 Comparison of final profiles for test T4 of the M1819-III-series.

The hydraulic conditions are similar to those used in the test with an unprotected dune, viz. T1 (see Figure 6.49).

As can be observed, fair resemblance is found although the extent and depth of the scour hole in front of the structure. Scour hole itself is somewhat under-predicted.

M2051-II-series (DELFT HYDRAULICS, 1986a)

This research programme was carried out in order to obtain insight into the effectiveness of dune toe revetments, especially in the extent of the scour hole in front of the structure. Small-scale tests were performed for two different slopes for both fixed and varying hydraulic conditions (Steetzel, 1986).

The hydraulic conditions used in test T1 and T4 are presented in Figure 6.79.

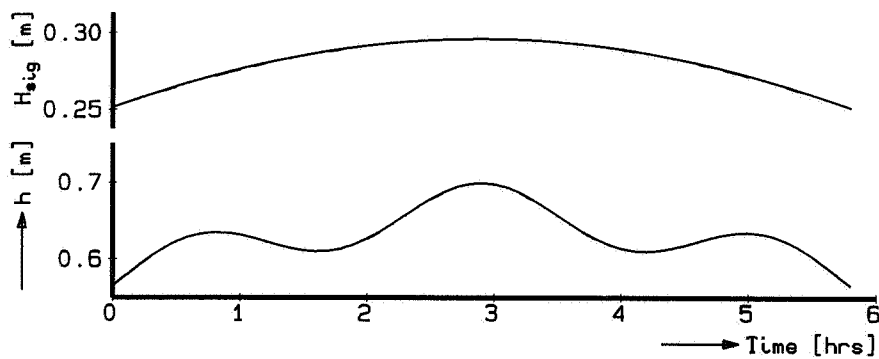


Figure 6.79 Hydraulic conditions used in test T1 and T4 of the M2051-II-series.

A comparison between the measured and computed post-storm profile for test T1 is presented in Figure 6.80.

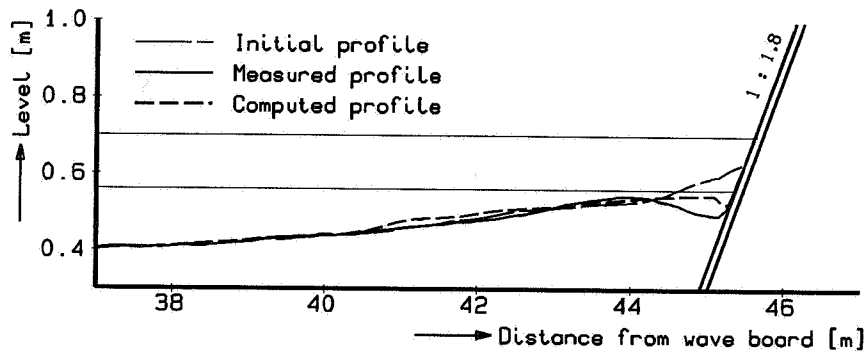


Figure 6.80 Comparison of scour-hole development for test T1 of the M2051-II-series.

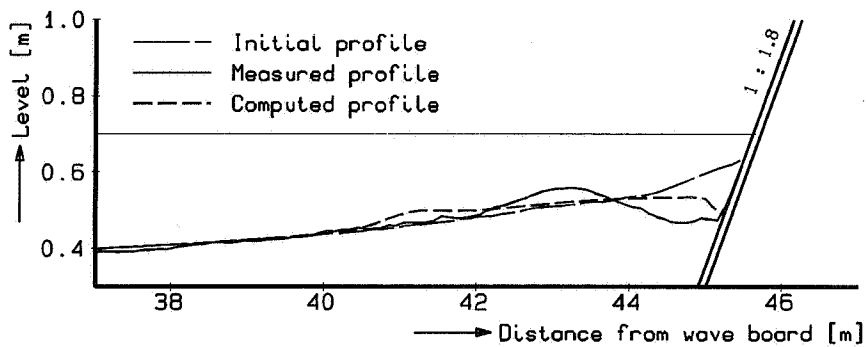


Figure 6.81 Comparison of scour-hole development for test T2 of the M2051-II-series.

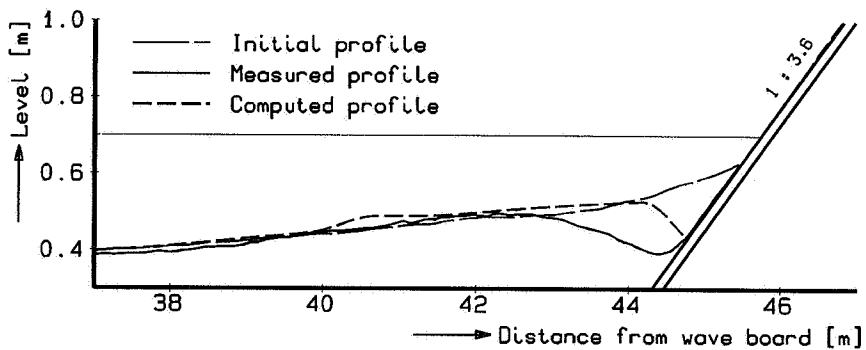


Figure 6.82 Comparison of scour-hole development for test T3 of the M2051-II-series.

Comparisons between the measured and computed scour hole development for the other tests, viz. test T2, T3 and test T4 are given in Figure 6.81 through Figure 6.83.

In general, fair agreement is found between the outcome of the mathematical model and the observed profile development. The final extent and depth of the scour holes is under-predicted by the mathematical model, although the level of the intersection between the beach and the revetment agrees well.

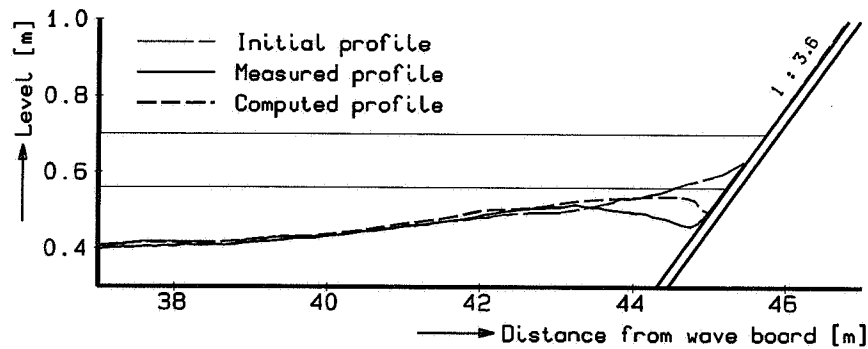


Figure 6.83 Comparison of scour-hole development for test T4 of the M2051-II-series.

H298-I-series, Test T1

An overview of all the tests performed in this research programme is presented in Table 6.11. The objective was to verify the results of former presented small-scale tests, viz. the M2051-II-series, and to study the profile development for low revetments (Steetzel, 1987b).

test	hydraulic conditions	h (m)	H_{sig} (m)	T_p (s)	brief description
T1	constant	4.20	1.50	5.4	high revetment
T2	constant	4.20	1.50	5.4	medium height
T3	constant	4.20	1.50	5.4	low revetment
T4	varying	< 4.20	< 1.85	< 5.4	as test T3
T5 ^{*)}	constant	4.20	1.50	5.4	unprotected dune

^{*)} Comparable to test T2 of M1263-III-series.

Table 6.11 Overview of the model tests of the H298-I-series.

A comparison between measured and computed scour hole development for large-scale test T1 is presented in Figure 6.84.

The results for test T2 through T4 will be discussed in the next section, whereas for the results of the 'unprotected dune case', viz. test T5, reference is made to Section 6.2.2 (see Figure 6.19).

As can be observed, the same comments as given for the small-scale tests also hold for the outcome of this large-scale test.

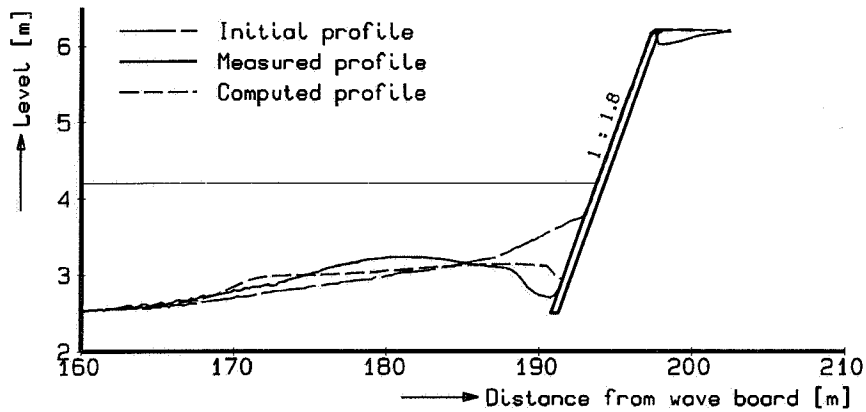


Figure 6.84 Comparison of scour-hole development for test T1 of the H298-I-series.

6.6.3 Low and hidden revetments

In the case of less high or even low revetments, erosion from the duneface is allowed up to a certain degree only. Some results of relevant laboratory tests and the accompanying model outcome are presented hereafter.

M1797-series, test T2 (DELFT HYDRAULICS, 1982b)

A comparison between measured and computed profile development is presented in Figure 6.85.

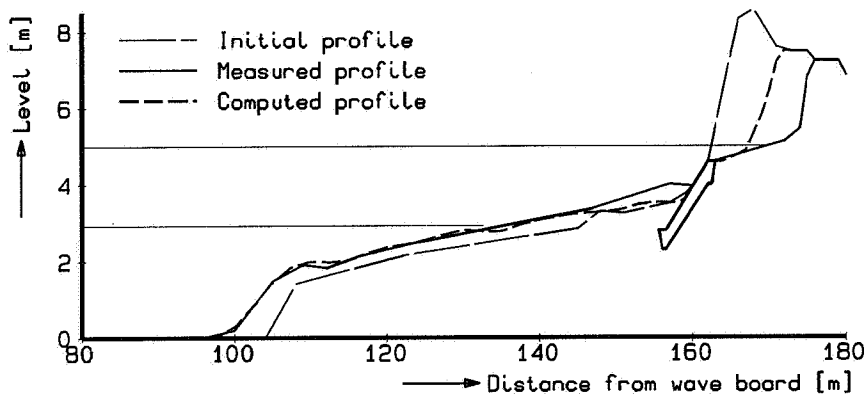


Figure 6.85 Comparison of final profiles for test T2 of the M1797-series.

It is noted that the hydraulic conditions are similar to those that were used in the test with an unprotected dune, viz. test T1 (see Figure 6.1). From a mutual comparison between both tests it becomes clear that the effect on the amount of dune erosion for such a low-crested revetment is only minor.

M1819-III-series, test T2 and T3 (DELFT HYDRAULICS, 1983d)

A comparison between measured and computed profile development for the very low revetment of test T2 is presented in Figure 6.86.

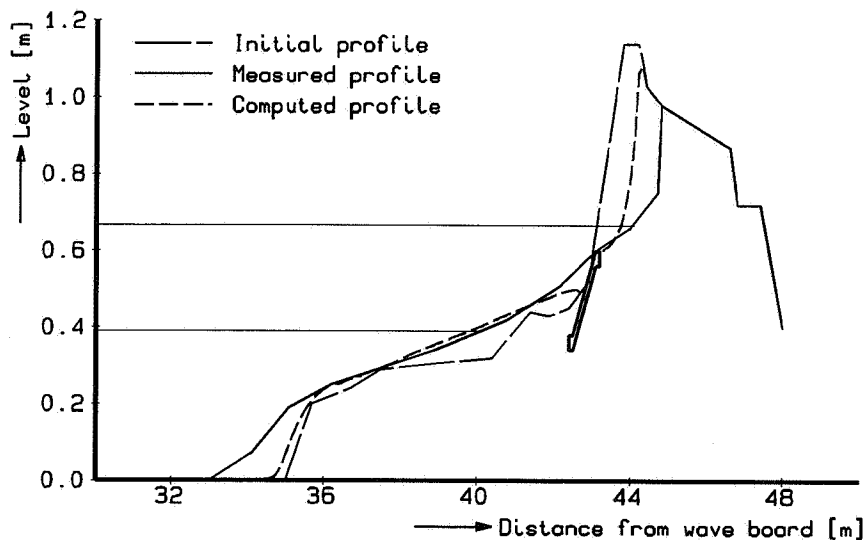


Figure 6.86 Comparison of final profiles for test T2 of the M1819-III-series.

It is noted that the hydraulic conditions are similar to those that were used in the test with an unprotected and completely protected dune, viz. test T1 and T4 (see Figure 6.49 for conditions).

For the hidden revetment as studied in test T3, the comparison between measured and computed final profile is presented in Figure 6.87.

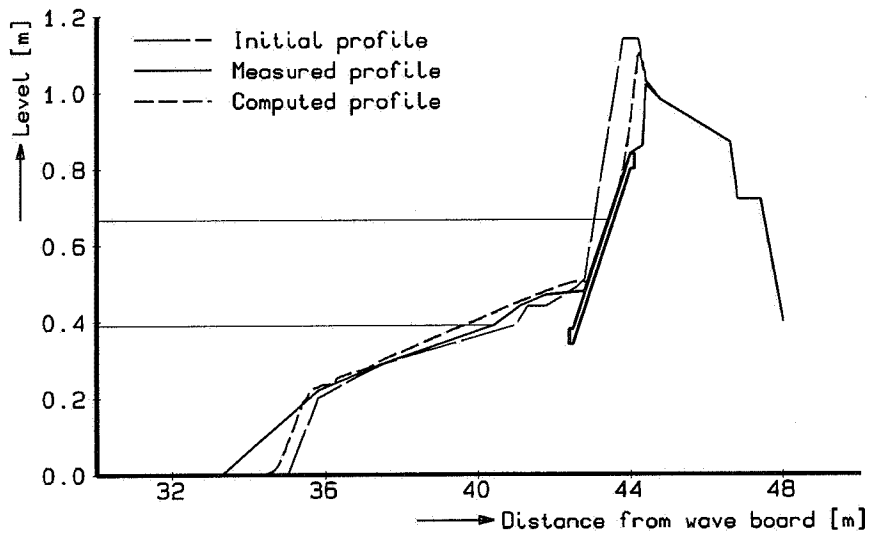


Figure 6.87 Comparison of final profiles for test T3 of the M1819-III-series.

H298-I-series, test T2, T3 and T4 (DELFT HYDRAULICS, 1987a)

The comparisons between measured and computed profile development for test T2 and test T3 are presented in Figure 6.88 and Figure 6.89 respectively (Steetzal, 1987b).

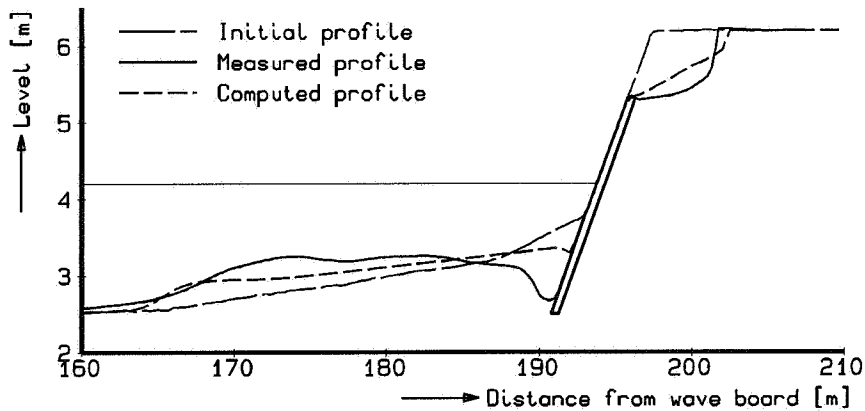


Figure 6.88 Comparison of final profiles for test T2 of the H298-I-series.

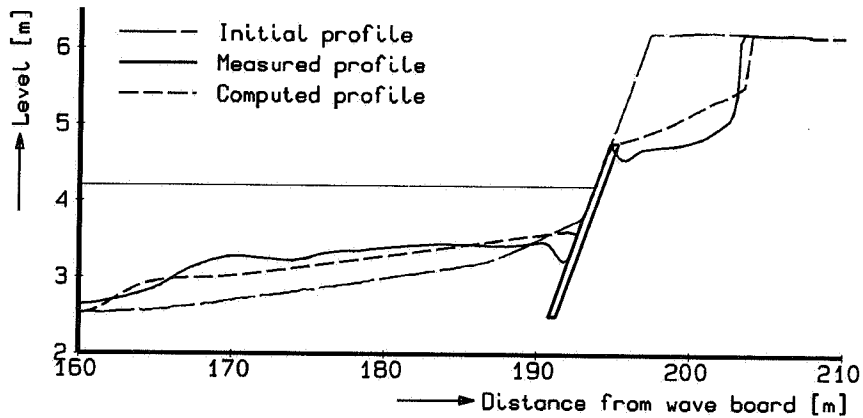


Figure 6.89 Comparison of final profiles for test T3 of the H298-I-series.

In comparison with the model outcome for the 'unprotected dune case', see Section 6.2 to 6.5, the observed and computed amount of dune erosion agree rather well. This unexpected result is, however, related to the under-prediction of the extent of the scour hole in front of the structure. A better agreement in this region would automatically diminish the agreement found near the dune face.

The hydraulic conditions applied during test T4 are presented in Figure 6.90.

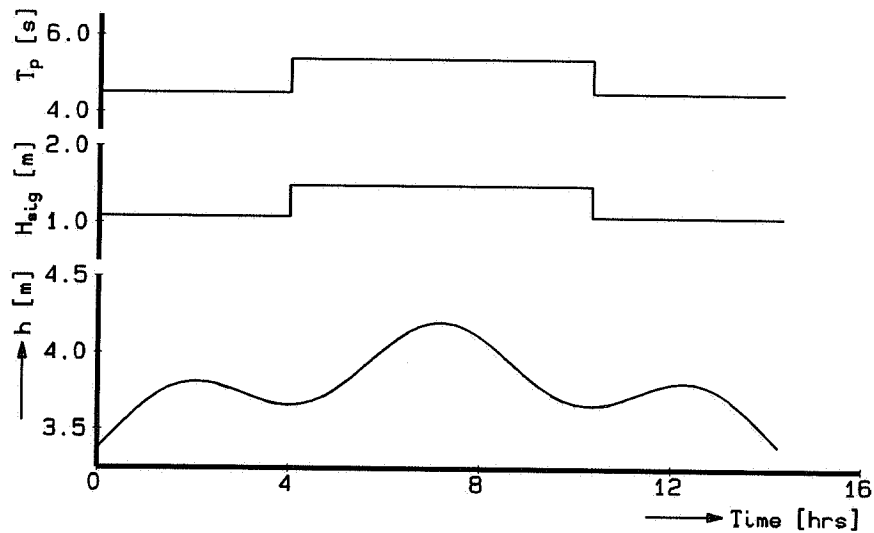


Figure 6.90 Hydraulic conditions used in test T4 of the H298-I-series.

The comparison between measured and computed profile development is presented in Figure 6.91.

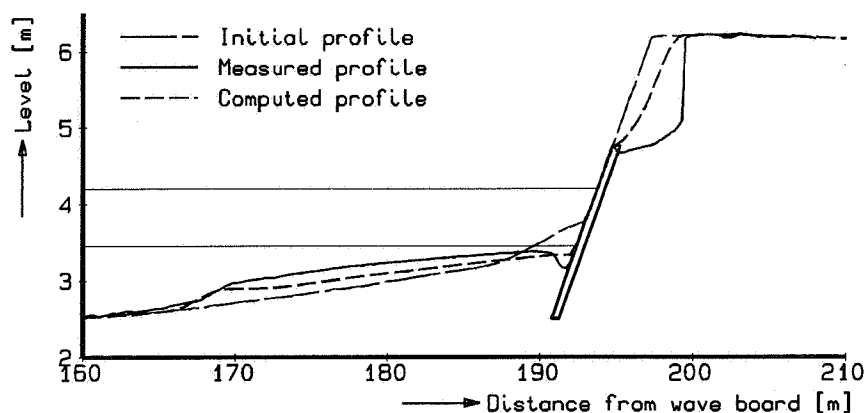


Figure 6.91 Comparison of final profiles for test T4 of the H298-I-series.

6.6.4 Scour hole development

The mathematical model under-predicts the final scour depth in the 'seawall case' by about 20%. Actually, this should be qualified as a rather good result, since the effect of a structure was incorporated in the mathematical model using a rather simple technique in which some apparently essential effects of, for example, wave reflection, wave down-rush and the roughness of the slope have not been accounted for (see Section 4.8.2).

6.6.5 Effect of dune erosion

The effect of erosion above the revetment can clearly be seen from a comparison of both the observed and computed profile development for different degrees of protection.

The measured cross-shore profiles after 3.5 hours of constant wave attack based on the tests T1, T2, T3 and T5 of the H298-I-series are shown in Figure 6.92.

As can be seen, an increasing level of the revetment results in both a 'landward' shift of the erosion profile and a gradual lowering of the landward part of this profile.

The computed effect is shown in Figure 6.93.

Although no perfect agreement is present, the overall effect of erosion on the development of the profile is reproduced correctly by the model.

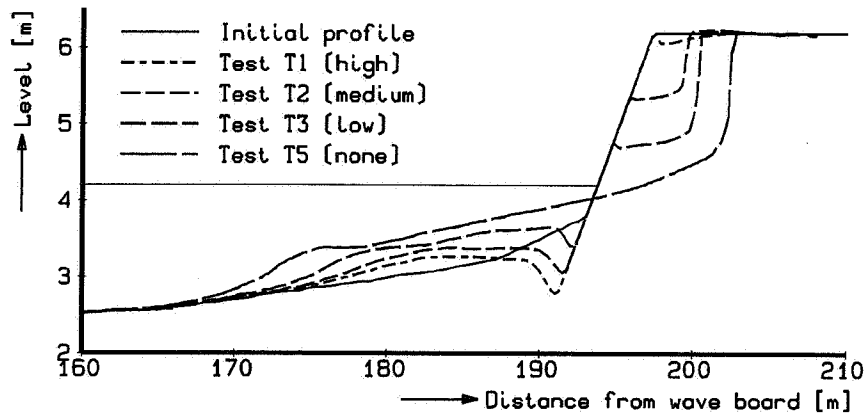


Figure 6.92 Relative effect of the revetment level based on measured cross-shore profiles.

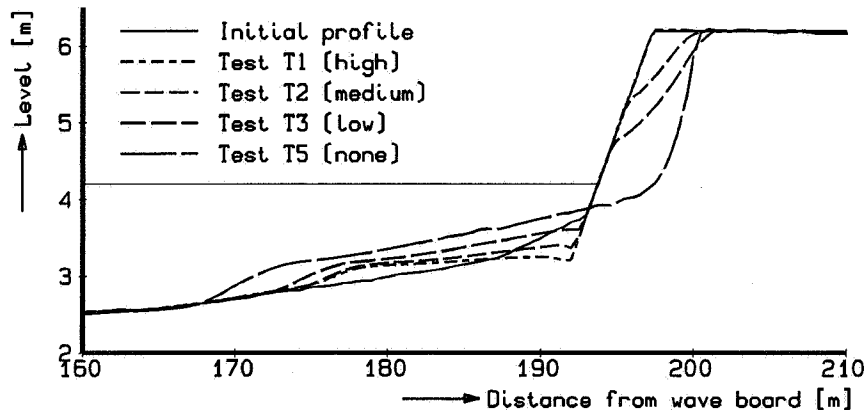


Figure 6.93 Relative effect of the revetment level based on computations.

6.6.6 Summary and conclusions

Although no special calibration was performed to incorporate the effect of structures on the profile development, the mathematical model can be used successfully in order to get a rough idea of the related impact.

6.7 Longshore effects

6.7.1 Introduction

As elaborated in Section 4.8.3 in more detail, the modelled longshore effects consist of:

- Wave and tide generated longshore currents;
- The accompanying longshore sediment transport;
- An assessment of the effect of an alongshore transport gradient.

Since the computation of the longshore flow is done according to basic standards, no further attention is paid to this aspect. Some remarks and comparisons for both the transport rates and the gradient effects are outlined in the following sections.

6.7.2 Longshore transport rates

The accompanying longshore transport rate is computed from the depth-integrated product of the suspension as a result of cross-shore wave breaking processes and the existing longshore current. Since no data for storm surge conditions is available, a mutual comparison with several well-known formulae for the cross-shore distribution of the longshore transport rate is computed for a schematic case.

For a uniform sloping 1:50 beach (with $D_{50} = 225 \mu\text{m}$ and $w_s = 0.025 \text{ m/s}$) and an incoming wave height of $H_{sig} = 5 \text{ m}$ and $T_p = 9 \text{ s}$ approaching at a wave angle of $\theta_0 = 20$ degrees at the -20 m depth contour (at $X_0 = -1000 \text{ m}$), the cross-shore distribution (for $r = 0.10 \text{ m}$) of the depth-averaged longshore current $v(x)$ is shown by the solid line in Figure 6.94.

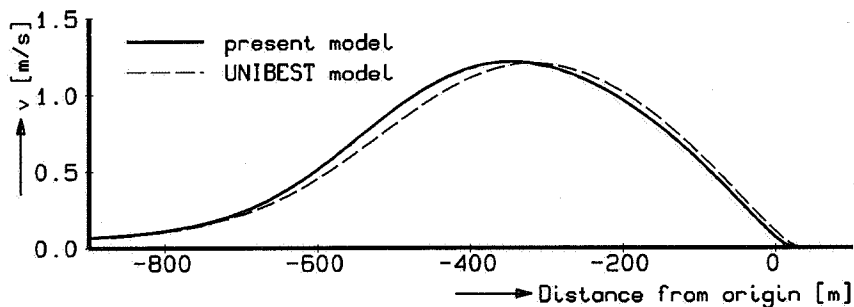


Figure 6.94 Computed cross-shore distribution of longshore current.

The maximum longshore velocity amounts about to 1.2 m/s.

In Figure 6.95, the cross-shore distribution of the longshore transport rate $S_y(x)$ according to the formulations described in the present work, viz. the DUROSTA-model, is compared

with the outcome of several other well-known formulae for longshore transport, namely those of Bijker, Van Rijn and Bailard.

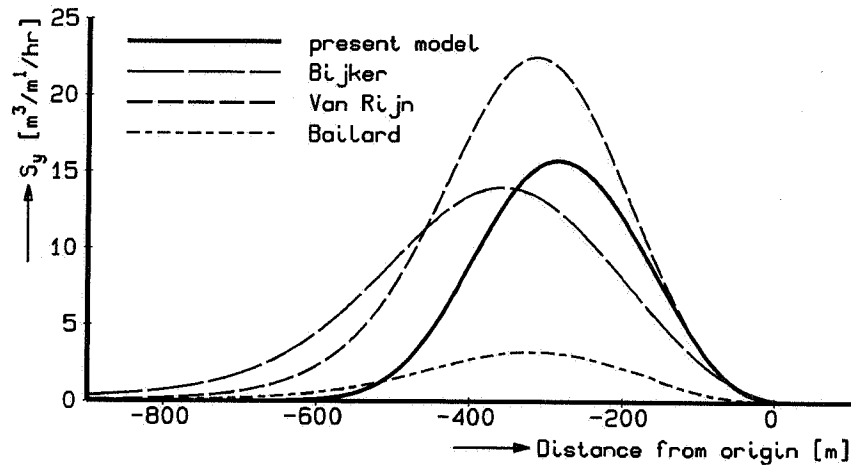


Figure 6.95 Computed distribution of longshore transport according to several longshore transport formulae.

These distributions have been determined using the longshore transport model UNI-LT, viz. the Longshore Transport module of DELFT HYDRAULICS' UNIBEST-package. For additional constants and parameters required for the other formulations, default values have been used. It is noted that the present model gives a similar current distribution. For the sake of convenience, the UNI-LT-result is also shown by the dotted line in Figure 6.94. The result is comparable with the outcome of the present model.

As can be seen from Figure 6.95, the outcome of the present model with respect to the longshore transport rate (excluding pores) is of the same order of magnitude as obtained by application of the other formulae. The cross-shore integrated total longshore transport amounts for the four presented distributions to $4.2 \cdot 10^3$, $5.4 \cdot 10^3$, $6.8 \cdot 10^3$ and $1.1 \cdot 10^3$ m³/hr respectively. Since only wave breaking processes are involved in the present model, the longshore transport rate at deeper water is definitely under-estimated, whereas the longshore transport rate in the breaker zone is fairly comparable with the results of both the 'Bijker'- and 'Van Rijn'-model.

It should be noted that the 'Bijker' formula probably over-estimates the longshore transport on the shoreface (a calibration constant, viz. *B*-value, for breaker zone conditions has been used for the complete stretch). Moreover, the 'Bailard'-model yields, as often occurs with similar computations, significantly lower transport rates.

Figure 6.96 shows the dependency of the wave height for several transport formulae, including the CERC-formula. It is noted that the required wave period for each of the computations was determined from the wave steepness which was assumed to be invariant. As can be seen from this, the amount of transport is under-estimated by the formulae which do not account for the additional effects of wave breaking.

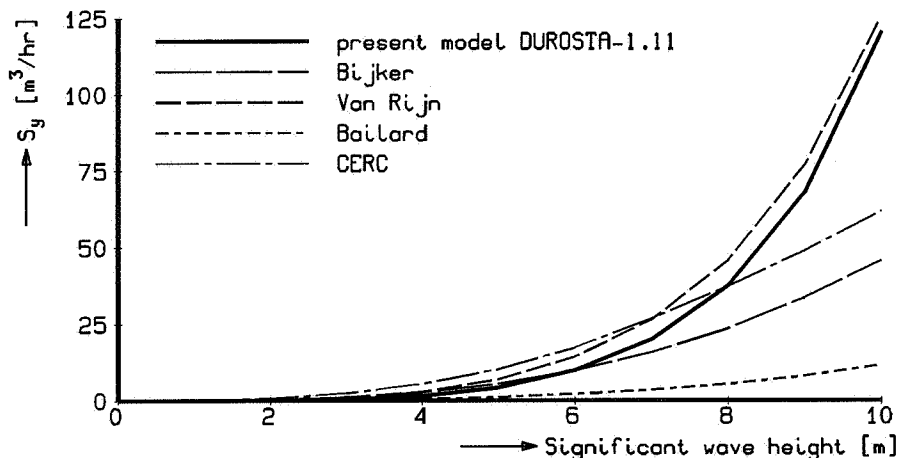


Figure 6.96 Computed rate of longshore transport according to several longshore transport formulae for a range of wave heights.

In general this $S_y - H_{sig}$ -dependency follows a constant power which is of the order of 2.5. For the present case however, the DUROSTA-model yields a 4.5-power as can be observed from Figure 6.97 in which the same results are presented on a log-log-scale.

It is noted that longshore transport in the swash zone is strongly influenced by onshore-offshore transport, because in fact longshore transport is caused by the nett effect of a slightly oblique onshore-offshore motion, see e.g. (Quick, 1991).

Since in the special case of dune erosion large amounts of sediment are moving around in the swash zone, a significant longshore transport peak will occur here. Omitting this contribution to the total transport rate may lead to a serious under-estimation of the transport rates due to a storm surge, see Section 8.6.3 and (Jaffe, 1992).

6.7.3 Effect of longshore transport gradients

Although it is believed that in the case of severe wave attack on a curved coastline a negative effect will undoubtedly be present, no (well-)documented cases of the effect of longshore transport gradients are presently known to the author.

Nevertheless, an application of the model for oblique wave attack on a curved coastline is

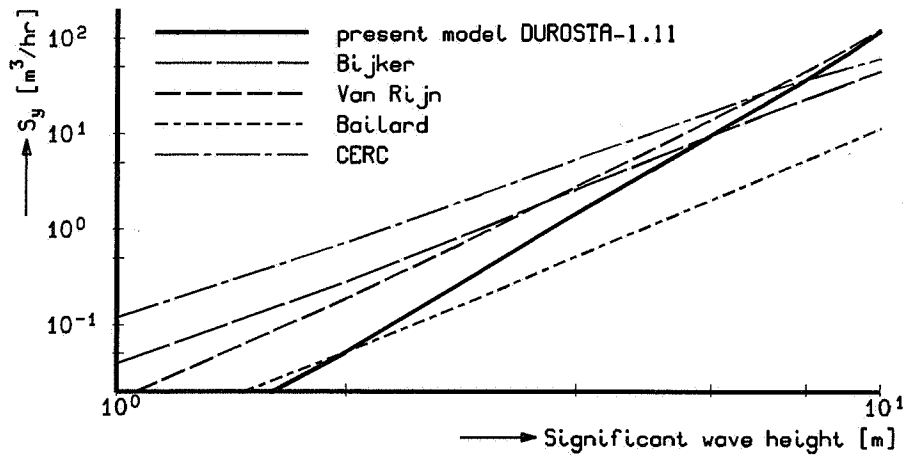


Figure 6.97 *Computed rate of longshore transport according to several longshore transport formulae for a range of wave heights; on log-log scale.*

presented in Section 8.6. For more details, reference is made to (Steetzel, 1990c).

6.7.4 Summary and conclusions

Although based on little evidence, the outcome of the model for applications with longshore effects is believed to be reliable in such a way that a first-order estimate of the related effects is trustworthy.

6.8 Summary and conclusions

6.8.1 Introduction

Based on a very large amount of well-documented information, the ultimate effect on the profile development of the formulations derived in Chapter 4 is assessed and a thorough verification of the cross-shore transport model is presented. Some conclusions with respect to the basic model- formulation for unprotected dunes as well as the model extension for both the impact of structures and longshore effects are summarized hereafter.

6.8.2 Unprotected dunes

Although the formation of an under water deposition area is predicted rather good by the present model, the amount of erosion above the surge level is under-estimated, due to both the model behaviour near the water line and the effect of a spatially non-uniform porosity.

6.8.3 Impact of structures

With high revetments and seawalls, the scour is fairly predicted.

From a mutual comparison between measured and computed scour depths it was concluded that the systematic under-prediction amounts to about 20 %.

For low revetments with optional erosion above the revetment, the erosion is under-predicted, whereas the predicted scour level is too deep.

6.8.4 Longshore effects

The predicted longshore effects, as far as current and longshore transport rates concern, are comparable with the outcome of other existing formulae.

A check for storm surge conditions could not be made since there were no data available on this subject.

6.8.5 Overall performance

Based on previously given arguments, the overall performance of the transport model with respect to the under water accretion is remarkably good.

The profile development near the water line and dunefoot is not perfect.

Since a closed volume balance is obeyed, any apparent sediment losses due to porosity effects are not predicted by the model.

It is clear that these two shortcomings of the present model should be solved in a next release of the model (see Section 9.3 for recommendations dealing with these facts).

7 SENSITIVITY ANALYSIS

7.1 Introduction

7.1.1 Objectives

This chapter summarizes the results of a systematic assessment of the sensitivity of the computational model for the main governing input data. Originally, this assessment has been carried out in order to compare the sensitivity of the new model (DUROSTA) with the existing DUROS-model (see (Vellinga, 1983)) as reported in more detail in (Steetzel, 1991, 1992c).

7.1.2 Governing parameters

In general terms, the change of a cross-shore profile due to a storm surge event depends on the dynamic balance between:

- the forces acting on the coast ('load');
- the ability of the coastal profile to withstand this impact ('strength').

The load is formed by the offshore hydraulic conditions which determine the actual wave attack on the coast, while the strength primarily depends on the composition and shape of the coastal profile itself. For example, a gently sloping beach will result in a smooth absorption of the incoming wave energy and will therefore not lead to significant profile changes.

7.1.3 Approach

In the following, the sensitivity of the cross-shore transport model to the three main governing parameters, namely:

- pre-storm profile;
- sediment characteristics;
- hydraulic conditions.

will be assessed while using a systematic procedure. As for this procedure, attention will be paid to the effect of variable conditions during an individual surge as well as to the effects of additional surges.

In order to quantify the effect of a small change in the basic input data on the resulting profile development, the total amount of erosion above the maximum storm surge level has been used as an indicator. This amount of erosion will be computed for small deviations from the standard input and, subsequently, they will be compared with the results of a reference case. The latter input and results are presented in the next section.

7.2 Reference input and results

7.2.1 Introduction

This section presents the input and results of a reference case, viz. the accompanying erosion quantity. With respect to the input, standard descriptions for the shape of the cross-shore profile, the sediment characteristics and the governing hydraulic conditions have been used, as elaborated in more detail in the following sections.

7.2.2 Reference profile

The standard cross-shore profile is derived from the average profile along the Dutch coast. This profile, called the reference profile, has a dune height of 15 m above MSL. The slope of the dune front equals 1:3 down to a level of MSL + 3.0 m. From MSL + 3.0 m down to MSL the beach slope is 1:20. From MSL down to MSL - 3.0 the slope is 1:60, further seaward the bottom slope equals 1:180.

This profile, as shown in Figure 7.3, has been used to define the shape of the sandy profiles in most of the DELFT HYDRAULICS' flume tests as referred to in Chapter 6.

7.2.3 Standard sediment characteristics

For the sediment present on the beach and in the dune a characteristic diameter of $D_{50} = 225 \mu\text{m}$ has been used as a representative value of the sand of the Dutch coastline. The fall velocity of the sediment in (salt) sea water of 5 °C is computed from:

$$\log(1/w_s) = 3.226 + 2.180 \log(D_{50}) + 0.476 [\log(D_{50})]^2 \quad (7.2.1)$$

as shown in Figure 7.1 (DELFT HYDRAULICS, 1983a).

The thus computed fall velocities can be used for the entire period during which storm surges (in the Netherlands) may occur. For $D_{50} = 225 \mu\text{m}$ $w_s = 0.0247$ m/s is found. For the porosity of the settled sediment a (constant) value of $p = 0.42$ has been used.

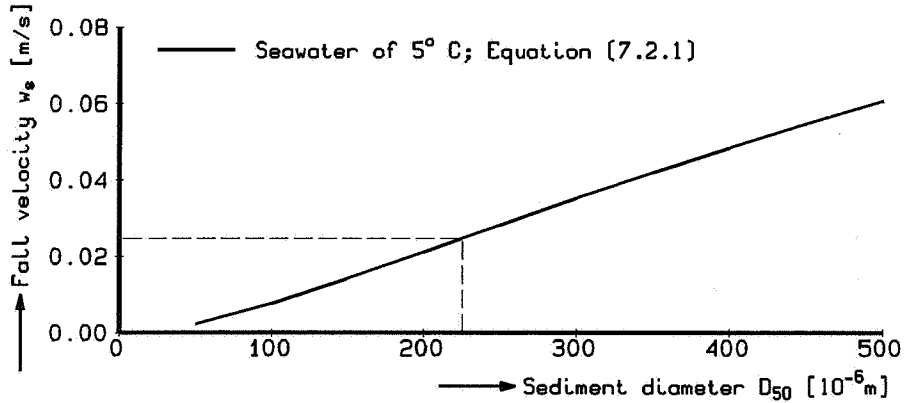


Figure 7.1 Fall velocity as a function of sediment diameter in sea water.

7.2.4 Standard hydraulic conditions

The governing conditions can be divided into two groups, namely the water level fluctuations and the wave conditions. For the input of the model the hydraulic conditions at the -20 m depth contour have been used.

Water level

The standard surge is composed of an astronomical tide (tidal effect) and a surge effect, both having a specific shape, as already shown in Figure 2.6.

The total variation in water level during the surge $h(t)$ can be determined from:

$$h(t) = h_0 + \hat{h}_a \cos \left[\frac{2\pi(t-t_{ma})}{T_a} \right] + \hat{h}_s \cos^2 \left[\frac{\pi(t-t_{ms})}{T_s} \right] \quad (7.2.2)$$

in which the first two terms on the right side denote the astronomical effect, with mean level $h_0 = 0.45$ m and first a first-order amplitude of $\hat{h}_a = 1.00$ m. The standard duration of the astronomical tide T_a is 12.42 hour. The third term on the right side symbolizes the surge effect with a maximum height of $\hat{h}_s = 3.55$ m and a storm duration of $T_s = 45$ hour. Furthermore, it is assumed that the maximum astronomical variation coincides with the maximum surge level, viz. $t_{ma} = t_{ms}$. Conclusively, the maximum water level equals $h_{max} = h_0 + \hat{h}_a + \hat{h}_s$.

Wave conditions

With respect to the wave conditions at the -20 m depth contour, both the wave height and the wave period during the storm are important.

The significant wave height variation $H_s(t)$ during the standard storm surge is based on some considerations as presented in (COW, 1982). The variation is subsequently modelled

as:

$$H_s(t) = \hat{H}_s \cos^2 \left[\frac{\pi(t-t_{ms})}{T_H} \right] \quad (7.2.3)$$

in which the maximum wave height (at time $t=t_{ms}$) equals $\hat{H}_s = 7.0$ m at the -20 m depth contour. Duration T_H , as based on the assessment of wave height measurements, equals $T_H = 125$ hour.

Assuming a constant characteristic wave steepness (viz. $H_s/T_p^2 = \text{constant}$), the wave period during the storm surge $T_p(t)$ is modelled according to:

$$T_p(t) = \hat{T}_p \cos \left[\frac{\pi(t-t_{ms})}{T_T} \right] \quad (7.2.4)$$

in which the maximum period \hat{T}_p equals 12.0 s and the duration is $T_T = T_H = 125$ hour.

The surge has been modelled for the period with $h(t) > \text{MSL} + 1$ m, namely during the time interval $0 \leq t \leq 32$ hour, so $t_{ms} = 16$ hour. The wave height varies from 5.93 to 7.00 m, while the wave period is restricted to the interval $11.04 < T_p \leq 12.00$ s.

An overview of the applied standard hydraulic conditions is shown in Figure 7.2.

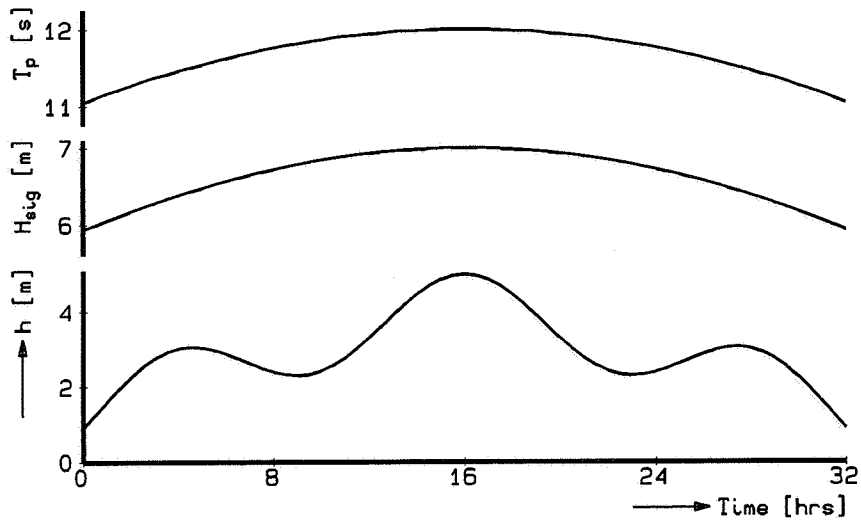


Figure 7.2 Overview of reference hydraulic conditions used for sensitivity assessment.

7.2.5 Result of computation

The computed effect of the 32 hours storm surge is presented in Figure 7.3. The final dune erosion above the storm surge level amounts to $203 \text{ m}^3/\text{m}^1$.

In the following this magnitude will be used as a reference value.

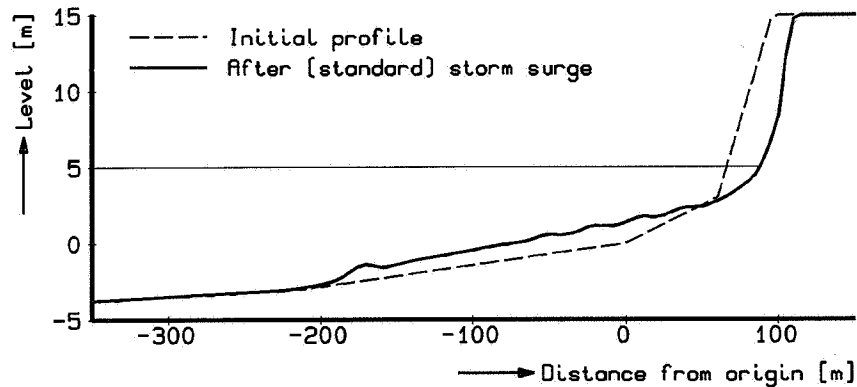


Figure 7.3 Computed post-storm profile for reference conditions.

7.3 Effect of pre-storm profile

7.3.1 Introduction

The initial profile is very essential for the amount of dune erosion. Two important zones can be recognized, namely:

- The nearshore zone, say the -20 m depth contour to the -3 m depth contour;
- The active zone, landward of the -3 m depth contour.

As a matter of fact it should be noted that the nearshore zone also plays an important role and cannot be considered as inactive.

In the case of the reference profile the -3 m depth contour is located just in the transition point between the $1:60$ and the $1:180$ bottom slope.

The effect of the initial profile in the active zone is implicitly accounted for by the prediction model (balance of sediment).

The bottom profile in the nearshore, say on the $1:180$ slope, will affect the wave impact on the dune. Examples are local wave height decay due to wave breaking on a nearshore bank and the gradual wave breaking processes in the case of a mild sloping bottom. Wave

height decay in the active zone will result in dissipation of the residual wave energy. In this case, the sediment transport capacity near the dune and consequently the dune erosion quantity will be less.

7.3.2 Various forms

With reference to the results of the model tests T21 to T28 of the M1819-I-series (as described extensively in Section 6.2.3), it was concluded that the presence of bars and troughs in the nearshore zone may lead to a spreading in the amount of dune erosion that is found of about 40 %.

The presence of a bars in both the nearshore and active zone will result in a decrease in the amount of dune erosion, whereas for reasons of sediment balance the presence of a trough in the active zone will give the opposite effect (see Section 6.2.3).

In the following, a systematic change in the outer slope is examined.

7.3.3 Slope of the nearshore zone

The bottom slope seaward of $MSL - 3.0$ equals $1:180$ for the reference profile. In order to show the effect of the slope of the nearshore zone, computations have been carried out for a set of slopes ranging from very mild ($1:720$) to very steep slopes ($1:60$).

Figure 7.4 shows the effect of the slope on the final erosion rate.

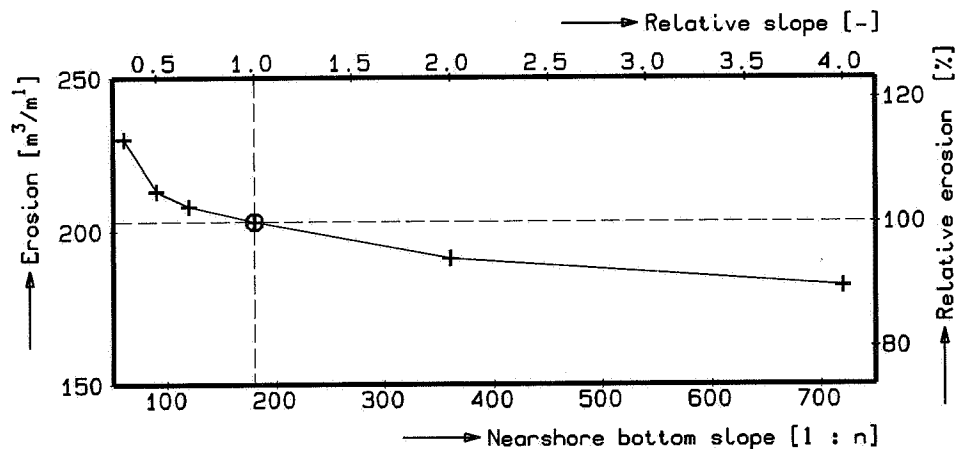


Figure 7.4 Effect of slope nearshore zone on the erosion rate.

The amount of dune erosion that was found for both extremes differs about 25 %. With an increasing slope the wave height at the -3 m-depth contour increases slightly also, resulting in increasing erosion rates.

It is remarked that from this result it can be concluded that performing model tests on rather steep slopes, viz. steeper than in prototype, will lead to an over-estimation of the amount of dune erosion.

7.3.4 Conclusions

The effect of the initial profile in the active zone is implicitly accounted for by the prediction model (balance of sediment).

The effect of the nearshore slope, well outside the active zone, is shown to have a significant effect on the amount of dune erosion. A steep outer slope leads to larger erosion rates.

It is noted here that the existing confusion with respect to the use of the 'deep water wave height', to be used in the DUROS-model has definitely been cleared up. See also (DELFT HYDRAULICS, 1987b).

7.4 Effect of sediment characteristics

7.4.1 Introduction

The characteristics of the sediment will affect the transport processes and, consequently, have also an impact on both the shape of the 'near-equilibrium' profile and the amount of dune erosion.

7.4.2 Direct effects

In order to assess the effect of the sediment characteristics on the amount of dune erosion, a set of four additional diameters has been used for the model input. The results are shown in Figure 7.5. The accompanying fall velocity is computed from Equation (7.2.1).

This impact of the sediment characteristics is significant. Finer grain sizes result in an increasing rate of erosion since finer sands 'need' a less steep slope for reasons of stability. A $\pm 10\%$ increase in diameter results in about $\pm 12\%$ decrease in erosion quantity.

It is remarked that in the present case, the same initial profile has been used for all computations, however in prototype the initial average slope of a beach with a smaller grainsize will be less steep.

Furthermore, it is noted that the outcome of the model for larger grain sizes tends to turn more doubtful because of the acting dominating transport mechanism. For coarser sediment the contribution of sediment suspension to the total net transport will reduce, while the effects of the bed load and the correlation component (see Section 4.2) will increase. Since

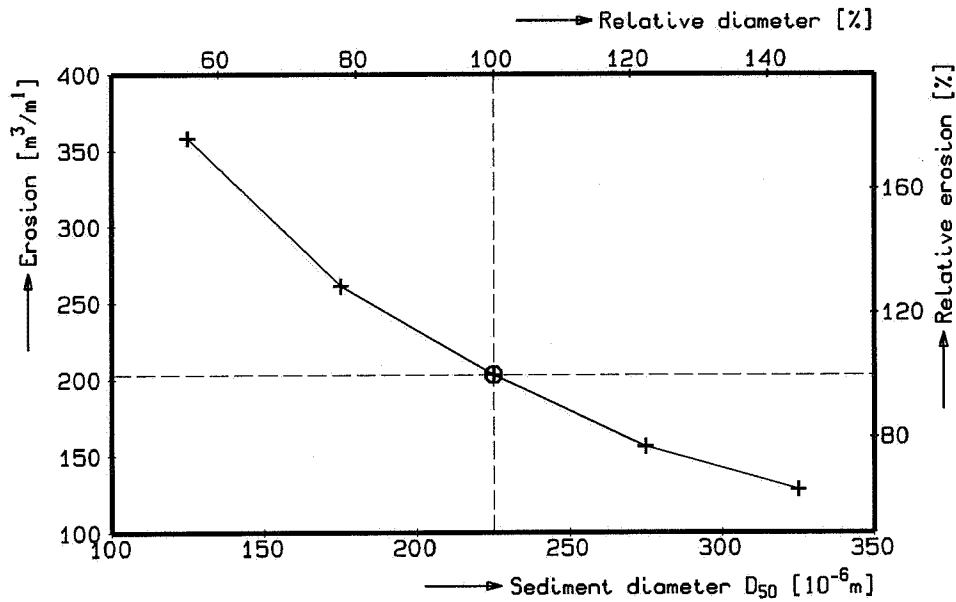


Figure 7.5 Effect of sediment diameter on the erosion rate.

the latter transport contributions are not incorporated in the present model, its application for e.g. gravel beaches as studied by Van der Meer (1988), is in principle not allowed.

7.4.3 Summary and conclusions

As could be expected finer sand will lead to an increased erosion rate, whereas coarser sand gives the opposite effect.

It should be noted that the effect of the H/Tw -parameter is still under investigation, see (Steezel, 1993).

7.5 Effect of hydraulic conditions during a storm surge

7.5.1 Introduction

Since there will almost always be uncertainty about the exact values of a surge level and the wave conditions during a specific storm surge, it is useful to assess the effect of small variations in these conditions on the amount of dune erosion.

Next the relative effects of changes in governing parameters will be determined with

reference to the standard conditions. This will be done for the (maximum) storm surge level, the duration of the storm, the wave conditions (height and period; both separate and combined) and the timing of the surge effect relative to the maximum astronomical effect. Furthermore, the additional effect of gust surges and gust oscillations will also be discussed.

Some attention on the effect of successive storm events will be paid to in Section 7.6.

7.5.2 Storm surge level

The relative effect of the storm-surge level on the erosion rate is determined by performing computations for different magnitudes of the mean water level h_0 which equals 0.45 m for the reference case. In this way the shape of the storm surge remains unchanged and the duration of the storm is not affected. The results of the computations are presented in Figure 7.6.

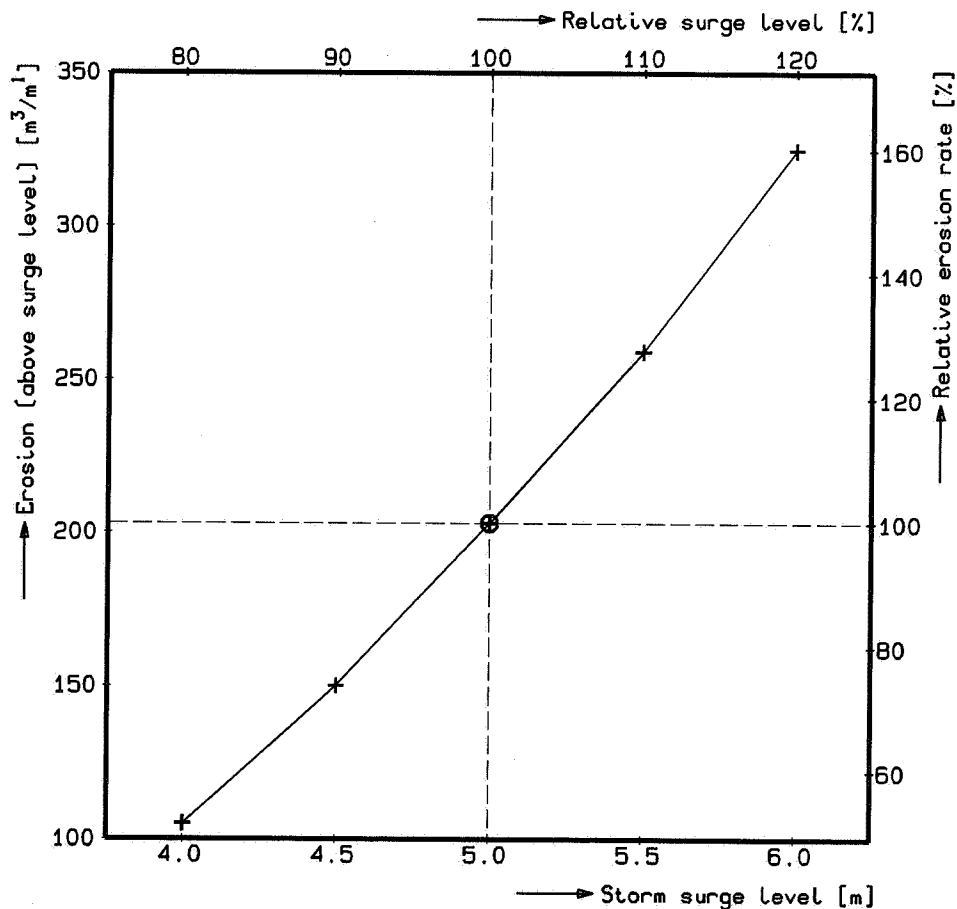


Figure 7.6 Effect of storm surge level on the erosion rate.

An increase of $\pm 10\%$ in storm surge level leads to an increase of the erosion rate of about $\pm 28\%$. Obviously the impact, and so the assessment of the storm surge level (or in fact the storm set-up) is very essential.

7.5.3 Storm duration

The computational model has been developed for relatively high storm surges at which the storm surge level minus 1.0 m is exceeded for a duration of 4 to 6 hours. For the reference case the duration amounts to 5.6 hours. Deviations thereof will affect the degree of dune erosion. In the next, the effect of the duration of the surge is examined by varying the basic duration of the surge effect T_s between 25 and 65 hour.

The results of the computations are presented in Figure 7.7.

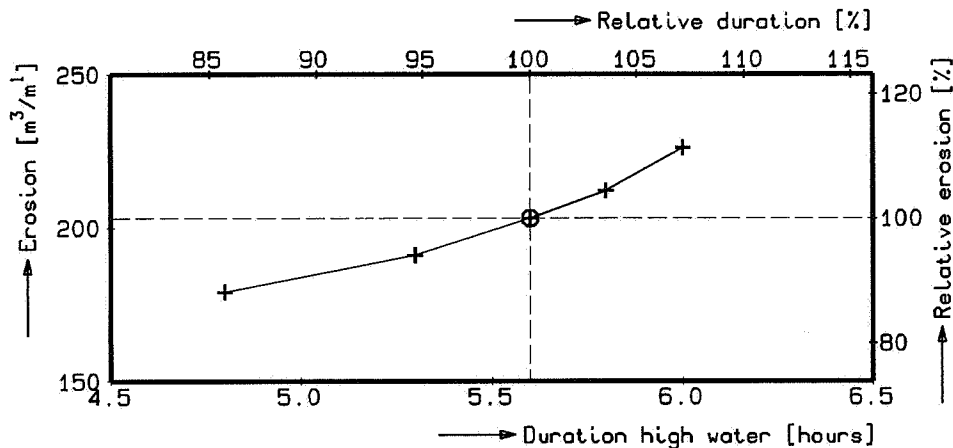


Figure 7.7 Effect of storm duration on the erosion rate.

The effective duration of the peak of the storm is computed as the length of the period in which the water level exceeds the storm surge level minus 1.0 m, and ranges from 4.8 to 6.0 hour. A variation of $\pm 10\%$ yields also about $\pm 10\%$ additional erosion, although a tendency is shown that an increase in storm duration has even a stronger effect.

This is because of the fact that due to the increased duration of the storm, the high water level for the neighbouring high waters also has increased and for this reason the contribution of these peaks to the total amount of erosion is considerable. It is noted that this characteristic is also responsible for the rough shape of this relation which differs from the normally occurring curve which usually looks like a sort of negative e -power.

7.5.4 Wave height

To study the effect of the offshore wave height, the accompanying erosion quantity has been computed for a range of \hat{H}_{sig} -magnitudes (for $\hat{T}_p = 12$ s). Since in the computations was dealt with a constant peak wave period mutually different magnitudes of the wave steepness were present, ranging from small (small waves) to long (high ones).

The results of the computations are presented in Figure 7.8.

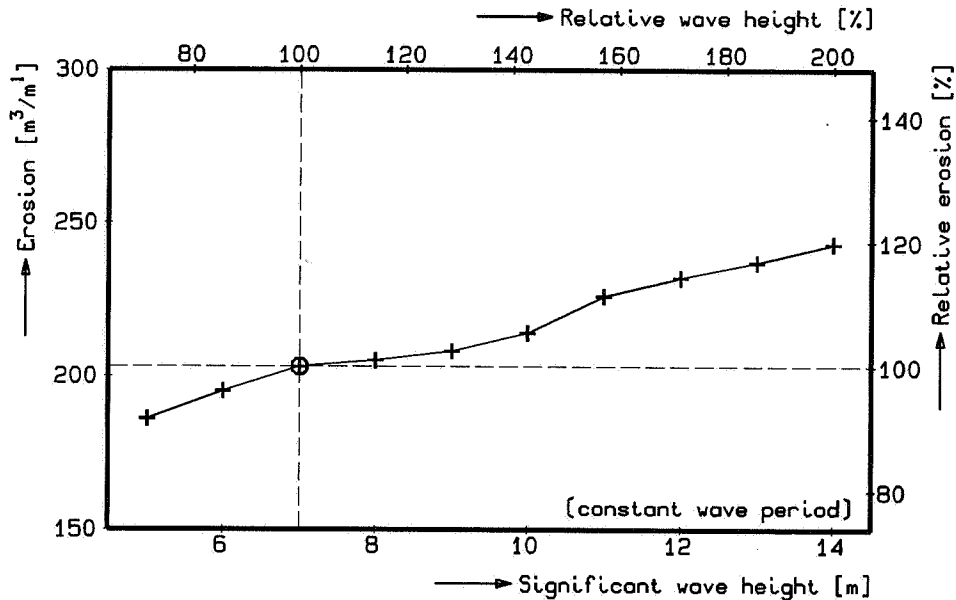


Figure 7.8 Effect of wave height on the erosion rate.

As can be seen from these results, a $\pm 10\%$ increase in offshore wave height will generate only about $\pm 2\%$ additional erosion. It is noted that the apparent 'dip' in this relation can probably be ascribed to mathematical effects.

In fact, an increased offshore wave height causes two effects on the nearshore wave height, namely:

- a direct slight increase in wave height (primary effect);
- an increase in wave set-up, yielding a greater water depth and so for a fixed breaking criterium a somewhat larger wave height (secondary effect).

From the computations it was concluded that the actual increase in nearshore wave height (and so in the amount of erosion) is primarily due to the secondary effect, viz. the elevated water level due the increased wave set-up.

7.5.5 Wave period

The effect of the wave period was examined by computing the erosion quantity for a series of five \hat{T}_p -values. The results of the computations are presented in Figure 7.9.

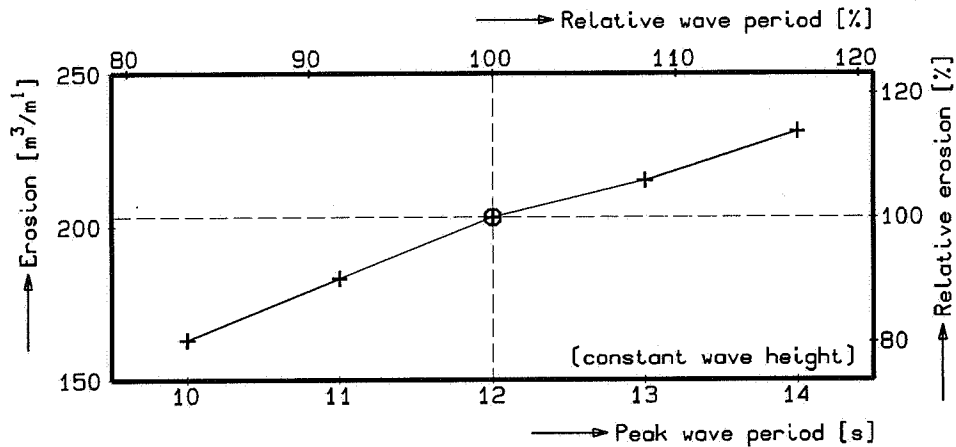


Figure 7.9 Effect of wave period on the erosion rate.

Because of the unchanged wave height, the shorter and longer periods result in relatively steep and mild waves. A $\pm 10\%$ change in wave period will result in about a $\pm 10\%$ variation in the amount of erosion.

Analysis of the wave height decay over the foreshore showed that this increase is mainly owing to the increased wave height in the nearshore zone.

It should be remarked that this effect goes beyond the relative impact of the wave height.

7.5.6 Wave height and period combined

In this section the combined effect of reduced or increased wave attack on the dune is assessed for various waves having an identical characteristic wave steepness, viz. $\hat{S} = \hat{H}_{sig}/L_0 \approx 0.031$.

The results of the computations are presented in Figure 7.10.

Relative to previously presented results, a larger offshore wave leads to significantly more erosion.

An increase of $\pm 10\%$ in wave attack, gives $\pm(5-10)\%$ additional erosion.

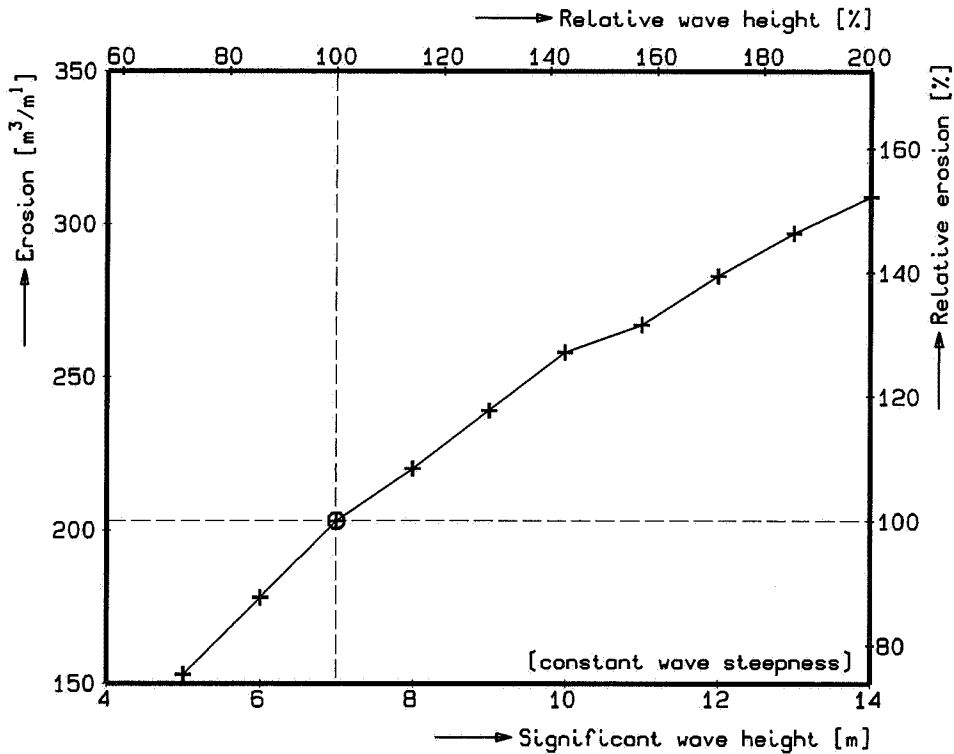


Figure 7.10 Effect of wave attack on the erosion rate.

7.5.7 Time shift of high water peaks

In the standard case, the maximum storm effect (at $t=t_{ms}$) coincides with the maximum, first-order astronomical effect (at $t=t_{ma}$). Since a mutual time shift affects the resulting water level, an effect on the amount of dune erosion will also be present.

An example of the effect of a mutual time shift on the resulting water level during the surge is shown in Figure 7.11.

The exceedance line in this figure, representing the time a specific water level is exceeded, is used to characterize both the duration and level of the high water peak. Accompanying parameters are t_{hw} denoting the duration in which the $(h_{max}-I)$ -level is exceeded and Z_5 denoting the level which is exceeded during 5 hours.

As can be seen a delay in the maximum surge effect will result in a slight drop of the maximum storm surge level.

The results with respect to the accompanying effect on the amount of erosion for a range of relative time shifts are shown in Figure 7.12.

Initially, the amount of erosion slightly decreases with increasing time shift. With further increased shifts the erosion quantity increases again due to the contribution from the second high water peak which is becoming more important now.

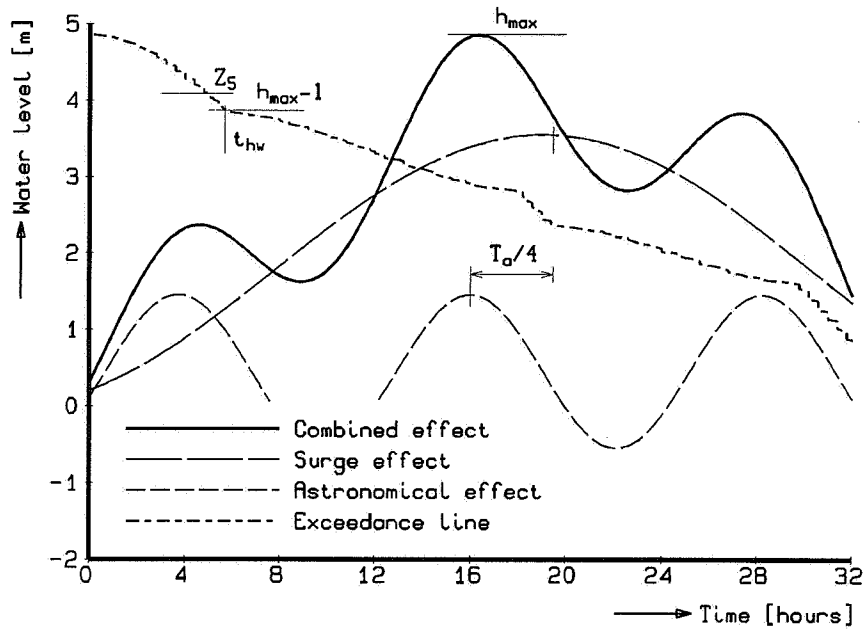


Figure 7.11 Effect of a time shift on the resulting water level fluctuation.

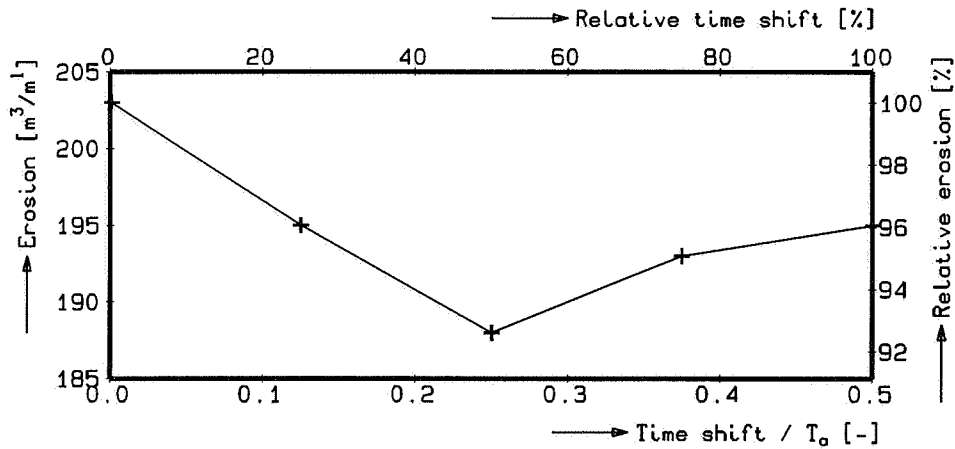


Figure 7.12 Effect of a time shift on the erosion rate.

In the case of a maximum relative time shift, viz. $T_a/2$, the maximum storm surge level is minimal though the effective duration of the (two) storm surge peak(s) is at a maximum (a 'twin surge').

From this it can be concluded that, compared to a scenario with coinciding high water peaks, the amount of erosion is over-estimated by a maximum of approximately 8 %.

7.5.8 Gust surges and gust oscillations

The effect of additional fluctuations in water level during the storm surge caused by of gust surges and gust oscillations were determined by adding a gust oscillation to the standard water level fluctuations.

Assuming a gust duration of about 60 minutes ($T_{gs} = 1.0$ hour) and a gust dimension of $\hat{h}_{gs} = 0.40$ m according to Van de Graaff (1984), having a \cos^2 -shape:

$$h_{gs}(t) = \hat{h}_{gs} \cos^2 \left[\frac{\pi(t - t_{mgs})}{T_{gs}} \right] \quad (7.5.1)$$

From the computations performed it was found that the ultimate effect of a gust surge on the final erosion rate is insignificant.

7.5.9 Conclusions

In Figure 7.13 the relative effects of the hydraulic conditions are summarized. All the effects are related to the characteristic magnitude of each parameter.

The effect of a divergent wave height is presented for an invariable wave period and vice versa. For the required degree of wave attack the wave height is altered, however, keeping the wave steepness, viz. the (H_{sig}/T_p^2) -ratio constant.

The effect of the storm surge level and so the storm set-up is very significant. The relative impact of the actual wave attack is about half as important.

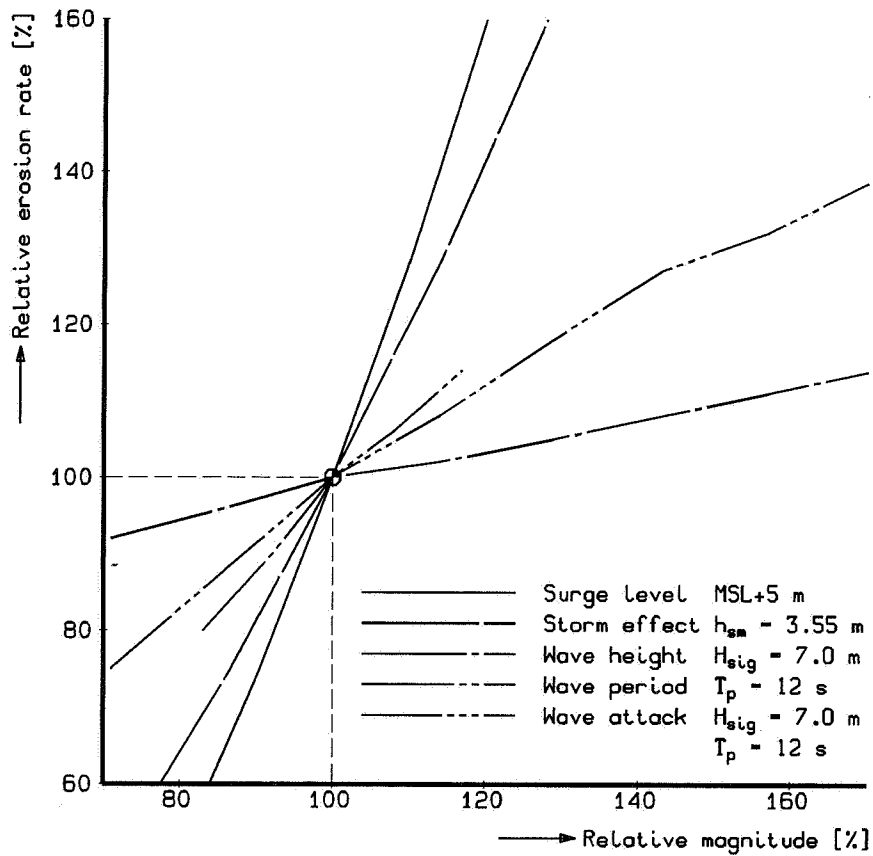


Figure 7.13 Effect of divergent hydraulic conditions on the erosion rate.

7.6 Effect of successive storm surges

7.6.1 Introduction

The effects of the detailed conditions during an individual storm surge were examined in the preceding section. In the following the effect of successive storm events will be discussed. The conditions used here are similar to those described in Section 7.2.

7.6.2 Additional storm event

An additional storm event will lead to an increased amount of dune erosion. To illustrate the effect of successive storm events (a repetition of the standard-32 hour

storm surge) some additional computations have been conducted using the post-storm profile of a preceding storm as the initial profile. The subsequent post-storm profiles for five storm events are presented in Figure 7.14.

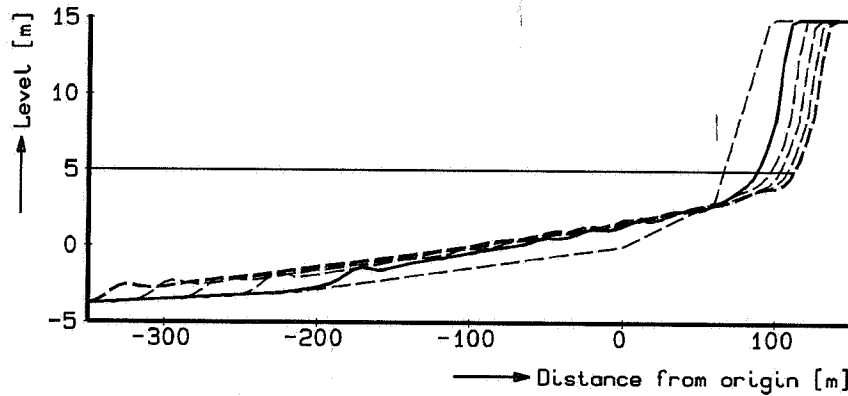


Figure 7.14 Computed post-storm profiles for five successive storm events.

It is noted that the impact of the first storm is similar to the result shown in Figure 7.3.

7.6.3 Dune erosion quantity

The accompanying development of the dune erosion quantity is shown in Figure 7.15. It is noted that no post-storm recovery is taken into account here. Besides, the contribution of dune erosion caused by numerical effects, viz. numerical smoothing in the mathematical program, tends to increase for successive computations.

A decent analytical elaboration of the final effect can be obtained by assuming a constant relative increase in the amount of erosion according to:

$$\Delta A_{i+1} = \xi \Delta A_i \quad (7.6.1)$$

in which ξ denotes the relative fraction of the erosion caused by storm $(i+1)$, expressed in the erosion rate due to the previous storm. For the present case $\xi \approx 0.4$ is found.

This leads to a total amount of erosion A_{tot} after n storm events equal to:

$$\begin{aligned} A_{tot} &= \sum_{i=1}^n \Delta A_i \\ &= \Delta A_1 + \xi \Delta A_1 + \xi(\xi \Delta A_1) + \dots \\ &= \Delta A_1 (1 + \xi + \xi^2 + \dots) \end{aligned} \quad (7.6.2)$$

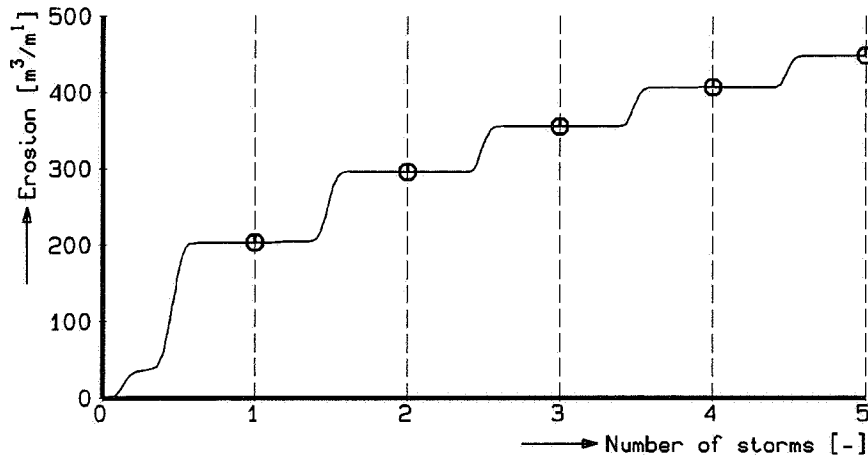


Figure 7.15 *Computed development of dune erosion quantity for five successive storm events.*

For an infinite sequence of storms, viz. $n \rightarrow \infty$, this expression yields:

$$A_{tot} = \Delta A_1 \left(\frac{1}{1 - \xi} \right) \quad (7.6.3)$$

in which the ultimate amount of erosion is expressed in terms of the effect of the initial first storm and the relative contribution of the next storm event.

7.6.4 Long-term 'near-equilibrium' profile

A series of successive storms has to lead to a more or less equilibrium beach profile. The successive profiles relative to the storm surge level and the position of the post-storm intersection between this level and the computed position of the duneface are shown in Figure 7.16.

According to Bruun's description of the average coastal profile in Denmark as already presented in Equation (3.3.1) follows a simple power curve (Bruun, 1954). This profile using the prototype-based shape factor is shown in the figure by the dashed line. As can be observed, the computed 'near-equilibrium' profile after 5 successive storm events shows a comparable contour.

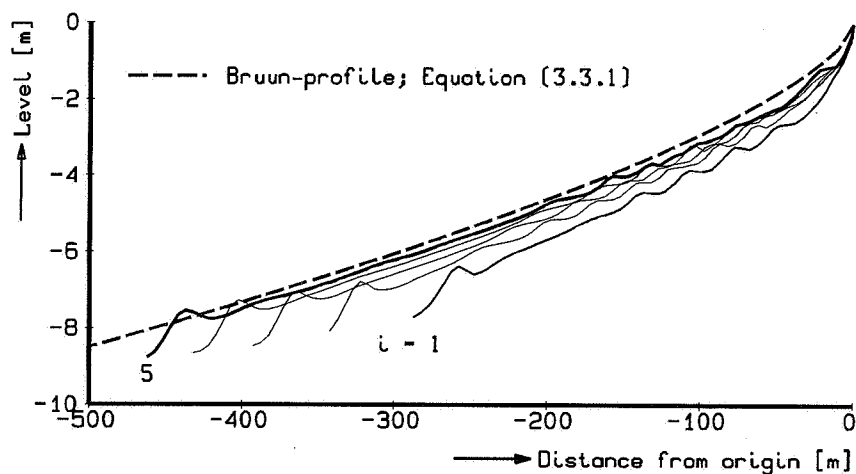


Figure 7.16 *Successive post-storm profiles compared with Bruun-profile.*

7.7 Summary and conclusions

7.7.1 Introduction

This section summarizes the outcome of the sensitivity analysis. More details are presented in (Steezel, 1992c).

7.7.2 Pre-storm profile

Since a profile observation just before a specific storm surge will hardly ever be available, the effect of a varying cross-shore profile has to be taken into account. This holds also for the nearshore slope which is shown to have a significant effect on the actually governing wave condition and so on the amount of dune erosion.

7.7.3 Sediment characteristics

Relative to, for example, the initial profile and the exact hydraulic conditions during the storm surge, the sediment characteristics can be assessed with less uncertainty. Finer sand leads to a milder slope of the post-storm erosion profile and, for reasons of sediment balance, so to an relative larger erosion rate. This is in accordance with the expressions belonging to the 'equilibrium profile' models of Bruun and Dean as discussed in

7.7.4 Hydraulic conditions during a storm surge

One of the predominant factors which determine the degree of dune erosion is the surge level.

The impact of the actual offshore wave height is shown to be of less importance.

As a consequence, in order estimate the governing hydraulic conditions for a design storm surge, much attention must be paid to the storm surge level. Detailed knowledge on the probability of very extreme wave heights occurring seems not useful, since the final effect on the amount of dune erosion is only limited. Moreover, since one has to deal with extreme events, the significant wave height at the seaward boundary will also be depth-limited (Steezel, 1990b). More information on the probability of accompanying wave periods occurring seems to be necessary.

It is noted that a general procedure for the assessment of the hydraulic conditions during a storm surge is presented in Section 8.2.

7.7.5 Effect of successive storms

An additional storm will lead to a relatively minor increase in the amount of erosion.

The long-term 'near-equilibrium' profile, obtained from successive computations for one individual standard surge, shows fair resemblance with the equilibrium Bruun profile.

8 APPLICATIONS

8.1 Introduction

For application of the mathematical cross-shore transport model various possibilities are available, since both groups of basic input data, namely the hydraulic conditions during the storm surge and the cross-shore profile present before the surge may be (more or less) arbitrary chosen.

In the case of the hydraulic conditions, the wave height and the water level fluctuations could be varied for example, in order to examine relative effects on profile development. With respect to the cross-shore profile one could use non-standard profiles and investigate the effect of nourishments and structures on the profile development. Also the effects of longshore transport gradients due to a gradient in tidal currents or due to a coastline curvature (non-straight coastlines) could be studied.

In order to demonstrate the capability of the computational model, some examples will be given of the relative effect of the basic input data.

First the relative effect of both nourishments and structures in the coastal profile will be examined briefly. Next the effects of oblique wave attack on the profile development, especially in the case of non-straight coastlines, will be illustrated.

The next section presents some remarks on the general assessment of the hydraulic conditions needed for the input of the computational model.

8.2 Assessment of hydraulic conditions

8.2.1 Approach

A storm surge is defined as an abnormal rise of water level along the shore, resulting principally from the atmospheric pressure and the winds of a storm. A general procedure for the assessment of the hydraulic conditions for storm surges is presented in Figure 8.1. Essential in this procedure is the separation between local astronomical and non-local storm effects. A detailed elaboration of the procedure is also given in (Steetzel, 1992d).

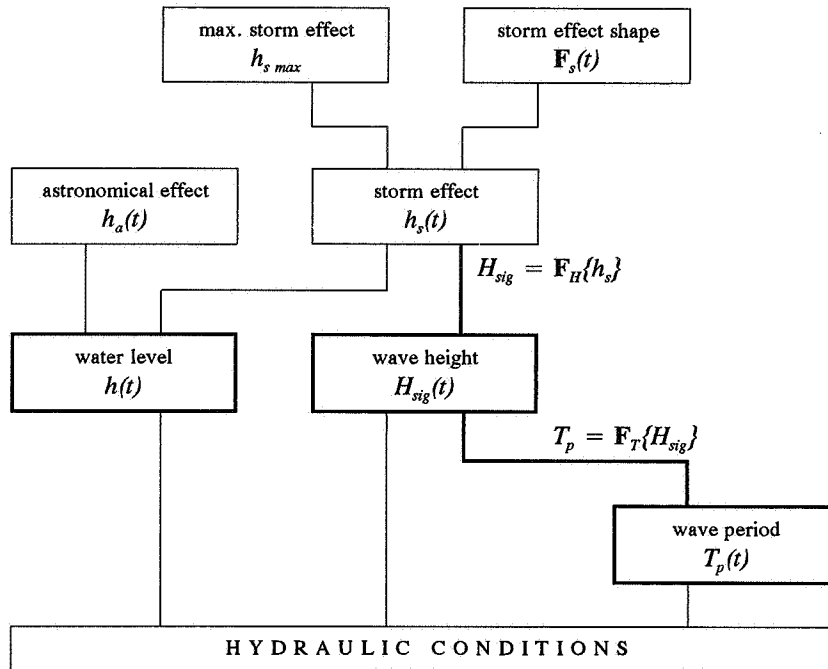


Figure 8.1 General procedure for the assessment of hydraulic conditions during a storm surge.

8.2.2 Water level

Starting with a specific maximum storm effect $h_{s,max}$ (with a certain probability of exceedance), the total storm effect $h_s(t)$ can be schematized by:

$$h_s(t) = h_{s,max} F_s(t) \quad (8.1)$$

in which $F_s(t)$ represents the shape of the storm effect, with $0 \leq F_s(t) \leq 1$.

This shape function could be described by a \cos^2 -function according to (COW, 1982):

$$F_s(t) = \cos^2 \left[\frac{\pi(t-t_{ms})}{T_s} \right] \quad (8.2)$$

in which:

t_{ms} time of the maximum storm effect with $h_s(t_{sm}) = h_{s,max}$ (hrs)

T_s total duration of storm (hrs)

Instead of a \cos^2 -function other schematizations, e.g. triangular relations, could be used as well.

Since, in general, high surge conditions coincide with long storm durations, the storm duration T_s is assumed to be correlated with the maximum surge effect (for example $(h_{s,max}/T_s) = \text{constant}$).

The astronomical effect h_a can be determined from the (local) tidal components according to:

$$h_a(t-t_{ma}) = a_0 + \sum_{i=1}^n a_i \cos(\phi_i t - g_i) \quad (8.3)$$

in which:

t_{ma}	time of maximum first-order astronomical tide	(hr)
n	number of tidal components	(-)
a_i	amplitude of i^{th} component	(m)
ϕ_i	angular frequency of i^{th} component	(rad/hr)
g_i	phase of i^{th} component, with $g_1 = 0$ rad	(rad)

Consequently, the combined resulting water level fluctuations $h(t)$ during the storm surge can now be computed from:

$$h(t) = h_a(t-t_{ma}) + h_s(t-t_{ms}) \quad (8.4)$$

for $(t_{ms} - \frac{1}{2}T_s) \leq t \leq (t_{ms} + \frac{1}{2}T_s)$.

It should be noted that in the present procedure it is assumed that the surge does not affect the shape of the astronomical tide.

8.2.3 Wave height

Since both the storm related water level and wave height fluctuations are due to the same large-scale, atmospheric phenomena, the wave conditions (say significant wave height $H_{sig}(t)$) can be related to the storm surge effect $h_s(t)$ according to the general relation:

$$H_{sig}(t) = F_H\{h_s(t)\} \text{ with } F_H(h_s) \geq 0 \text{ m} \quad (8.5)$$

An example of such a relation, determined for deep water conditions along the Dutch coast, is:

$$h_s = a (H_{sig})^2 + b H_{sig} + c \quad (8.6a)$$

$$\text{or: } H_{sig} = \frac{\sqrt{b^2 + 4a(h_s - c)} - b}{2a} \quad (8.6b)$$

in which the constants $a = 0.0456 \text{ m}^{-1}$, $b = 0.0332$ and $c = -0.087 \text{ m}$ hold for the Dutch coast (DELFT HYDRAULICS, 1990d).

This relation is shown in Figure 8.2, in which also a basic relation is presented.

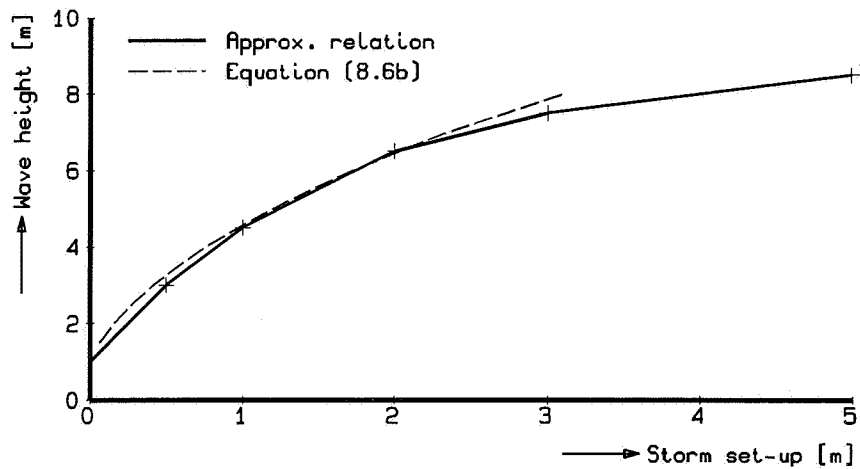


Figure 8.2 Assumed relation between storm set-up and significant wave height at deep water.

A comparison with data from a measurement at the LEG-station near Hoek van Holland is presented in Figure 8.3 showing a series of measurements with a length of one hour during a winter storm in 1990 (Steetzel, 1992d).

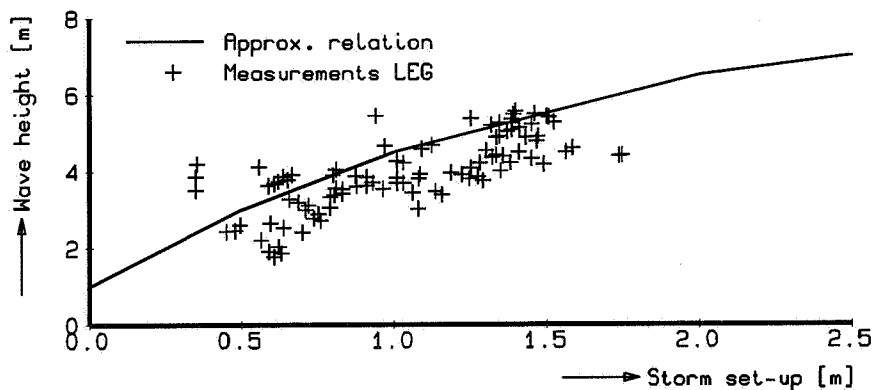


Figure 8.3 Comparison between basic and measured relation.

From this kind of comparisons it was concluded that the uncoupling of astronomical tide and storm set-up indeed is a promising and reliable approach.

8.2.4 Wave period

The wave period is basically associated with the wave height according to:

$$T_p(t) = F_T\{H_{sig}(t)\} \text{ with } F_T(H_{sig}) \geq 0 \text{ m} \quad (8.7)$$

for example by a characteristic deep water wave steepness \hat{S} :

$$T_p = \sqrt{\frac{2\pi H_{sig}}{g\hat{S}}} \quad (8.8)$$

For $\hat{S} = 0.035$ (3.5%), being a typical estimate for North Sea storm conditions, the latter equation results in:

$$T_p = 4.28 \sqrt{H_{sig}} \quad (8.9)$$

which is, together with other percentages of \hat{S} , presented in Figure 8.4.

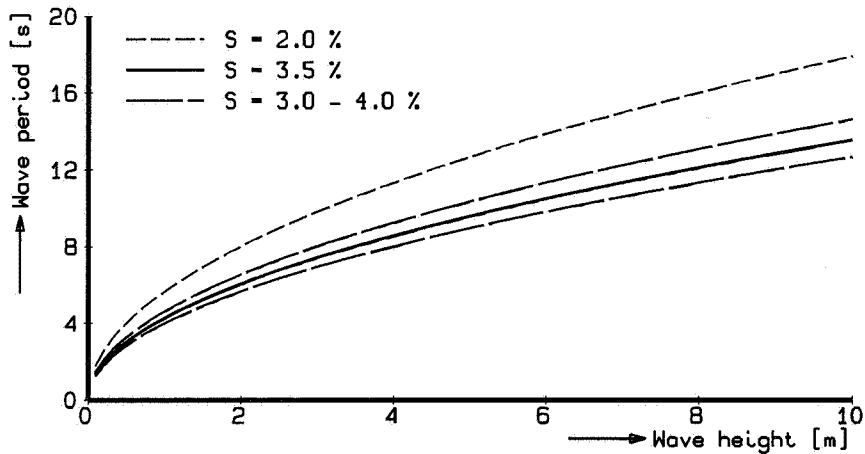


Figure 8.4 Assumed relation between significant wave height and peak wave period.

For the previously applied data set (see Figure 8.3), the measured relation between wave height and wave period is shown in Figure 8.5, demonstrating that the assumed dependency is indeed useful (Steetzel, 1992d).

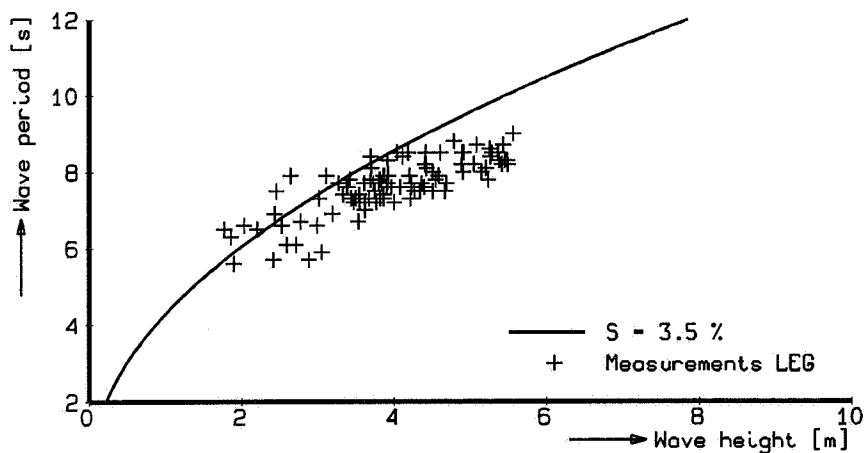


Figure 8.5 Comparison with measured data during 1990-storm surge.

8.2.5 Application

It is noted that the procedure as shown in Figure 8.1 can be used for coastal management studies. The computation of erosion rates for a series of storm events for decreasing probabilities of exceedance yields a relation between the exceedance probability and the accompanying duneface recession. An example of such an application is presented by Wind and Peerbolte (1992).

The probability of reaching or exceeding a certain magnitude of dune erosion can be estimated with probabilistic methods, see e.g. (Van de Graaff, 1983, 1986) and Section 9.2.

8.3 Standard case for comparison

8.3.1 Cross-shore profile

As a standard case for mutual comparison a rather steep cross-shore profile with a beach of about 100 m width and a rather steep shoreface (tidal gully) is chosen, as shown in Figure 8.6. This kind of profiles can be found in the southern part of the Netherlands. The profile is comparable to one of the tested profiles in the Deltaflume (see Chapter 6).

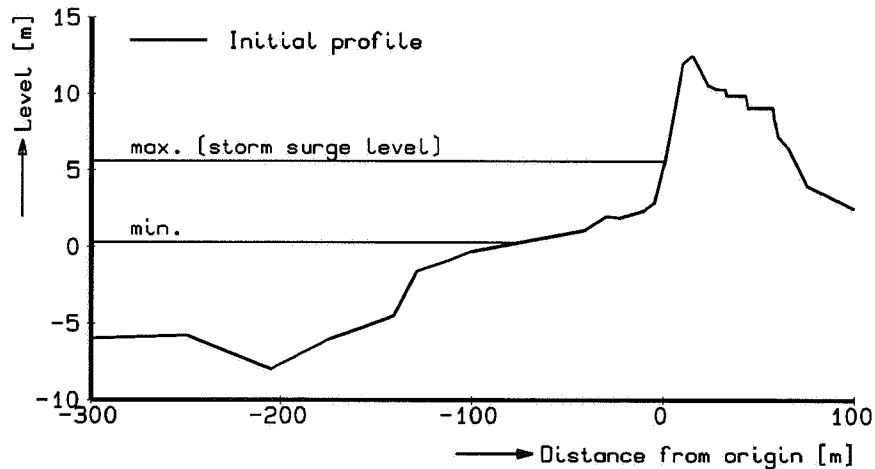


Figure 8.6 Standard cross-shore profile used for applications.

8.3.2 Hydraulic conditions

The two horizontal levels, as indicated in Figure 8.6, refer to the minimum and maximum water level (storm surge level +5.60 m) during a specific storm surge.

The hydraulic conditions during the 20 hour storm surge are shown in Figure 8.7.

The wave heights range from 2 to 4 m. Two distinct time intervals can be defined namely: from 0 to 10 hours low waves with low water levels and higher waves at higher water levels during the next period.

8.3.3 Computed profile development

In Figure 8.8 the results of the computed profile development are shown.

The momentary profiles given at $t=0$, 10 and 20 hours show some minor dune erosion during the first half of the storm, whereas seriously increased erosion rates occur during the subsequent period.

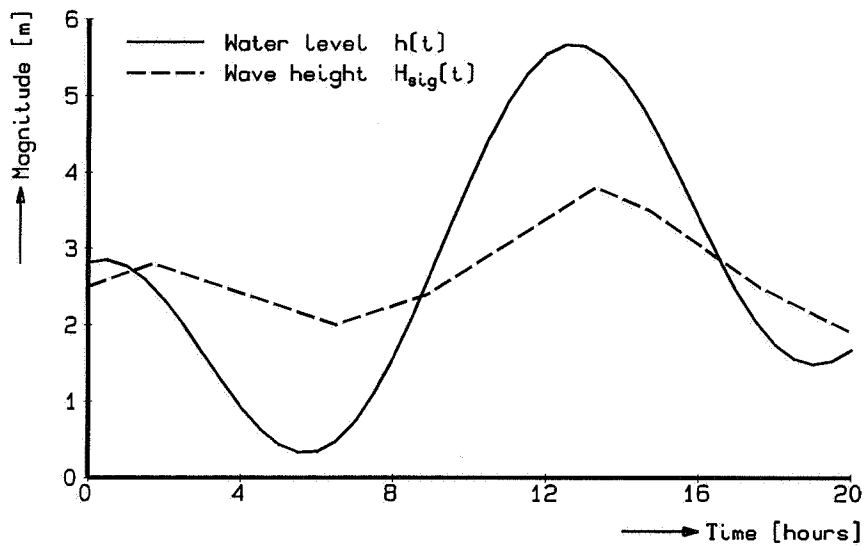


Figure 8.7 Hydraulic conditions used for application.

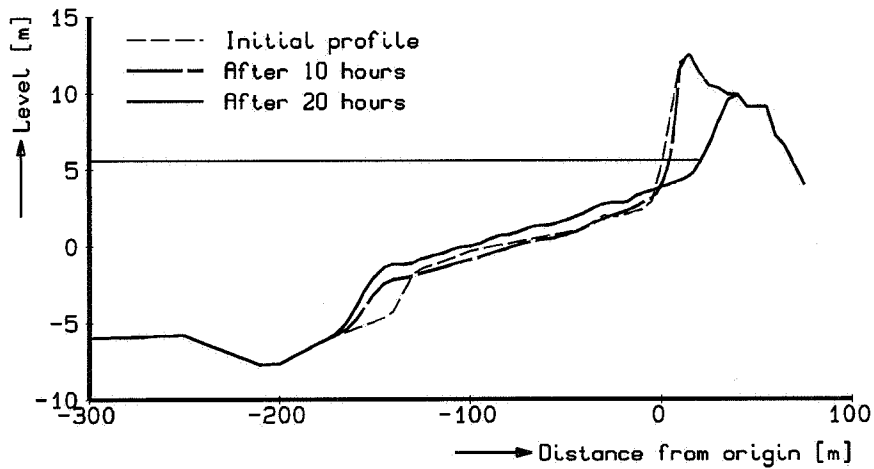


Figure 8.8 Computed profile development for standard cross-shore profile.

During the time interval with increasing water levels erosion from the duneface occurs resulting in an elevation of the upper beach, whereas at decreasing water levels material from the upper beach is transported further seaward and deposited in the deeper part of the profile.

The final retreat of the duneface amounts to about 25 m (up to about 35 m from the origin) and the erosion above maximum storm surge level equals $141 \text{ m}^3/\text{m}^1$.

8.4 Effect of a beach/dune nourishment

In order to strengthen a dune a buffer of sand can be nourished on the beach in order to reduce the retreat of the duneface during storm conditions. This method is frequently used in the Netherlands, see e.g. (Van de Graaff et al., 1991).

The beach and dune nourishment shown in Figure 8.9 amounts to $242 \text{ m}^3/\text{m}^1$.

In this figure also the final result of the computation after 20 hours is shown, as well as the final result of the standard case also without nourishment after 20 hours.

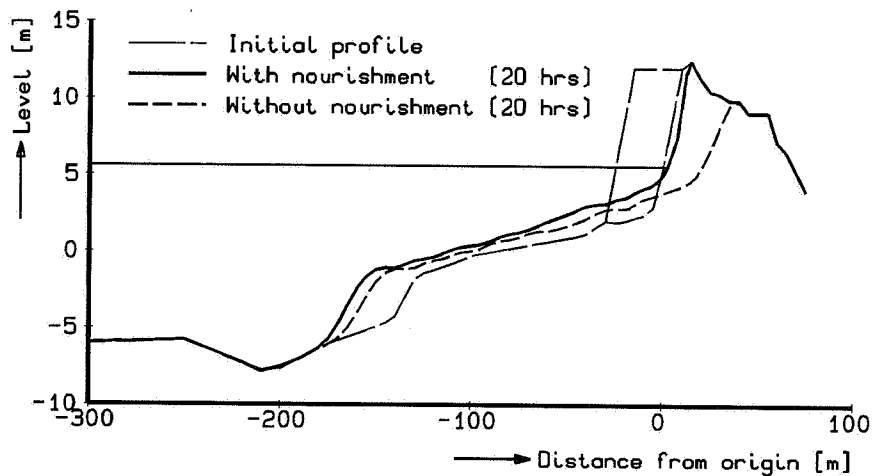


Figure 8.9 *Computed effect of beach/dune nourishment in comparison to a profile without nourishment.*

The final position of the duneface is relatively located at a more seaward position, although the amount of erosion (above storm surge level) is increased by 30% (185 instead of $141 \text{ m}^3/\text{m}^1$). In this case the final retreat of the duneface amounts to about 30 m.

It will be obvious that for separate beach-nourishment configurations, the typical characteristics of the beach fill and various design storms should be assessed to study their relative effect. An example of such an elaboration using the SBEACH-model (see Section 3.4), is given in (Larson and Kraus, 1989b).

8.5 Effect of structures

8.5.1 Introduction

Some examples will be presented for both dune revetments (seawalls) and alongshore dams. The main goal of a (partial) revetment in the duneface is to reduce the amount of dune erosion, or even obstruct dune erosion during extreme storm conditions. Some considerations on the effectiveness of dune toe-revetments are presented in (Steezel, 1988).

Essential for the actual rate of reduction is the level of the top of the revetment with respect to both the storm surge level and the maximum dune level. A very high revetment (seawall or dike-like structure) will obstruct erosion completely, whereas a very low structure (say below storm surge level) does not have any particular influence on the amount of erosion.

8.5.2 High revetments (seawall)

The main goal of a high revetment in the duneface as shown in Figure 8.10 is to prevent the dune itself from erosion during extreme wave conditions.

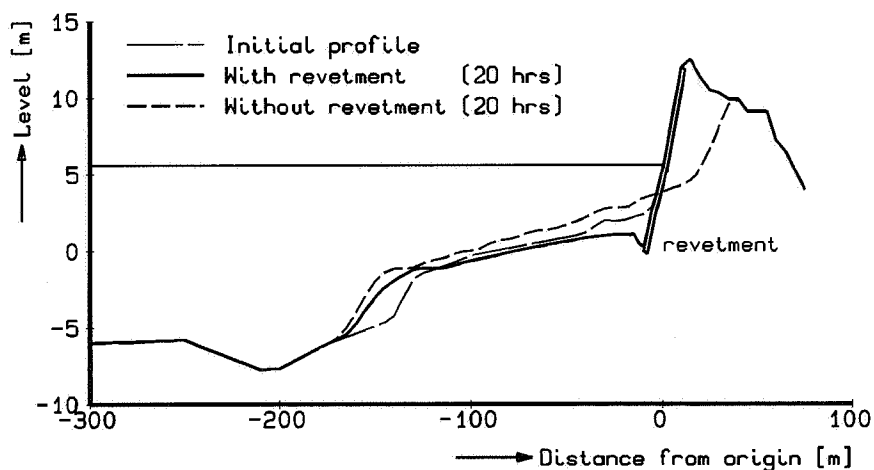


Figure 8.10 *Computed effect of high revetment in comparison to a profile without a revetment.*

In this figure the final result of the computation after 20 hours is shown, as well as the final result of the standard case without revetment.

Due to cross-shore transports the beach partly disappears due to (some) lowering of the local profile. An important feature of the observed erosion profile is the formation of a pronounced scour hole in front of the revetment. This phenomena is comparable with the

results of large-scale model tests in the Deltaflume (see Chapter 6).

Relative to the situation without a revetment a seawall is, of course, very effective in preventing landward erosion, but has clearly a great impact on the development of the profile in front of the wall. This influence has been described by several researchers, see e.g. (Barnett and Wang, 1988).

Of course, one has to be sure that scouring in front of the structure will not undermine the revetment, since this will cause very serious problems such as a complete failure of the revetment. The subsequent amount of dune erosion in a failed cross-section will probably even exceed the rate for an unprotected dune!

Finally, it is noted that although much attention has been paid to all related effects with respect to seawalls by numerous researchers, although as yet no identical judgement on its effectiveness was achieved, see e.g. (Kraus, 1988). A comprehensive overview of all relevant effects is presented by Tait and Griggs (1990).

8.5.3 Low revetments

In the case of a revetment with a crest level lower than the maximum wave run-up, the amount of dune erosion is only partly reduced.

In Figure 8.11 the final result of the computation after 20 hours is shown for a revetment of intermediate height as well as the final result of the standard case without any revetment.

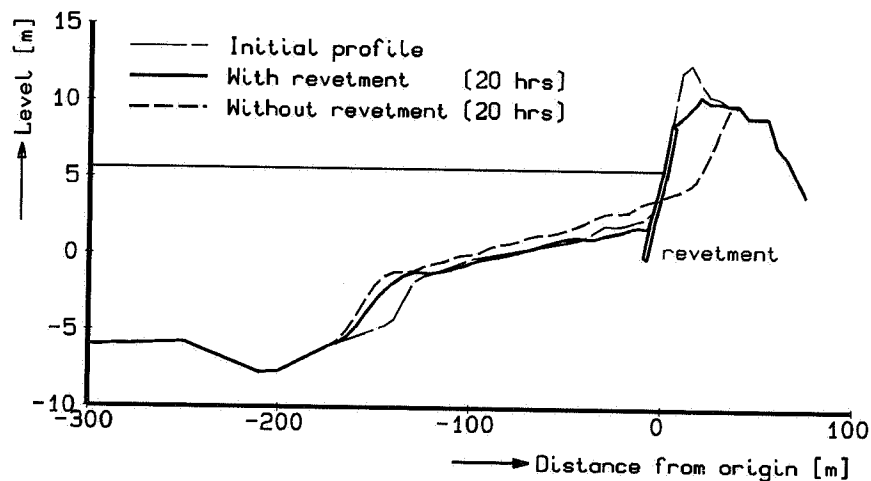


Figure 8.11 *Computed effect of lower revetment in comparison to a profile without a revetment.*

The amount of erosion above the crest of the revetment amounts to $37 \text{ m}^3/\text{m}^1$. There will be no effect on the amount of dune erosion above storm surge level if the crest lies at the level of the normal erosion profile, say at $+3.5 \text{ m}$.

It is remarked that relative to the seawall case hardly any information on the behaviour of low revetments was found in literature.

8.5.4 Nearshore low dam

Figure 8.12 shows the computed effect of a nearshore dam on the beach on the final profile after the storm surge.

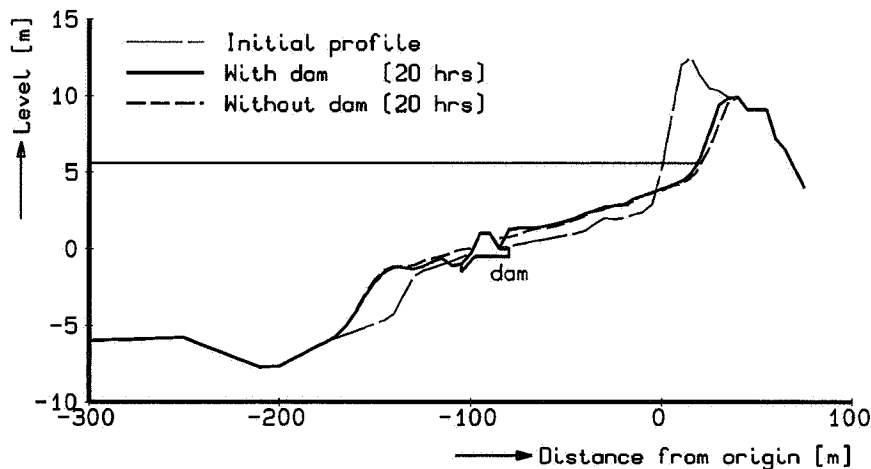


Figure 8.12 Computed effect of dam in comparison to a profile without any construction.

In the case of a low dam and extreme events and so high water levels, the amount of erosion at the duneface is hardly affected by the presence of such a structure. The amount of dune erosion is reduced by only 10% (127 instead of $141 \text{ m}^3/\text{m}^1$), see also (Douglas and Weggel, 1987).

Relative to the situation without a structure, some local effects occur. Landward of the dam some additional settlement of eroded sediment is present, while on the other side a scour hole may be formed comparable with the situation with a seawall, see Section 8.5.2.

Previous results are in agreement with the outcome of laboratory studies as reported by Sorensen and Beil (1988), Lamberti et al. (1985) and Sawaragi et al. (1988).

8.6 Effect of oblique wave attack

8.6.1 Introduction

Due to oblique wave attack the effective attack on the dune reduces. In the following some results of this effect will be illustrated.

8.6.2 Computational results

In Figure 8.13 the cross-shore profiles for both oblique wave attack of 30 degrees and perpendicular wave attack of the standard case are presented.

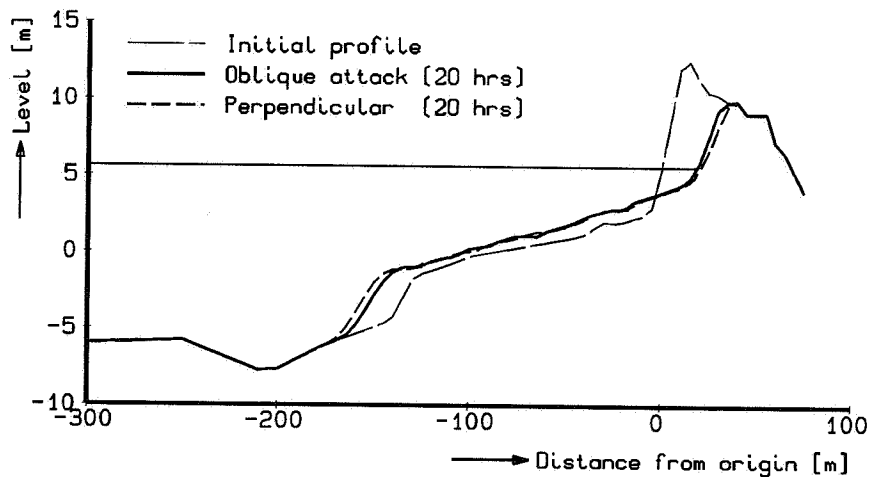


Figure 8.13 *Computed effect of oblique wave attack (at 30 degrees) in comparison to the effect of perpendicular wave attack.*

The amount of erosion above storm surge level has slightly decreased, namely by 9 % (129 instead of 141 m^3/m^1).

8.6.3 Erosion quantities

In Figure 8.14 the amount of erosion above storm surge level is presented as a function of the angle of wave attack.

Due to a decrease in effective wave attack (both due to friction and refraction effects) the amount of erosion decreases with increasing angle of wave attack. However, for this particular situation, up to an angle of about 30 degrees, this effect is still insignificant, say <10 %.

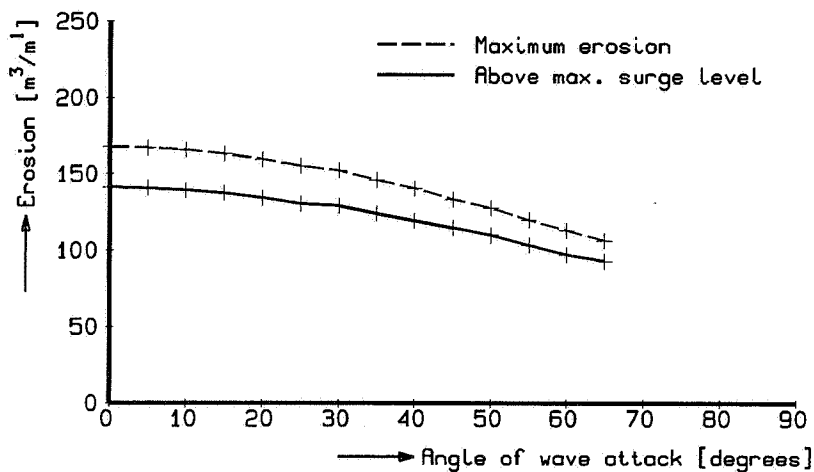


Figure 8.14 Computed effect of angle of wave attack on dune erosion quantity.

The latter is in agreement with the results of a verification study in which the dune erosion process was investigated in a three-dimensional model (DELFT HYDRAULICS, 1981b).

8.6.4 Longshore transport rates

During periods with intensive cross-shore transports and, consequently, large amounts of suspended sediment across the breaker zone, the longshore current present due to oblique wave attack or tidal influences will result in a significant longshore transport rate.

The cross-shore integrated, longshore transport rate will vary during the storm surge. For constant hydraulic conditions this longshore transport rate will decrease in time due to decreasing cross-shore transports (reaching near-equilibrium conditions).

Figure 8.15 presents the total amount of both cross-shore and time-integrated longshore transport as a function of the angle of wave attack.

The total amount of longshore transport due to a specific storm surge increases with increasing wave angle until about 30 degrees after which it decreases to zero at 90 degrees. This result can be compared with $S(\phi)$ -relations used in one-line coastline modelling.

The magnitude of these computed transports indicate that storm-surge conditions may have a significant effect on the yearly mean longshore transport rate and, consequently, should be taken in account when computing coastline development. This is in agreement with the findings by Jaffe (1992), who examined the contribution of extreme events to sediment transport in the surf zone.

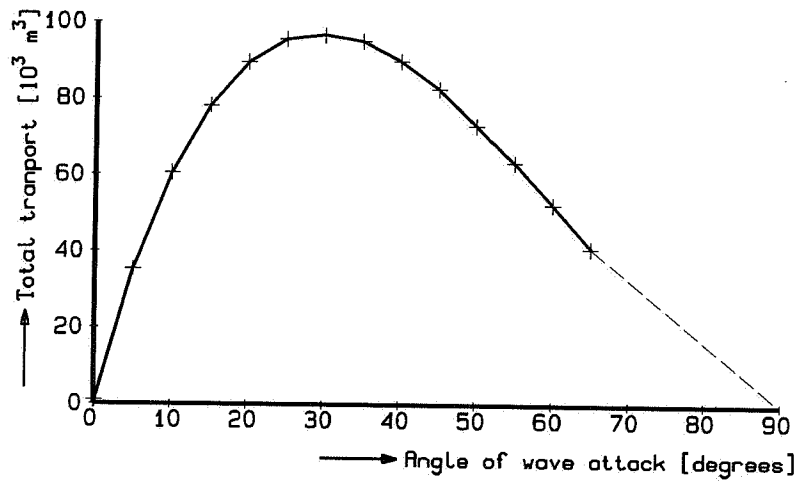


Figure 8.15 Computed effect of angle of wave attack on longshore transport rate.

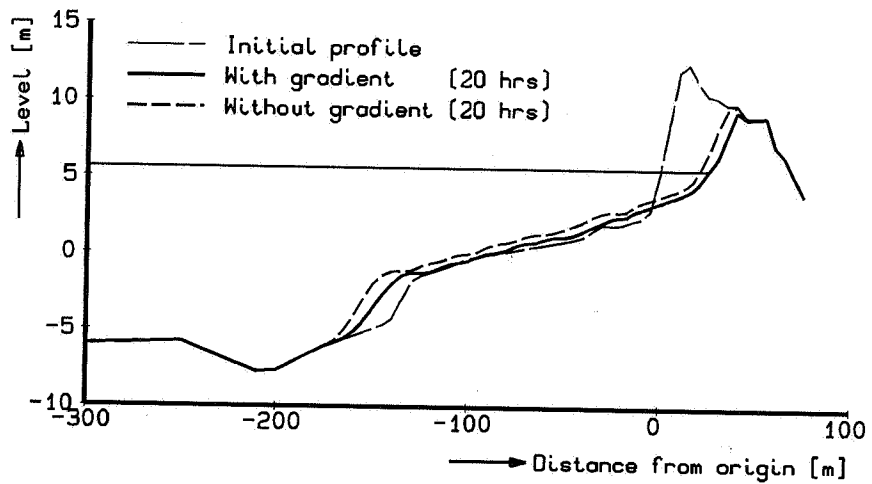


Figure 8.16 Computed effect of coastal curvature in comparison to a non-curved coastline.

8.6.5 Coastal curvature

Due to a positive coastal curvature the amount of longshore transport increases along the coast, resulting in a loss of sediment between two adjacent rays.

In Figure 8.16 the computed effect of a coastal curvature of $R = 3000$ m is shown which represents a shift in coastline orientation of about 2 degrees for each 100 m.

As can be seen from the comparison of situations with and without longshore transport gradients, the coastal profile is effectively shifted landward across a distance of about 10 m due to the coastline curvature. The amount of erosion (above storm surge level) increases by about 20% (167 instead of 141 m^3/m^1). The loss of sediment in alongshore direction is about 133 m^3/m^1 .

A further elaboration of the effect of a coastal curvature on the additional dune erosion rate is presented in (DELFT HYDRAULICS, 1983b; Steetzel, 1990b).

8.7 Conclusions

Incorporation of physical processes such as suspended sediment concentration and secondary flow field (undertow) in the dynamical cross-shore transport model results in a reliable outcome even in applications well beyond the standard ones.

Consequently, the model is useful to predict storm surge effects and to examine the relative effects of various measures on the profile development.

9 CONCLUDING REMARKS

9.1 Introduction

The aim of the research described in this thesis was to augment the insight into the process of dune erosion, which would enable development of a new computational model for prediction of the impact of a storm surge on a sandy coast. The use of a so-called erosion profile model, i.e. the existing DUROS-model to determine these effects was judged to be unsuitable for a number of coastal problems. Problematic examples of such problems are the assessment of the effects in the case of a 'non-standard' geometry or hydraulic condition, the impact of structures present in the coastal profile and the supplementary effect of alongshore transport gradients. By computing the actual development of the coastal profile during a storm surge, the shortcomings of the 'erosion profile approach' can be excluded. This new approach, however, calls for detailed knowledge on the transport processes involved. As could be gathered from the title of this work, a significant part of its content actually deals with the analysis and description of the cross-shore transport process under breaking waves.

The evaluation and main findings of the research programme to study the transport phenomenon and ultimately application of the developed mathematical model are summarized concisely in the next section. In the very last section some recommendations for the further improvement of the model are presented.

9.2 Evaluation and main findings

9.2.1 Contributions to the cross-shore transport rate

As already indicated above, considerable attention has been paid to the derivation of a reliable formulation for the assessment of the cross-shore transport rate during storm surge conditions. Since intensive breaking of waves generates high turbulence levels which cause large amounts of sediment to suspend, accordingly, the transport of this suspended sediment is the predominant transport mechanism during these conditions.

Beginning with the basic procedure for nett transport computation, two elementary contributions to the nett transport rate $s(z)$ have been recognized, namely a mean contribution $\bar{s}(z)$ based on the product of time-averaged concentrations and time-averaged velocities and a more complicated correlation contribution $s'(z)$ which is due to the fluctuating components. The relative magnitude of these contributions to the nett transport rate has been assessed for simple, local harmonic fluctuations of concentration and velocity

terms as well as for the more complicated depth-integrated effect of both terms. For the latter effect, both an analytical approximation as well as a mathematical model for the solution of the non-stationary diffusion equation have been applied.

Based on these analyses as well as on the results of some detailed experiments carried out by other researchers, it was concluded that the magnitude of the depth-integrated correlation component S' for the hydraulic conditions involved, is relatively small compared to the depth-integrated mean flow component \bar{S} . Consequently, the nett transport rate can be assessed from the mean component as a first order of magnitude. More details on the arguments that were used for these elaboration are presented in Section 4.2.

Apart from the tremendous advantage that knowledge of the intra-wave fluctuations is unnecessary for this reason, the vertical distribution of the time-averaged flow field (undertow) and the time-averaged sediment concentrations have still to be described.

9.2.2 Sediment concentrations

The time-averaged vertical profile of the suspended sediment concentration, denoted as $C(z)$, as present under breaking waves has been analyzed starting with an examination of the apparent mixing profile for a reliable data set obtained in DELFT HYDRAULICS' Deltaflume. Based on this, the vertical distribution of the mixing coefficient $\varepsilon(z)$ is proved to be appropriately described by a simple linear relation with the elevation above the bed according to Equation (4.3.15). Both the governing parameters, viz. the reference mixing rate at the bed level ε_0 and the vertical mixing gradient μ , were related to the local hydraulic conditions as given by Equations (5.3.7) and (5.3.10) respectively.

From the formulation of the mixing profile, the final formulation of the vertical profile of the suspended sediment can be derived which is described by a power-relation as provided in Equation (4.3.19).

While the mixing parameters ε_0 and μ and the sediment's fall velocity w_s determine the shape of the concentration profile, its overall magnitude is controlled by the reference concentration at the bed level, viz. C_0 . From an extensive analysis of numerous relations with conceivable governing parameters it was found that the most favourable correlation occurred when using the breaking-wave dissipation. A appropriate relation with especially the turbulent dissipation rate D_t was used whilst the wave height/water depth ratio γ was also accounted for. In the final equation, viz. Equation (5.4.11), the amount of suspended sediment is thus related to both the intensity of wave breaking and the way the individual waves break, say spilling or plunging.

9.2.3 Secondary flow

The description of the time-averaged velocity profile, denoted as $u(z)$, is based on the vertical distribution of the time-averaged shear stress below the level of the mean wave trough. Using the previously derived first-order distribution of the sediment mixing coefficient as a reliable estimate for the fluid-related mixing coefficient, the accompanying expression for the secondary flow profile was derived. Using a relation between the mean

velocity and the mean shear stress near the bed, viz. u_0 and τ_0 , the exact shape of this profile is controlled by both the mass flux and the shear stress acting on the lower zone.

9.2.4 Cross-shore transport computation

Since during an extreme wave attack the suspended transport based on time-averaged concentrations and velocities is dominant, an assessment of its magnitude was derived by multiplying the time-averaged profiles of suspended sediment and horizontal water motion. Doing this for the zone below the wave troughs yields an expression for the resulting offshore transport rate consisting of three terms as provided in Equation (4.5.4). The landward-directed transport above the mean wave trough level is based on the mean sediment concentration at the mean water level and the amount of passing water, e.g. the mass flux. A justification of this procedure using data from a large-scale flume test showed that the derived formulations indeed resulted in a the right order of magnitude for the transport rate, although additional transport correction factors for bottom slope and swash effects will be required.

9.2.5 Mathematical model

Using the wave energy decay model ENDEC to determine the cross-shore distribution of the hydraulic conditions, the accompanying distribution of the cross-shore transport rate can be computed also using former previously derived expressions. By computing the changing bottom profile from the mass balance of sediment and repeating this procedure in a time loop, a mathematical model is established.

The outcome of the initial computations for a large-scale test were used to tune the performance of the model with respect to the formation of the under water profile. Finally, the applicability of the DUROSTA-model was extended by adjusting and adding computational routines for the incorporation of the effects of both structures and longshore transports.

9.2.6 Performance, sensitivity and accuracy

The performance of the mathematical model was determined by a comprehensive comparison between observed and computed profile changes using data from several large-scale and small-scale model tests and a limited number of prototype data.

In general, good agreement was found between the shape, slope and position of the 'seaward' erosion profiles especially for the large-scale model tests. The amount of erosion above the storm surge level is under-estimated systematically, due to both the model's behaviour near the water line and the effects of the non-constant porosity.

Although the outcome of small-scale tests do not allow for a comparable elaboration, the results of a systematic assessment of the model's sensitivity show that the dependencies on the governing parameters are correctly reproduced by the model.

With respect to the model's accuracy for unprotected dunes, the average under-prediction of the dune erosion rate was estimated to be about 10 %.

The performance of both the model extensions is discussed briefly in the following.

9.2.7 Effect of structures

A structure has been modelled by incorporation of a non-erodible section in the cross-shore profile. By using an actually rather straightforward adaptation of the computational routine for the assessment of the bottom changes per time step, a useful extension of the basic model is achieved.

Some main features, viz. scour in front of structures and sheltering effects of dams are represented correctly, although with respect to the exact scouring depth a systematic under-prediction is found.

9.2.8 Longshore effects

The longshore transport during storm surges, as computed from the product of longshore current and breaking wave induced sediment concentrations yields considerable large magnitudes. Consequently, the presence of a gradient in this longshore transport rate may cause a significant impact on the amount of dune erosion to be expected during these conditions. Although no verification data are available to check the outcome of the model for these cases, the model results seem nevertheless reliable.

Moreover, for non-extreme conditions, the present formulation results in an alongshore transport rate which is comparable to the magnitude found by using other commonly applied longshore transport formulae such as those of Bijker, Van Rijn and Bailard.

9.2.9 Overall conclusion

A predictive model for sediment load and cross-shore transport due to extreme wave attack has been developed which gives a reliable description of the transports and profile development during a storm surge. Even the computed longshore transport rates seem plausible.

Comparison between model results and available large-scale data sets indicate that the model gives reliable results, although in some cases discrepancies were found.

By using this model the amount of erosion can be determined for (more or less) arbitrary coastal profiles, e.g. with bars and tidal gullies or with (partly) protected dunes (dune revetments) due to arbitrary storm surge conditions.

The model, which also predicts beach profile changes in front of dune revetments, is to be used as a tool to check the safety of the narrow stretch of sandy beaches and dunes which protect the Dutch population against the sea. It should be used in addition to (or will replace at the long-term) the model that is used for the present guide line for the assessment

of the safety of dunes (TAW, 1984, 1990).

Finally, it is noted that the presented results correspond remarkably well with the recommendations expressed in the summarizing chapter of a previous (Dutch) thesis on dune erosion modelling, i.e. Vellinga's dissertation (Vellinga, 1986). If the recommendations in this work turn out to follow those of Vellinga's, the author is sure that it will result in a superior model at the end.

9.3 Recommendations for further research

9.3.1 Introduction

In order to increase both the accuracy and reliability of the present model, i.e. to achieve an initial notable update of the present DUROSTA-1.11-model, special attention should be paid in the first place to the effects of a non-constant compaction on the sediment balance as well as to the swash-induced transports on the beach. These and other adaptations of the present model are discussed briefly in the following.

The possibly incorporation of the presented formulations for the transport rate in more complex morphological models is dealt with in the subsequent (and last) section.

9.3.2 Further update of the present model

The significant difference between the porosity of the bed material in the duneface and the sand settled in the erosion profile leads, relative to a case in which this effect is not taken into account, to an increase in dune erosion quantity. It is therefore recommended that this effect be accounted for by adjusting the initially computed retreat of the dunefoot (Steetzel, 1993).

The profile development in the swash zone, say between water line and duneface, does not agree well with the measurements. The erosion, i.e. lowering of the bed level, in the mathematical model is concentrated too much near the water line, whereas in nature a smoother transition towards the duneface area is found. Some ideas to improve this are elaborated in (Steetzel, 1993).

In order to account for the effect of especially post-storm hydraulic conditions on the development of the cross-shore profile, the ability of the incoming waves to move sand towards the coast, viz. the post-storm recovery, has to be modelled also. A feasible solution to do this may be the incorporation of the Ω -factor as discussed in Section 4.2. It is noted that incorporation of this 'wave asymmetry' effect was not considered in an earlier stage of the research programme since this contribution seemed to be not relevant in the 'eroding phase' of the design storm surge, viz. has no significant effect on the maximum amount of dune erosion.

Furthermore, additional verification for new data sets and (perhaps) re-calibration of the transport model is preferable. It is recommended that data be used from well-documented large-scale tests. The tests carried out within the framework of the Large Installations Plan in DELFT HYDRAULICS' Deltaflume are a useful example of such tests (DELFT HYDRAULICS, 1993).

Finally, it is noted that for the use of this model for rather unknown design conditions, the effect of the uncertainties of the governing parameters should be taken into account in the ultimate computed recession of the duneface. This requires also a probabilistic version of the present model, see e.g. (Van de Graaff, 1983, 1986).

9.3.3 Supplementary extension of model

Apart from an update of the present model, a more extended version would also be preferable. In order to perform computations in complicated coastal areas (e.g. near the extremity of an island situated at an outer delta), it is proposed that the derived transport formulation be incorporated into a two-dimensional horizontal mathematical model. By using a 2DH- (or in fact quasi-3D-) mathematical model, the impact of a design storm surge can be assessed in more detail. Since both the theoretical and mathematical procedures are available now, it is recommended that such a model be constructed and that at least one exploratory computation be performed for an illustrative part of the Dutch coastline (e.g. the Isle of Texel).



REFERENCES

- Al-Salem, A.A., 1993: Sediment transport in oscillatory boundary layers under sheet-flow conditions; *Ph.D. Thesis, Delft University of Technology (to appear)*.
- Bagnold, R.A., 1962: Autosuspension of transported sediment, turbidity currents; *Proceedings of the Royal Society of London, Series A265, pp.315-319*.
- Bagnold, R.A., 1966: An approach to the sediment transport problem from general physics; *Geological Survey Professional Paper 422-I, 37 pp.*
- Bailard, J.A., and D.L. Inman, 1981: An energetics bedload model for a plane sloping beach, local transport; *Journal of Geophysical Research, Vol.86, No.C3, pp.2035-2043*.
- Bailard, J.A., 1982: Modelling on-offshore sediment transport in the surfzone; *Proceedings 18th International Conference on Coastal Engineering, pp.1419-1438*.
- Bakker, W.T., 1974: Sand concentration in oscillatory flow; *Proceedings 14th International Conference on Coastal Engineering, pp.1129-1148*.
- Barnett, M.R., and H. Wang, 1988: Effects of a vertical seawall on profile response; *Proceedings 21th International Conference on Coastal Engineering, pp.1493-1507, Malaga*.
- Battjes, J.A., 1974: Computation of set-up, longshore currents, run-up and overtopping due to wind-generated waves; *Communications on Hydraulics, Department of Civil Engineering, Delft University of Technology, 74-2, 244 pp.*
- Battjes, J.A., and J.P.F.M. Janssen, 1978: Energy loss and set-up due to wave breaking of random waves; *Proceedings 16th International Conference on Coastal Engineering, pp.569-589*.
- Bijker, E.W., 1967: Some considerations about scales for coastal models with movable bed; *Ph.D. Thesis, Delft University of Technology; also: Publication No.50 DELFT HYDRAULICS*.
- Bosman, J.J., and H.J. Steetzel, 1986: Time- and bed-averaged concentrations under waves; *Proceedings 20th International Conference on Coastal Engineering, pp.986-1000, Taipei*.
- Bosman, J.J., E.T.J.M van der Velden and C.H. Hulsbergen, 1987: Sediment concentration measurements by transverse suction; *Coastal Engineering, Vol.11, No.4, Elsevier Science Publishers, Amsterdam*.
- Bruun, P., 1954: Coast erosion and development of beach profiles; *Technical Memo No.44, Beach Erosion Board, U.S. Army Corps of Civil Engineers*.
- Bruun, P., 1962: Sea level rise as a cause of the shore erosion; *Journal of the Waterways and Harbour Division, ASCE, Vol.88, WW1, pp.117-130*.
- Bruun, P., 1992: Discussion of: Bodge, K., Representing equilibrium beach profiles with an exponential expression; *Journal of Coastal Research, Vol.8, No.3*.
- Centrum voor Onderzoek Waterkeringen (COW), 1982: Hydraulische randvoorwaarden ten behoeve van modelonderzoek naar duinafslag (Hydraulic conditions to be used in dune erosion tests); *Note S-81.015 (in Dutch)*.
- Chen, Z., 1992a: Cross-shore transport modelling in terms of sediment concentrations and velocities; *Proceedings 23th International Conference on Coastal Engineering, Venice, Italy (to appear)*.
- Chen, Z., 1992b: Sediment concentration and sediment transport due to action of waves and a current; *Ph.D. Thesis, Delft University of Technology, Delft*.
- Dally, W.R., 1980: A numerical model for beach profile evolution; *Ms.S. Thesis, University of Delaware*.

REFERENCES *(continued)*

- Dean, R.G., 1977: Equilibrium beach profiles; *U.S. Atlantic and Gulf coasts, Ocean Engineering Report No.12, Department of Civil Engineering, University of Delaware, Newark, 45 pp.*
- Dean, R.G., 1982: Models for beach profile response; *Technical Report No.30, University of Delaware, Newark.*
- Dean, R.G., 1987: Coastal sediment processes: Towards engineering solutions; *Proceedings Coastal Sediments '87, pp.1-24.*
- Dean, R.G., 1991: Equilibrium beach profiles: Characteristics and applications; *Journal of Coastal Research, Vol.7, No.1, pp.53-84.*
- Deigaard, R., and J. Fredsøe, 1989: Shear stress distribution in dissipative water waves; *Coastal Engineering, Vol.13, pp.357-378.*
- Deigaard, R., P. Justesen and J. Fredsøe, 1991: Modelling of undertow by a one-equation turbulence model; *Coastal Engineering, Vol.15, pp.431-458.*
- DELFT HYDRAULICS, 1981a: Schaalserie duinafslag, verslag modelonderzoek (Scale series on dune erosion, experimental research report); *Report MI263, part II (in Dutch).*
- DELFT HYDRAULICS, 1981b: Onderzoek naar duinafslag tijdens stormvloed, toetsing van de resultaten van het twee-dimensionale onderzoek door middel van onderzoek in een drie-dimensionaal model (Verification of dune erosion results from two-dimensional tests in a three-dimensional model); *Research report MI653 (in Dutch).*
- DELFT HYDRAULICS, 1982a: Rekenmodel voor de verwachting van duinafslag tijdens stormvloed (Dune erosion prediction model); *Research report MI263, part IV (in Dutch).*
- DELFT HYDRAULICS, 1982b: Duinafslag tijdens superstormvloed, Noorderstrand Schouwen (Dune erosion during a super storm surge, Noorderstrand Schouwen); *Research report MI797 (in Dutch).*
- DELFT HYDRAULICS, 1982c: Duinafslag ter plaatse van de hotels 'La Specia' en 'De blanke top' in Zeeuwsch-Vlaanderen (Dune erosion at the hotels 'La Specia' en 'De blanke top' in Zeeuwsch-Vlaanderen); *Research report MI811 (in Dutch).*
- DELFT HYDRAULICS, 1982d: Systematisch onderzoek naar duinafslag bepalende factoren (Systematic investigation of parameters relevant for dune erosion); *Research report MI819, part I (in Dutch).*
- DELFT HYDRAULICS, 1983a: Valsnelheid van zand in zeewater van 5°C (Settling velocities of sand in sea water of 5°C); *Note MI263, part IV-b (in Dutch).*
- DELFT HYDRAULICS, 1983b: Duinafslag bij gebogen kusten, orde-grootte bepaling van de gradiënt in het langtransport tijdens duinafslag aan een gebogen kust (Dune erosion at curved beaches, determination of the order of magnitude of the longshore sediment transport gradient under dune erosion conditions); *Research report MI263, part V (in Dutch).*
- DELFT HYDRAULICS, 1983c: Verification of predictive computational model for beach and dune erosion during storm surges; Verification for field data of dune erosion caused by Hurricane Eloise at Walton County in Florida, september 1975; *Research report MI263.*
- DELFT HYDRAULICS, 1983d: Oriënterend onderzoek naar de werking van een duinvoetverdediging tijdens superstormvloed (Investigations on the effectiveness of a dune toe revetment during critical storm surge); *Research report MI819, part III (in Dutch).*
- DELFT HYDRAULICS, 1984a: Schaalserie duinafslag, proeven op grote schaal in de Deltagoot (Scale series on dune erosion, large scale tests in the Delta Flume); *Research report MI263, part III (in Dutch).*

REFERENCES *(continued)*

- DELFT HYDRAULICS, 1984b: Duinafslag tijdens superstormvloed op Walcheren, Golflinks en Vijgeter, onderzoek naar de werking en sterkte van de duinvoetverdediging (Dune erosion due to design storm surge at Walcheren, Golflinks en Vijgeter, investigation of stability and effect of the dune revetments); *Research report M1958 (in Dutch)*.
- DELFT HYDRAULICS, 1985a: Dwarstransport tijdens duinafslag (Cross-shore transport during dune erosion); *Research report M1263, part V (in Dutch)*.
- DELFT HYDRAULICS, 1985b: Systematisch onderzoek naar de werking van duinvoetverdedigingen, een eerste analyse van de relevante processen op basis van reeds uitgevoerd modelonderzoek (Systematic research on the effectiveness of dune toe revetments, a first analysis of the relevant processes based on results of earlier experiments); *Research report M2051, part I (in Dutch)*.
- DELFT HYDRAULICS, 1986a: Systematisch onderzoek naar de werking van duinvoetverdedigingen, modelonderzoek op kleine schaal (Systematic research on the effectiveness of dune toe revetments, small scale model investigations); *Research report M2051, part II (in Dutch)*.
- DELFT HYDRAULICS, 1986b: Three-dimensional modelling of suspended transport for currents and waves; *Research report H461/Q250/Q422*.
- DELFT HYDRAULICS, 1987a: Systematisch onderzoek naar de werking van duinvoetverdedigingen, modelonderzoek op grote schaal (Systematic research on the effectiveness of dune toe revetments, large scale model investigations); *Research report H298, part I (in Dutch)*.
- DELFT HYDRAULICS, 1987b: Toe te passen golfrandvoorwaarden in duinafslagberekeningen (Governing wave condition for dune erosion computations); *Research report H298, part VI (in Dutch)*.
- DELFT HYDRAULICS, 1987c: Duinafslag bij steile vooroevers, onderzoek naar de effecten van een diepe geul op de mate van duinafslag (Dune erosion at steep beaches, investigation on the effects of a deep gully on the amount of dune erosion); *Research report H490 (in Dutch)*.
- DELFT HYDRAULICS, 1988: Ontgrondingskuilen: Analyse van de voor de kuilvorm bepalende factoren op basis van uitgevoerd modelonderzoek en beschikbare literatuurgegevens (Scour holes: Analysis of the scour governing parameters based on performed model tests and available literature); *Research report H298, part IV (in Dutch)*.
- DELFT HYDRAULICS, 1990a: DUROSTA, Tijdsafhankelijk dwarstransportmodel voor extreme condities (DUROSTA, dynamical cross-shore transport model for extreme conditions); *Research report H298, part III (in Dutch)*.
- DELFT HYDRAULICS, 1990b: Golfhoogteafname tijdens extreme condities (Wave height decay during extreme hydraulic conditions); *Research report H298, part II (in Dutch)*.
- DELFT HYDRAULICS, 1990c: Effect langstransportgradiënten op de mate van duinafslag, berekeningen met het DUROSTA-model (Effect of longshore transport gradients on the amount of dune erosion, computation with the DUROSTA-model); *Research report H298, part V (in Dutch)*.
- DELFT HYDRAULICS, 1990d: Gedragsmodel DUINVOET (Model DUINVOET); *Research report H1173 (in Dutch)*.
- DELFT HYDRAULICS, 1991: DUROSTA: Tijdsafhankelijk dwarstransportmodel voor extreme hydraulische condities (DUROSTA: Time dependent cross-shore transport model for extreme hydraulic conditions); *Manual version 1.11 (in Dutch)*.
- DELFT HYDRAULICS, 1992a: Verificatie DUROSTA (Verification DUROSTA); *Research report H1201, part I (in Dutch)*.

REFERENCES *(continued)*

- DELFT HYDRAULICS, 1992b: Vergelijking DUROS/DUROSTA (Comparison DUROS/DUROSTA); *Research report HI201, part II (in Dutch)*.
- DELFT HYDRAULICS, 1992c: Krokusstormen, duinafslag voorjaarsstormen 1990 ('Krokus' storm surge, dune erosion spring surges 1990); *Research report HI201, part III (in Dutch)*.
- DELFT HYDRAULICS, 1993: LIP 11D Deltaflume experiments; *Research report HI572 (to appear)*.
- Dette, H.H., and K. Uliczka, 1986: Velocity and sediment concentration fields across surf zones; *Proceedings 20th International Conference on Coastal Engineering, Ch.79, Taipei*.
- Dette, H.H., and K. Uliczka, 1988: Seegangserzeugte Wechselwirkung zwischen Vorland und Vorstrand, sowie Küstenschutzbauwerk (Wave induced adjustment of foreshore and beach and effect of dune protection); *University of Hannover, Technical Report No.7-9, SFB 205/TP A6 (in German)*.
- Douglas, S.L., and J.R. Weggel, 1987: Performance of a perched beach; Slaughter beach; *Proceedings Coastal Sediments '87, pp.1369-1384, New Orleans*.
- Draper, N., and H. Smith, 1966: Applied regression analysis; *ed. J. Wilney & Sons, New York*.
- Edelman, T., 1970: Analyse van stormvloedsprofielen in Noord-Holland, Texel en Ameland na de storm van 20 februari 1970 (Analysis of post-storm profiles in Noord-Holland, Texel and Ameland after the storm of february 20, 1970); *Report WWK 70-6, Ministry of Transport and Public Works (Rijkswaterstaat), the Netherlands (in Dutch)*.
- Fredsøe, J., O.H. Anderssen and S. Silberg, 1985: Distribution of suspended sediment in large waves; *Journal of Waterway, Port, Coast and Ocean Engineering, Vol.111, No.6*.
- Graaff, J. van de, 1977: Dune erosion during a storm surge; *Coastal Engineering, Vol. 1, No.2*.
- Graaff, J. van de, 1983: Probabilistic design of dunes; *Proceedings Coastal Structures Conference, pp.820-832*.
- Graaff, J. van de, 1984: Probabilistische methoden bij het duinontwerp: Achtergronden van de TAW-leidraad duinafslag (Probabilistic design of dunes: Background information on the TAW-guideline); *Delft University of Technology, Delft (in Dutch)*.
- Graaff, J. van de, 1986: Probabilistic design of dunes; an example from the Netherlands; *Coastal Engineering, Vol. 9*.
- Graaff, J. van de, 1988: Sediment concentration due to wave action; *Ph.D. Thesis, Delft University of Technology, Delft*.
- Graaff, J. van de, H.D. Niemeyer and J. van Overeem, 1991: Beach nourishment, philosophy and coastal protection policy; *Coastal Engineering, Vol.16, pp.3-22*.
- Greenwood, B., and P.D. Osborne, 1990: Vertical and horizontal structure in cross-shore flows, An example of undertow and wave set-up on a barred beach; *Coastal Engineering, Vol.14, pp.543-580, Amsterdam*.
- Hallermeier, R.J., 1978: Uses for a calculated limit depth to beach erosion; *Proceedings 16th International Conference on Coastal Engineering*.
- Horikawa, K., A. Watanabe and S. Katori, 1982: A Laboratory study on suspended sediment due to wave action; *Proceedings 18th International Conference on Coastal Engineering, Cape Town*.

REFERENCES *(continued)*

- Horikawa, K. (ed), 1988: Nearshore dynamics and coastal processes: Theory, measurement, and predictive models; *University of Tokyo press*.
- Hughes, S.A., and T.Y. Chiu, 1981: Beach and dune erosion during severe storms; *Coastal and Oceanographic Engineering Department, University of Florida, Gainesville, Report UFL/COEL-TR/043, 288 pp.*
- Ifuku, M., and T. Kakinuma, 1988: Suspended sediment in the surf zone; *Proceedings 21th International Conference on Coastal Engineering, pp.1661-1675.*
- Jaffe, B.E., 1992: The contribution of suspension events to sediment transport in the surf zone; *Proceedings 23th International Conference on Coastal Engineering, Venice, Italy (to appear).*
- Kana, T.W., 1979: Suspended sediment in breaking waves; *Technical Report No.18, Coastal Research Division, Department of Geology, University of South Carolina.*
- Kajima, R., T. Shimizu, K. Maruyama and S. Saito, 1983: Experiments on beach profile change with a prototype wave flume; *Proceedings 18th International Conference on Coastal Engineering, pp.1385-1404.*
- Kobayashi, N., 1987: Analytical solution for dune erosion by storms; *Journal of Waterway, Port, Coastal and Ocean Engineering, ASCE, Vol.113, No.4.*
- Kraus, N.C., 1988: The effect of seawalls on the beach: Extended literature review; *Journal of Coastal Research, Special Issue No.4, pp.1-28.*
- Kraus, N.C., and M. Larson, 1988a: Beach profile change measured in the tank for large waves, 1956-1957 and 1962; *Technical Report CERC-88-6, Coastal Engineering Research Center, U.S. Army Engr., Waterways Experiment Station, Vicksburg.*
- Kraus, N.C., and M. Larson, 1988b: Prediction of initial profile adjustment of nourished beaches to wave action; *Proceedings of Beach Preservation Technology '88, Florida Shore and Beach Preservation Association, Tallahassee, Florida, pp.123-147.*
- Kriebel, D.L., 1982: Beach and dune response to hurricanes; *M.Sc. Thesis University of Delaware, Dep. of Civil Engineering, Newark, Delaware.*
- Kriebel, D.L., 1986: Verification study of a dune erosion model; *Shore and Beach, Vol.54, No.3, pp.13-21.*
- Kriebel, D.L., 1987: Beach recovery following Hurricane Elena; *Proceedings Coastal Sediments '87, ASCE, Vol.I, pp.990-1005.*
- Kriebel, D.L., 1990: Advances in numerical modelling of dune erosion; *Proceedings 22th International Conference on Coastal Engineering, pp.2304-2317, Delft.*
- Kriebel, D.L., and R.G. Dean, 1985: Numerical simulation of time-dependent beach and dune erosion; *Coastal Engineering, No.9, pp.221-245.*
- Kuriyama, Y., 1991: Investigation of cross-shore sediment transport rate and flow parameters in the surf zone using field data; *Report of the Port and Harbour Research Institute, Vol.30, No.2.*
- Lamberti A., A. Petrillo and M. Ranieri, 1985: A comparative analysis of some types of submerged barriers as beach defence structure; *Proceedings 21th IAHR congress, Melbourne, Australia.*
- Larson, M., 1988: Quantification of beach profile change; *Lund University, Institute of Science and Technology, Report No.1008, 293 pp.*

REFERENCES (continued)

- Larson, M., and N.C. Kraus, 1989a: SBEACH, Numerical model for simulating storm-induced beach change, empirical foundation and model development; *Technical Report CERC-89-9, Coastal Engineering Research Center, U.S. Army Engr., Vicksburg.*
- Larson, M., and N.C. Kraus, 1989b: Prediction of beach fill response to varying waves and water level; *Proceedings of Coastal Zone '89, ASCE, pp.607-621.*
- Lauder, B.E., and D.B. Spalding, 1972: Mathematical models of turbulence; *Academic, San Diego, California.*
- Leatherman, S.P., 1979: Beach and dune erosion interactions during storm surge conditions; *Quarterly Journal of Engineering Geology, Vol.12, pp.281-290.*
- Madsen, O.S., and W.D. Grant, 1976: Quantitative description of sediment transport by waves; *Proceedings 15th International Conference on Coastal Engineering, pp.1093-1112.*
- Meer, J.W. van der, 1988: Rock slopes and gravel beaches under wave attack; *Ph.D. Thesis, Delft University of Technology; also: Publication No.396 DELFT HYDRAULICS.*
- Meulen, T. van der, and M.R. Gourlay, 1968: Beach and dune erosion tests; *Proceedings 11th International Conference on Coastal Engineering, pp.701-707, London.*
- Möller, J.P., and D.H. Swart, 1988: Extreme erosion event on a artificial beach; *Proceedings 21th International Conference on Coastal Engineering, pp.1882-1896, Malaga.*
- Moore, B., 1982: Beach profile evolution in response to changes in water level and wave height; *M.Sc.Thesis Dept. of Civil Eng., Univ. of Delaware, Newark, DE.*
- Nadaoka, K., and T. Kondah, 1982: Laboratory measurements of velocity field structure in the surf zone by LDV; *Coastal Engineering in Japan, Vol.25.*
- Nadaoka, K., S. Ueno and T. Igavashi, 1988: Field observation of three-dimensional large-scale eddies on sediment suspension in the surf zone; *Coastal Engineering in Japan, Vol.31.*
- Nairn, R.B., 1990: Prediction of cross-shore sediment transport and beach profile evolution; *Ph.D. Thesis, Univ. of London.*
- Nielsen, P., 1979: Some basic concepts of wave sediment transport; *Series Paper no.20 ISVA, Technical University of Denmark.*
- Nielsen, P., 1984: Field measurements of time-averaged suspended sediments concentrations; *Coastal Engineering, Vol.8, pp.51-72.*
- Nielsen, P., 1985: A short manual on coastal bottom boundary layers and sediment transport; *Public Works Department New South Wales, Coastal Engineering Branch, Technical Memorandum TM 85/1.*
- Nielsen, P., 1992: Combined convection-diffusion modelling of sediment suspensions; *Proceedings 23th International Conference on Coastal Engineering, Venice (to appear).*
- Okayasu, A., T. Shibayama and N. Nimura, 1986: Velocity field under plunging waves; *Proceedings 20th International Conference on Coastal Engineering, pp.660-674, Taipei.*
- Okayasu, A., T. Shibayama and K. Horikawa, 1988: Vertical variation of undertow in the surf zone; *Proceedings 21th International Conference on Coastal Engineering, pp.478-491, Malaga.*
- Overtorn, M.F., J.S. Fisher and T. Fenaish, 1987: Numerical analysis of swash forces on dunes; *Proceedings Coastal Sediments '87, pp.632-641, New Orleans.*

REFERENCES (continued)

- Overtorn, M.F., and J.S. Fisher, 1988: Simulation modelling of dune erosion; *Proceedings 21th International Conference on Coastal Engineering*, pp.1857-1867, Malaga.
- Perigrene, P.H., and I.A. Svendsen, 1978: Spilling breakers, bores and hydraulic jumps; *Proceedings 16th International Conference on Coastal Engineering*, pp.540-550.
- Pilkey, O.H., R.S. Young, S.R. Riggs, A.W.S. Smith, H. Wu and W.D. Pilkey, 1993: The concept of shoreface profile equilibrium; A critical review; *Journal of Coastal Research*, Vol.9, No.1, pp.255-278.
- Pratikto, W.A., 1992: The relationship between dune erodibility and sand grain size and dune density; *Thesis, North Carolina State University, Raleigh, 1992*.
- Quick, M.E., 1991: Onshore-offshore sediment transport on beaches; *Coastal Engineering*, Vol.15, pp.313-332.
- Ras, S.L, and J.A. Amesz, 1989: Concentratie- en diffusiecoëfficiëntenverdeling onder onregelmatige en brekende golven (Concentration and diffusion coefficient distribution due to irregular and breaking waves); *M.Sc. Thesis, Delft University of Technology, Delft (in Dutch)*.
- Rector, R.I., 1954: Laboratory study of equilibrium beach profiles; *Beach Erosion Board, Technical Memorandum No.41*.
- Ribberink, J.S., 1987: Analytical solutions for nett sediment transport using the convection-diffusion equation; *Personal communication*.
- Ribberink, J.S., and A.A. Al-Salem, 1990: Bedforms, sediment concentrations and sediment transport under simulated wave conditions ; *Proceedings 22th International Conference on Coastal Engineering, Delft*.
- Ribberink, J.S., and A.A. Al-Salem, 1991: Near-bed sediment transport and suspended sediment concentrations under waves; *International Symposium on 'The transport of suspended sediment and its mathematical modelling', Florence, Italy*.
- Ribberink, J.S., and A.A. Al-Salem, 1992: Time-dependent sediment transport phenomena in oscillatory boundary-layer flow under sheetflow conditions; *Research report DELFT HYDRAULICS, H840-20, part VI*.
- Ribberink, J.S., and Z. Chen, 1993: Sediment transport of fine sands under asymmetric oscillatory flow: Experimental study in the large oscillating water tunnel of DELFT HYDRAULICS; *Research report DELFT HYDRAULICS, H840-20, part VII*.
- Rijn, L.C. van, 1989: Handbook sediment transport by currents and waves; *Report H461, DELFT HYDRAULICS*.
- Rijn, L.C. van, 1990: Principles of fluid flow and surface waves in rivers, estuaries, seas and oceans; *Aqua publications, The Netherlands*.
- Rijn, L.C. van, M.W.C. Nieuwjaar, T. van der Kaay, E. Nap and A. van Kampen, 1993: Transport of fine sands by currents and waves; *Journal of Waterway, Port, Coastal and Ocean Engineering*, Vol.119, No.2.
- Roelvink, J.A., and M.J.F. Stive, 1989: Bar generating cross-shore flow mechanism on a beach; *Journal of Geophysical Research*, Vol.94, No.C4, pp.4785-4800.
- Sargent, F.E., and W.A. Birkemeier, 1985: Application of the Dutch method for estimating storm-induced due erosion; *Technical Report CERC-85-2, Coastal Engineering Research Center, U.S. Army Engr., Waterways Experiment Station, Vicksburg*.

REFERENCES (continued)

- Sato, S., K. Homma and T. Shibayama, 1990: Laboratory study on sand suspension due to breaking waves; *Coastal Engineering in Japan*, Vol.33, No.1, pp.219-231.
- Sawaragi, T., I. Deguchi and S.K. Park, 1988: Experimental study on the function of submerged breakwater to control cross-shore sediment transport on artificially nourished beaches; *Coastal Engineering in Japan*, Vol.31, No.1.
- Sawaragi, T., I. Deguchi and S.K. Park, 1988: Experimental study on the function of submerged breakwater to control cross-shore sediment transport on artificially nourished beaches; *Coastal Engineering in Japan*, Vol.31, No.1.
- Shibayama, T., and K. Horikawa, 1982: Sediment transport and beach transformation; *Proceedings 18th International Conference on Coastal Engineering*, pp.1439-1458.
- Sleath, J.F.A., 1984: Sea bed mechanics; *John Wilney & Sons, New York*.
- Songvissessomja, S., and N. Samarasinghe, 1988: Profile of suspended sediment due to prototype wave; *Proceedings 6th Congress Asian and Pacific Regional Division, IAHR*, pp.97-104.
- Sorensen, R.M., and N.J. Beil, 1988: Perched beach profile response to wave action; *Proceedings 21th International Conference on Coastal Engineering, Malaga*.
- Steezel, H.J., 1984a: Beweging van vaste deeltjes in een niet-stationaire waterbeweging (Behaviour of solid particles in a non-stationary water motion); *Literature study M.Sc. Thesis, Delft University of Technology, Delft (in Dutch)*.
- Steezel, H.J., 1984b: Sedimentsuspensie in een oscillerende waterbeweging vlak boven een zandbed (Sediment suspension under oscillatory water motion close above a sandbed); *M.Sc. Thesis, Delft University of Technology, Delft (in Dutch)*.
- Steezel, H.J., 1985: Dwarstransport tijdens duinafslag (Cross-shore transport during dune erosion); *Research report DELFT HYDRAULICS M1263, part V (in Dutch)*.
- Steezel, H.J., 1986: Systematisch onderzoek naar de werking van duinvoetverdedigingen, modelonderzoek op kleine schaal (Systematic research on the effectiveness of dune toe revetments, small scale model investigations); *Research report DELFT HYDRAULICS M2051, part II (in Dutch)*.
- Steezel, H.J., 1987a: A model for beach and dune profile changes near dune revetments; *Proceedings Coastal Sediments '87, Vol.1, pp.87-97, New Orleans*.
- Steezel, H.J., 1987b: Systematisch onderzoek naar de werking van duinvoetverdedigingen, modelonderzoek op grote schaal (Systematic research on the effectiveness of dune toe revetments, large scale model investigations); *Research report DELFT HYDRAULICS H298, part I (in Dutch)*.
- Steezel, H.J., 1987c: Duinafslag bij steile vooroevers, onderzoek naar de effecten van een diepe geul op de mate van duinafslag (Dune erosion at steep beaches, investigation on the effects of a deep gully on the amount of dune erosion); *Research report DELFT HYDRAULICS H490 (in Dutch)*.
- Steezel, H.J., 1988: Ontgrondingskuilen: Analyse van de voor de kuilvorm bepalende factoren op basis van uitgevoerd modelonderzoek en beschikbare literatuurgegevens (Scour holes: Analysis of the scour governing parameters based on performed model tests and available literature); *Research report DELFT HYDRAULICS H298, part IV (in Dutch)*.
- Steezel, H.J., 1990a: DUROSTA, Tijdsafhankelijk dwarstransportmodel voor extreme condities (DUROSTA, dynamical cross-shore transport model for extreme conditions); *Research report DELFT HYDRAULICS H298, part III (in Dutch)*.

REFERENCES *(continued)*

- Steezel, H.J., 1990b: Golfhoogteafname tijdens extreme condities (Wave height decay during extreme hydraulic conditions); *Research report DELFT HYDRAULICS H298, part II (in Dutch)*.
- Steezel, H.J., 1990c: Effect langtransportgradiënten op de mate van duinafslag, berekeningen met het DUROSTA-model (Effect of longshore transport gradients on the amount of dune erosion, computation with the DUROSTA-model); *Research report DELFT HYDRAULICS H298, part V (in Dutch)*.
- Steezel, H.J., 1990d: Cross-shore transport during storm surges; *Proceedings 22th International Conference on Coastal Engineering, Vol.2, pp.1922-1932, Delft*.
- Steezel, H.J., 1991: A model for profile changes during storm surges; *Proceedings Coastal Sediments '91, Vol.1, pp.618-630, Seattle*.
- Steezel, H.J., and P.J. Visser, 1992: Profile development of dunes due to overflow; *Proceedings 23th Conference on Coastal Engineering, Venice (to appear)*.
- Steezel, H.J., 1992a: Bresgroei; 2DV-ontwikkeling initiële bres (Breach growth; 2DV-development of an initial small breach); *Research report DELFT HYDRAULICS H1242, part II (in Dutch)*.
- Steezel, H.J., 1992b: Verificatie DUROSTA (Verification DUROSTA); *Research report DELFT HYDRAULICS H1201, part I (in Dutch)*.
- Steezel, H.J., 1992c: Vergelijking DUROS/DUROSTA (Comparison DUROS/DUROSTA); *Research report DELFT HYDRAULICS H1201, part II (in Dutch)*.
- Steezel, H.J., 1992d: Krokusstormen, duinafslag voorjaarsstormen 1990 ('Krokus' storm surge, dune erosion spring surges 1990); *Research report DELFT HYDRAULICS H1201, part III (in Dutch)*.
- Steezel, H.J., 1993: Verfijning DUROSTA-model (Update DUROSTA-model); *Research report DELFT HYDRAULICS H1865 (to appear; in Dutch)*.
- Stive, M.J.F., and M.W. Dingemans, 1984: Calibration and verification of a one-dimensional wave energy decay model; *DELFT HYDRAULICS, Research report M1882*.
- Stive, M.J.F., and J.A. Battjes, 1985: Calibration and verification of a dissipation model for random breaking waves; *Journal of Geophysical Research, No. C5, pp.9159-9167*.
- Stive, M.J.F., and H.G. Wind, 1986: Cross-shore mean flow in the surf zone; *Coastal Engineering, Vol.10, pp.325-340*.
- Stive, M.J.F., 1988a: A model for cross-shore transport sediment transport; *Proceedings 20th International Conference on Coastal Engineering, Taipei*.
- Stive, M.J.F., 1988b: Cross-shore flow in waves breaking on a beach; *Ph.D. Thesis, Delft University of Technology; also: Publication No.395 DELFT HYDRAULICS*.
- Stive, M.J.F., 1991: Cross-shore transport modelling on different scales; *Workshop Coastal Sediments '91, Seattle*.
- Svendsen, I.A., 1984a: Wave heights and set-up in the surf zone; *Coastal Engineering, Vol.8, pp.303-329*.
- Svendsen, I.A., 1984b: Mass flux and undertow in a surf zone; *Coastal Engineering, Vol.8, pp.347-365*.
- Svendsen, I.A., and J.B. Hansen, 1986: The interactions of waves and currents over a longshore bar; *Proceedings 20th International Conference on Coastal Engineering, Taipei*.

REFERENCES (continued)

- Svendsen, I.A., and J.B. Hansen, 1988: Cross-shore currents in surf-zone modelling; *Coastal Engineering*, Vol.12, pp.23-42.
- Svendsen, I.A., and R.S. Lorentz, 1989: Velocities in combined undertow and longshore currents; *Coastal Engineering*, Vol.13, pp.55-79.
- Swart, D.H., 1974: Offshore sediment transport and equilibrium beach profiles; *Ph.D. Thesis, Delft University of Technology*; also: *Publication No.131, DELFT HYDRAULICS*.
- Swart, D.H., 1990: Extreme storm event; *Personal communication*.
- Tait, J.F., and G.B. Griggs, 1990: Beach response to the presence of a seawall, a comparison of field observations; *Shore and Beach*, Vol.4, pp.11-28.
- Technische Adviescommissie voor de Waterkeringen (TAW), 1984: Leidraad voor de beoordeling van de veiligheid van duinen als waterkering (Guide for the safety of dune as a water retaining structure); *Staatsuitgeverij, The Hague (in Dutch)*.
- Technical Advisory Committee on Water Defences (TAW), 1990: Guide to assessment of the safety of dunes as a sea defence; *Report 140, Centre for civil engineering research and codes (CUR), Gouda, The Netherlands*.
- Tsuchiyata, Y., T. Yamashita and M. Uemoto, 1988: A model of undertow in the surf zone; *Coastal Engineering in Japan*, Vol.30, No.2, pp.63-73.
- You, Z.-J., D.L. Wilkinson and P. Nielsen, 1991: Velocity distribution of waves and currents in combined flow; *Coastal Engineering*, Vol.15, pp.525-543.
- Yushieh, M.A., and T.Y. Chiu, 1970: Dune erosion model study; *University of Florida, Gainesville, Report UFL/COEL-70/009, 72 pp.*
- Vellinga, P., 1983: Predictive computational model for beach and dune erosion during storm surges; *Proceedings of the Conference on Coastal Structures '83, ASCE, pp.806-819*.
- Vellinga, P., 1986: Beach and dune erosion during storm surges; *Ph.D. Thesis, Delft University of Technology*; also: *Publication No.372, DELFT HYDRAULICS*.
- Verhagen, H.J., 1989: Coastal protection and dune management in the Netherlands; *Journal of Coastal Research*, Vol.6, No.1, pp 169-179.
- Visser, P.J., 1984: Uniform longshore flow current measurements and calculation; *Proceedings 19th International Conference on Coastal Engineering, pp.2192-2207, Houston*.
- Vriend, H.J. de, and M.J.F. Stive, 1987: Quasi-3D modelling of nearshore currents; *Coastal Engineering*, Vol.11, pp.565-601.
- Vriend, H.J. de, and J.S. Ribberink, 1988: A quasi-3D model of coastal morphology; *Proceedings 21th International Conference on Coastal Engineering, Malaga*.
- Watanabe, A., 1982: Numerical models of nearshore currents and beach deformation; *Coastal Engineering in Japan*, Vol.25, pp.147-161.
- Wind, H.G., and E.B. Peerbolte, 1992: Coastal zone management, tools for initial design; *Proceedings EURO-Coast 1992, Kiel, Germany*.

LIST OF SYMBOLS

symbol	unity	description
A	$m^{1/3}$	non-dimensionless shape factor in equilibrium profile
A	m^3/m^1	(cumulative) dune erosion quantity above the maximum storm surge level
A_c	m^3/m^1	computed estimate of erosion quantity A
A_m	m^3/m^1	measured estimate of erosion quantity A
A_x	m^3/m^1	(cumulative) erosion quantity landward of position x
A_z	m^3/m^1	(cumulative) erosion quantity above level z
B	m^3/m^1	constant in A -fit
c	m/s	wave phase velocity
c_f	-	friction factor ($=g/C^2$)
c_g	m/s	wave group velocity
C	$m^{1/2}/s$	Chézy coefficient
C	kg/m^3	(characteristic) sediment concentration; (time-averaged) sediment concentration
\bar{C}	kg/m^3	(time-averaged) sediment concentration
C'	kg/m^3	fluctuating component of sediment concentration
C_0	kg/m^3	reference concentration (at level $z=0$)
d	m	water depth ($=h-z_b$)
d_{max}	m	water depth below maximum surge level at seaward end of erosion profile
d_t	m	water depth below mean wave trough level ($=d-\bar{H}/2$)
D	m	grain size diameter
D	W/m^3	wave energy dissipation rate
D_{br}	W/m^3	wave energy dissipation rate due to breaking
D_{eq}	W/m^3	equilibrium wave energy dissipation rate
D_t	W/m^3	turbulent energy dissipation rate
D_{50}	m	geometric mean sediment diameter; grain size diameter such that 50 % of the grains by weight have a diameter smaller than $D=D_{50}$
exp		exponent
E	J/m^2	wave energy per unit area

LIST OF SYMBOLS (continued)

symbol	unity	description
f_c	-	distribution function of suspended sediment
f_c'	-	time function describing fluctuations according to analytical solution of $C(z,t)$
f_c	-	shape function describing time-averaged profiles according to an analytical solution of $C(z,t)$
f_p	s^{-1}	peak frequency ($=1/T_p$)
f_w	-	Jonsson's friction factor
F	-	Froude number ($=U/\sqrt{gh}$)
$F\{\}$		arbitrary function
g	m/s^2	gravitational constant
g	rad	phase of tidal component
h	m	water level with respect to the reference level (positive upward)
h_a	m	(amplitude of) astronomical component of $h(t)$
h_{gs}	m	(amplitude of) gust surge
h_s	m	(amplitude of) storm set-up related component of $h(t)$
h_0	m	mean water level
H	m	wave height
\bar{H}	m	mean wave height
H_m	m	maximum wave height in energy dissipation formulation
H_{rms}	m	root mean square wave height
H_{sig}	m	significant wave height
\hat{H}_{sig}	m	maximum significant wave height during storm surge
H_0	m	wave height at deep water
H_{0s}	m	significant wave height at deep water
i	-	counter for position steps
I_0	m	basic constant in mass flux computation
I_1	m	basic constant in sediment load function
I_2	m^2	basic constant in nett transport computation
I_3	m	basic constant in nett transport computation

LIST OF SYMBOLS (continued)

symbol	unity	description
j	-	counter for time steps
k	m^{-1}	wave number
k	m^2/s^2	time-averaged turbulent energy
k_d	m^2/s^2	estimate of time-averaged turbulent energy per unit of mass at mean water level
k_0	m^2/s^2	estimate of time-averaged turbulent energy per unit of mass at bottom boundary
K	$m^5/W/s$	constant in equilibrium transport equation according to Dean
K_c	-	dimensionless constant in reference concentration formulation
K_{cor}	-	dimensionless calibration constant in transport equation
K_{lin}	s^{-1}	constant in secondary flow equation related to linear contribution to $u(z)$
K_{log}	m/s	constant in secondary flow equation related to logarithmical contribution to $u(z)$
K_r	-	dimensionless constant in roller area formulation
K_{st}	-	constant in correction function for slope effects
K_{sw}	-	constant in correction function for swash effects
K_t	s	constant at upper boundary $z=d_t$
K_0	s	constant at lower boundary $z=0$ in secondary profile formulation
K_1	-	additional constant ($= 1 - w_s/\mu$)
K_2	-	additional constant ($= 1 + \mu d/\varepsilon$)
K_e	-	constant in reference mixing formulation
K_μ	-	constant in mixing gradient formulation
l	m	length
ln		natural logarithm
log		$^{10}\log$
L	m	characteristic length scale
L	m	wave length
L_s	kg/m^2	sediment load ($= \int_d C(z) dz$)
L_0	m	wave length at deep water ($= (g/2\pi) T^2$)

LIST OF SYMBOLS (continued)

symbol	unity	description
m	kg/m/s	mass flux
m_b	kg/m/s	breaking wave contribution to mass flux
m_r	kg/m/s	roller contribution to mass flux
M		non-dimensionless constant in velocity related transport or concentration formulation
n	-	number of points
n	-	scale factor ($= X_{prot}/X_{model}$)
n	-	ratio of wave group and phase velocity ($= c_g/c$)
n_d	-	depth scale factor
n_l	-	length scale factor
n_t	-	time scale factor
n_w	-	scale factor for fall velocity
N	-	power in velocity related transport or concentration formulation
N	-	ratio of sediment volume to total volume at the bed
p	-	porosity
p	-	mixing increase rate ($= \Delta r_c/\Delta z$)
P	J/s/m	wave energy flux ($= E c_g$)
P_{br}	-	portion of breaking waves
P_i	-	parameter in analytical solution of $C(z,t)$
P_t	J/s/m	turbulent energy flux ($= E c_g$)
Q_b	-	fraction of breaking waves in energy dissipation formulation
Q_i	-	parameter in analytical solution of $C(z,t)$
r	m	roughness length
r_c	m	concentration decay length scale ($= \varepsilon/w_s$)
r_{c0}	m	reference concentration decay length scale at level $z=0$ ($= \varepsilon_0/w_s$)
R	-	correlation coefficient
R_{cl}	m	coastal curvature
R_s	-	ratio of transport components ($= S_{corr}/S_{mean}$)

LIST OF SYMBOLS (continued)

symbol	unity	description
R_S	-	ratio of depth-integrated transport components ($= S_{corr}/S_{mean}$)
s	$m^3/m^2/s$	(time-averaged) sediment transport per unit width at a specific level
s_{corr}	$m^3/m^2/s$	correlation contribution to s ($= \overline{u' C'}$)
s_{mean}	$m^3/m^2/s$	mean contribution to s ($= \overline{u C}$)
S	$m^3/m^1/s$	(time-averaged) depth-integrated sediment transport per unit width
S	-	wave steepness
\hat{S}	-	characteristic wave steepness
S_{corr}	$m^3/m^1/s$	correlation contribution to S
S_l	$m^3/m^1/s$	contribution of lower zone ($0 < z \leq d_s$) to S
S_{max}	-	maximum wave steepness
S_{mean}	$m^3/m^1/s$	mean contribution to S
S_p	$m^3/m^1/s$	estimate of S based on measured profile development
S_u	$m^3/m^1/s$	contribution of upper zone ($z > d_s$) to S
S_{uc}	$m^3/m^1/s$	estimate of S based on $\overline{u}(z)$ and $\overline{C}(z)$
S_x	$m^3/m^1/s$	sediment transport per unit width in cross-shore direction
S_y	$m^3/m^1/s$	sediment transport per unit width in alongshore direction
t	s	time (wave period related time scale)
t	hr	time (storm surge related time scale)
t_{hw}	hr	characteristic duration of high water; time the $(h_{max} - 1)$ -level is exceeded
t_{ma}	hr	moment of maximum first-order astronomical component
t_{mgs}	hr	moment of maximum gust surge
t_{ms}	hr	moment of maximum storm set-up
T	s	wave period
T_a	hr	duration of first-order component of astronomical tide
T_{gs}	hr	duration of gust surge
T_H	hr	interval of wave height component
T_p	s	peak (of spectrum) wave period

LIST OF SYMBOLS *(continued)*

symbol	unity	description
\hat{T}_p	s	maximum peak period during storm surge
T_s	hr	duration of storm effect
T_T	hr	interval of wave period component
u'	m/s	fluctuation in horizontal velocity
u	m/s	time-averaged value of horizontal component of velocity field (overbar omitted)
\bar{u}	m/s	time-averaged value of horizontal component of velocity field
u_{rms}	m/s	root mean square orbital velocity
u_0	m/s	(virtual) velocity at reference level
U	m/s	characteristic velocity
v	m/s	time-averaged magnitude of horizontal alongshore component of velocity field
v_0	m/s	(virtual) alongshore velocity at reference level
w	m/s	time-averaged value of vertical component of velocity field (overbar omitted)
w_s	m/s	fall velocity of sediment with grain size $D = D_{50}$, in stagnant water
x	m	horizontal cross-shore coordinate
x_{max}	m	seaward limit of erosion profile with respect to dune foot
X_{cl}	m	coastal position related to coastal curvature
X_0	m	seaward boundary of cross-shore profile
y	m	additional vertical ordinate
y	m	horizontal alongshore coordinate
y^*	m	characteristic penetration depth
z	m	vertical coordinate (positive upward)
z_b	m	vertical coordinate of bed profile with respect to the reference level
z_s	m	vertical coordinate of structure with respect to the reference level
Z_0	m	reference level for A_x -computations
Z_5	m	characteristic level of storm surge; the water level which is exceeded during 5 hours

LIST OF SYMBOLS (continued)

symbol	unity	description
α	rad	phase shift in velocity fluctuations
α	m/s^2	constant in shear stress equation ($= 1/\rho \, d\tau/dz$)
α_i	-	additional constant in analytical solution of $C(z,t)$
α_D	-	power in F_D -function
α_k	-	constant in penetration depth formulation
β	rad	phase shift in concentrations fluctuations
β	m^2/s^2	constant in shear stress equation ($= \tau_0/\rho$)
γ	-	numerical smoothing factor in bottom scheme
γ	m/s	integration constant in secondary flow equation ($= u_0$)
γ	-	breaker index ($= \gamma_{rms}$)
γ_{rms}	-	breaker index ($= H_{rms}/d$)
γ_{sig}	-	breaker index ($= H_s/d$)
δ	-	fraction
Δ	-	relative density of sediment with respect to water ($= (\rho_s - \rho_f)/\rho_f$)
$\Delta\alpha$	m	shift in coast line angle
Δs	m	alongshore interval at $x = X_{ct}$
Δx	m	horizontal cross-shore step
Δy	m	horizontal alongshore step
Δz	m	vertical step
ε	m^2/s	mixing coefficient of the sediment (subscript s omitted)
ε_f	m^2/s	mixing (or diffusion) coefficient of the fluid
ε_s	m^2/s	mixing (or diffusion) coefficient of the sediment
ε_t	m^2/s	mixing coefficient at level $z = d_t$
ε_0	m^2/s	reference mixing coefficient at level $z = 0$
ζ	m	alongshore water level
η	m	(time-averaged) mean elevation of the water level above the mean level \bar{h} due to wave set-up or set-down (overbar omitted)
θ	rad	angle of wave attack with respect to shore normal

LIST OF SYMBOLS *(continued)*

symbol	unity	description
θ_0	rad	angle of wave attack at seaward boundary
θ_{cr}	-	critical Shields parameter
Λ	-	time lag parameter
μ	m/s	vertical mixing gradient ($= \Delta \varepsilon / \Delta z$)
μm		micro-meter ($= 10^{-6}$ m)
ν	m ² /s	kinematic viscosity coefficient
ξ	-	relative erosion of additional storm surge
π		constant ($= 3.1415926535\dots$)
ρ	kg/m ³	mass density of fluid (water) (subscript f omitted)
ρ_b	kg/m ³	mass density of settled sediment ($= (1-p) \rho_s$)
ρ_s	kg/m ³	mass density of sediment
σ	-	standard deviation
τ	N/m ²	(time-averaged) shear stress (overbar omitted)
τ_{cr}	N/m ²	critical shear stress
τ_t	N/m ²	(time-averaged) shear stress at wave trough level $z = d_t$ (overbar omitted)
τ_0	N/m ²	reference (time-averaged) shear stress at level $z = 0$ (overbar omitted)
ν	m ² /s	kinematic viscosity
ϕ	rad	angle of wave attack, with respect to cross-shore direction
ω	rad/s	angular frequency ($= 2 \pi / T$)

LIST OF TABLES

	<i>page</i>
2.1 Existing problems, related examples, proposed solutions and model development phases.	12
2.2 General overview of investigations and additional data.	13
2.3 Overview of test series carried out at DELFT HYDRAULICS which were used for the development of the present model.	15
6.1 Overview of (model) test-series used for verification.	131
6.2 Overview of the tests of the M1263-III-series.	135
6.3 Summary of ultimate dune erosion quantities for model tests of the M1263-III-series.	138
6.4 Overview of the tests of the M1819-I-series.	145
6.5 Overview of model tests with fixed hydraulic conditions of the M1819-I-series.	146
6.6 Overview of dune erosion quantities for model tests with fixed hydraulic conditions of the M1819-I-series.	151
6.7 Overview of model tests with varying hydraulic conditions of the M1819-I-series.	152
6.8 Overview of dune erosion quantities for model tests with varying hydraulic conditions of the M1819-I-series.	160
6.9 Overview of the model tests of the GWK-series.	162
6.10 Overview of symbols used for accuracy assessment.	180
6.11 Overview of the model tests of the H298-I-series.	187

LIST OF FIGURES

	<i>page</i>
1.1 Dunes as a primary sea defence system.	1
2.1 Overview of causal relations for beach and dune erosion.	6
2.2 Position of the dunefoot in the period 1910 until 1980 at the coast of Den Helder.	7
2.3 Effects of a storm surge.	8
2.4 Outline of the erosion-profile method according to Vellinga.	9
2.5 Example of erosion profile and subsequent dune erosion according to Vellinga.	10
2.6 Example of the standard North Sea storm surge hydrograph.	11
2.7 Example of large-scale model test result for an unprotected dune; test T5 of H298-I-test series.	13
2.8 Photo of wave attack on a dune in the Deltaflume.	14
2.9 Plan of approach for model development.	16
3.1 Cross-shore evolution scales; after (Stive, 1991).	18
4.1 Magnitude of reduction parameter Ω as a function of the time-lag parameter Λ for a number of harmonics.	39
4.2 Example of active/passive behaviour of near-bottom concentration.	41
4.3 Example of computed concentration profiles during a wave cycle.	42
4.4 Example of computed development of concentrations at different levels.	42
4.5 Example of computed profiles of the transport contributions.	43
4.6 Vertical distributions of sediment transport rate over the water depth according to (Chen, 1992a)	44
4.7 Schematic description of the time-averaged concentration profile.	48
4.8 Procedure for the examination of concentration profiles.	49
4.9 Photo of the measurement carriage equipped with concentration measurement device (left) and velocity measurement devices (right) in the Deltaflume.	50
4.10 Example of some measured suspended sediment concentration profiles; test T3 of H298-I-series, position $x = 187$ m.	51
4.11 Illustration of the fit procedure to compute the best estimate of the local tangent.	54
4.12 Example of C(z)-fit procedure; test T1F1 of H298-I-series.	55
4.13 Schematic description of the vertical distribution of the mixing coefficient.	57
4.14 Influence of near-bottom mixing rate on the concentration profile.	59
4.15 Influence of the μ -parameter on the concentration profile.	59
4.16 Influence of the fall velocity on the concentration profile.	61
4.17 Influence of the (μ/w_s) -ratio on the concentration profile.	62
4.18 Schematic description of the mean shear stress distribution.	66
4.19 Composition of the secondary flow profile.	69
4.20 Example of measured velocities and accompanying computed flow profile.	74
4.21 Example of nett transport computation based on velocity and concentration profile; test T3I4 at location $x = 181$ m.	79
4.22 Example of the development of erosion rates; test T3 of H298-I-series.	81
4.23 Example of transport computation based on measurement of an observed profile development; test T3 of H298-I-series.	82
4.24 Comparison between computed and measured transport rates.	83
4.25 Detailed comparison between computed and measured transport rates on linear scales.	84
4.26 Definitions and coordinate system used in the computational program.	85
4.27 Aggregate flow-chart of the computational model.	86
4.28 Example of longshore flow profile for three types of boundary conditions.	94
4.29 Schematic outline of double-ray approach for a uniform curved coastline.	96
5.1 Outline of the applied calibration procedure.	100
5.2 Schematic example of profiles used for the wave-height decay fit procedure.	102
5.3 Result of the fit procedure for test T2 of the M1263-III-test series.	104

LIST OF FIGURES *(continued)*

	<i>page</i>	
5.4	Standard deviation for a range of α -values.	105
5.5	Standard deviation as a function of breaker index for two friction factors.	106
5.6	Standard deviation for a range of friction factors.	106
5.7	Computed reference mixing as a function of estimated breaker index.	108
5.8	Computed reference mixing/velocity ratio as a function of estimated breaker index.	109
5.9	Computed mixing rate at trough level as a function of estimated breaker index.	110
5.10	Computed mixing increase rate μ as a function of estimated breaker index.	111
5.11	Computed μ/c -ratio as a function of estimated breaker index.	111
5.12	Relation between measured reference concentration and computed (breaking) dissipation rates.	113
5.13	Relation between measured reference concentration and computed (turbulent) dissipation rates.	115
5.14	Assumed behaviour of breaking-function.	116
5.15	Dependency of estimated breaker index.	117
5.16	Comparison between measured and computed reference concentrations.	118
5.17	Comparison between measured and computed reference concentrations on linear scales.	119
5.18	Measured profile development for test T2 of the M1263-III-series.	121
5.19	Detail of measured profile development for test T2 of the M1263-III-series.	121
5.20	Detail of computed profile development for test T2 of the M1263-III-series.	123
5.21	Measured profile development for test T04 of the M1819-III-series.	124
5.22	Computed profile development for test T04 of the M1819-III-series.	125
5.23	Location of measurements; test T3 of the H298-I-test series, phase I, viz. 9.5 - 12.5 hrs).	126
5.24	Computed cross-shore distribution of reference concentration compared with measured magnitudes.	127
5.25	Computed vertical distribution of suspended sediment concentration compared with measured profiles for three data sets.	127
5.26	Comparison between computed and measured time-averaged velocities.	128
5.27	Comparison between computed and measured secondary flow profiles.	128
6.1	Hydraulic conditions used in test T1 (and T2) of the M1797-series.	132
6.2	Comparison between measured and computed post-storm profiles for test T1 of the M1797-series.	133
6.3	Hydraulic conditions used in the M1811-series.	133
6.4	Comparison between the measured and computed post-storm profiles for the M1811-series.	134
6.5	Overview of profiles for test T1 of the M1263-III-series.	136
6.6	Comparison between measured and computed post-storm profiles for test T1 of the M1263-III-series.	136
6.7	Overview of profiles for test T2 of the M1263-III-series.	137
6.8	Comparison between measured and computed post-storm profiles for test T2 of the M1263-III-series.	137
6.9	Hydraulic conditions used for test T3 of the M1263-III-series.	138
6.10	Overview of profiles for test T3 of the M1263-III-series.	139
6.11	Comparison between measured and computed post-storm profiles for test T3 of the M1263-III-series.	139
6.12	Development of erosion quantity for both constant and varying conditions.	140
6.13	Overview of profiles for test T4 of the M1263-III-series.	140
6.14	Hydraulic conditions used for test T4 of the M1263-III-series.	141
6.15	Comparison between measured and computed post-storm profiles for test T4 of the M1263-III-series.	141
6.16	Overview of profiles for test T5 of the M1263-III-series.	142
6.17	Comparison between measured and computed post-storm profiles for test T5 of the M1263-III-series.	142
6.18	Overview of profiles for test T5 of the H298-I-series.	143
6.19	Comparison between measured and computed post-storm profiles for test T5 of the H298-I-series.	144

LIST OF FIGURES *(continued)*

	<i>page</i>	
6.20	Overview of profile used for tests with fixed hydraulic conditions.	145
6.21	Comparison of final profiles for test T01 of M1819-I-series (fixed conditions).	146
6.22	Comparison of final profiles for test T02 of M1819-I-series (fixed conditions).	147
6.23	Comparison of final profiles for test T03 of M1819-I-series (fixed conditions).	147
6.24	Comparison of final profiles for test T04 of M1819-I-series (fixed conditions).	147
6.25	Comparison of final profiles for test T05 of M1819-I-series (fixed conditions).	148
6.26	Comparison of final profiles for test T06 of M1819-I-series (fixed conditions).	148
6.27	Comparison of final profiles for test T07 of M1819-I-series (fixed conditions).	148
6.28	Comparison of final profiles for test T08 of M1819-I-series (fixed conditions).	149
6.29	Comparison of final profiles for test T09 of M1819-I-series (fixed conditions).	149
6.30	Comparison of final profiles for test T10 of M1819-I-series (fixed conditions).	149
6.31	Comparison of final profiles for test T11 of M1819-I-series (fixed conditions).	150
6.32	Comparison of final profiles for test T12 of M1819-I-series (fixed conditions).	150
6.33	Comparison of final profiles for test T13 of M1819-I-series (fixed conditions).	150
6.34	Comparison of final profiles for test T29 of M1819-I-series (fixed conditions).	151
6.35	Hydraulic conditions used in tests T21-T28 of M1819-I-series.	152
6.36	Overview of profiles used in the tests with varying hydraulic conditions.	153
6.37	Observed profile development during storm surge for test T21 of the M1819-I-series.	154
6.38	Comparison of the final profiles for test T21 of the M1819-I-series (varying conditions).	154
6.39	Erosion development during test T21 of the M1819-I-series.	154
6.40	Comparison of final profiles for test T22 of M1819-I-series (var. conditions).	155
6.41	Comparison of final profiles for test T23 of M1819-I-series (var. conditions).	155
6.42	Comparison of final profiles for test T24 of M1819-I-series (var. conditions).	156
6.43	Comparison of final profiles for test T25 of M1819-I-series (var. conditions).	156
6.44	Comparison of final profiles for test T26 of M1819-I-series (var. conditions).	156
6.45	Comparison of final profiles for test T27 of M1819-I-series (var. conditions).	157
6.46	Comparison of final profiles for test T28 of M1819-I-series (var. conditions).	157
6.47	Overview of measured post-storm profiles for test T21-T27 of the M1819-I-series.	158
6.48	Overview of computed post-storm profiles for test T21-T27 of the M1819-I-series.	159
6.49	Hydraulic conditions used in the M1819-III-series.	160
6.50	Comparison between measured and computed final profiles for test T1 of the M1819-III-series.	161
6.51	Comparison of profile development for test T1 of the GWK-series.	163
6.52	Comparison of profile development for test T2 of the GWK-series.	163
6.53	Detailed comparison of profile development for test T2 of the GWK-series.	164
6.54	Comparison of profile development for test T3 of the GWK-series.	165
6.55	Comparison of profile development for test T4 of the GWK-series.	165
6.56	Detailed comparison of profile development for test T4 of the GWK-series.	166
6.57	Comparison of profile development for test T5 of the GWK-series.	166
6.58	Detailed comparison of profile development for test T5 of the GWK-series.	167
6.59	Comparison of profile development for test T6 of the GWK-series.	167
6.60	Hydraulic conditions during the 1953-storm surge.	169
6.61	Computed erosion due to 1953-storm surge.	170
6.62	Hydraulic conditions during hurricane Eloise.	170
6.63	Computed erosion due to the hurricane Eloise.	171
6.64	Hydraulic conditions during the extreme event.	172
6.65	Computed erosion due to the extreme event.	172
6.66	Effect of the water level on the erosion quantity.	174
6.67	Effect of the wave height on the erosion quantity.	175
6.68	Effect of the wave period on the erosion quantity.	176
6.69	Comparison between measured and computed erosion rates for tested hydraulic conditions.	176
6.70	Effect of dune height on the erosion quantity.	177
6.71	Effect of bars and troughs on the erosion quantity.	178
6.72	Overview of test results for all tested conditions.	179
6.73	Comparison between measured and computed erosion rates; linear scales.	180

LIST OF FIGURES *(continued)*

	<i>page</i>	
6.74	Detail of the comparison between measured and computed erosion rates; linear scales.	181
6.75	Comparison between measured and computed erosion rates; logarithmical scales.	181
6.76	Comparison between measured and computed erosion rates for small-scale data.	182
6.77	Comparison between measured and computed erosion rates for large-scale data.	183
6.78	Comparison of final profiles for test T4 of the M1819-III-series.	184
6.79	Hydraulic conditions used in test T1 and T4 of the M2051-II-series.	185
6.80	Comparison of scour-hole development for test T1 of the M2051-II-series.	185
6.81	Comparison of scour-hole development for test T2 of the M2051-II-series.	186
6.82	Comparison of scour-hole development for test T3 of the M2051-II-series.	186
6.83	Comparison of scour-hole development for test T4 of the M2051-II-series.	187
6.84	Comparison of scour-hole development for test T1 of the H298-I-series.	188
6.85	Comparison of final profiles for test T2 of the M1797-series.	188
6.86	Comparison of final profiles for test T2 of the M1819-III-series.	189
6.87	Comparison of final profiles for test T3 of the M1819-III-series.	190
6.88	Comparison of final profiles for test T2 of the H298-I-series.	190
6.89	Comparison of final profiles for test T3 of the H298-I-series.	191
6.90	Hydraulic conditions used in test T4 of the H298-I-series.	191
6.91	Comparison of final profiles for test T4 of the H298-I-series.	192
6.92	Relative effect of the revetment level based on measured cross-shore profiles.	193
6.93	Relative effect of the revetment level based on computations.	193
6.94	Computed cross-shore distribution of longshore current.	194
6.95	Computed distribution of longshore transport according to several longshore transport formulae.	195
6.96	Computed rate of longshore transport according to several longshore transport formulae for a range of wave heights.	196
6.97	Computed rate of longshore transport according to several longshore transport formulae for a range of wave heights; on log-log scale.	197
7.1	Fall velocity as a function of sediment diameter in sea water.	201
7.2	Overview of reference hydraulic conditions used for sensitivity assessment.	202
7.3	Computed post-storm profile for reference conditions.	203
7.4	Effect of slope nearshore zone on the erosion rate.	204
7.5	Effect of sediment diameter on the erosion rate.	206
7.6	Effect of storm surge level on the erosion rate.	207
7.7	Effect of storm duration on the erosion rate.	208
7.8	Effect of wave height on the erosion rate.	209
7.9	Effect of wave period on the erosion rate.	210
7.10	Effect of wave attack on the erosion rate.	211
7.11	Effect of a time shift on the resulting water level fluctuation.	212
7.12	Effect of a time shift on the erosion rate.	212
7.13	Effect of divergent hydraulic conditions on the erosion rate.	214
7.14	Computed post-storm profiles for five successive storm events.	215
7.15	Computed development of dune erosion quantity for five successive storm events.	216
7.16	Successive post-storm profiles compared with Bruun-profile.	217
8.1	General procedure for the assessment of hydraulic conditions during a storm surge.	220
8.2	Assumed relation between storm set-up and significant wave height at deep water.	222
8.3	Comparison between basic and measured relation.	222
8.4	Assumed relation between significant wave height and peak wave period.	223
8.5	Comparison with measured data during 1990-storm surge.	224
8.6	Standard cross-shore profile used for applications.	225
8.7	Hydraulic conditions used for application.	226
8.8	Computed profile development for standard cross-shore profile.	226
8.9	Computed effect of beach/dune nourishment in comparison to a profile without nourishment.	227
8.10	Computed effect of high revetment in comparison to a profile without a revetment.	228

LIST OF FIGURES *(continued)*

	<i>page</i>
8.11 Computed effect of lower revetment in comparison to a profile without a revetment.	229
8.12 Computed effect of dam in comparison to a profile without any construction.	230
8.13 Computed effect of oblique wave attack (at 30 degrees) in comparison to the effect of perpendicular wave attack.	231
8.14 Computed effect of angle of wave attack on dune erosion quantity.	232
8.15 Computed effect of angle of wave attack on longshore transport rate.	233
8.16 Computed effect of coastal curvature in comparison to a non-curved coastline.	233

Appendix: Elaboration of basic integrals

In the following, the basic integrals I_i for $i = 0, \dots, 3$ are elaborated in more detail.

Integral I_0

The depth-integral I_0 (in m), as used in the expression for the mass flux (continuity condition), see Equation (4.4.20), is defined as follows:

$$I_0 = \int_{z_1}^{z_2} \ln \left[1 + \frac{\mu z}{\varepsilon_0} \right] dz \quad (A.1)$$

with $z_1 = 0$ and $z_2 = d_t$.

Substitution of:

$$Y = 1 + \frac{\mu z}{\varepsilon_0} \quad \text{with} \quad dY = \frac{\mu}{\varepsilon_0} dz \quad (A.2)$$

while using the integration bounds:

$$\begin{aligned} z_1 = 0 &\quad \Rightarrow \quad Y_1 = 1 \\ z_2 = d_t &\quad \Rightarrow \quad Y_2 = 1 + \frac{\mu}{\varepsilon_0} d_t \end{aligned} \quad (A.3)$$

yields:

$$I_0 = \frac{\varepsilon_0}{\mu} \int_{Y_1}^{Y_2} \ln Y \, dY = \frac{\varepsilon_0}{\mu} \left[Y (\ln Y - 1) \right]_{Y_1}^{Y_2} \quad (A.4)$$

Substitution of the bounds and subsequent elaboration results in:

$$I_0 = \frac{\varepsilon_0}{\mu} \left[\left(1 + \frac{\mu d_t}{\varepsilon_0} \right) \left(\ln \left[1 + \frac{\mu d_t}{\varepsilon_0} \right] - 1 \right) + 1 \right] \quad (A.5a)$$

or:

$$I_0 = \frac{\varepsilon_0}{\mu} \left[K_2 (\ln K_2 - 1) + 1 \right] \quad (A.5b)$$

with:

$$K_2 = 1 + (\mu/\varepsilon_0) d_t \quad (A.6)$$

In the case of the continuity equation for the longshore current according to Equation (4.8.12), the depth-integration is restricted to the mean water depth. So in the K_2 -formula the level d_t has to be replaced by d .

Integral I_1

The depth-integral I_1 (in m) is used in both the formulation of the sediment load L_s as the uniform contribution to the nett transport rate below the wave trough level. This latter transport contribution, see Equation (4.5.5), is defined as:

$$I_1 = \int_{z_1}^{z_2} \left[l + \frac{\mu z}{\varepsilon_0} \right]^{(-w_s/\mu)} dz \quad (A.7)$$

in which $z_1 = 0$ and $z_2 = d_t$.

Substitution of:

$$Y = l + \frac{\mu z}{\varepsilon_0} \text{ with } dY = \frac{\mu}{\varepsilon_0} dz \quad (A.8)$$

while using the integration bounds:

$$\begin{aligned} z_1 = 0 & \Rightarrow Y_1 = l \\ z_2 = d_t & \Rightarrow Y_2 = l + \frac{\mu}{\varepsilon_0} d_t \end{aligned} \quad (A.9)$$

yields:

$$I_1 = \frac{\varepsilon_0}{\mu} \int_{Y_1}^{Y_2} Y^{(-w_s/\mu)} dY = \frac{\varepsilon_0}{\mu} \frac{l}{1 - w_s/\mu} Y^{(1 - w_s/\mu)} \Bigg|_{Y_1}^{Y_2} \quad (A.10)$$

Substitution of the bounds and subsequent elaboration results in:

$$I_1 = \frac{\varepsilon_0}{\mu} \frac{l}{1 - w_s/\mu} \left[\left(l + \frac{\mu d_t}{\varepsilon_0} \right)^{1 - w_s/\mu} - l \right] \quad (A.11a)$$

or:

$$I_1 = \frac{\varepsilon_0}{\mu} \frac{l}{K_1} \left[K_2^{K_1} - l \right] \quad (A.11b)$$

in which the dimensionless constants K_1 and K_2 are defined as:

$$K_1 = 1 - w_s/\mu \quad (A.12)$$

$$K_2 = l + (\mu/\varepsilon_0) d_t \quad (A.13)$$

Due to a different upper integration limit z_2 in both the sediment load formulation, Equation (4.3.22a), and the formulation of the longshore current, Equation (4.8.21), namely d instead of d_t , the latter K_2 -relation has to be adjusted.

Integral I_2

The depth-integral I_2 (in m^2) denotes the linear contribution to the nett transport rate below the wave trough level and is defined as, see Equation (4.5.6):

$$I_2 = \int_{z_1}^{z_2} z \left[1 + \frac{\mu z}{\varepsilon_0} \right]^{(-w_s/\mu)} dz \quad (A.14)$$

in which $z_1 = 0$ and $z_2 = d_t$.

Substitution of:

$$Y = \frac{\mu z}{\varepsilon_0} \quad \text{with} \quad dY = \frac{\mu}{\varepsilon_0} dz \quad (A.15)$$

while using the integration bounds:

$$\begin{aligned} z_1 = 0 &\Rightarrow Y_1 = 0 \\ z_2 = d_t &\Rightarrow Y_2 = \frac{\mu}{\varepsilon_0} d_t \end{aligned} \quad (A.16)$$

yields:

$$\begin{aligned} I_2 &= \left(\frac{\varepsilon_0}{\mu} \right)^2 \int_{Y_1}^{Y_2} Y (1+Y)^{(-w_s/\mu)} dY \\ &= \left(\frac{\varepsilon_0}{\mu} \right)^2 \frac{1}{1-w_s/\mu} \int_{Y_1}^{Y_2} Y d[(1+Y)^{(1-w_s/\mu)}] \\ &= \left(\frac{\varepsilon_0}{\mu} \right)^2 \frac{1}{1-w_s/\mu} \left\{ Y (1+Y)^{(1-w_s/\mu)} \Big|_{Y_1}^{Y_2} - \int_{Y_1}^{Y_2} (1+Y)^{(1-w_s/\mu)} dY \right\} \\ &= \left(\frac{\varepsilon_0}{\mu} \right)^2 \frac{1}{1-w_s/\mu} \left\{ Y (1+Y)^{(1-w_s/\mu)} - \frac{1}{2-w_s/\mu} (1+Y)^{(2-w_s/\mu)} \right\} \Big|_{Y_1}^{Y_2} \end{aligned} \quad (A.17)$$

Substitution of the bounds and subsequent elaboration results in:

$$I_2 = \frac{\varepsilon_0}{\mu} \frac{1}{1-w_s/\mu} \left[\left(1 + \frac{\mu d_t}{\varepsilon_0} \right)^{(1-w_s/\mu)} \left(d_t - \frac{\varepsilon_0}{\mu} \frac{1 + (\mu/\varepsilon_0)d_t}{2-w_s/\mu} \right) + \frac{\varepsilon_0}{\mu} \frac{1}{2-w_s/\mu} \right] \quad (A.18a)$$

or:

$$I_2 = \frac{\varepsilon_0}{\mu} \frac{1}{K_1} \left[K_2 K_1 \left(d_t - \frac{\varepsilon_0}{\mu} \frac{K_2}{K_1+1} \right) + \frac{\varepsilon_0}{\mu} \frac{1}{K_1+1} \right] \quad (A.18b)$$

in which:

$$K_1 = 1 - w_s/\mu \quad (A.19)$$

$$K_2 = 1 + (\mu/\varepsilon_0)d_t \quad (A.20)$$

Using the latter equations for the longshore transport computation according to Equation (4.8.22), will require another upper integration limit, namely d instead of d_t . Consequently, both the I_2 - and K_2 -formula have to be adjusted.

Integral I_3

The depth-integral I_3 (in m) denotes the logarithmical contribution to the nett transport rate below the wave trough level and is defined as, see Equation (4.5.7):

$$I_3 = \int_{z_1}^{z_2} \ln \left[1 + \frac{\mu z}{\varepsilon_0} \right] \left[1 + \frac{\mu z}{\varepsilon_0} \right]^{(-w_s/\mu)} dz \quad (A.21)$$

in which $z_1 = 0$ and $z_2 = d_t$.

Substitution of:

$$Y = \ln \left(1 + \frac{\mu z}{\varepsilon_0} \right) \text{ with } dY = \frac{\mu}{\varepsilon_0} \frac{1}{1 + (\mu/\varepsilon_0)z} dz \quad (A.22)$$

and so:

$$dz = \frac{\varepsilon_0}{\mu} \exp(Y) dY \quad (A.23)$$

while using the integration bounds:

$$\begin{aligned} z_1 = 0 & \Rightarrow Y_1 = 0 \\ z_2 = d_t & \Rightarrow Y_2 = \ln \left[1 + \frac{\mu}{\varepsilon_0} d_t \right] \end{aligned} \quad (A.24)$$

yields:

$$\begin{aligned} I_3 &= \frac{\varepsilon_0}{\mu} \int_{Y_1}^{Y_2} Y \exp \left(\frac{-w_s}{\mu} Y \right) \exp(Y) dY \\ &= \frac{\varepsilon_0}{\mu} \frac{\exp(Y(1 - w_s/\mu))}{(1 - w_s/\mu)^2} (Y(1 - w_s/\mu) - 1) \Big|_{Y_1}^{Y_2} \end{aligned} \quad (A.25)$$

Substitution of the bounds and subsequent elaboration results in:

$$I_3 = \frac{\varepsilon_0}{\mu} \frac{1}{(1 - w_s/\mu)^2} \left[\left(1 + \frac{\mu}{\varepsilon_0} d_t \right)^{(1 - w_s/\mu)} \left((1 - w_s/\mu) \ln \left(1 + \frac{\mu}{\varepsilon_0} d_t \right) - 1 \right) + 1 \right] \quad (A.26a)$$

or:

$$I_3 = \frac{\varepsilon_0}{\mu} \frac{1}{K_1^2} \left[K_2^{K_1} (K_1 \ln(K_2) - 1) + 1 \right] \quad (A.26b)$$

in which both dimensionless constants K_1 and K_2 are defined as:

$$K_1 = 1 - w_s/\mu \quad (A.27)$$

$$K_2 = 1 + (\mu/\varepsilon_0)d_t \quad (A.28)$$

Using former equations for the longshore transport computation, see Equation (4.8.23), will result in another upper integration limit, namely d instead of d_t . Consequently the K_2 -formula has to be adjusted.

Curriculum Vitae

Henk Steetzel werd geboren op 22 januari 1958 te Groesbeek. Hij volgde middelbaar onderwijs aan de Nijmeegse Scholengemeenschap te Nijmegen waar hij het havo-diploma behaalde in 1975.

Daarna werd in Arnhem de HTS bezocht waar hij bij de afdeling Weg- en Waterbouwkunde in 1979 zijn diploma met lof in ontvangst nam. Tijdens de studie werd stage gelopen bij zowel de Dienst Bovenrivieren van de Rijkswaterstaat als bij Adviesbureau Arnhem van de Heidemij.

Na vervulling van de dienstplicht werd in 1980 begonnen met de studie voor civiel ingenieur aan de Technische Universiteit te Delft. Deze studie werd in 1984 besloten met een bij WL (Waterloopkundig Laboratorium) uitgevoerd onderzoek naar sedimentsuspensie boven een zandbed onder invloed van een oscillerende waterbeweging. In 1984 werd cum laude het ingenieursdiploma behaald.

In november 1984 trad Henk Steetzel in dienst van WL waar hij onder andere het werk van Pier Vellinga met betrekking tot het duinafslagonderzoek voortzette. Naast de fysische modellering werd in dit onderzoek ook aandacht besteed aan de interferentie met constructies. Dit onderzoek heeft uiteindelijk geleid tot het duinafslagmodel als beschreven in dit proefschrift.

Thans is hij werkzaam als senior research engineer, betrokken bij diverse projecten met een kustmorfologisch karakter, waaronder het onderzoek naar het proces van bresgroei tijdens de doorbraak van een zandige waterkering, zoals dat thans in opdracht van de Technische Adviescommissie voor de Waterkeringen (TAW) wordt uitgevoerd. Hierbij is zijn aandachtsgebied langzamerhand verschoven van de modellering van processen dwars op de kust (dwarstransport) naar de meer grootschalige morfodynamica van kustgebieden. De voorspelling van de grootschalige ontwikkeling van de eilanden en buitendelta's van de Nederlandse Waddenkust zoals thans in uitvoering in opdracht van Rijkswaterstaat ten behoeve van de eerstvolgende Kustnota, is hiervan een treffend voorbeeld.

.....

